WCAP-7665

PWR FLECHT
(FULL LENGTH EMERGENCY COOLING HEAT TRANSFER)
FINAL REPORT

F. F. Cadek

D. P. Dominicis

R. H. Leyse

April 1971

APPROVED: L. S. Tong
Program Technical Director

APPROVED: H. A. Sindt
Project Engineer

Work Performed Under Contract AT(10-1)-1230,
Subcontract S-7045 Between Westinghouse
Electric Corporation & Idaho Nuclear Corporation

WESTINGHOUSE ELECTRIC CORPORATION
Nuclear Energy Systems
P. O. Box 355
Pittsburgh, Pennsylvania 15230

LEGAL NOTICE

This report was prepared as an account of Government sponsored work. Neither the United States, nor the Commission, nor any person acting on behalf of the Commission:

A. Makes any warranty or representation, expressed or implied, with respect to the accuracy, completeness, or usefulness of the information contained in this report, or that the use of any information, apparatus, method, or process disclosed in this report may not infringe privately owned rights; or

B. Assumes any liabilities with respect to the use of, or for damages resulting from the use of any information, apparatus, method, or process disclosed in this report.

As used in the above, "person acting on behalf of the Commission" includes any employe or contractor of the Commission, or employe of such contractor, to the extent that such employe or contractor of the Commission, or employe of such contractor prepares, disseminates, or provides access to, any information pursuant to his employment or contract with the Commission, or his employment with such contractor.

TABLE OF CONTENTS

Section	Title	Page
1	INTRODUCTION	1-1
	1.1 OBJECTIVE	1-1
	1.2 REPORT CONTENTS AND RELATIONSHIP TO OVERALL PROGRAM	1-1
2	TEST DESCRIPTION	2-1
	2.1 TEST BUNDLE DESCRIPTION	2-1
	2.1.1 Geometry	2-1
	2.1.2 Thermocouple Locations	2-7
	2.1.3 Pressure Transducer Locations	2-11
	2.2 FACILITY DESCRIPTION	2-11
	2.3 TEST PROCEDURE	2-16
3	DISCUSSION OF TEST RESULTS	3-1
	3.1 SUMMARY OF RUN CONDITIONS AND TEST RESULTS	3-1
	3.2 GROUP I AND GROUP II STAINLESS CLAD HEAT TRANSFER RESULTS	3-10
	3.2.1 Data Verification	3-10
	3.2.1.1 Reproducibility and Test Bundle Symmetry	3-10
	3.2.1.2 Effect of Bundle Size and Radial Variation of the Heat Transfer Coefficient	3-12
	3.2.1.3 Effect of Flow Housing Temperature	3-18
	3.2.2 System Parameter Effects on Heat Transfer	3-21
	3.2.2.1 Initial Clad Temperature	3-21
	3.2.2.2 Flooding Rate	3-24
	3.2.2.3 Inlet Coolant Subcooling	3-24
	3.2.2.4 Pressure	3-31
	3.2.2.5 Peak Power Generation	3-31

TABLE OF CONTENTS (Cont.)

Section	Title	Page
3.2.2.6	Power Decay Rate	3-35
3.2.2.7	Heat Transfer Behavior with Borated Coolant	3-39
3.2.3	Heat Transfer Behavior at Different Elevations	3-39
3.2.4	Variable Flooding Rate Tests	3-44
3.2.4.1	Variable Flooding Rate Test Results	3-44
3.2.4.2	Fallback Effect on Heat Transfer	3-50
3.2.4.3	Comparison of Constant and Variable Flooding Rate Heat Transfer Results	3-50
3.2.5	Flow Blockage Tests	3-58
3.2.5.1	Effect of Flow Blockage on Temperature Response	3-62
3.2.5.2	Effect of Flow Blockage on Midplane Heat Transfer Coefficients	3-64
3.2.5.3	Effect of Flow Blockage at Other Elevations	3-64
3.2.5.4	Heat Transfer in the Variable Flooding Rate Test with Flow Blockage	3-67
3.3	HEAT TRANSFER REGIMES AND CORRELATIONS	3-69
3.3.1	Heat Transfer and Flow Regimes	3-69
3.3.1.1	Movie Observations	3-69
3.3.1.2	Heat Transfer and Flow Regimes	3-77
3.3.2	Constant Flooding Rate Heat Transfer Correlations	3-80
3.3.3	Variable Flooding Rate Correlations	3-88
3.4	GROUP III ZIRCALOY CLAD TEST RESULTS	3-95
3.4.1	Test Results	3-95
3.4.1.1	"Early" Group III Tests - Runs 2443 and 2544	3-95
3.4.1.2	Later Group III Tests - Runs 8874 and 9573	3-96
3.4.2	Comparison to Stainless Steel Results	3-98

TABLE OF CONTENTS (Cont.)

Section	Title	Page
	3.4.2.1 Comparison of Zircaloy and Stainless Steel Temperature Response	3-98
	3.4.2.2 Comparison of Zircaloy and Stainless Steel Heat Transfer Coefficients	3-101
	3.5 PRESSURE TRANSDUCER RESULTS	3-110
	3.5.1 Radial Pressure Drop	3-110
	3.5.2 Axial Pressure Drop	3-110
	3.5.2.1 Axial Pressure Drop in Constant Flooding Rate Tests	3-110
	3.5.2.2 Axial Pressure Drop in Variable Flooding Rate Tests	3-113
	3.5.2.3 Axial Pressure Drop in the Flow Blockage Test	3-113
	3.6 LOCAL COOLANT AND GUIDE TUBE TEMPERATURES	3-113
	3.7 LIQUID CARRYOVER RESULTS	3-123
4	RELATION OF FLECHT RESULTS TO REACTOR LOCA ANALYSIS	4-1
	4.1 ASSUMPTIONS AND LIMITATIONS OF FLECHT TESTS	4-1
	4.1.1 Separate Effects	4-1
	4.1.2 Electrically Heated Rods	4-2
	4.1.3 Number of Heater Rods	4-4
	4.1.4 Other Differences	4-5
	4.2 APPLICATION OF FLECHT RESULTS TO REACTOR LOCA ANALYSIS	4-5
5	CONCLUSIONS	5-1
	5.1 SYSTEM PARAMETER EFFECTS	5-1
	5.2 ELEVATION EFFECTS	5-2
	5.3 VARIABLE FLOODING RATE TEST RESULTS	5-2
	5.4 FLOW BLOCKAGE TEST RESULTS	5-2
	5.5 HEAT TRANSFER REGIMES AND CORRELATIONS	5-3
	5.6 ZIRCALOY-STAINLESS STEEL COMPARISON	5-3
	5.7 PRESSURE TRANSDUCER DATA	5-3

TABLE OF CONTENTS (Cont.)

Section	Title	Page
	5.8 LOCAL COOLANT DATA	5-3
	5.9 LIQUID CARRYOVER	5-4
	5.10 APPLICATION TO REACTOR LOCA ANALYSIS	5-4
	5.11 MATERIALS EVALUATION	5-4
6	REFERENCES	6-1
APPENDIX A	HEATER ROD DEVELOPMENT	A-1
	A.1 OBJECTIVES	A-1
	A.2 HEATER ROD DESIGN	A-1
	A.3 GROUP I HEATER ROD DEVELOPMENT	A-2
	A.3.1 Insulation Selection	A-3
	A.3.2 Thermocouple Arrangement	A-3
	A.3.3 Testing of Short-Length Heaters	A-5
	A.3.4 Full Length Heater Testing	A-6
	A.4 "EARLY" GROUP III HEATER ROD EXPERIENCE	A-6
	A.4.1 Single Rod Heat Transfer Tests	A-7
	A.4.2 Boron Nitride Outgassing	A-10
	A.5 GROUP II HEATER ROD DEVELOPMENT	A-12
	A.5.1 Resistance Element Selection	A-12
	A.5.2 Thermocouple Calibration	A-13
	A.5.3 Part and Full Length Heater Testing	A-13
	A.6 GROUP III HEATER ROD DEVELOPMENT	A-14
APPENDIX B	MATERIALS EVALUATION	B-1
	B.1 INTRODUCTION	B-1
	B.2 SPECIMEN SELECTION, PREPARATION AND EXAMINATION	B-2
	B.3 RESULTS OF METALLOGRAPHIC EXAMINATIONS	B-3
	B.3.1 Metallographic Structure	B-3
	B.3.2 Oxide Thickness	B-5
	B.3.3 Hydrogen Uptake	B-11
	B.3.4 Microhardness Measurements	B-11
	B.3.5 Materials Characterization	B-16
	B.3.5.1 Tensile and Burst Test Results	B-16

TABLE OF CONTENTS (Cont.)

Section	Title	Page
	B.3.5.2 Texture	B-16
	B.3.5.3 Grain Size	B-16
	B.3.5.4 Hydride Orientation	B-19
	B.4 DISCUSSION OF RESULTS	B-19
	B.4.1 Metal-Water Reaction	B-19
	B.4.2 Hydrogen Uptake	B-22
	B.5 CONCLUSIONS	B-24
	B.6 REFERENCES	B-25
APPENDIX C	FLECHT DATA SUMMARY SHEETS	C-1
APPENDIX D	DERIVATION OF VARIABLE FLOODING RATE TIME SHIFT CORRELATIONS	D-1
APPENDIX E	QUENCH TEMPERATURE DETERMINATION AND ANALYSIS	E-1

LIST OF ILLUSTRATIONS

Figure	Title	Page
2-1	7 x 7 Test Section Simulating a PWR Assembly and Power Distribution	2-2
2-2	10 x 10 Test Section Simulating a PWR Assembly and Power Distribution	2-3
2-3	Heater Rod Axial Power Profile	2-4
2-4	FLECHT Heater Rod Schematic Design	2-5
2-5	FLECHT Egg-Crate Support Grid	2-6
2-6	Location of Instrumented Heater Rods in the 7 x 7 Array	2-8
2-7	Location of Instrumented Heater Rods in the 10 x 10 Array	2-9
2-8	Steam Temperature Detector	2-12
2-9	Location of Steam Temperature Detectors Relative to Midplane	2-13
2-10	FLECHT Test Facility Flow Sheet	2-14
2-11	FLECHT Test Facility	2-15
2-12	Reactor Power Decay Curve	2-17
2-13	Sketch of PWR FLECHT Upper Plenum Modified for Fallback	2-18
3-1	Typical Transient Midplane Clad Temperature Behavior for Constant and Variable Flooding Rate Tests	3-2
3-2	Reproducibility of Heat Transfer Coefficient for Two Runs at Various Elevations	3-11
3-3	Test Bundle Symmetry-Heat Transfer Coefficient for Symmetrical Rods for 10 x 10 and 7 x 7 Bundles	3-13
3-4	Heat Transfer Coefficients at Midplane of Equivalent Heater Rods in the 7 x 7 and 10 x 10 Bundles, Runs 1002 and 3541	3-15
3-5	Heat Transfer Coefficients at the Midplane of Equivalent Heater Rods in the 7 x 7 and 10 x 10 Bundles, Runs 1720 and 3920	3-16
3-6	Radial Variation of Heat Transfer Coefficient for 10 x 10 and 7 x 7 Bundles	3-17
3-7	Effect of Housing Temperature on Temperature Rise, Turnaround Time and Quench Time	3-19

LIST OF ILLUSTRATIONS (Cont.)

Figure	Title	Page
3-8	Effect of Housing Temperature on Heat Transfer Coefficient	3-20
3-9	Effect of Low Housing Temperature at Elevations Below Midplane	3-22
3-10	Effect of Initial Clad Temperature on Midplane (6') Heat Transfer Coefficient at 6, 2 and 1 in./sec Flooding Rates	3-23
3-11	Effect of Initial Clad Temperature on Temperature Rise, Turnaround Time and Quench Time	3-25
3-12	Effect of Flooding Rate on Midplane (6') Heat Transfer Coefficients at 1600, 2000 and 2200°F Initial Clad Temperature	3-26
3-13	Effect of Flooding Rate on Temperature Rise, Turnaround Time and Quench Time	3-27
3-14	Effect of Flooding Rate on Temperature Rise (LOG-LOG)	3-28
3-15	Effect of Subcooling on Heat Transfer Coefficient	3-29
3-16	Effect of Inlet Coolant Subcooling on Temperature Rise, Turnaround Time and Quench Time	3-30
3-17	Effect of Pressure on Heat Transfer Coefficient at Constant Subcooling	3-32
3-18	Effect of Pressure on Temperature Rise, Turnaround Time and Quench Time	3-33
3-19	Effect of Peak Power on Heat Transfer Coefficient for 6 and 2 in./sec Flooding Rate	3-34
3-20	Effect of Peak Power on Temperature Rise, Turnaround Time and Quench Time	3-36
3-21	Comparison of Power Decay Rates for Runs 5948, 6948, and 6848	3-37
3-22	Effect of Power Decay Rate on Heat Transfer Coefficient	3-38
3-23	Effect of Borated Coolant on Heat Transfer Coefficient	3-41
3-24	Variation of Heat Transfer Coefficient with Elevation for 1, 6, and 10 in./sec Flooding Rates	3-42
3-25	Variation in Temperature Rise, Turnaround Time and Quench Time with Elevation	3-43
3-26	Flooding Rates for Variable Flow Tests	3-45
3-27	Typical Clad Temperature Histories for Variable Flow Tests with Fallback	3-46

LIST OF ILLUSTRATIONS (Cont.)

Figure	Title	Page
3-28	Typical Heat Transfer Coefficients for Variable Flow Tests with Fallback	3-48
3-29	Midplane Heat Transfer Coefficients for Three Different Variable Flooding Rates	3-49
3-30	Effect of Fallback at 9/6 (17 sec) - 1 in./sec Variable Flooding Rate	3-51
3-31	Effect of Fallback at 6 (4 sec) - 1 in./sec Variable Flooding Rate	3-52
3-32	Effect of Fallback at 1 in./sec Flooding Rate	3-53
3-33	Comparison of Heat Transfer Coefficients for Constant and Variable Flooding Rate A Tests with Fallback	3-54
3-34	Comparison of Heat Transfer Coefficients for Constant and Variable Flooding Rate A Tests without Fallback	3-55
3-35	Comparison of Heat Transfer Coefficients for Constant and Variable Flooding Rate B Tests with Fallback	3-56
3-36	Comparison of Heat Transfer Coefficients for Constant and Variable Flooding Rate C Tests with Fallback	3-57
3-37	Group I Flow Blockage Plate	3-59
3-38	Group II Flow Blockage Plate	3-60
3-39	Schematic of Group II Flow Blockage Geometries	3-61
3-40	Effect of Flow Blockage with Bypass Flow on Midplane Heat Transfer Coefficients	3-65
3-41	Effect of Flow Blockage without Bypass Flow on Midplane Heat Transfer Coefficients	3-66
3-42	Comparison of Variable and Constant Flooding Rate Flow Blockage Heat Transfer Coefficients	3-68
3-43	FLECHT Flow Regimes	3-70
3-44	Clad Quench Behavior	3-71
3-45	Nucleate Boiling, Transition Boiling and Film Boiling Regimes	3-72
3-46	Dispersed Flow Regime and Start of Transition Flow Regime	3-74
3-47	Transition Flow Regime, Early Part at High Elevation	3-75
3-48	Transition Flow Regime, Later Part	3-76
3-49	Heat Transfer Coefficients at Several Elevations for Run 4442	3-78

LIST OF ILLUSTRATIONS (Cont.)

Figure	Title	Page
3-50	Comparison of Heat Transfer and Flow Regimes for FLECHT Runs 3642, 4442 and 5642	3-79
3-51	Schematic Diagram of FLECHT Heat Transfer Coefficient vs Dimensionless Time	3-81
3-52	The Effect of Flooding Rate on Measured and Predicted Heat Transfer Coefficients	3-85
3-53	The Effect of Pressure on Measured and Predicted Heat Transfer Coefficients	3-86
3-54	The Effect of Elevation on Measured and Predicted Heat Transfer Coefficients	3-87
3-55	Comparison Between Measured and Predicted Integrated Midplane Heat Transfer Coefficients	3-89
3-56	Schematic Representation of the Use of ξ to Compare Constant and Variable Flooding Rate Heat Transfer Coefficients	3-91
3-57	Comparison between Measured and Predicted Heat Transfer Coefficients for a Variable Flooding Rate Run	3-93
3-58	Comparison of Zircaloy and Stainless Steel Clad Temperature Response	3-99
3-59	Comparison of the Quench Temperature between Zircaloy and Stainless Steel Clad	3-100
3-60	Comparison of Zircaloy and Stainless Steel Clad Heat Transfer Coefficients at 10 in/sec	3-103
3-61	Comparison of Zircaloy and Stainless Steel Clad Heat Transfer Coefficients at 4 in./sec	3-104
3-62	Comparison of Zircaloy and Stainless Steel Clad Heat Transfer Coefficients at 6 (8 sec) -1 in./sec	3-105
3-63	Comparison of Zircaloy and Stainless Steel Quench Behavior, 10 in./sec	3-106
3-64	Comparison of Zircaloy and Stainless Steel Quench Behavior, 4 in./sec	3-107
3-65	Comparison of Zircaloy and Stainless Steel Quench Behavior, 6 (8 sec) - 1 in./sec	3-108
3-66	Bundle Radial Pressure Difference Between Thimble Tap and Housing at Bottom of Heated Length	3-111
3-67	Effect of Flooding Rate and Initial Clad Temperature on Axial Pressure Drop	3-112
3-68	Comparison of Axial Pressure Drop for Constant and Variable Flooding Rate Tests	3-114

LIST OF ILLUSTRATIONS (Cont.)

Figure	Title	Page
3-69	Effect of Fallback on Axial Pressure Drop	3-115
3-70	Effect of Flow Blockage on Axial Pressure Drop	3-116
3-71	Local Coolant, Steam Probe and Guide Tube Wall Temperatures versus Time for Reference Run Conditions	3-118
3-72	Measured Steam and Clad Temperatures for 4 in./sec Flow Blockage Run	3-119
3-73	Measured Steam and Clad Temperatures for 1 in./sec Flow Blockage Run	3-120
3-74	Measured Steam Temperatures for Variable Flooding Rate Test without Blockage	3-121
3-75	Liquid Carryover Data, Run 9379-Variable Flooding Rate Test	3-124
3-76	Liquid Carryover Data, Run 9480-1 in./sec Flooding Rate Test	3-125
4-1	Comparison of Thermal Response of PWR FLECHT and Reactor Fuel Rods	4-3
A-1	Temperature Response of Stainless Steel Clad Heater Rods	A-4
A-2	FLECHT Run 2443-Comparison of Normal and Degraded Quenches	A-8
B-1	Microstructure of a Rod Section Heated to 900°F	B-6
B-2	Microstructure of a Rod Section Heated to 1500°F	B-6
B-3	Microstructure of a Rod Section Heated to 1960°F	B-7
B-4	Microstructure of a Rod Section Heated to 2365°F	B-7
B-5	Zirconium-Oxygen Phase Diagram	B-8
B-6	Oxide Film-Two Feet Above Midplane	B-12
B-7	Oxide Film at the Midplane	B-12
B-8	Photomicrograph of Zirc-Oxide Film on Rod No. 3D-Midplane Bundle No.2	B-13
B-9	Photomicrograph of Zirc-Oxide Film on Rod No. 5B-Midplane Bundle No. 2	B-14
B-10	General Hardness Pattern	B-15
B-11	Inverse Pole Figure for As-Fabricated Heater Rod	B-18
B-12	Comparison of Measured versus Calculated Values of Oxide Thickness	B-20
B-13	Comparison of Maximum Oxide and α-Zirconium Layer Thickness	B-23

LIST OF ILLUSTRATIONS (Cont.)

Figure	Title	Page
D-1	Time Shift Relationship for V_{inL} = 1 in./sec, Midplane Elevation	D-2
D-2	Time Shift Relationships for Several V_{inL}, 4 ft Elevation	D-4
D-3	Time Shift Relationships for Several V_{inL}, Midplane Elevation	D-5
D-4	Time Shift Relationships for Several V_{inL}, 8 ft Elevation	D-6
D-5	Comparison of Equations (1), (2) and (3)	D-7
E-1	Use of Multi-Scan Quench Curves to Determine Quench Temperatures	E-2
E-2	Effect of Flooding Rate V_{in} on Quench Temperature	E-5
E-3	Effect of Initial Clad Temperature on Quench Temperature	E-6
E-4	Effect of Inlet Coolant Subcooling on Quench Temperature	E-7
E-5	Effect of Pressure on Quench Temperature	E-8
E-6	Effect of Peak Power on Quench Temperature	E-9
E-7	Effect of Local Subcooling on Quench Temperature	E-10

LIST OF TABLES

Table	Title	Page
2-1	Thermocouple Axial Location Designation	2-10
3-1	FLECHT Data Summary, Stainless Steel Clad Constant Flow Tests, Hot Rod Midplane Elevation (6-Foot)	3-4
3-2	FLECHT Data Summary, Stainless Steel Clad Variable Flow Tests, Hot Rod Midplane Elevation (6-Foot)	3-7
3-3	FLECHT Data Summary, Zircaloy Clad Tests, Hot Rod Midplane Elevation (6 Foot)	3-8
3-4	Comparison of 7 x 7 and 10 x 10 Arrays	3-14
3-5	Effect of Power Decay Rate on Temperature Rise, Turnaround Time and Quench Time	3-39
3-6	Effect of Variable Flooding Rates on Temperature Behavior	3-47
3-7	Midplane Temperature Response for Various Flow Blockage Configurations and Test Conditions	3-63
3-8	Comparison of Zircaloy and Stainless Steel Clad Variable Flooding Rate Test Results	3-102
3-9	Summary of Coolant Temperature Data	3-122
A-1	Ability of Heaters to Withstand Quenching	A-6
A-2	Midplane Diameter and Midplane Temperature Following Quench After Heating to Various Temperatures, Run No. 2443	A-9
A-3	Quench Testing of Group III Heaters	A-16
B-1	Group III Test Results	B-2
B-2	Metallographic Specimen Locations	B-4
B-3	Oxide Film Thickness for Bundles 1 and 2	B-9
B-4	Oxide Film and α-Zirconium Thickness for Bundles 3 and 4	B-10
B-5	Mechanical Properties Tests	B-17
E-1	Quench Temperature Data	E-3

ACKNOWLEDGEMENTS

The authors wish to acknowledge: Dr. J. O. Cermak and Dr. R. F. Farman for their contribution to test program planning and data analysis; Dr. A. S. Kitzes for direction of the heater rod development and test operation activities; Mr. H. Skreppen for test facility design and construction; Mr. S. Frank and Dr. H. C. Yeh for their analysis of heat transfer regimes and development of heat transfer correlations; Dr. P. T. Chu for developing the data reduction code; Mr. D. Coleman for reduction of test data; and Mr. W. Spencer and the technicians of Test Engineering who performed the tests.

ABSTRACT

The objective of the PWR FLECHT (Full Length Emergency Cooling Heat Transfer) program was to obtain experimental reflooding heat transfer data under simulated loss-of-coolant accident conditions for use in evaluating the heat transfer capabilities of pressurized water reactor emergency core cooling systems.

Eighty-seven valid runs which investigated the effects of peak power, power decay rate, maximum initial clad temperature, constant and variable flooding rates, inlet coolant subcooling, pressure, flow blockage, borated coolant, and clad material were performed.

The report summarizes the results of the entire PWR FLECHT program including material previously presented in WCAP-7435, 7444 and 7544. The test results reported include transient heat transfer coefficients and clad temperatures at different radial and axial locations, axial and radial pressure drop data, local coolant temperature and measurements of carry-over water. The effects of each of the test parameters on heat transfer behavior are discussed and heat transfer correlations as a function of system parameters are presented. Results of the heater rod development and materials evaluation tasks are also included.

The test results have verified the basic assumptions used in current reactor loss-of-coolant accident analysis. In particular, the effectiveness of bottom flooding and the importance of liquid entrainment as a heat transfer mechanism have been demonstrated.

SECTION 1

INTRODUCTION

1.1 OBJECTIVE

The objective of the PWR FLECHT (Full Length Emergency Cooling Heat Transfer) test program was to obtain experimental reflooding heat transfer data under simulated loss-of-coolant accident conditions for use in evaluating the heat transfer capabilities of PWR emergency core cooling systems.

To achieve this objective, the test program was planned to investigate the effects of the following parameters on transient heat transfer coefficients:

- Initial Clad Temperature
- Flooding Rate
- Power
- Inlet Coolant Subcooling
- Pressure

In addition, various special tests were included for validation purposes and to investigate the effects of such things as soluble poison, cladding damage, power decay rate, variable flooding rate, entrained liquid "fallback" and metal-water reaction.

The data resulting from these tests has been analyzed, and models and correlations which can be used to evaluate PWR emergency core cooling system capabilities have been developed.

1.2 REPORT CONTENTS AND RELATIONSHIP TO OVERALL PROGRAM

The test program was divided into three groups, according to the type of heater rods employed:

Group I--Low peak temperature tests, using stainless steel clad heater rods with Nichrome heating elements.

Group II--High peak temperature tests, using stainless steel clad heater rods with Kanthal heating elements.

Group III--High peak temperature tests, using Zircaloy-4 clad heater rods with Nichrome or Kanthal heating elements.

This report summarizes the results of the entire program. Results of the Group I, II and III test series are presented and the models and correlations which have been developed from the data are described. Final reports on the heater rod development and materials evaluation activities conducted under this program are included in the appendices. Portions of the information presented in this report have been included in previously issued PWR FLECHT technical reports, which include the following:

WCAP-7200, PWR FLECHT Conceptual Design Report, May 1968--The conceptual design of the PWR FLECHT Program is presented. Test planning, including test conditions and data requirements, facility design, and heater rod development are discussed. A reference design for the initial series of tests is presented.

WCAP-7288, PWR FLECHT Final Test Plan, January 1969--A description of the test bundle, including final thermocouple location, is presented along with a run schedule. The completed facility and test instrumentation are described. The procedures for running a test are discussed. A section on error analysis is included.

WCAP-7435, PWR FLECHT Group I Test Report, January 1970--The results of fifty-one runs of the Group I test series are presented. In this series, transient heat transfer coefficient and clad temperature behavior, at different radial and axial test bundle locations were investigated over the following range of parameters:

- Peak Power Density — 0.69 to 1.40 kw/ft
- Maximum Initial Clad Temperature — 800 to 2000°F
- Flooding Rate — 2 to 18 in./sec
- Inlet Subcooling — 16 to 189°F
- System Pressure — 15 to 90 psia

In addition to the effects of the above parameters, the effects of borated coolant and simulated flow blockage due to clad swelling were also investigated.

WCAP-7444, PWR FLECHT Interim Materials Evaluation Report, January 1970--The results of the metallographic examination of heater rods from the two "early" Group III PWR FLECHT tests, conducted in 1969, are summarized. Information on hydrogen content, grain size, and extent of metal-water reaction is included. Also presented are the results of the materials characterization of as-fabricated Group III heater rod cladding.

WCAP-7544, PWR FLECHT Group II Test Report, September 1970--The results of twenty-seven Group II tests are presented. This series extended the range of initial temperatures (to 2200°F), flooding rates (to 0.6 in./sec), and flow blockages investigated in Group I. The effects of power decay rate, variable flooding rate, and entrained water "fallback" were also examined.

SECTION 2

TEST DESCRIPTION

2.1 TEST BUNDLE DESCRIPTION

2.1.1 Geometry

The PWR-FLECHT tests were conducted with 7 x 7 and 10 x 10 heater rod bundles having principal dimensions typical of commercial PWR fuelassemblies, as follows:

Heated length - 12 feet
Heater pitch - 0.563 inches, square pitch
Heater diameter - 0.422 inches
Control rod thimble diameter - 0.545 inches
Instrumentation tube diameter - 0.463 inches

Figure 2-1 shows the location of the non-power producing elements (control rod guide thimbles and instrumentation tube) and the radial power profile for the heated rods (1.1, 1.0 and 0.95 radial peak to average) in the 7 x 7 assembly. The non-power producing elements and a radial power profile for the 10 x 10 bundle are shown in Figure 2-2. The heater rod axial power profile is shown in Figure 2-3. The axial and radial power distributions employed are typical of those found in actual PWR fuel assemblies.

Figure 2-4 is a schematic representation of the heater rod design. Further information regarding heater rod design and development is contained in Appendix A.

The heater rods were supported radially within the test bundle by eight "egg-crate" grids of the type shown in Figure 2-5. One grid was located at the bottom of the heated length and one at the top. The remaining grids were spaced at equal intervals between the top and bottom grids.

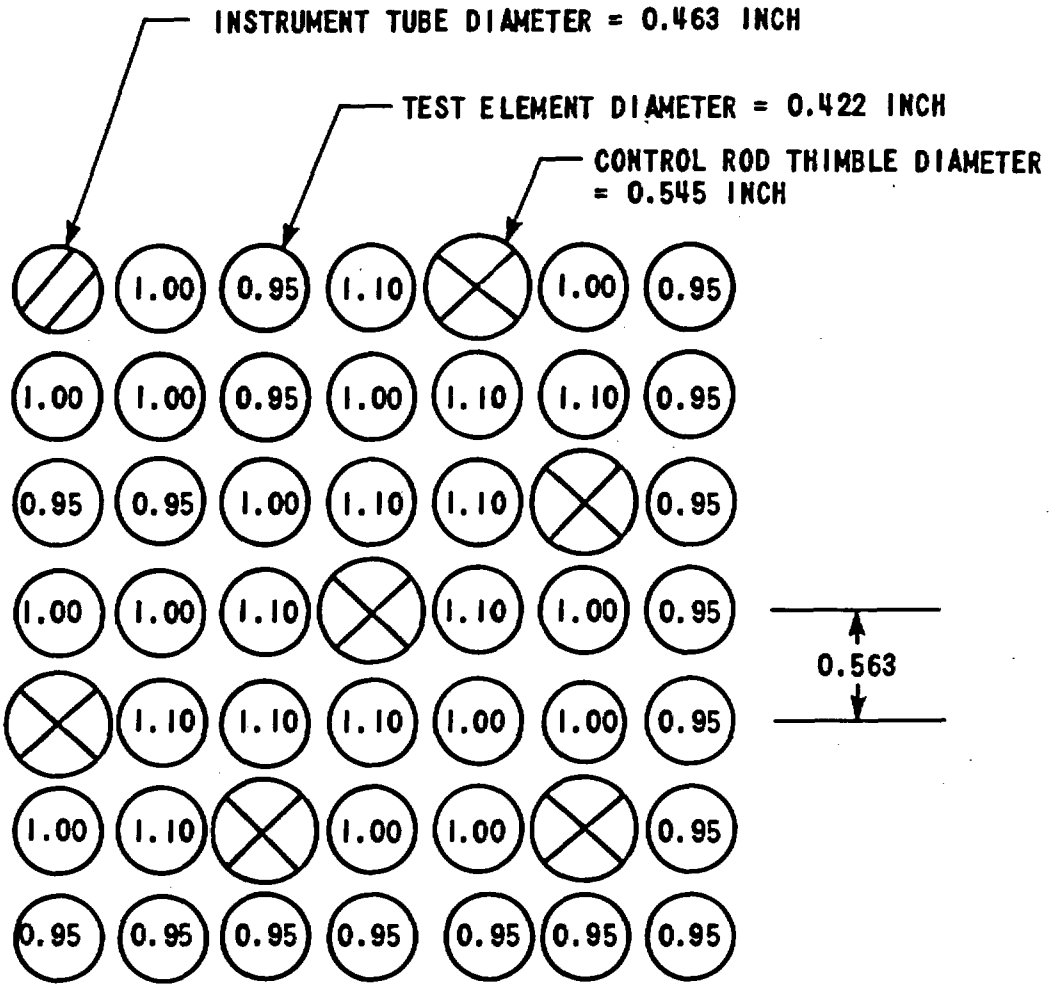

Figure 2-1. 7 x 7 Test Section Simulating a PWR Assembly and Power Distribution

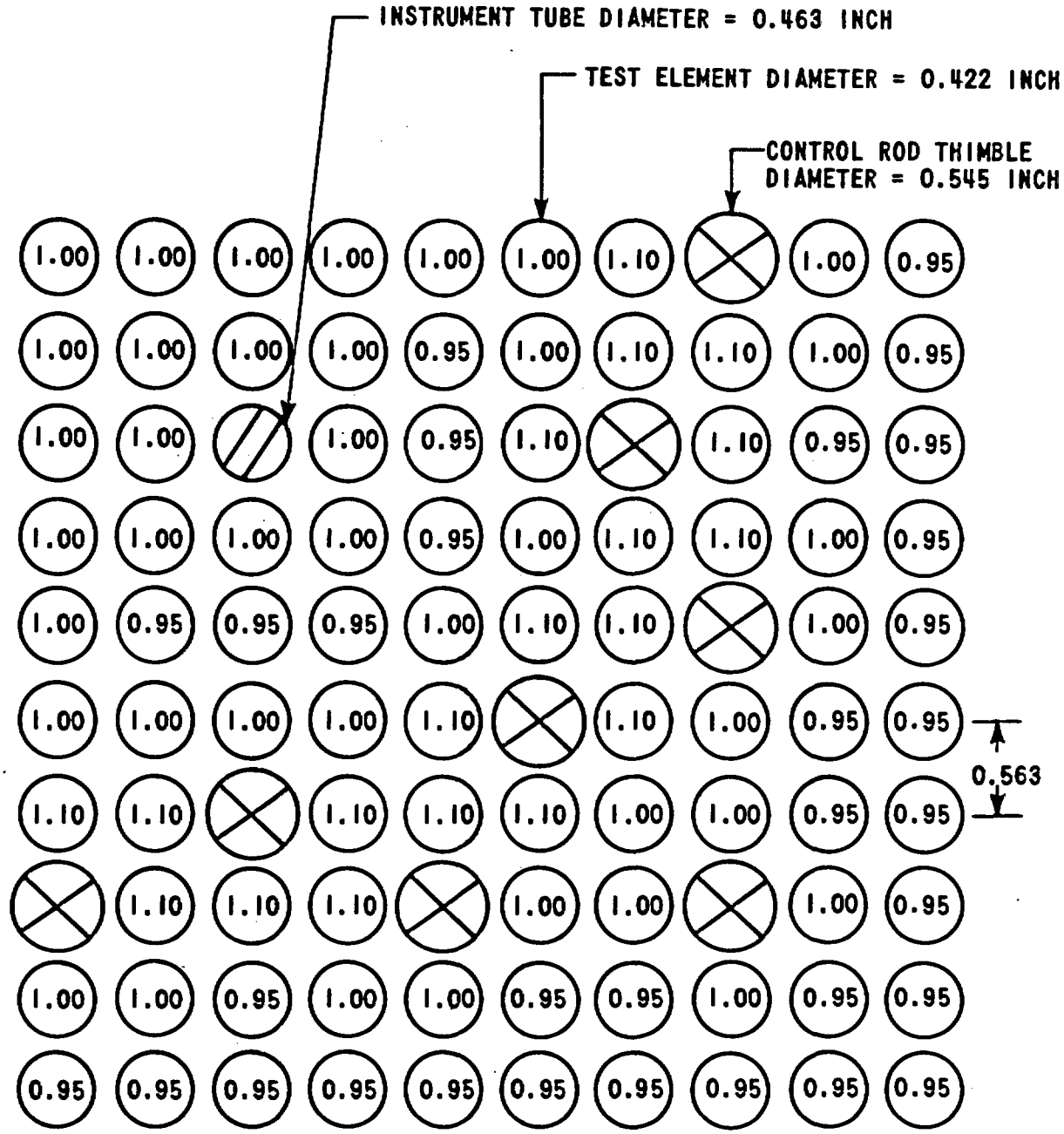

Figure 2-2. 10 x 10 Test Section Simulating a PWR Assembly and Power Distribution

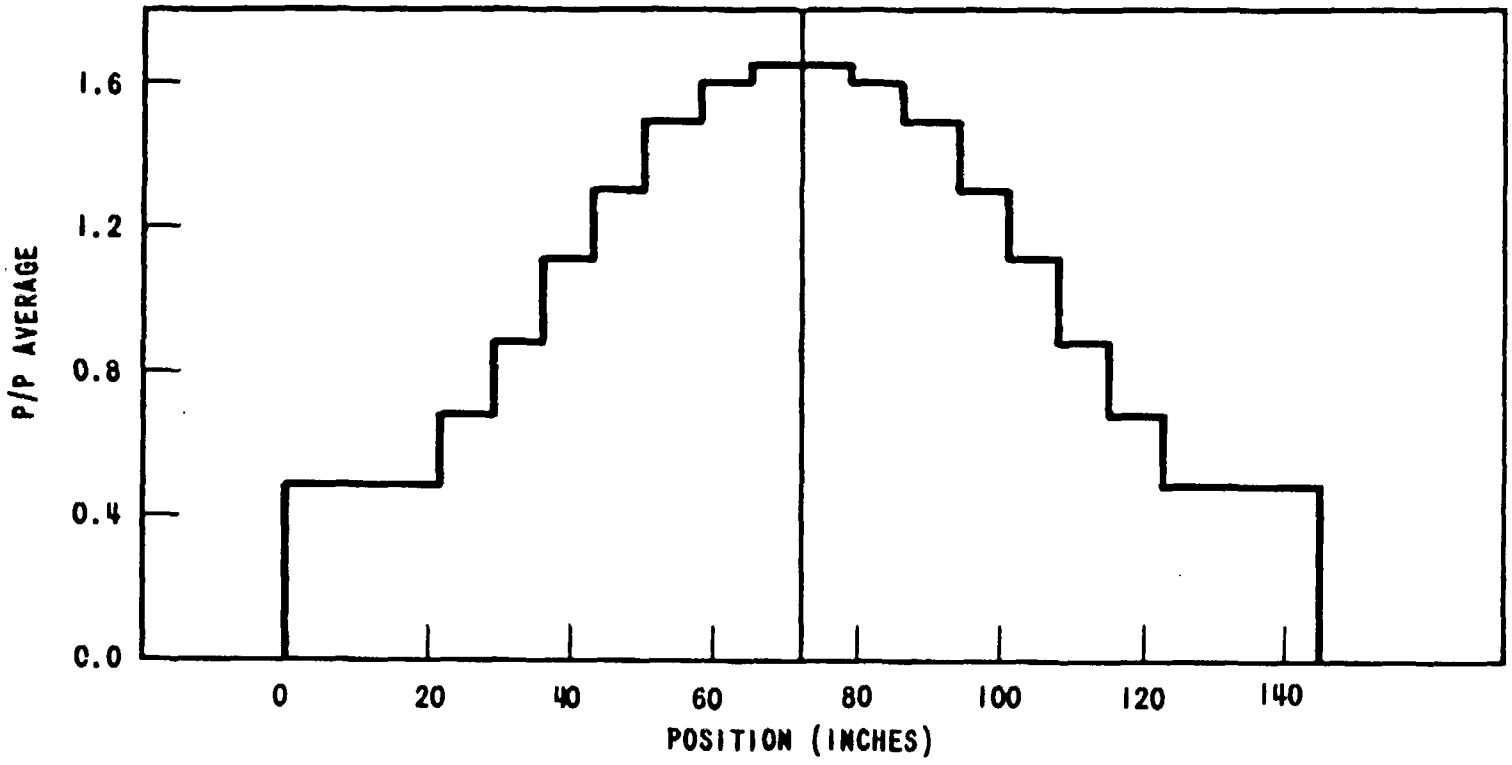

Figure 2-3. Heater Rod Axial Power Profile

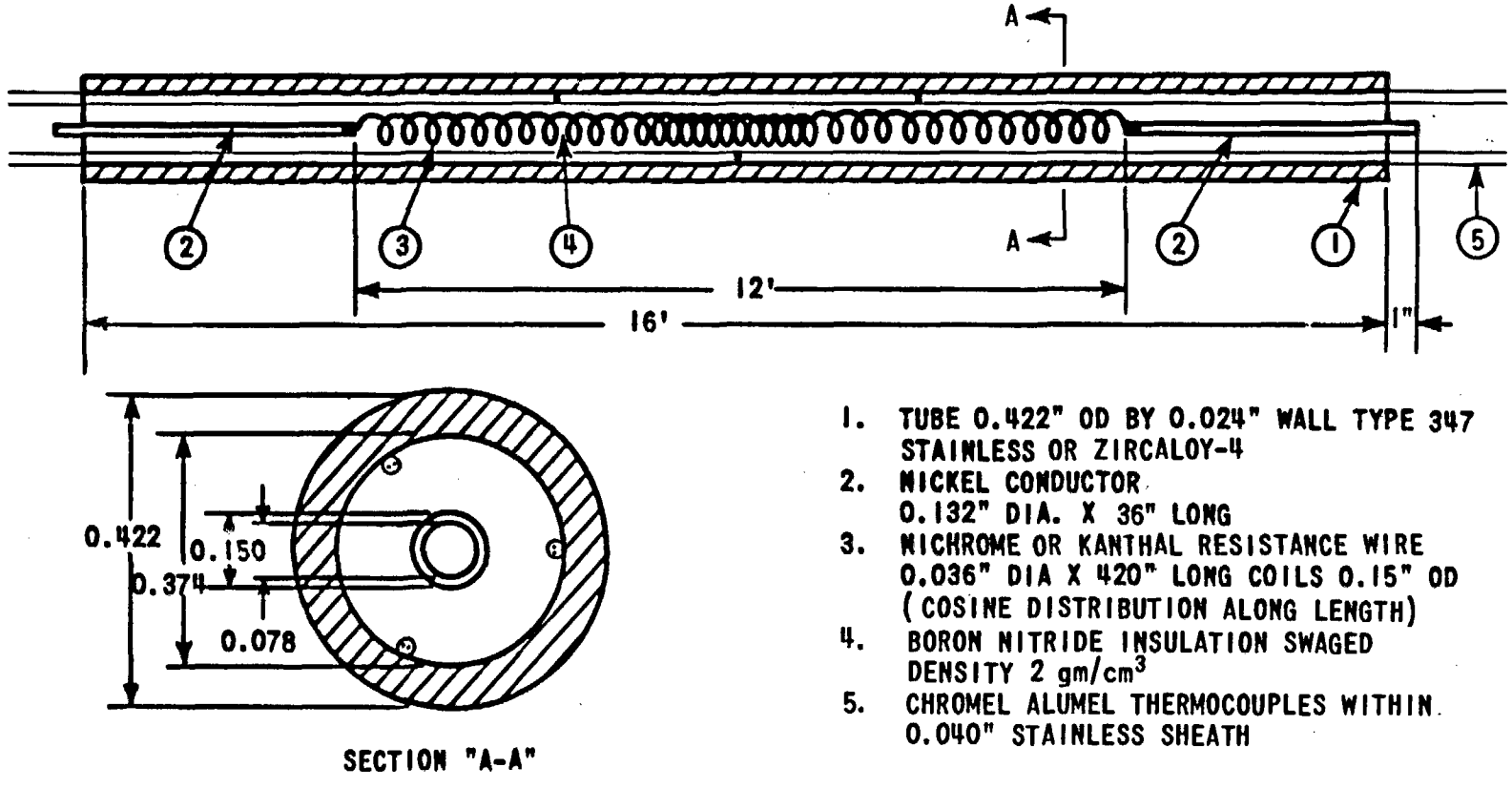

1. TUBE 0.422" OD BY 0.024" WALL TYPE 347 STAINLESS OR ZIRCALOY-4
2. NICKEL CONDUCTOR 0.132" DIA. X 36" LONG
3. NICHROME OR KANTHAL RESISTANCE WIRE 0.036" DIA X 420" LONG COILS 0.15" OD (COSINE DISTRIBUTION ALONG LENGTH)
4. BORON NITRIDE INSULATION SWAGED DENSITY 2 gm/cm^3
5. CHROMEL ALUMEL THERMOCOUPLES WITHIN 0.040" STAINLESS SHEATH

Figure 2-4. FLECHT Heater Rod Schematic Design

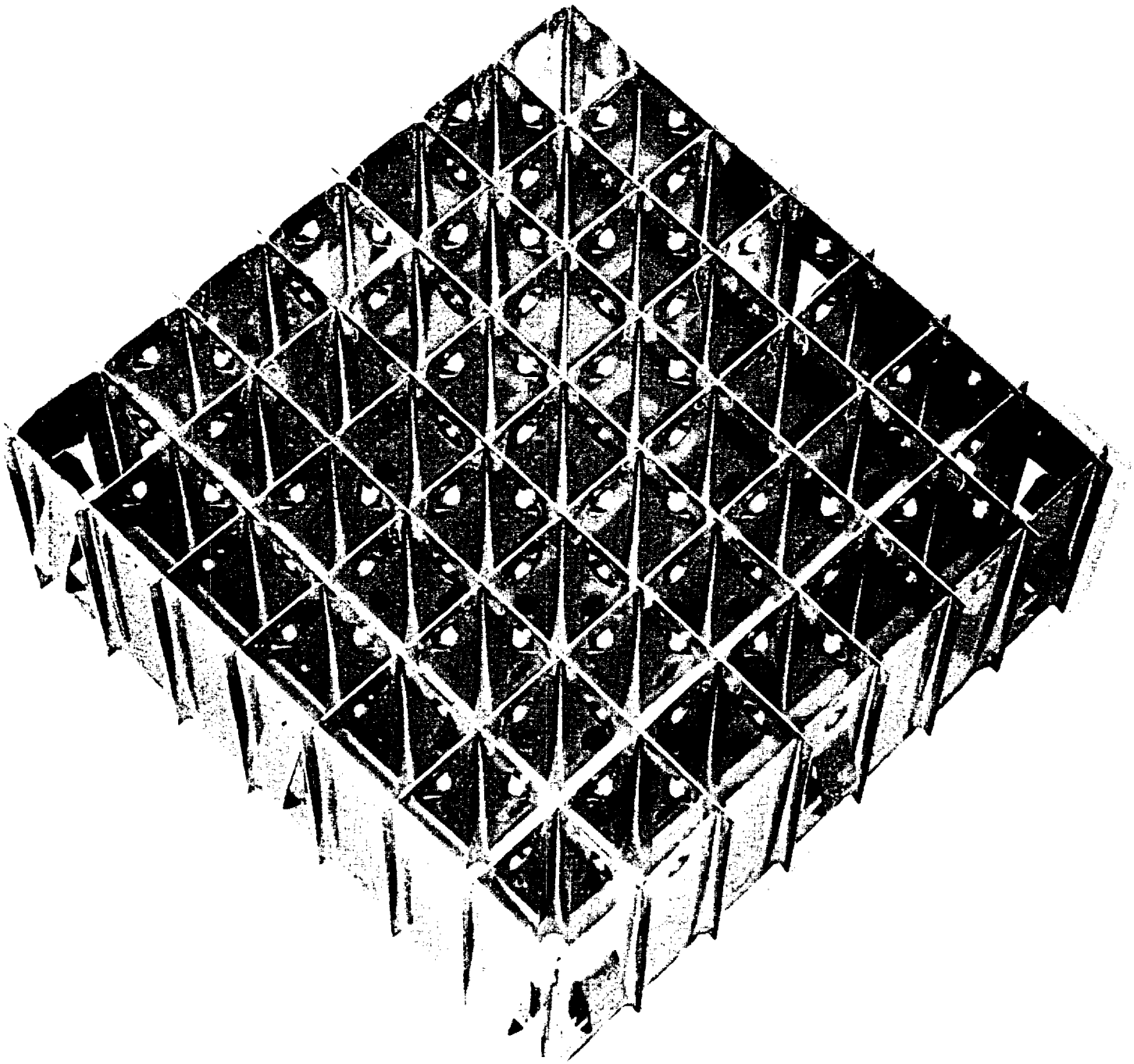

Figure 2-5. FLECHT Egg-Crate Support Grid

2.1.2 Thermocouple Locations

Chromel-alumel thermocouples, located on the inside surface of the heater rod cladding, were distributed radially and axially throughout the bundle. Figures 2-6 and 2-7 show the radial locations of instrumented heater rods for the 7 x 7 and 10 x 10 bundles, respectively. Table 2-1 indicates the axial thermocouple locations in five and three thermocouple-instrumented heater rods. It also defines the nomenclature used for thermocouple identification in the remainder of this report. The column and row designations on Figures 2-6 and 2-7, along with the appropriate axial or elevation designation, pinpoint the precise thermocouple location within the bundle. For example, the 7 x 7 heater rod thermcouple 4E3 was in the 4th column, row E (refer to Figure 2-6) at the number 3 or six-foot axial location (refer to Table 2-1). The special six-thermocouple heater rods included in the 10 x 10 Group II flow blockage assembly contained thermocouples located at the 4 ft, 6 ft, 6 ft 4 in., 6 ft 8 in., 8 ft and 10 ft elevations.

During the early tests (prior to the Group II flow blockage tests), ten thermocouples were provided to measure local coolant temperatures at five axial positions and two different radial locations. Six thermocouples were also provided to measure thimble wall temperatures at three axial positions and two different radial locations. These thermocouples were introduced by way of the control rod thimbles. The junctions of the local coolant thermocouples were located 1/16 in. from the surface of the guide tubes. The thimble wall thermocouples were held in contact with the thimble tube outer surface by means of thin, stainless steel bands. Additional measurements of local coolant temperatures were also made by two "steam probes". The "steam probes" consisted of a thermocouple mounted inside a guide tube and surrounded by a radiation shield. Holes in the guide tube above and below the thermocouple permitted the coolant to contact the thermocouple.

All of the above local coolant and guide tube thermocouples were significantly affected by radiation from adjacent heater rods and subsequent measurements were therefore made by two modified "steam probes", located as shown in Figures 2-6 and 2-7. In this modification, steam was bled from the flow housing through the radiation shield at approximately eight feet per second.

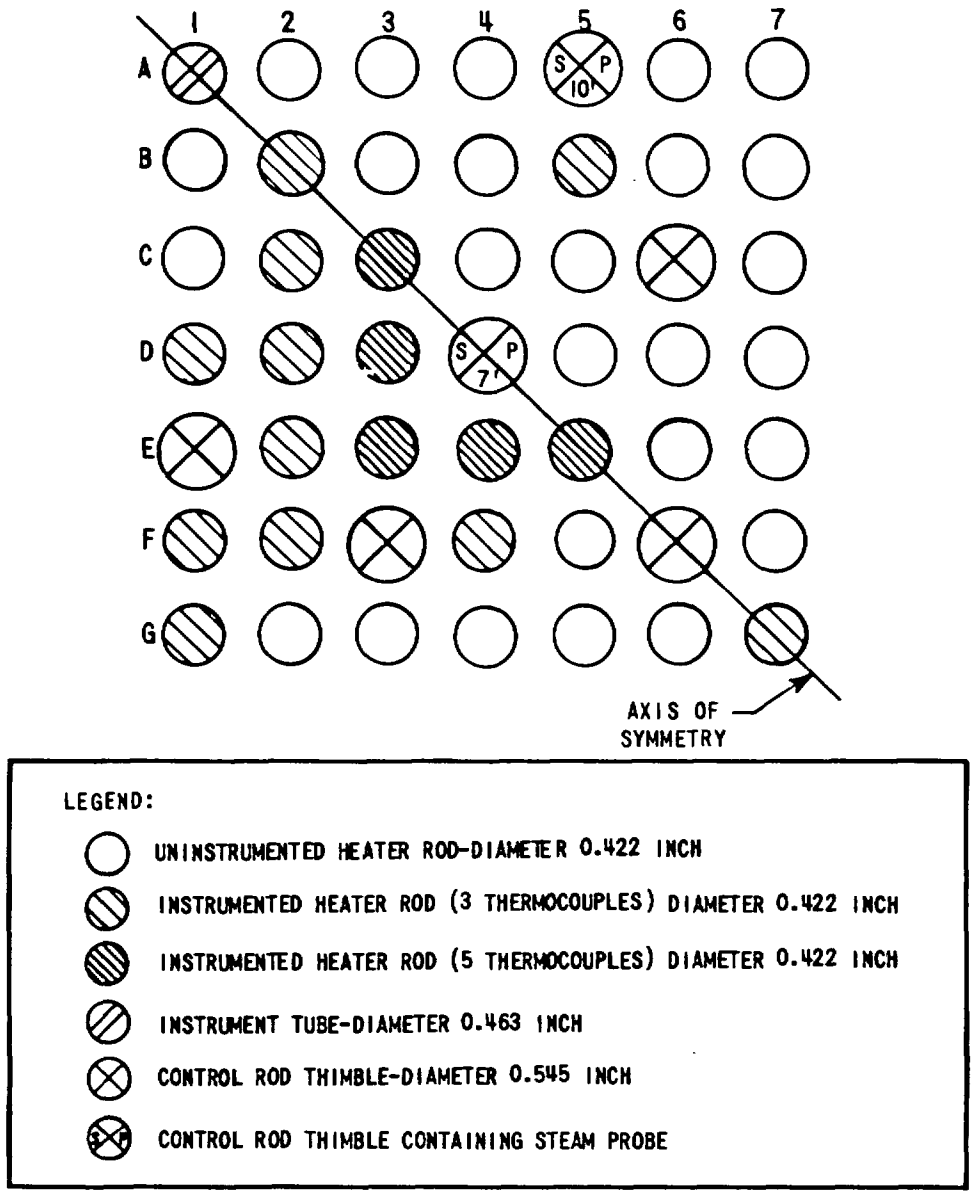

Figure 2-6. Location of Instrumented Heater Rods in the 7 x 7 Array

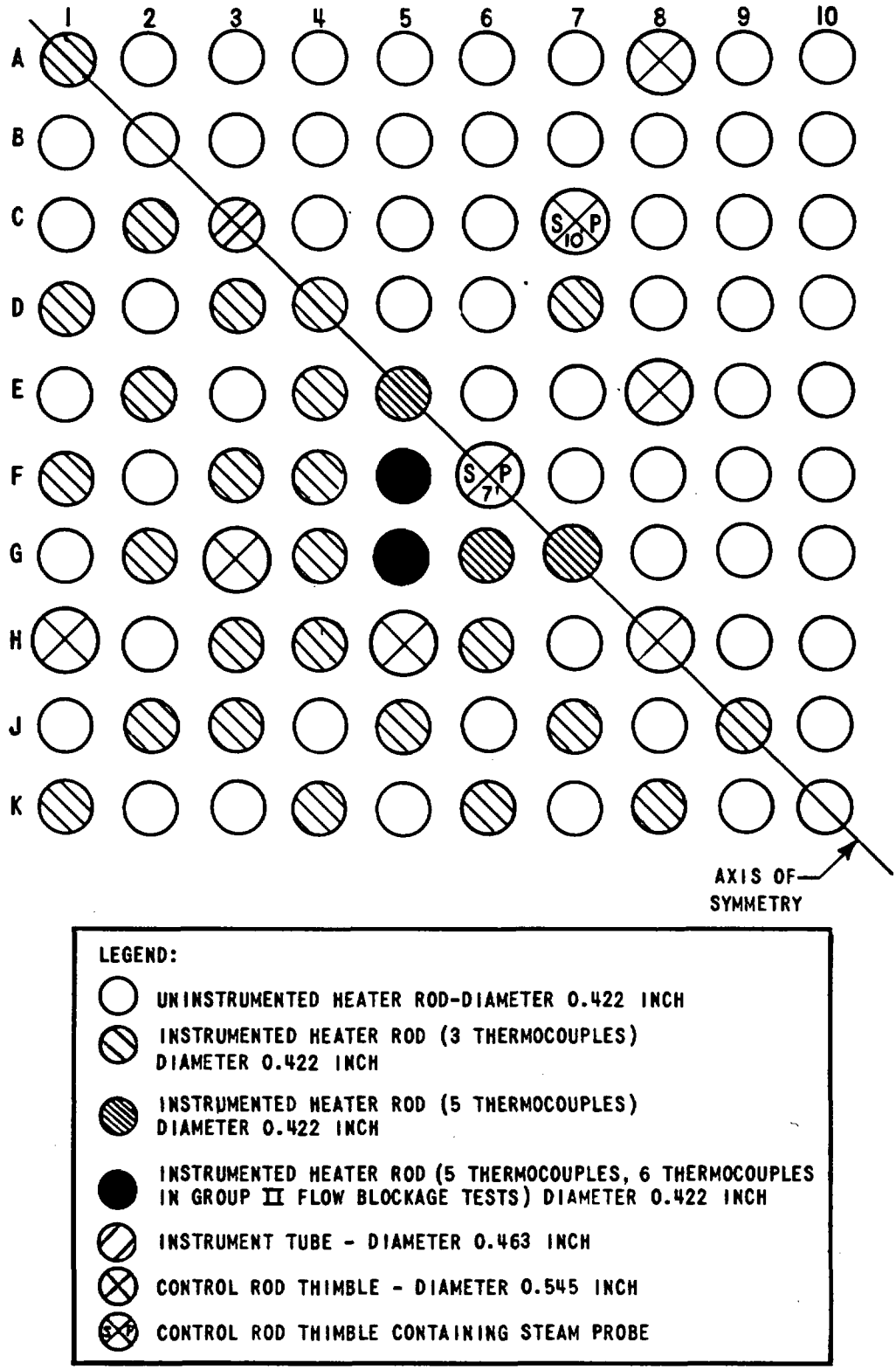

Figure 2-7. Location of Instrumented Heater Rods in the 10 x 10 Array

TABLE 2-1

THERMOCOUPLE AXIAL LOCATION DESIGNATION

Axial Location from Bottom of Heated Length (ft)	Axial Location Designation	
	5 T/C Heater Rod	3 T/C Heater Rod
10	1	1
8	2	
6	3	2
4	4	3
2	5	

Thermocouple Designation Example:

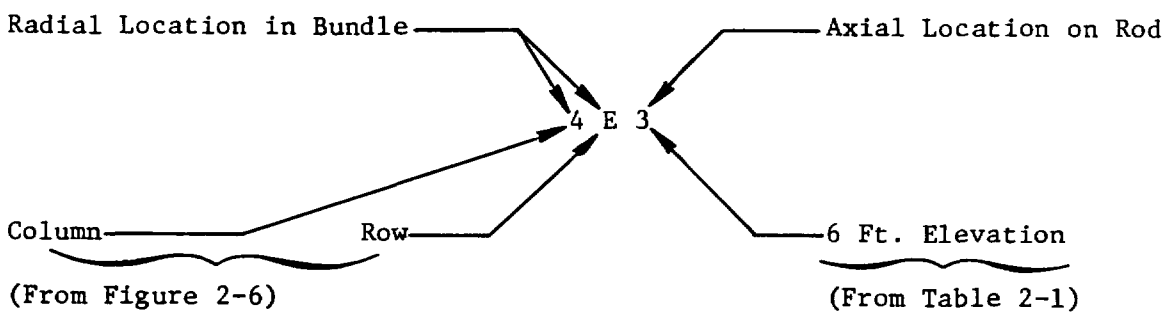

The heat transfer coefficient at the thermocouple was therefore sufficient to offset the effects of radiation and provide rapid thermocouple response to changing steam temperatures. A schematic representation of the modified "steam probe" design is given in Figure 2-8. The axial locations of the "steam probes" as well as two additional bare thermocouples located in the outlet plenum, are shown in Figure 2-9.

2.1.3 Pressure Transducer Locations

Pressure transducers were utilized to obtain axial and radial pressure measurements. Five pressure taps were located along the flow housing wall at zero, two, four, six and eight-foot locations from the bottom of the active heater length. Radial pressure measurements at the bottom of the heated length were obtained by means of pressure taps in two of the control rod thimbles.

2.2 FACILITY DESCRIPTION

As can be seen from Figure 2-10, the FLECHT facility was operated as a once-through system. It consisted of a flow housing for the test bundle, a coolant accumulator, a coolant catch vessel, a steam boiler for back-pressure regulation, a gas supply system for coolant injection, and the required piping and valves. A photograph of the FLECHT facility is shown in Figure 2-11. A detailed description of the facility and associated instrumentation is presented in Reference 1.

The flow housing was fabricated from 0.70-inch-thick carbon steel and was designed for operation at up to 100 psig and 800°F. Separate square housings, having internal dimensions of 4.200 and 5.889 inches, respectively, were used for 7 x 7 and 10 x 10 testing. The plenum chambers were flanged and could be used with either flow housing.

The 10 x 10 flow housing was equipped with three rectangular quartz glass ports for viewing and photographic study. The upper plenum had one circular quartz glass port. Power was supplied by a 1500 kva transformer to three silicon-controlled rectifier (SCR) power control units. To simulate the estimated

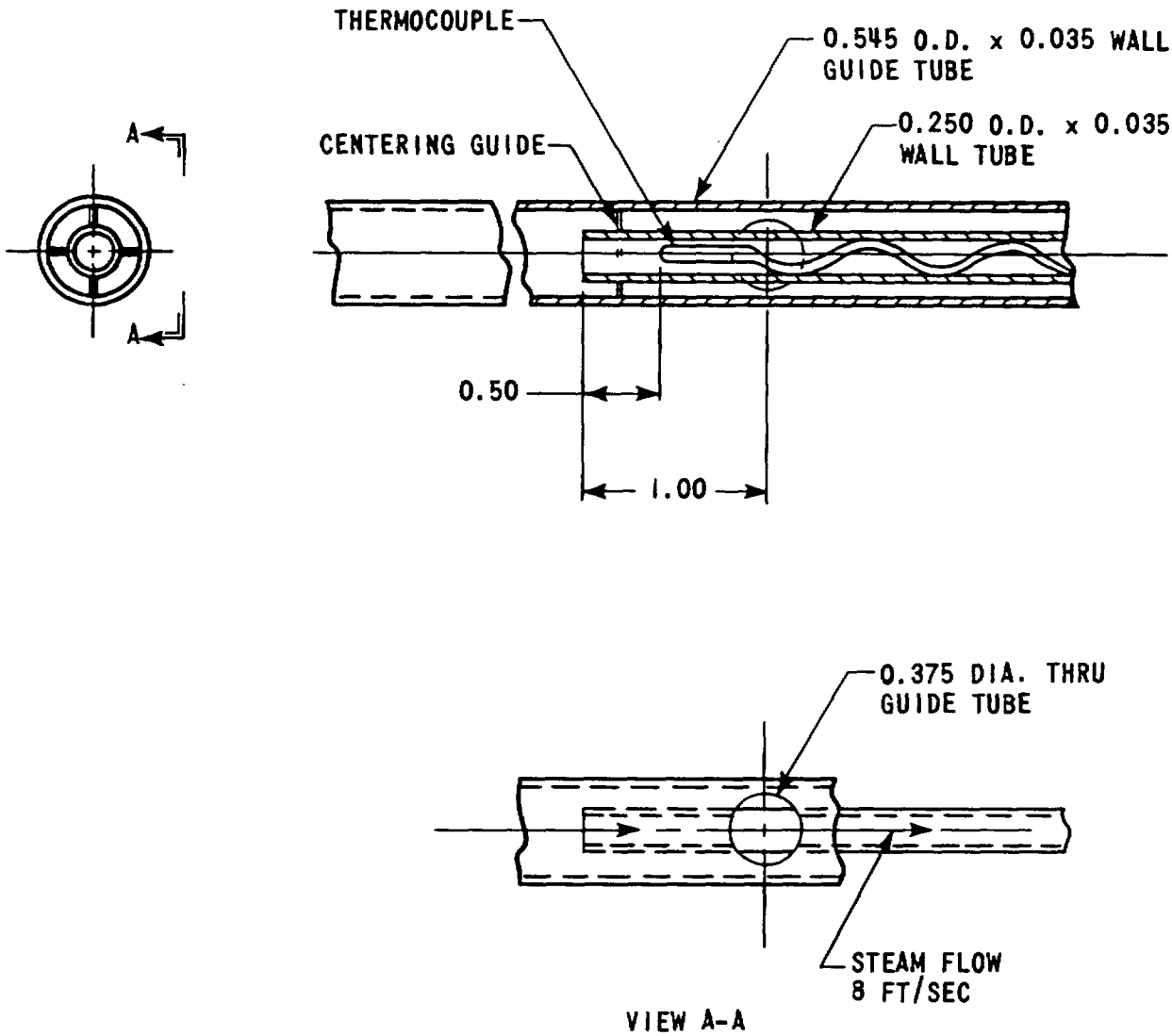

Figure 2-8. Steam Temperature Detector

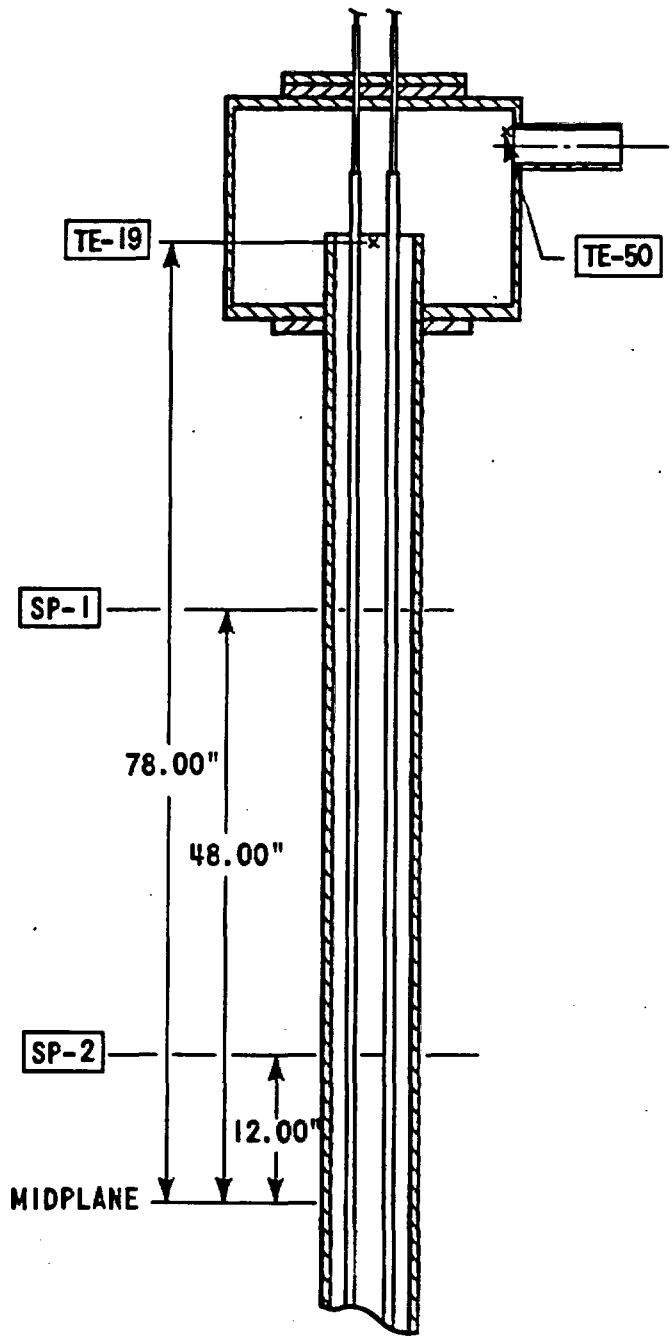

Figure 2-9. Location of Steam Temperature Detectors Relative to Midplane

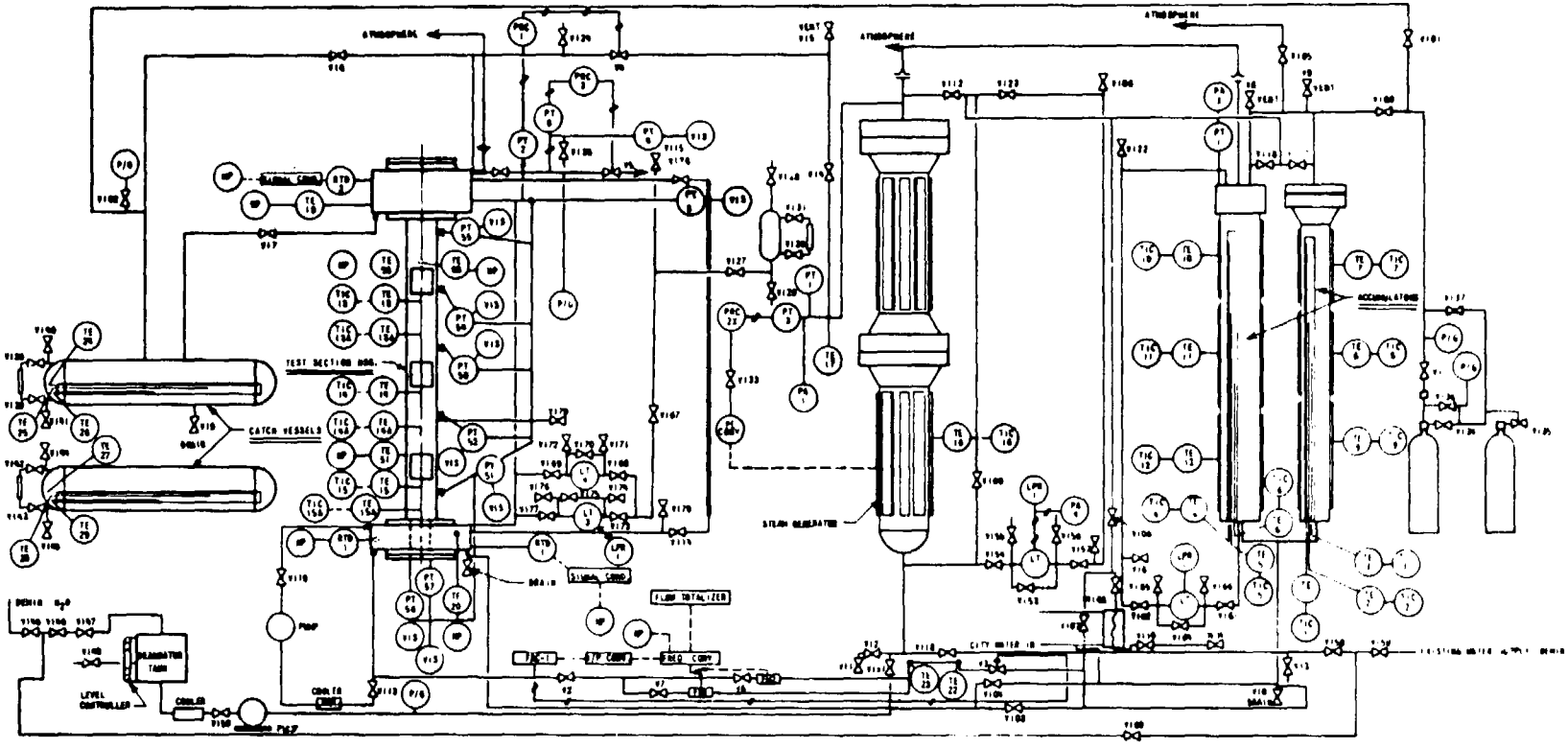

Figure 2.10. FLECHT Test Facility Flow Sheet

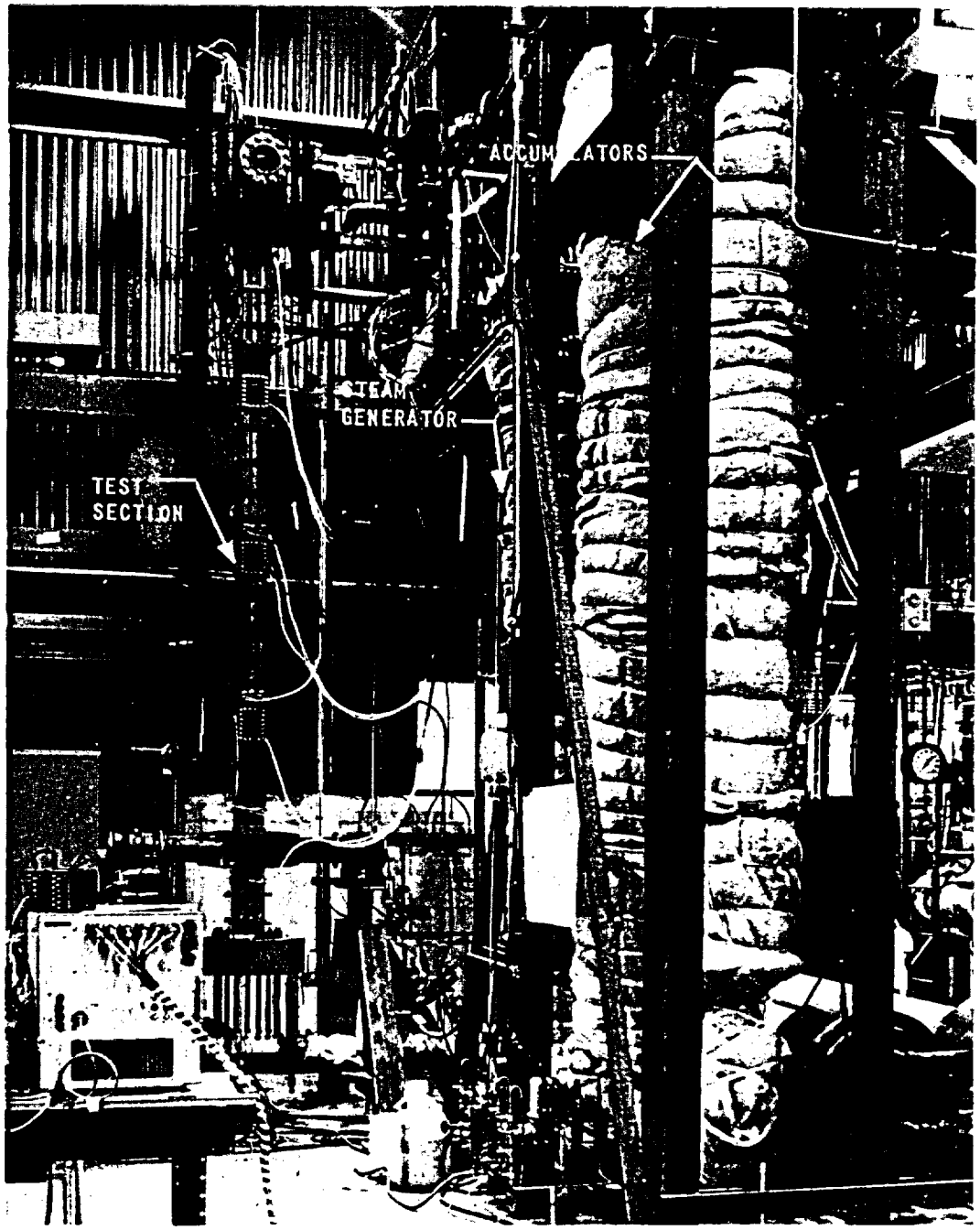

Figure 2-11. FLECHT Test Facility

decay heat generated by a shutdown reactor, the three SCR power control units were biased automatically through a curve-follower programmer. The programmer consisted of an instrument with a pen following the decay heat curve (refer to Figure 2-12) drawn on electrostatic paper. The pen of the programmer mechanically drove three potentiometers to bias each power control unit. The potentiometers were offset to obtain the required radial power profile.

2.3 TEST PROCEDURE

The accumulator was filled with demineralized water and pressurized with gas to about 500 psi above the pressure in the test section housing. The accumulator was maintained at a constant pressure during the experimental run and the required coolant temperature was established by means of externally clamped-on heaters. A small amount of water was allowed to enter the test section housing to a level just below the heated length of the test rods.

The housing walls were heated by supplying power to the test bundle for a short period of time and allowing the housing to heat up by radiant and convective heat transfer. Clamped-on heaters along the upper and lower ends of the housing supplied heat to these regions, thus allowing the housing to achieve a temperature distribution similar to that of the rods. When the housing walls reached the specified temperature distribution, the housing was then pressurized with steam from the boiler. Coolant drainage and trace heating were utilized to assure that the coolant water in the test section housing and in the pipeline between the test section housing and the accumulator was at the correct temperature when water injection was initiated.

Power was supplied to the bundle and the rods were allowed to heat up until the desired initial temperature was reached, at which time flooding was automatically initiated. On initiation of coolant injection, decay of test rod power was automatically started at a programmed rate, corresponding to the reactor decay heat. Test housing pressure was regulated by releasing steam to the atmosphere. For the tests without "fallback," the ejected water, after partial separation, was drained from the upper plenum, collected in the catch vessel, and measured. The upper plenum was modified as shown in Figure 2-13 for the tests with "fallback" effect simulation to permit ejected water to return to the flow housing. In addition, the outlet plenum was preheated to

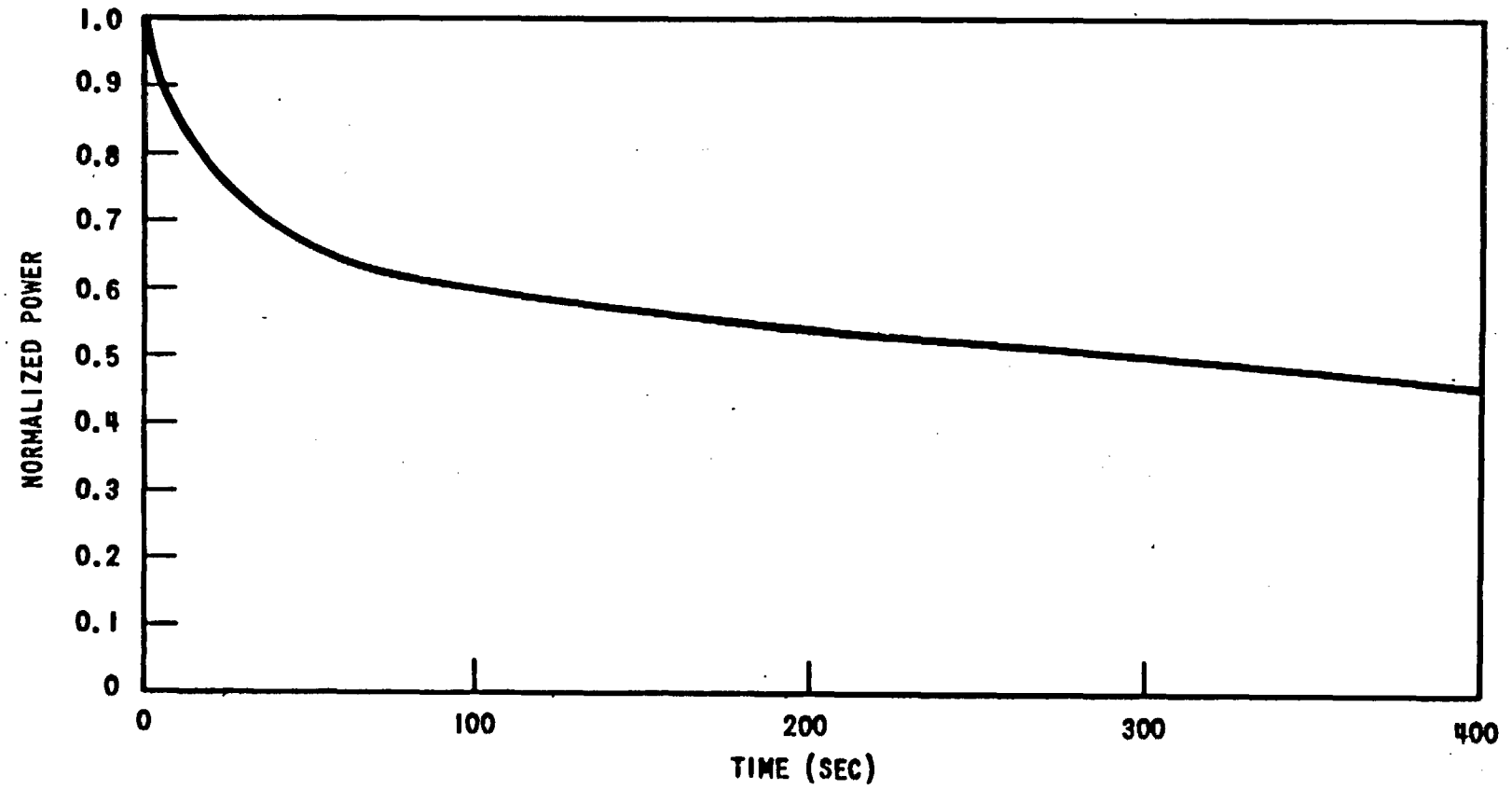

Figure 2-12. Reactor Power Decay Curve

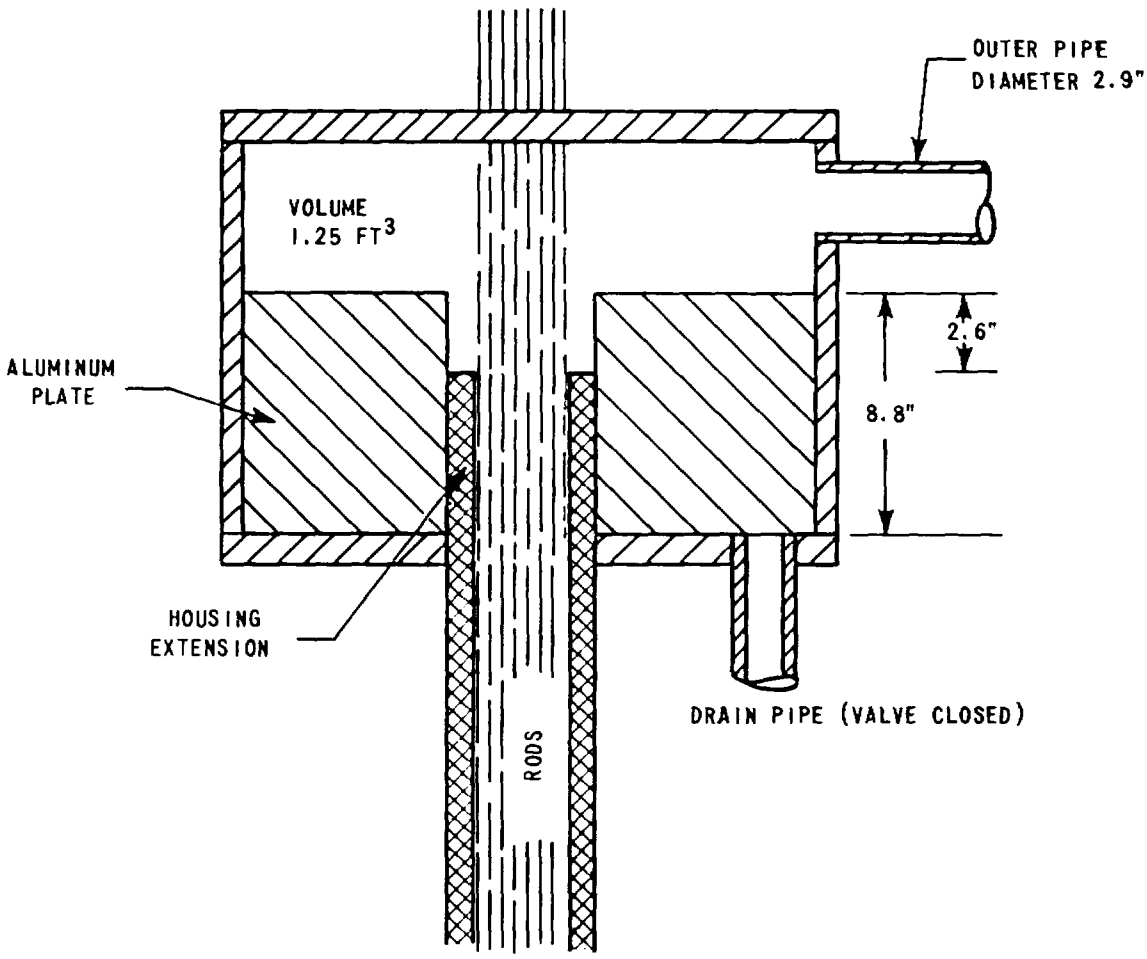

Figure 2-13. Sketch of PWR FLECHT Upper Plenum Modified for Fallback

approximately 350°F for the tests with "fallback" to simulate heat release from the vessel upper internals. A VIDAR digital data acquisition system scanned the heater rod thermocouples at a rate of approximately 25 channels per second during the test. After digitizing, the signal values were recorded in BCD-form on magnetic tape and later reduced and plotted by an off-line CDC 6600 digital computer.

Time correlation of the thermocouple signals with the start of flood was achieved by VIDAR scanning of a synchronous timer and a flooding event elapsed timer on successive channels. The local coolant thermocouples and pressure transducer readings were continuously monitored on pen recorders and Visicorders. Housing temperatures were recorded on a smaller Hewlett-Packard digital data acquisition system.

Coolant flow rates were measured with Potter turbine flowmeters and/or rotameters. The power of each of the radial sections of the heater rod bundle was detected by a potential and a current transformer. Outputs of these transformers were multiplied by three Hall-effect devices and continuously recorded on three null-balance recorders.

The injection of water was terminated manually after quenching of the upper elevation thermocouples and the power was shut off.

SECTION 3

DISCUSSION OF TEST RESULTS

3.1 SUMMARY OF RUN CONDITIONS AND TEST RESULTS

In this report, a particular run is characterized by the transient temperature behavior of the midplane (six-foot elevation) of the hottest rod. For each run, the hot rod was designated as the one which reached the highest midplane temperature during the test and was reasonably close to the nominal initial clad temperature for the run.

Typical transient midplane clad temperature behavior for constant and variable flooding rate tests is illustrated in Figure 3-1. In the constant flooding rate tests, midplane temperatures continued to increase after flooding was initiated until the heat transfer coefficient became large enough to turn the temperature around. The temperature then continued to decrease until the quench front (onset of clad wetting) reached the bundle midplane, at which time the clad temperature dropped rapidly to saturation.

Variable flooding rate tests exhibited a somewhat different behavior, which was dependent on the flooding rate program followed. Thus, for Run 7350, the midplane clad temperature increased slightly to a second peak following the reduction in flooding rate from 6.3 to 1.0 in./sec. The parameters shown for the variable flooding rate curve in Figure 3-1 are used to characterize the variable flow test results. The same parameters are used to characterize constant flooding rate tests, except that those associated with the second temperature rise are not applicable. These parameters are:

1. Temperature Rise 1, $\Delta T_{rise\ 1}$. Defined as the difference between the clad temperature at the start of flooding (initial clad temperature) and the first peak temperature.

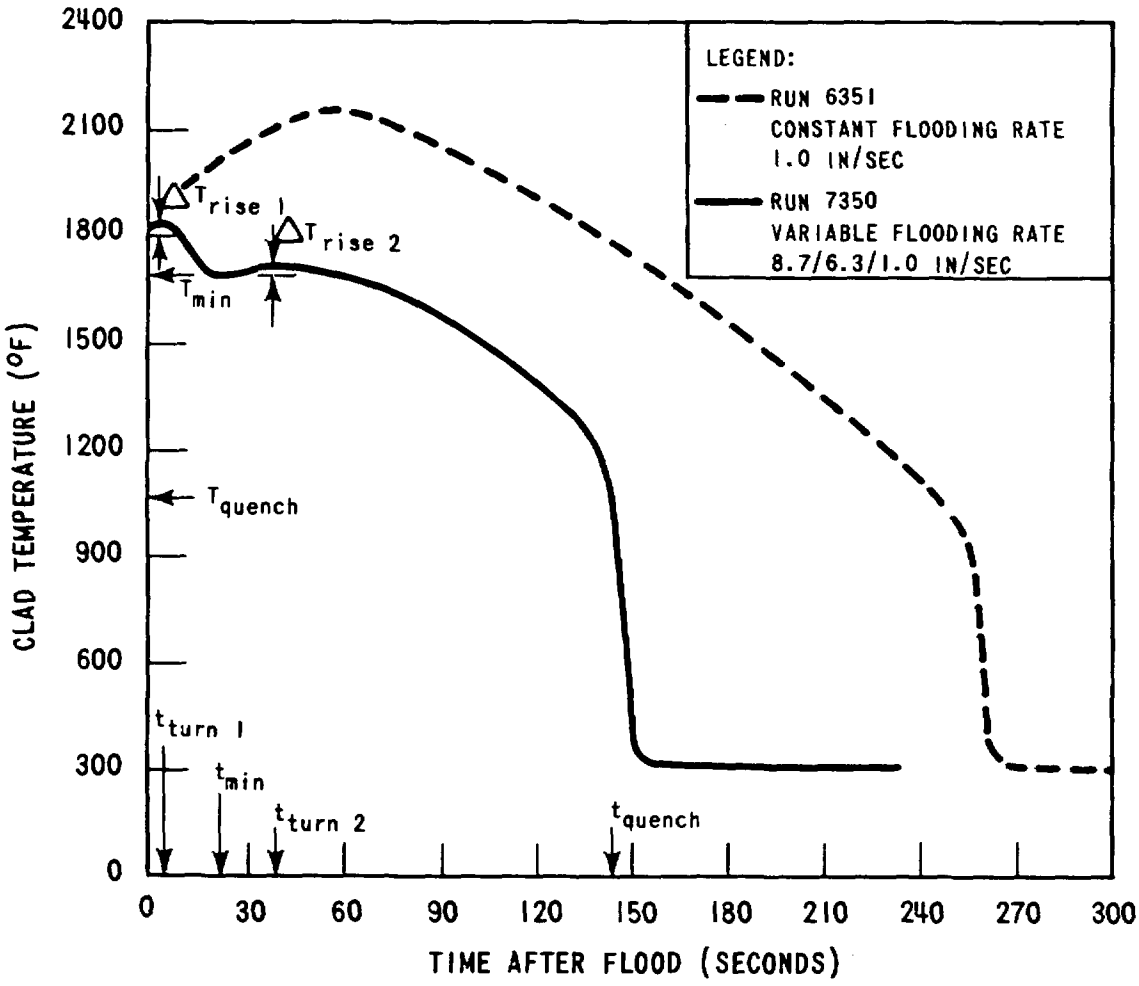

Figure 3-1. Typical Transient Midplane Clad Temperature Behavior for Constant and Variable Flooding Rate Tests

2. Turnaround Time 1, $t_{turn\ 1}$. Defined as the time after flooding at which the clad temperature reaches its first maximum.

3. Minimum Temperature, T_{min}. Defined as the minimum clad temperature reached after the first peak temperature, after which the clad temperature again increases.

4. Minimum Time, t_{min}. Defined as the time after flooding at which T_{min} is reached.

5. Temperature Rise 2, $\Delta T_{rise\ 2}$. Defined as the difference between T_{min} and the second peak temperature.

6. Turnaround Time 2, $t_{turn\ 2}$. Defined as the time after flooding at which the clad temperature reaches its second maximum.

7. Quench Time, t_{quench}. Defined as the time after flooding at which clad temperatures start to drop very rapidly (i.e., almost vertically) to saturation.

8. Quench Temperature, T_{quench}. Defined as the clad temperature at t_{quench}.

Tables 3-1 through 3-3 summarize the exact run conditions and measured temperature behavior for the midplane elevation of the hottest rod of each PWR-FLECHT run. Additional data for Group I and II runs was contained in Appendix A of References 2 and 3. Appendix C of this report contains additional data for runs performed subsequent to publication of References 2 and 3. It should be noted that the quench temperature data presented in Tables 3-1 through 3-3 and Appendices A and C is approximate. More accurate quench temperature data and a discussion of parameter effects on quench temperatures are contained in Appendix E.

Although the preceding parameters are useful for characterizing test results and for parameter sensitivity studies, an understanding of heat transfer coefficient behavior is necessary to apply FLECHT test results to the prediction of reactor fuel behavior. Heat transfer coefficients were therefore calculated for each run using the DATAR computer code. This code performs a transient conduction calculation based on a known temperature (heater rod thermocouple)

TABLE 3-1

FLECHT DATA SUMMARY, STAINLESS STEEL CLAD CONSTANT FLOW TESTS, HOT ROD MIDPLANE ELEVATION (6-Foot)

Run No.	Pressure (psia)	Peak Power (kw/ft)	Decay Power[a]	Flooding Rate (in./sec)	Inlet Subcooling (°F)	Initial Temperature (°F)	Temperature Rise (°F)	Turnaround Time (sec)	Quench Temperature (°F)	Quench Time (sec)	Bundle Size	Remarks
1	60	1.24	A	5.9	137	1326	137	25	730	124	7 x 7	High Housing Temp
2	59	1.24	A	5.8	136	1646	46	10	735	130	7 x 7	High Housing Temp
3A	56	1.24	A	5.8	141	1812	74	7	784	116	7 x 7	High Housing Temp
3B	56	1.24	A	6.0	142	1761	76	7	671	126	7 x 7	High Housing Temp
3C	57	1.24	A	5.9	132	1764	63	6	822	124	7 x 7	High Housing Temp
4	57	1.24	A	17.6	134	1589	9	2	907	44	7 x 7	High Housing Temp
0105	56	1.24	A	6.0	137	801	226	36	728	75	7 x 7	
0307	58	1.24	A	9.8	139	1210	59	5	827	50	7 x 7	
0408	59	1.24	A	10.0	140	1625	30	3	797	51	7 x 7	
0509	58	1.24	A	9.9	137	2017	20	3	797	64	7 x 7	
0610	15	1.24	A	5.8	138	1403	134	20	908	104	7 x 7	
0711	15	1.24	A	5.9	137	1600	82	15	932	104	7 x 7	
0812	15	1.24	A	5.9	136	1807	55	7	841	105	7 x 7	
0913	15	1.24	A	9.8	136	1601	42	6	1006	61	7 x 7	
1002	56	1.24	A	6.0	137	1605	70	6	808	76	7 x 7	
1116	73	1.24	A	6.0	142	1611	63	7	864	75	7 x 7	
1314	57	1.24	A	5.8	189	1604	81	8	991	65	7 x 7	
1417	90	1.24	A	5.8	150	1611	70	7	822	73	7 x 7	
1615	30	1.24	A	5.8	130	1594	105	9	834	105	7 x 7	
1720	61	1.24	A	5.9	25	1617	53	7	794	165	7 x 7	
1806	56	1.24	A	5.9	135	1606	94	9	919	52	7 x 7	Unheated Housing
1902	55	1.24	A	5.9	133	1612	53	6	765	132	7 x 7	Hot Housing
2322	15	1.24	A	4.0	148	1612	168	43	899	185	7 x 7	
2636	57	1.24	A	5.9	131	1600	60	5	1015	54	7 x 7	50% Flow Blockage
2737	58	1.24	A	5.9	137	1799	42	4	1015	56	7 x 7	50% Flow Blockage
2838	57	1.24	A	5.9	144	1600	79	7	950	47	7 x 7	75% Flow Blockage
2939	56	1.24	A	5.9	140	1808	61	5	1057	49	7 x 7	75% Flow Blockage
3100	57	1.24	A	2.1	144	1609	131	14	1048	89	7 x 7	75% Flow Blockage
3300	58	1.24	A	4.0	137	1632	81	7	1164	62	7 x 7	75% Flow Blockage

[a]Defined in Figure 3-21

TABLE 3-1 (Continued)

FLECHT DATA SUMMARY, STAINLESS STEEL CLAD CONSTANT FLOW TESTS, HOT ROD MIDPLANE ELEVATION (6-Foot)

Run No.	Pressure (psia)	Peak Power (kw/ft)	Decay Power[a]	Flooding Rate (in./sec)	Inlet Subcooling (°F)	Initial Temperature (°F)	Temperature Rise (°F)	Turnaround Time (sec)	Quench Temperature (°F)	Quench Time (sec)	Bundle Size	Remarks
3440	55	1.24	B	5.9	132	1204	138	13	780	65	10 x 10	
3541	57	1.24	B	5.9	141	1598	90	8	752	71	10 x 10	
3642	57	1.24	B	5.9	141	1805	62	5	804	87	10 x 10	
3724	57	1.24	B	1.9	141	1187	427	60	790	175	10 x 10	
3823	57	1.24	B	1.9	22	1200	394	57	779	233	10 x 10	
3920	55	1.24	B	5.8	16	1608	54	5	745	162	10 x 10	
4027	57	0.69	B	1.9	141	1592	103	28	712	130	10 x 10	
4129	60	1.40	B	1.9	134	1596	372	55	850	224	10 x 10	
4225	59	1.24	B	1.9	139	1596	247	35	799	192	10 x 10	
4321	58	1.24	B	3.9	140	1604	107	14	813	102	10 x 10	
4442	59	1.24	B	5.8	138	1813	69	5	805	74	10 x 10	
4526	57	0.69	B	5.9	139	1608	26	5	849	54	10 x 10	
4628	59	1.40	B	5.9	150	1606	85	6	856	71	10 x 10	
4718	55	1.24	B	5.9	86	1610	49	6	753	103	10 x 10	
5019	55	1.24	B	9.8	17	1605	39	4	779	118	10 x 10	
5123	55	1.24	B	1.9	24	1607	241	45	810	246	10 x 10	
5231	18	1.24	B	5.9	53	1603	96	11	543	170	10 x 10	
5332	28	1.24	B	5.9	87	1604	61	7	738	96	10 x 10	
5433	71	1.24	B	5.9	156	1614	72	7	807	61	10 x 10	
5534	84	1.24	B	5.9	162	1614	58	7	874	54	10 x 10	
5642	60	1.24	B	5.8	141	1811	67	6	767	75	10 x 10	
5730	60	1.24	B	6.0	145	1602	59	7	758	66	10 x 10	Borated Coolant

[a]Defined in Figure 3-21

TABLE 3-1 (Continued)

FLECHT DATA SUMMARY, STAINLESS STEEL CLAD CONSTANT FLOW TESTS, HOT ROD MIDPLANE ELEVATION (6-Foot)

Run No.	Pressure (psia)	Peak Power (kw/ft)	Decay Power[a]	Flooding Rate (in./sec)	Inlet Subcooling (°F)	Initial Temperature (°F)	Temperature Rise (°F)	Turnaround Time (sec)	Quench Temperature (°F)	Quench Time (sec)	Bundle Size	Remarks
5948	58	1.24	A	1.0	142	1632	370	66	928	254	7 x 7	
6047	57	1.40	A	6.2	140	2006	51	4	853	76	7 x 7	
6155	57	1.24	A	5.9	143	2212	31	3	902	78	7 x 7	
6256	60	1.24	A	3.9	134	2199	39	4	838	102	7 x 7	
6351	59	1.24	A	1.0	136	1795	321	57	914	256	7 x 7	
6553	59	1.24	A	1.0	148	2012	278	62	926	257	7 x 7	
6658	60	1.24	A	2.0	140	2195	85	7	900	163	7 x 7	
6749	58	1.24	A	0.6	153	1605	---	---	---	---	7 x 7	Power Scram at 107 Sec.
6848	59	1.24	C	1.0	144	1603	532	94	952	265	7 x 7	
6948	58	1.24	B	1.0	147	1602	465	95	944	266	7 x 7	
7057	58	1.24	A	0.8	145	1603	506	111	960	285	7 x 7	
7158	54	1.24	A	2.0	149	2156	88	9	805	156	7 x 7	
7845	55	1.24	B	4.3	142	1600	80	5	715	119	10 x 10	75% Flow Blockage
7946	58	1.24	B	1.0	143	1595	193	15	729	239	10 x 10	75% Flow Blockage
8054	56	1.24	B	3.9	135	1570	80	5	685	108	10 x 10	75-90% Flow Blockage
8162	57	1.24	B	1.1	142	1595	195	15	690	242	10 x 10	75-90% Flow Blockage
8265	57	1.24	B	3.9	137	1600	90	6	710	107	10 x 10	75-90-100(4)% Flow Blockage
8366	58	1.24	B	1.0	143	1580	245	17	695	246	10 x 10	75-90-100(4)% Flow Blockage
8567	60	1.24	B	3.9	133	1558	84	6	740	113	10 x 10	75-90-100(16)% Flow Blockage
8668	57	1.24	B	1.0	138	1600	220	17	700	253	10 x 10	75-90-100(16)% Flow Blockage
8764	57	1.24	B	0.6	146	1605	---	---	---	---	10 x 10	75-90-100(16)% Flow Blockage Power Scram at 97 Sec
9278	58	1.24	B	1.0	142	2028	258	57	908	260	7 x 7	Fallback

[a]Defined in Figure 3-21

TABLE 3-2

FLECHT DATA SUMMARY, STAINLESS STEEL CLAD VARIABLE FLOW TESTS, HOT ROD MIDPLANE ELEVATION (6-foot)

Run No.	Pressure (psia)	Peak Power (kw/ft)	Decay Power[a]	Flooding Rate (in./sec)[b]	Inlet Subcooling (°F)	Initial Clad Temperature (°F)	$\Delta T_{rise\ 1}$ (°F)	$t_{turn\ 1}$ (sec)	T_{min} (°F)	t_{min} (sec)	$\Delta T_{rise\ 2}$ (°F)	$t_{turn\ 2}$ (sec)	T_{quench} (°F)	t_{quench} (Sec)	Bundle Size	Remarks
7350	57	1.24	B	8.7/6.3-1.0	145	1805	35	3	1687	23	29	39	1063	144	7 x 7	
7452	56	1.24	B	9.0/6.7-1.0	145	2200	25	3	----	--	---	--	----	---	7 x 7	Power Off At 121 sec
7569	57	1.24	B	8.5/6.9-1.0	145	1805	35	3	1623	25	7	36	1050	127	7 x 7	Fallback
7670	57	1.24	B	8.8/5.7-1.0	140	2195	25	3	----	--	---	--	1025	148	7 x 7	Fallback
7771	56	1.40	B	8.6/6.4-1.0	142	2195	40	3	----	--	---	--	1025	167	7 x 7	Fallback
8463	60	1.24	B	3.9-1.0	140	1600	88	6	1580	14	35	26	670	221	10 x 10	75-90-100 (4)% Flow Blockage
8975	60	1.24	B	5.8-1.0	148	2301	45	4	2181	13	69	36	930	249	7 x 7	Fallback
9077	55	1.24	B	6.2-1.0	142	2138	42	4	2151	10	100	54	815	276	7 x 7	Fallback
9176	58	1.24	B	5.9-1.0	140	2197	34	4	2202	9	79	41	827	239	7 x 7	Fallback Low Housing Temp
9379	61	1.24	B	6.0-1.0	148	2146	45	4	2145	8	135	47	964	252	7 x 7	

[a]Defined in Figure 3-21
[b]See Figure 3-26

TABLE 3-3

FLECHT DATA SUMMARY, ZIRCALOY CLAD TESTS,
HOT ROD MIDPLANE ELEVATION (6 ft)

Run No.	Pressure (psia)	Peak Power (kw/ft)	Decay Power[a]	Flooding Rate (in./sec)	Inlet Subcooling (°F)	Initial Clad Temperature (°F)	$\Delta T_{rise\ 1}$ (°F)	$t_{turn\ 1}$ (sec)	T_{min} (°F)	t_{min} (sec)	$\Delta T_{rise\ 2}$ (°F)	$t_{turn\ 2}$ (sec)	T_{quench} (°F)	t_{quench} (sec)	Bundle Size	Remarks
2443	56	1.24	A	10.0	138	2035	67	6	----	----	----	----	----	----	7 x 7	Degraded quench [illegible] Hot T/C
2544	58	1.24	A	4.0	140	2015	127	12	----	----	----	----	----	----	7 x 7	Degraded quench [illegible] Hot T/C
8874	64	1.24	B	6.0-1.0[b]	141	2297	63	4	2060	12	87	40	971	204	7 x 7	Fallback
9573	61	1.24	B	1.1	140	1970	350 at 18 seconds				----	----	----	----	7 x 7	

[a]Defined in Figure 3-21
[b]See Figure 3-26

on the inside surface of the rod cladding, and a known power generation rate. The code calculated the rod surface temperature, surface heat flux and heat transfer coefficient as a function of time. The local fluid temperature was assumed to be equal to the saturation temperature.

Inputs to the program were the transient heater rod thermocouple temperature history, heat generation rate as a function of time, and the temperature-dependent material properties. In determining the heat generation rate, the following empirical factors were applied to the nominal axial power distribution described in Section 2.1:

Elevation (ft)	Factor
2	1.030
4	1.016
6	0.977
8	1.016
10	1.030

These factors were due to a change in heater resistance which occurred as a result of swaging the heater rods during manufacture. It should be noted that the peak powers reported in Tables 3-1 through 3-3 and elsewhere in this report do not include the 0.977 midplane power distribution factor.

A calculation of the heat flux and mass of cladding reacted due to Zircaloy-water reaction was added to the DATAR code for the Group III tests. The calculation was based on the following parabolic rate correlation of Baker and Just (Reference 4):

$$W = 11.8784\ t^{1/2} e^{-(20,700/T)}$$

where:

W is the mass of Zircaloy reacted per unit surface area in lbm/ft^2,

t is the time in seconds, and

T is the absolute temperature in °R.

Using the above equation in incremental form, the mass of Zircaloy reacted and the heat flux due to metal-water reaction at any instant in time (assuming an energy release of 2,800 Btu/lbm reacted) was obtained. This heat flux was added to the heat flux determined by the code's conduction calculation to give an overall heat transfer coefficient.

The transient clad temperature and heat transfer coefficient outputs were obtained from the DATAR code both as printout and plots. The graphs presented in Appendix C of the report were obtained directly from the computer plotting routine.

A detailed discussion of the assumptions and numerical techniques employed in the analysis is included in Reference 2.

3.2 GROUP I AND GROUP II STAINLESS CLAD HEAT TRANSFER RESULTS

3.2.1 Data Verification

3.2.1.1 Reproducibility and Test Bundle Symmetry

Figure 3-2 compares heat transfer coefficients at the 4, 6 and 8 ft elevations. These coefficients were obtained for the same central rod from two runs with identical test conditions. Reproducibility of the heat transfer coefficient was excellent.

The data below shows the good repeatability of the transient clad temperature behavior for the same two runs.

Run	Initial Clad Temperature (°F)	Temperature Rise (°F)	Turnaround Time (sec)	Quench Temperature (°F)	Quench Time (sec)
4442	1813	69	5	805	74
5642	1811	67	6	767	75

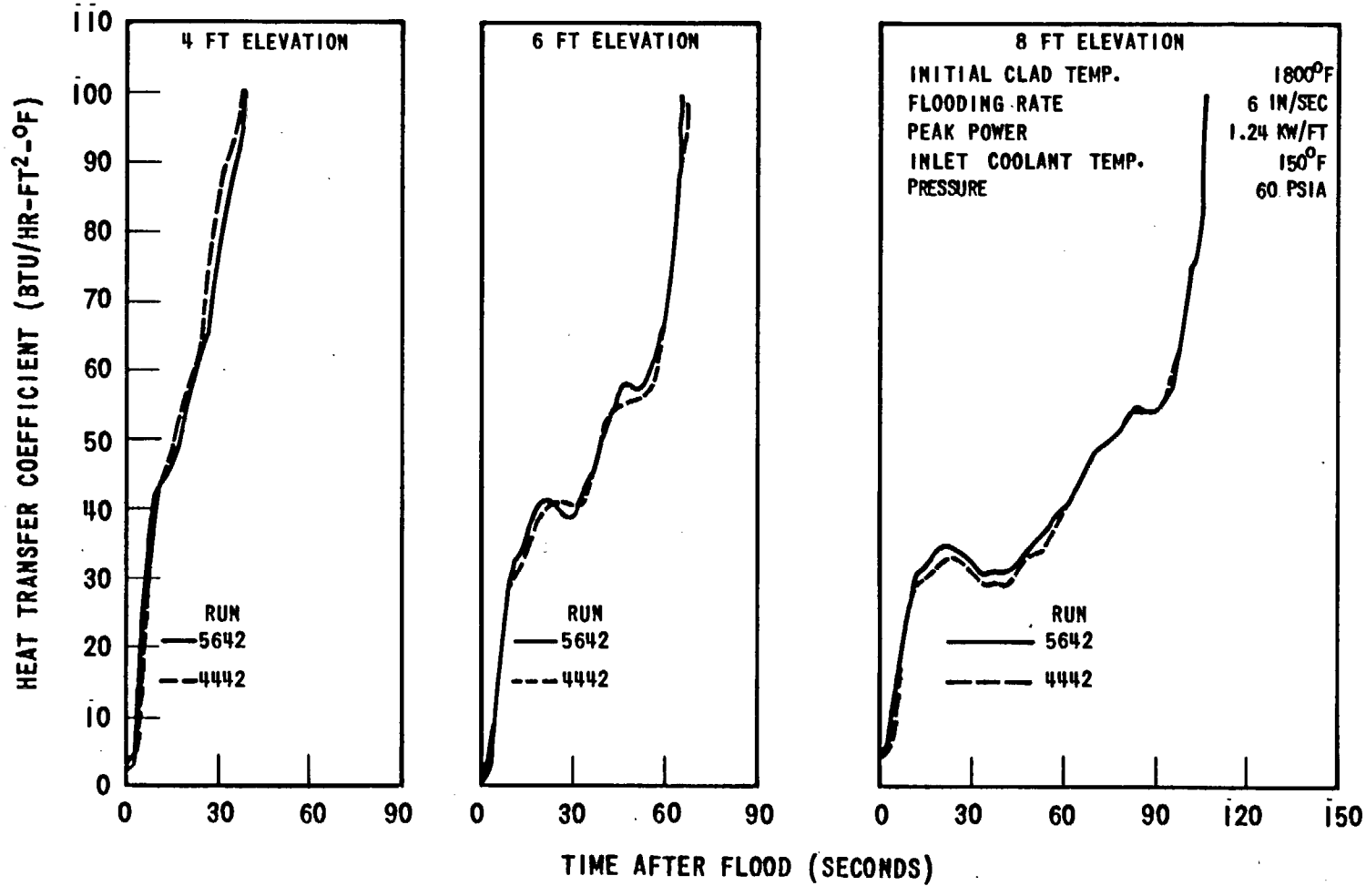

Figure 3-2. Reproducibility of Heat Transfer Coefficient for Two Runs at Various Elevations

To limit the total number of thermocouples to a manageable number, two way symmetry of the 49 and 100 rod bundles was utilized. In each bundle, one instrumented rod was installed in the uninstrumented half as a check. Figure 3-3 shows a typical comparison of the heat transfer coefficient for symmetric rods in the 49 and 100 rod bundles. Figure 3-3 shows that diagonal symmetry existed in both bundles. Checks on bundle symmetry were also done for low flooding rate tests and again symmetry was found to be good.

3.2.1.2 Effect of Bundle Size and Radial Variation of the Heat Transfer Coefficient

An evaluation of the effect of bundle size was made to demonstrate the validity of tests performed with the 7 x 7 rod bundle array. Tests which are valid comparisons between the 7 x 7 and 10 x 10 bundles are listed in Table 3-4. In these tests, the nominal run conditions were the same and, in addition, the housing temperatures agreed fairly well (within 100°F, based on the average housing temperature). Table 3-4 indicates generally good agreement between the transient temperature behavior of the 7 x 7 and 10 x 10 bundles. Similarly, midplane heat transfer coefficients were also found to be in good agreement for these runs as shown in Figures 3-4 and 3-5.

The radial variation of midplane heat transfer coefficients in the 10 x 10 and 7 x 7 bundles is shown in Figure 3-6. The heat transfer behavior of the outer rod of the 10 x 10 assembly agreed closely with that of the inner rods, whereas the outer rod heat transfer coefficient of the 7 x 7 assembly was found to be higher than the inner rods by approximately 5 - 10 Btu/hr-ft^2-°F. It is believed that this latter condition may be due to Rod 1F in the 10 x 10 bundle being surrounded on three sides by heater rods, whereas Rod 1D in the 7 x 7 bundle was adjacent to a guide tube. Thus, radiation loss to the guide tube may account for the increased heat transfer at this location in the 7 x 7 bundle.

It was concluded that with the exception of the behavior of the boundary rod there was no difference in results between the 7 x 7 and 10 x 10 bundles and that heat transfer coefficients were relatively uniform across the bundle interior for both assemblies.

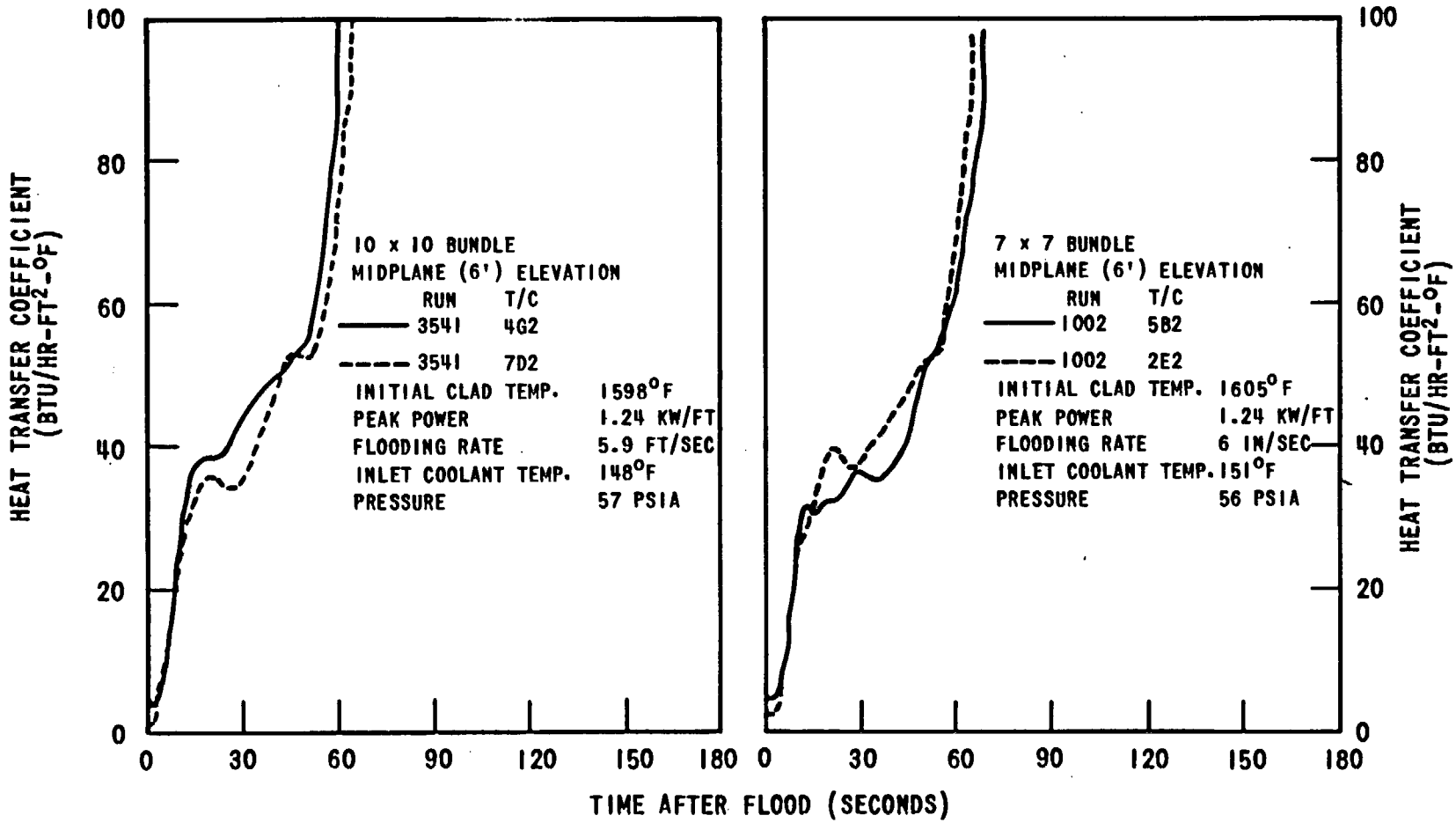

Figure 3-3. Test Bundle Symmetry-Heat Transfer Coefficient for Symmetrical Rods for 10 x 10 and 7 x 7 Bundles

TABLE 3-4

COMPARISON OF 7 x 7 AND 10 x 10 ARRAYS

Run No.	Pressure (psia)	Peak Power (kw/ft)	Flooding Rate (in/sec)	Inlet Subcooling (°F)	Initial Temperature (°F)
1002	56	1.24	6.0	137	1605
3541	57	1.24	5.9	141	1598
1720	61	1.24	5.9	25	1617
3920	55	1.24	5.8	16	1608

Run No.	Temperature Rise (°F)	Turnaround Time (sec)	Quench Temperature (°F)	Quench Time (sec)	Bundle Size
1002	70	6	808	76	7 x 7
3541	90	8	752	71	10 x 10
1720	53	7	794	165	7 x 7
3920	54	5	745	162	10 x 10

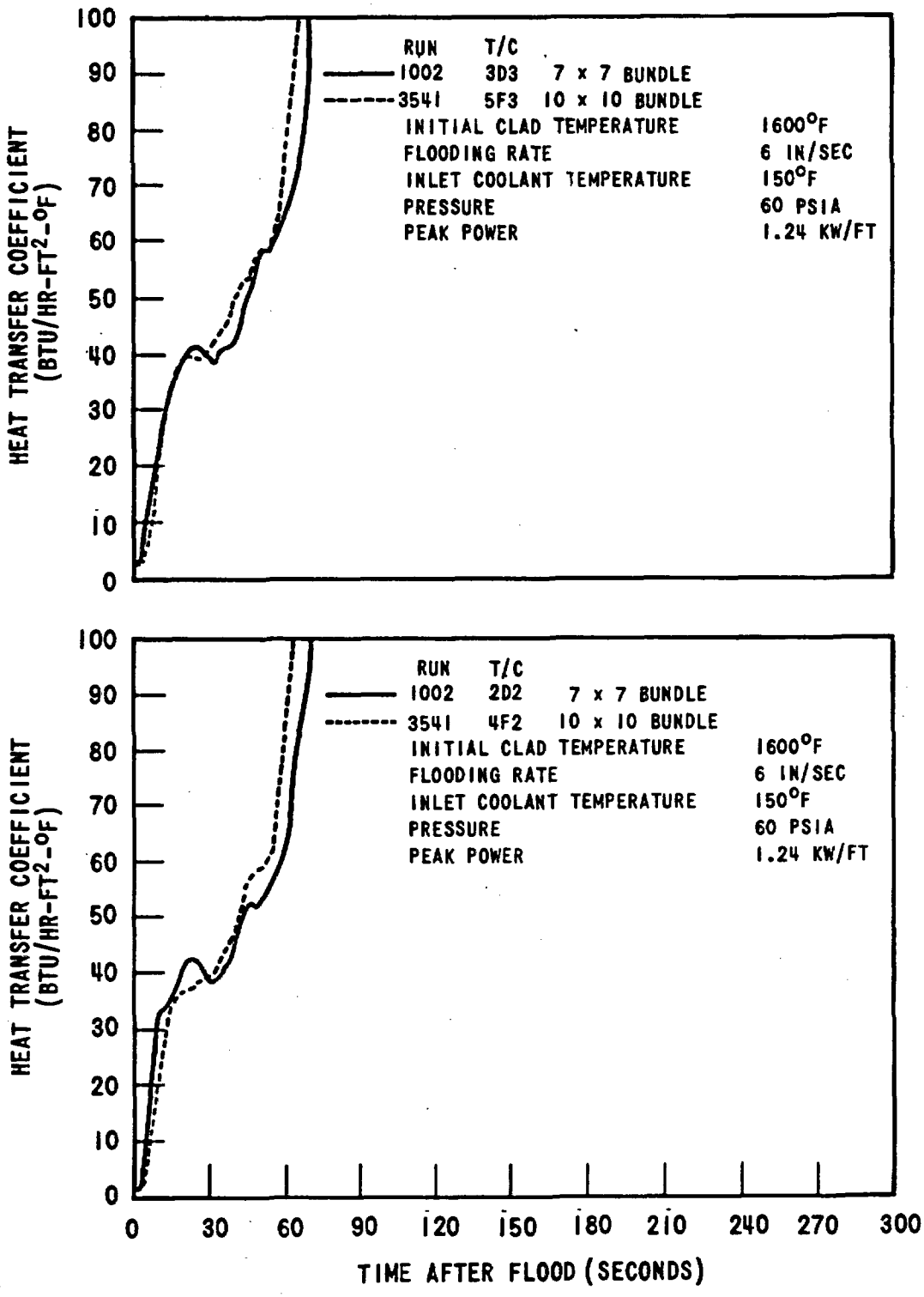

Figure 3-4. Heat Transfer Coefficients at Midplane of Equivalent Heater Rods in the 7 x 7 and 10 x 10 Bundles, Runs 1002 and 3541

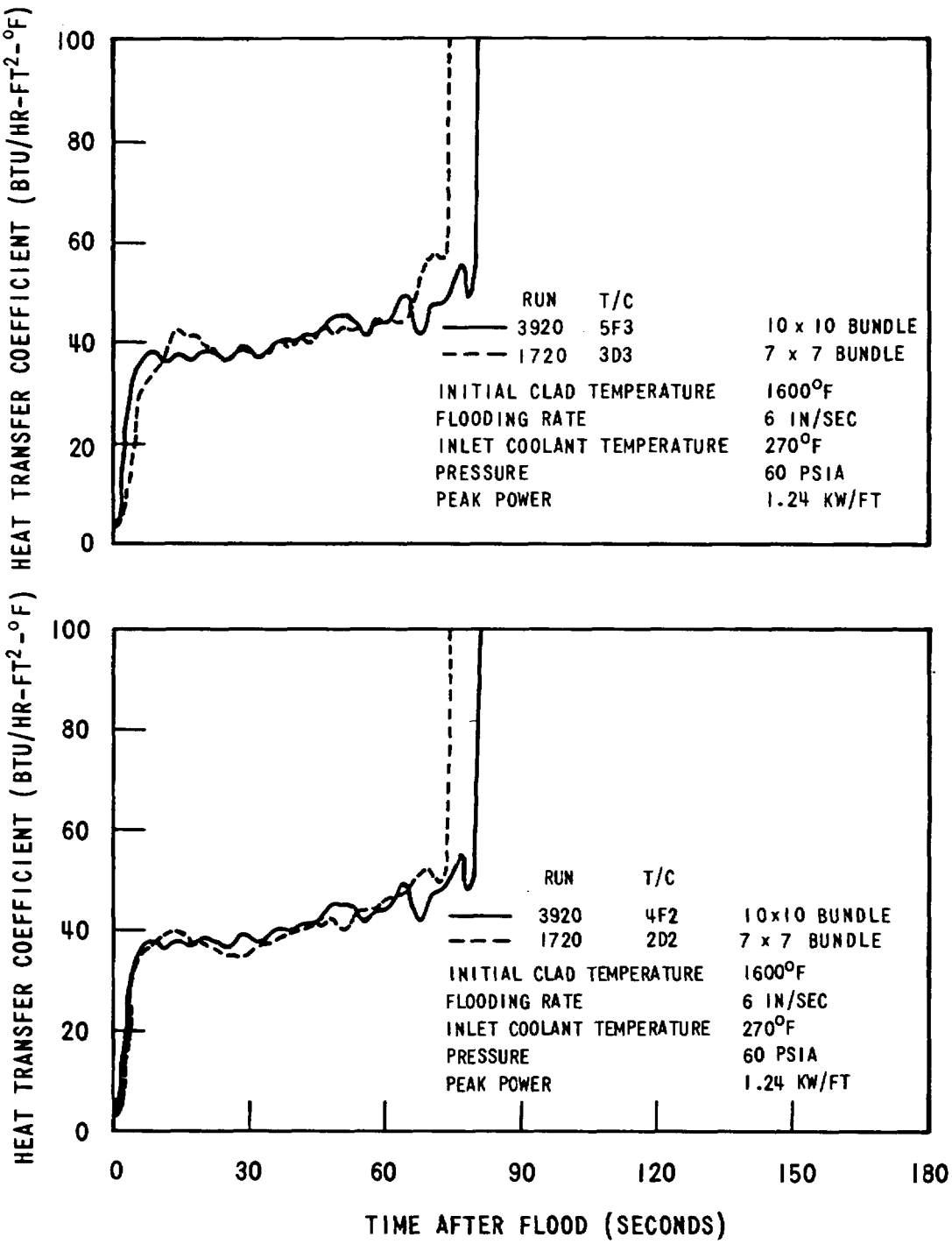

Figure 3-5. Heat Transfer Coefficients at the Midplane of Equivalent Heater Rods in the 7 x 7 and 10 x 10 Bundles, Runs 1720 and 3920

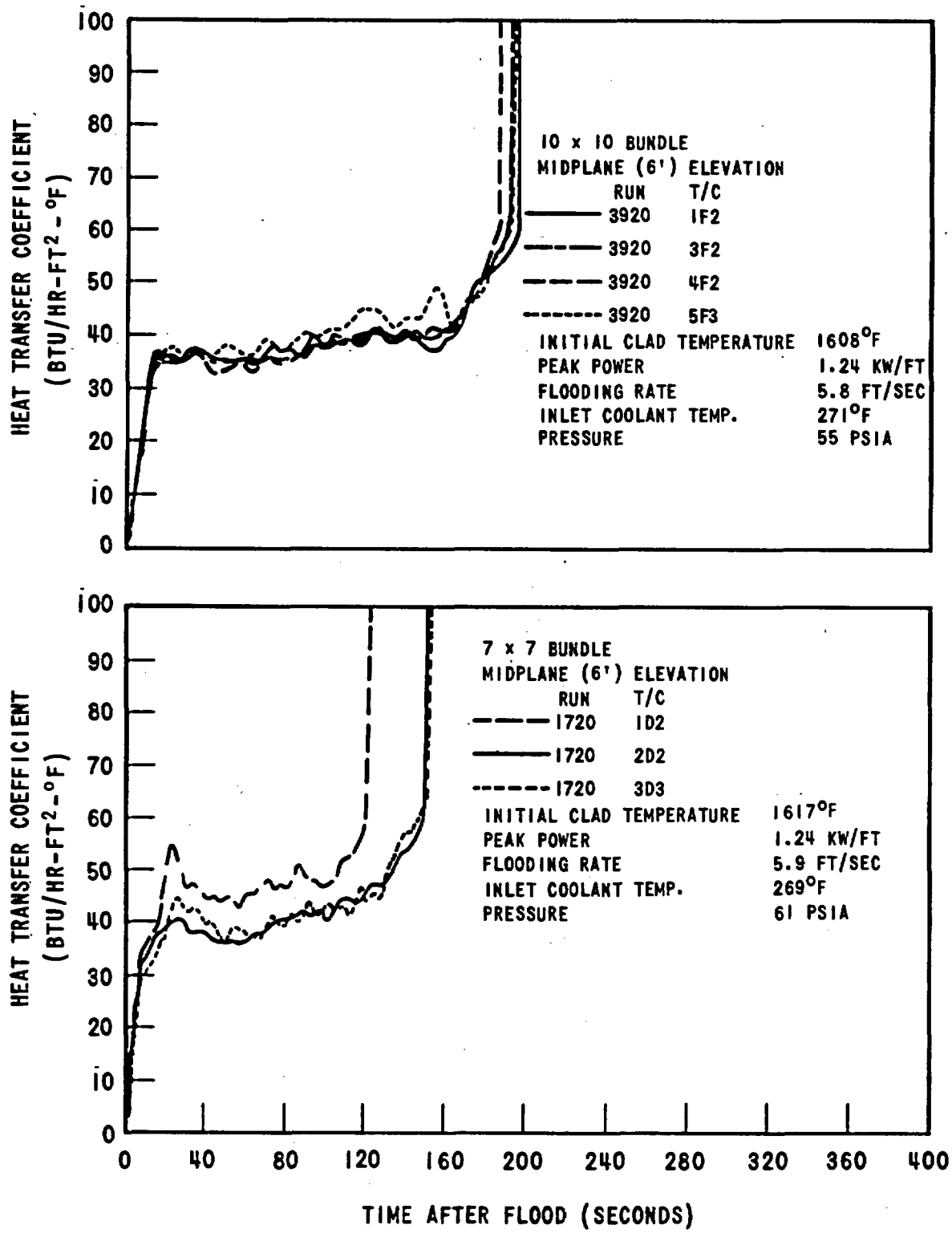

Figure 3-6. Radial Variation of Heat Transfer Coefficient for 10 x 10 and 7 x 7 Bundles

3.2.1.3 Effect of Flow Housing Temperature

As noted in Section 2, the flow housing was heated in order to minimize cold wall effects and simulate the effects of a larger array. Three identical tests were performed with different average housing temperatures in order to investigate the effect of flow housing temperature on heat transfer behavior. The results are shown in Figures 3-7 and 3-8. These figures show that at a 6 in./sec flooding rate, flow housing temperature had a strong influence on quench time and heat transfer coefficient while having little effect on the temperature rise and turnaround time. The unheated housing case was found to have the shortest quench time and the highest heat transfer coefficient after the first ten seconds.

Because of the strong dependence of quench behavior on housing temperature, it was necessary to choose a criterion for specifying the housing temperature distribution for each FLECHT test. Logically, the rod bundle housing should simulate the local energy input to the peripheral flow channels of an additional row of heater rods. Although the flow housing could not precisely match a row of rods at all times, the integrated energy release over the period of time from start of flooding to midplane quench could be simulated satisfactorily. Thus, the housing temperature was chosen to allow it to release the same amount of energy per fraction of unit cell flow area as would be released by an additional row of heater rods over the distance from the inlet to the midplane and up to the time of quench of the midplane thermocouples. This included both the generated and stored energy of the rods. Further, the axial energy distribution of the housing was specified to match the heater rods.

The relationship between the quench time and average temperature between 0 and 6 feet was obtained from the experimental data and by extrapolation of this data to other conditions. Therefore, the proper initial housing temperature was determined as a function of flooding rate, power density, inlet coolant temperature, pressure and initial heater rod temperature.

This method produced consistent heat transfer results which also showed very good reproducibility. The validity of the method is further demonstrated by the excellent agreement obtained between the results for the 49 and 100-rod bundles.

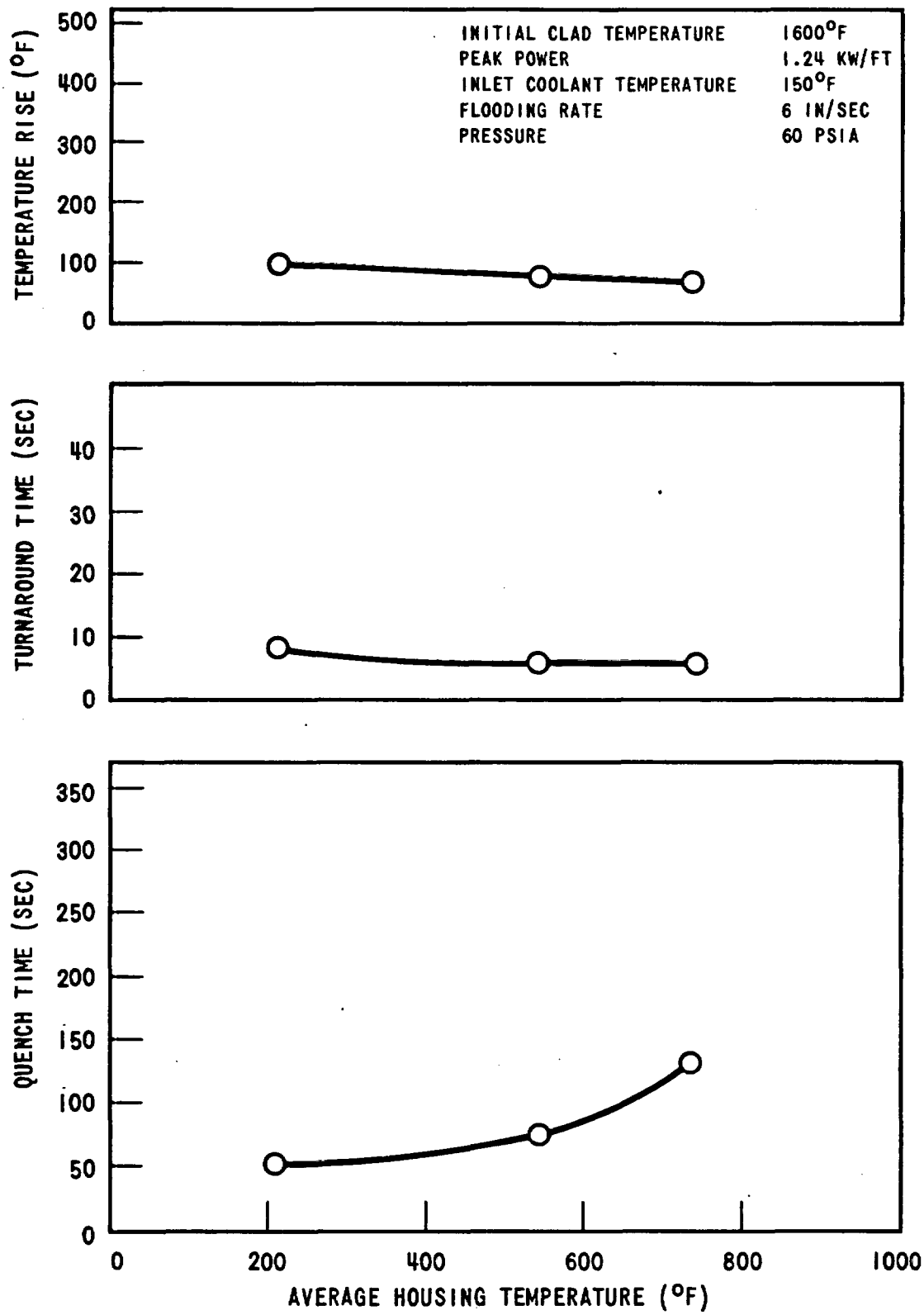

Figure 3-7. Effect of Housing Temperature on Temperature Rise, Turnaround Time and Quench Time

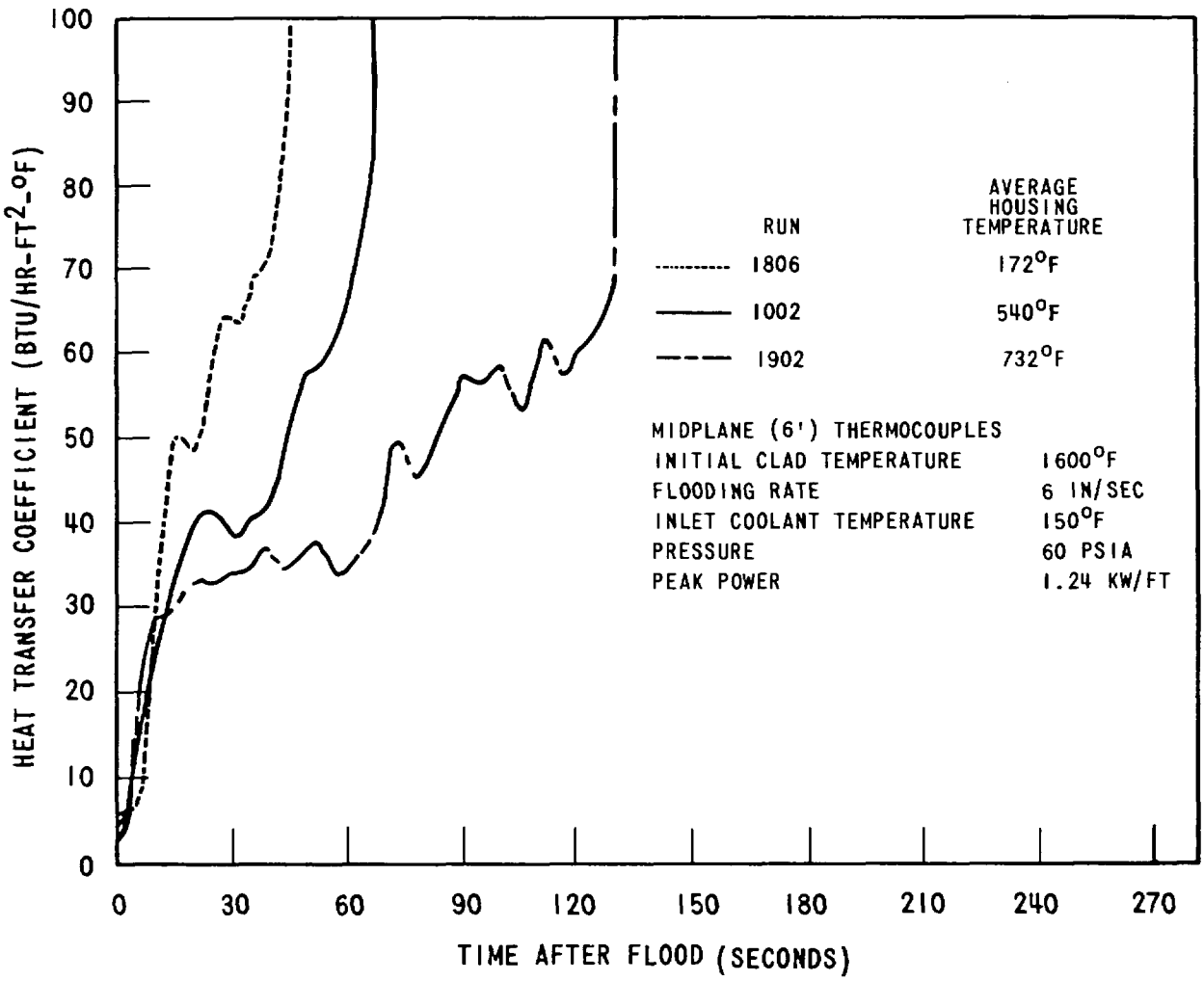

Figure 3-8. Effect of Housing Temperature on Heat Transfer Coefficient

The effect of matching the energy input from the housing and an equivalent outer row of rods over a shorter period of time was also investigated. Run 9077 was performed with the normal housing temperature distribution. The next run (9176) was performed with the same set of test conditions, but with reduced housing temperatures below the bundle midplane. The purpose of these tests was to determine if the reduction in housing temperatures would decrease the steam generation rate at early times, resulting in decreased heat transfer coefficients and higher peak temperatures.

As can be seen in Figure 3-9, the reduction in housing temperatures did not have any significant effect on the peak temperatures reached during the two runs. As anticipated, however, the reduction in housing temperatures did cause a slight decrease in the value of the first peak heat transfer coefficient and reduced the quench time by about thirty seconds.

3.2.2 System Parameter Effects on Heat Transfer

3.2.2.1 Initial Clad Temperature

Figure 3-10 shows the effect of initial clad temperature on the midplane heat transfer coefficient for flooding rates of 6, 2, and 1 in./sec. For short periods after flooding, the heat transfer coefficient in the 6 and 2 in./sec cases increased with clad temperature. Heat transfer at the midplane during this time period is dependent on the vapor generation rate and amount of water entrainment which occurs at the lower elevations. As initial clad temperatures increased, the vapor generation and amount of entrainment increased because the heat transfer is a function of $T_{clad} - T_{sat}$. The increased vapor generation and entrainment caused higher heat transfer coefficients at the upper elevations, although the effect was not as great as might have occurred with an axially uniform power distribution. Because of the cosine power shape of the heater rods, an increase in the initial midplane clad temperature of 400°F resulted in an increase of only about 150°F in the temperature at the 2-foot elevation. At later times the heat transfer coefficient trend tended to reverse and decrease with increasing initial clad temperature. At 1 in./sec, the effect of initial clad temperature on the heat transfer coefficient was smaller than in the above cases.

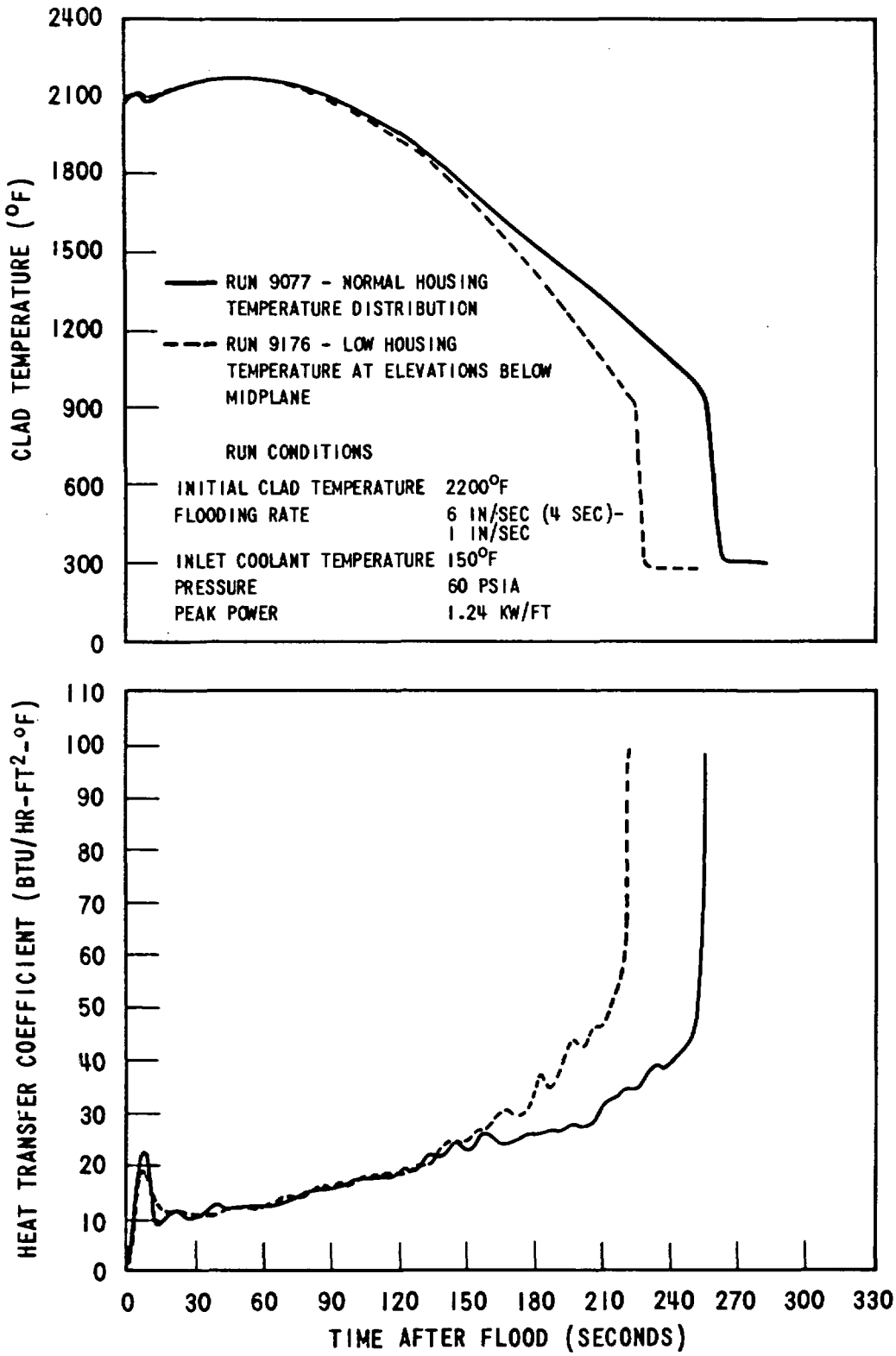

Figure 3-9. Effect of Low Housing Temperature at Elevations Below Midplane

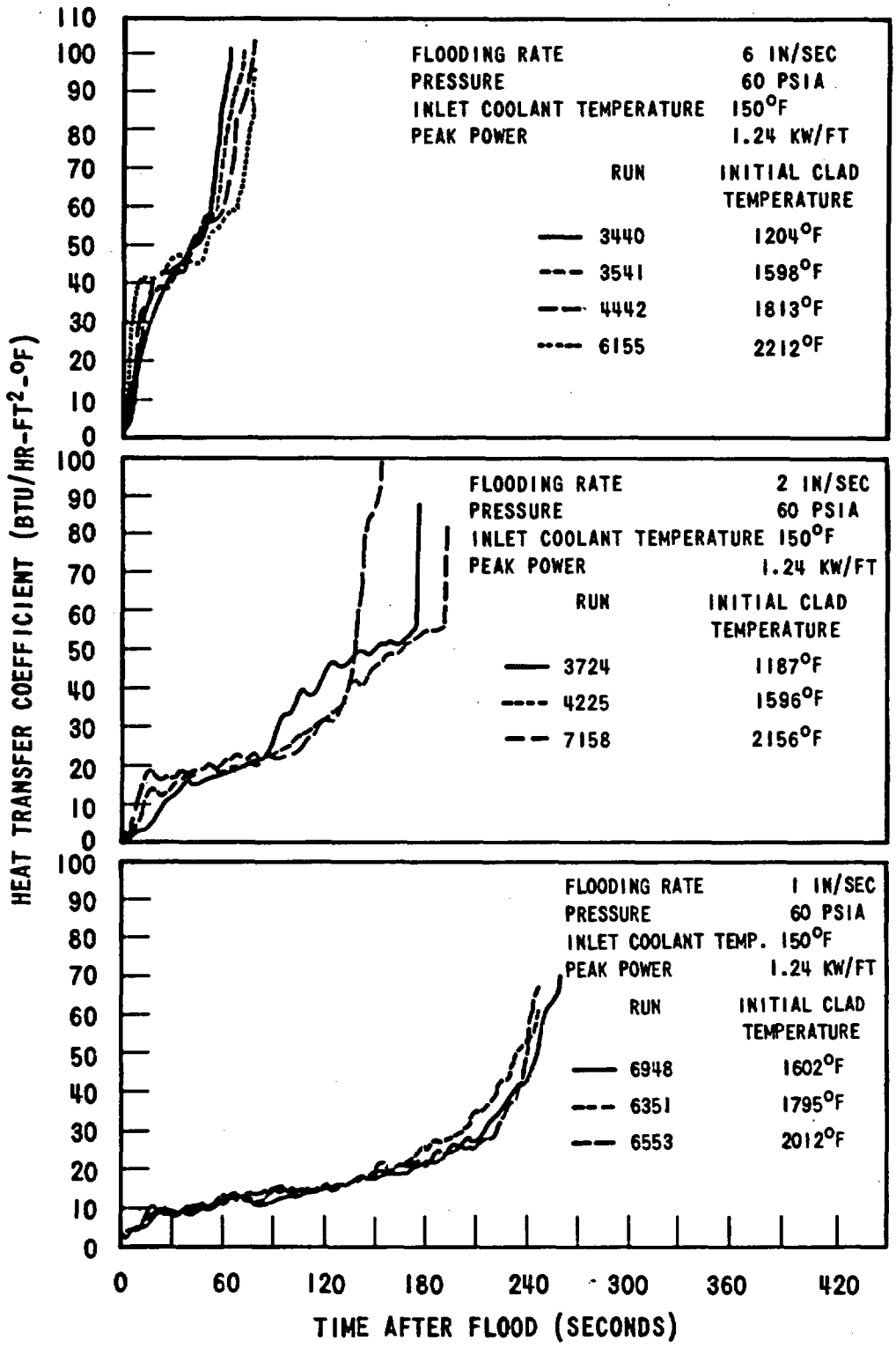

Figure 3-10. Effect of Initial Clad Temperature on Midplane (6') Heat Transfer Coefficient at 6, 2 and 1 In/Sec Flooding Rates

The effect of initial clad temperature on temperature response is shown in Figure 3-11. Temperature rise and turnaround time decreased with increased initial clad temperature, since at early times the heat transfer coefficient and the temperature difference for heat removal, $T_{clad} - T_{sat}$, both increased with clad temperature. Figure 3-11 also indicates that quench times were not strongly affected by initial clad temperature. The absence of a strong effect of initial clad temperature on quench time was apparently caused by the heat transfer trend reversal, i.e. higher at early time and lower at later time.

3.2.2.2 Flooding Rate

Figure 3-12 illustrates the effect of flooding rate on midplane heat transfer coefficients for 1600, 2000 and 2200°F initial clad temperature. The figure indicates increased heat transfer coefficients with flooding rate for all initial clad temperatures. This was due to an increase in the vapor generation rate and amount of entrainment throughout the test. This resulted from the greater clad surface area per unit of time exposed to the coolant at high flooding rates. Figures 3-13 and 3-14 show the effect of flooding rate on transient clad behavior. Increasing the flooding rate and hence the heat transfer coefficient reduced temperature rise, turnaround time and quench time.

3.2.2.3 Inlet Coolant Subcooling

Figure 3-15 shows the effect of inlet coolant subcooling on heat transfer coefficient in 6 in./sec and 2 in./sec tests at 60 psia pressure. For early times at both flooding rates the trend was toward increased heat transfer coefficient with decreased subcooling. This resulted from the higher steam generation rate at low subcooling which caused liquid entrainment to occur at an earlier time. At later times, low subcooling caused a decreased heat transfer coefficient and a longer quench time. This was due to the quench front moving more slowly up the channel because of the high steam generation rate. Figure 3-16 shows that lower inlet subcooling decreased temperature rise and turnaround time slightly, consistent with the above explanation. Quench time was

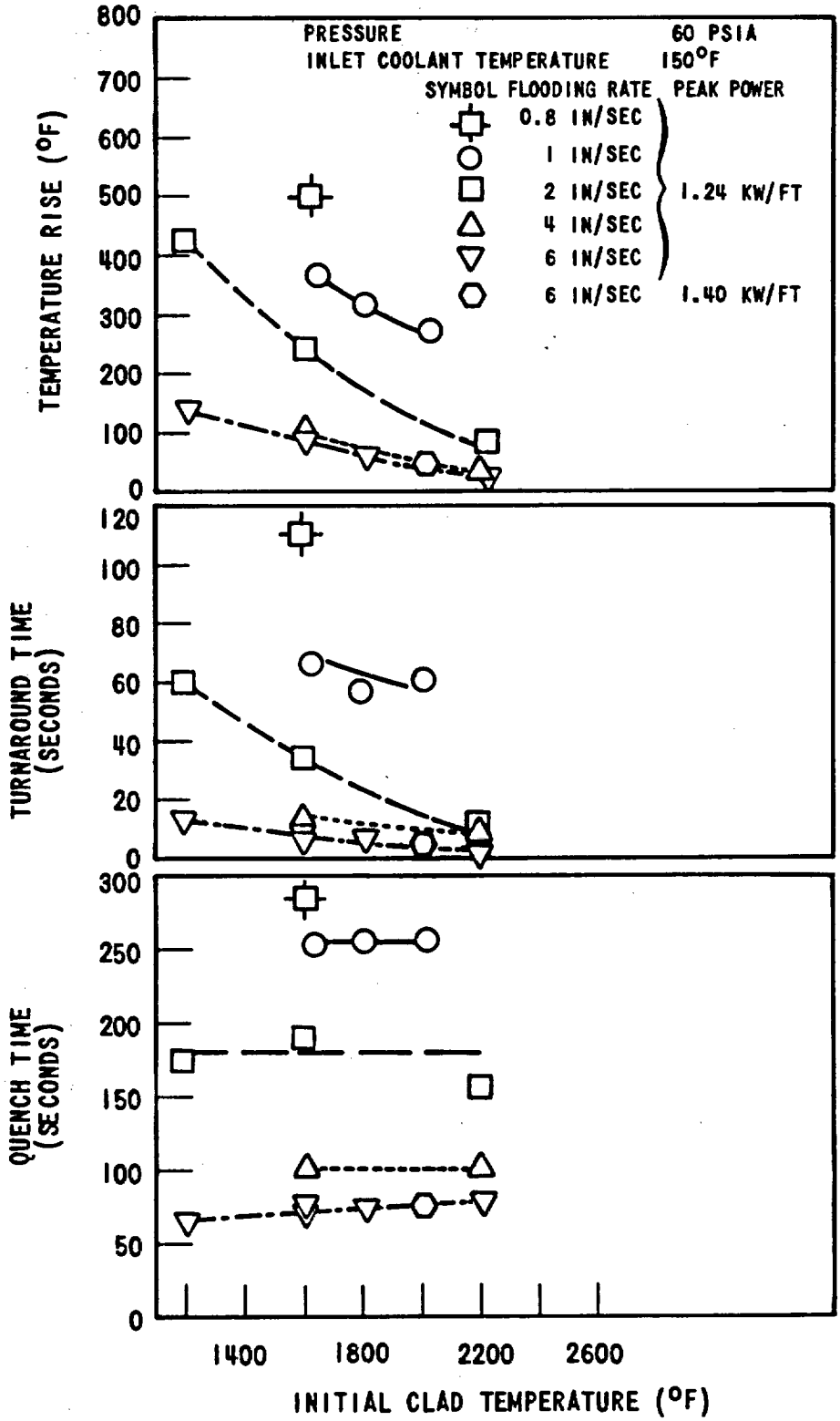

Figure 3-11. Effect of Initial Clad Temperature on Temperature Rise, Turnaround Time and Quench Time

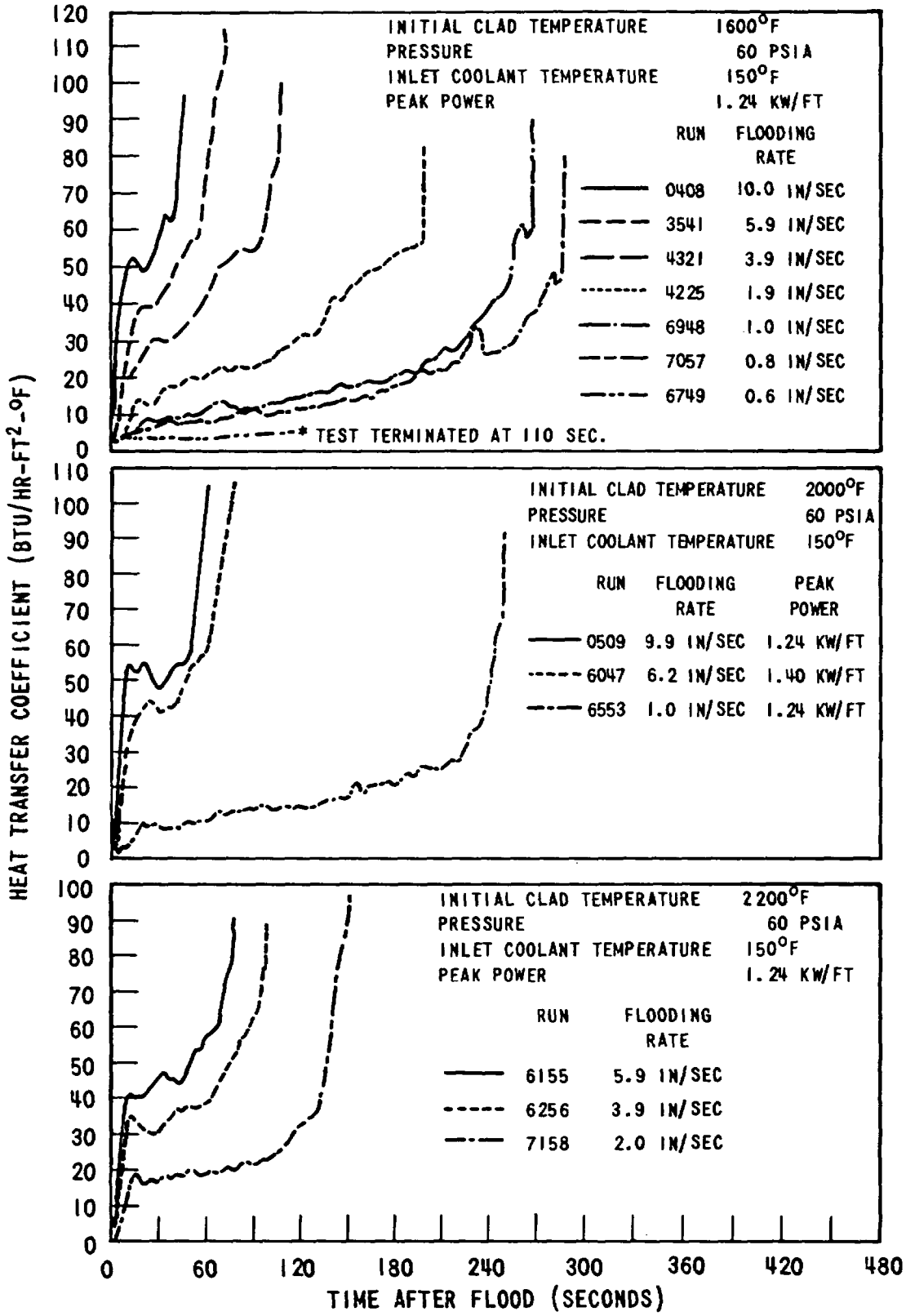

Figure 3-12. Effect of Flooding Rate on Midplane (6') Heat Transfer Coefficients at 1600, 2000 and 2200°F Initial Clad Temperature

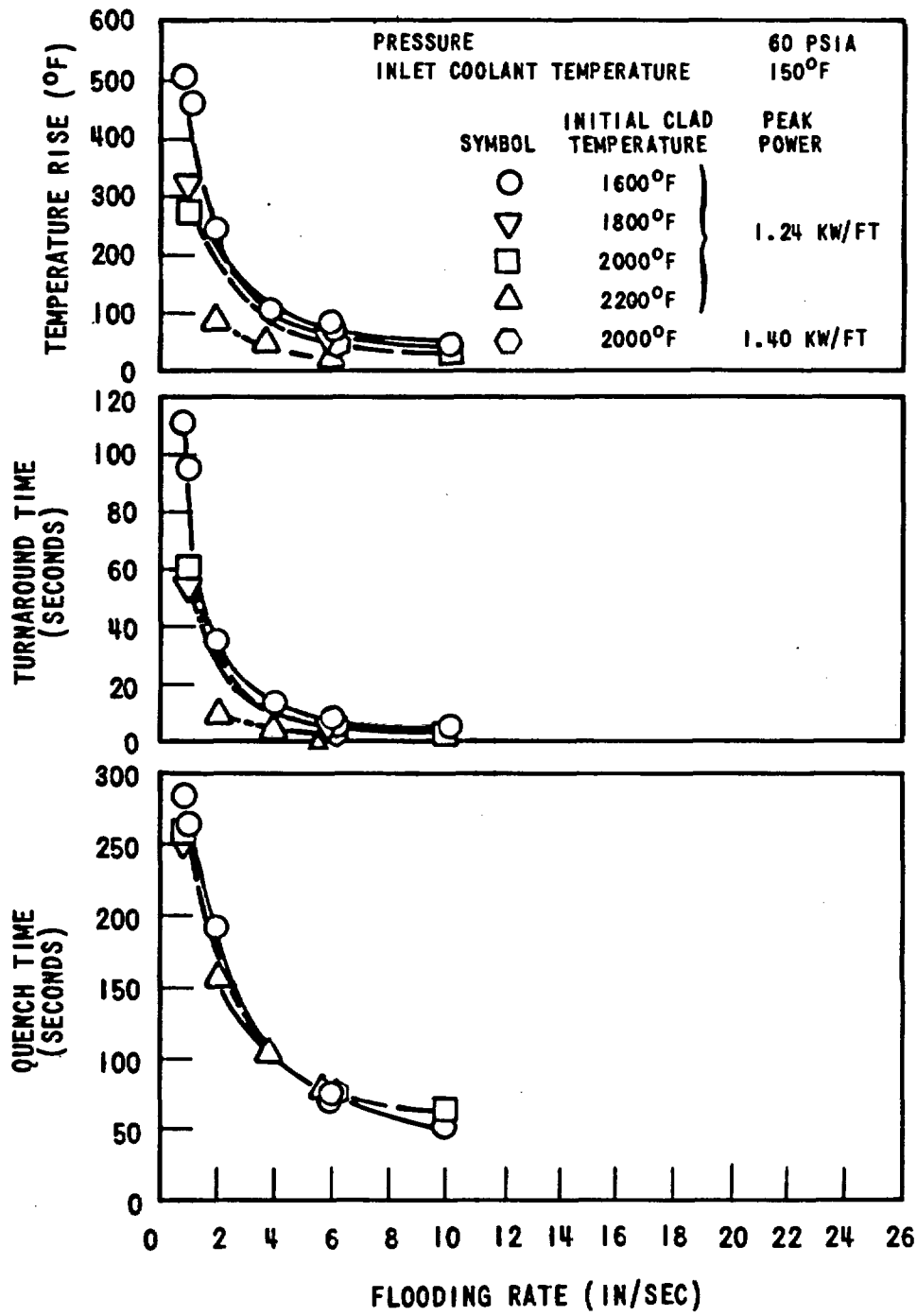

Figure 3-13. Effect of Flooding Rate on Temperature Rise, Turnaround Time and Quench Time

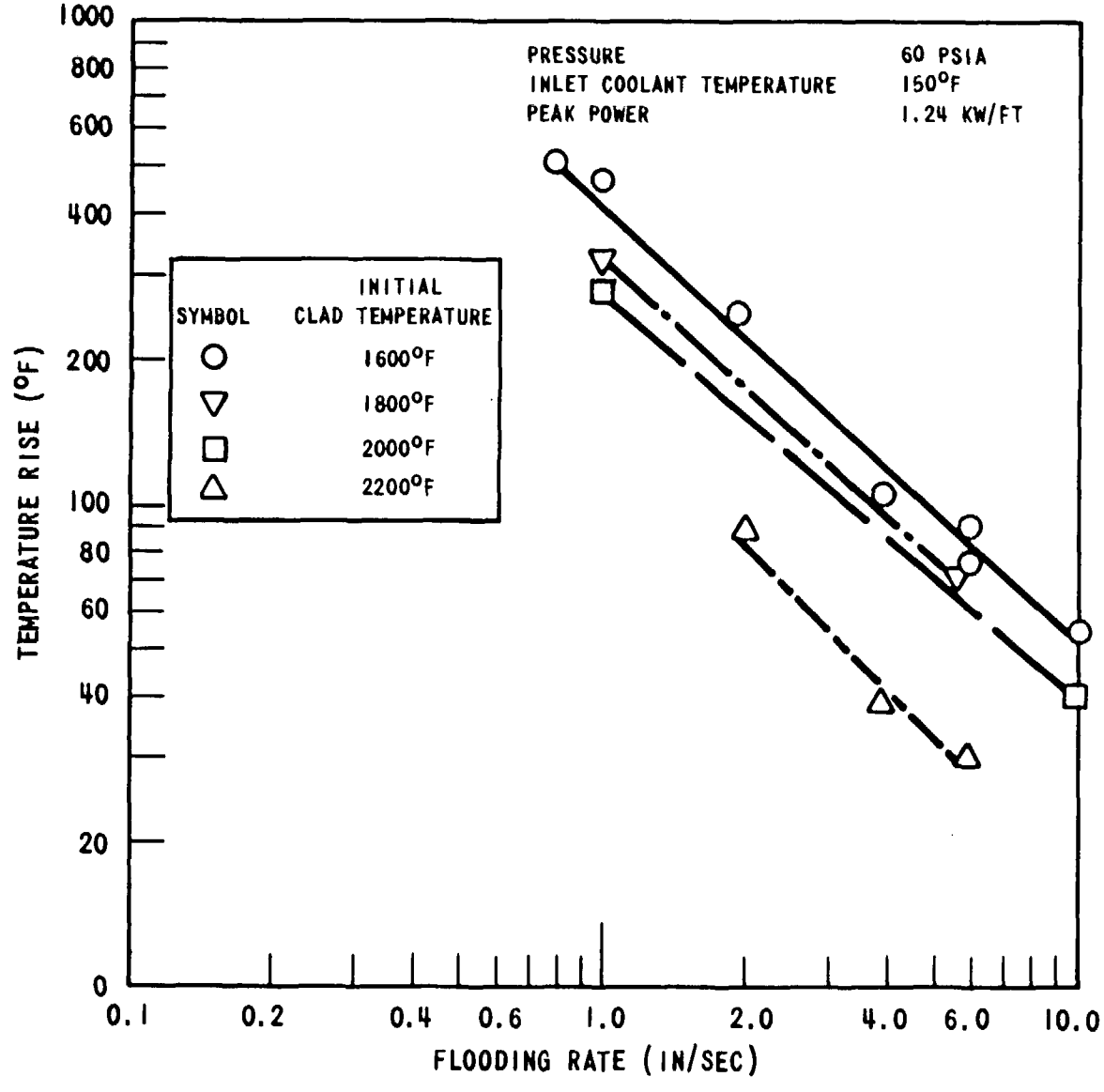

Figure 3-14. Effect of Flooding Rate on Temperature Rise (LOG-LOG)

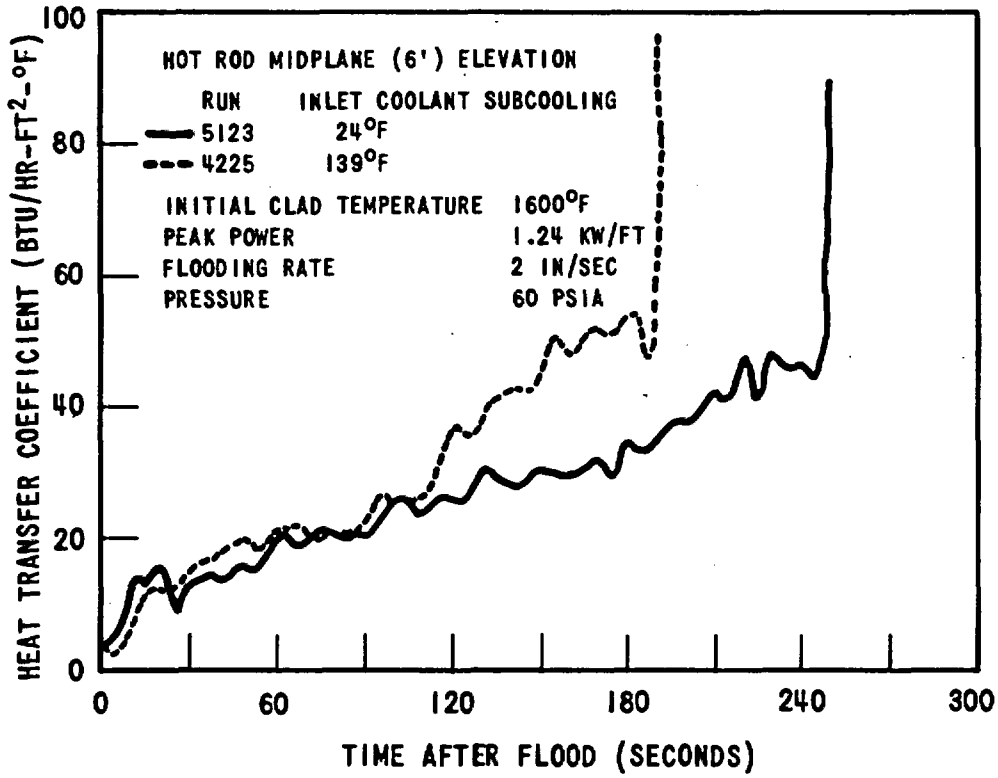

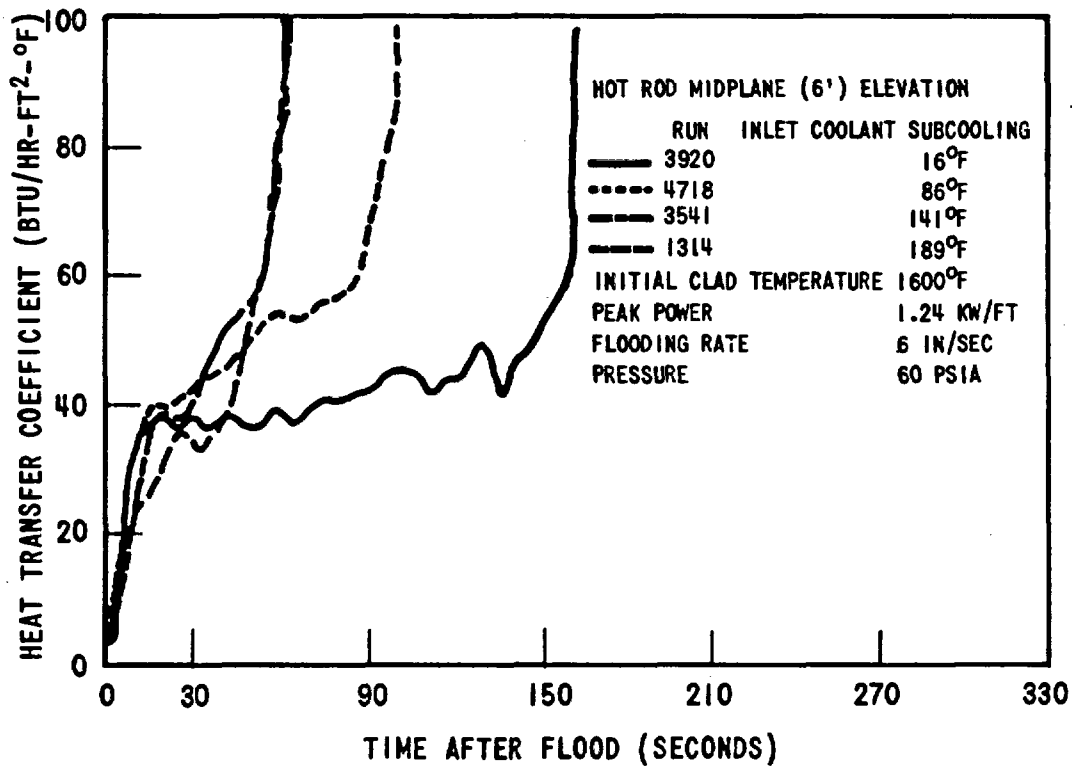

Figure 3-15. Effect of Subcooling on Heat Transfer Coefficient

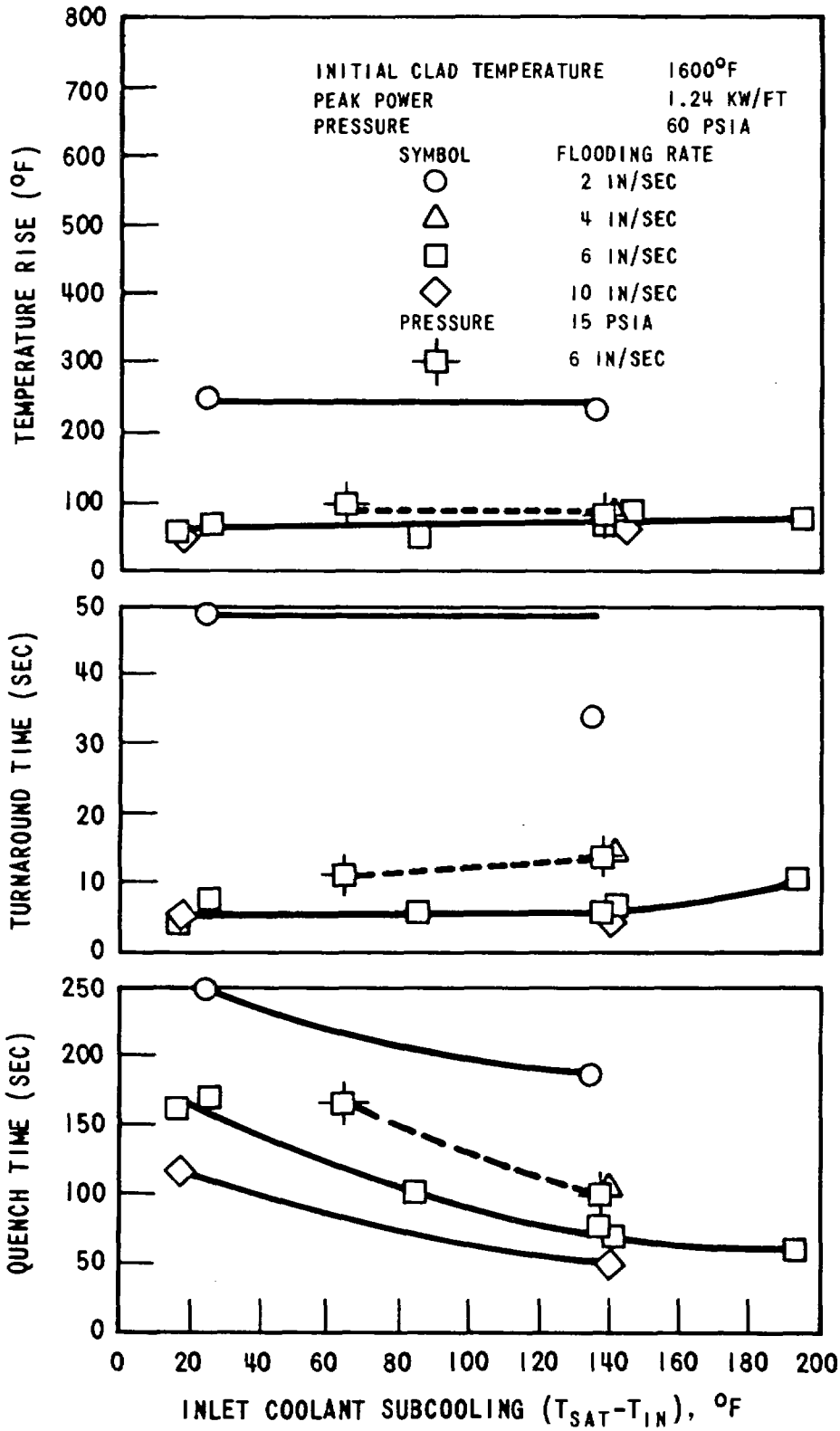

Figure 3-16. Effect of Inlet Coolant Subcooling on Temperature Rise, Turnaround Time and Quench Time

increased as mentioned previously and the effect was similar for all flooding rates. For the 15 psia tests shown in Figure 3-16 the magnitude of the change in temperature rise, turnaround time, and quench time with subcooling was comparable to the 60 psia cases. The effect of pressure will be discussed in the next subsection.

3.2.2.4 Pressure

Decreasing the system steam pressure while maintaining constant subcooling lowered the heat transfer coefficient as shown in Figure 3-17. This was probably due to significant changes in the two phase mixture properties with change in pressure. Also, previous work suggests that the steam velocity necessary for entrainment increases with decreasing pressure (Ref. 5), which would also tend to decrease the heat transfer coefficient. The turnaround time, temperature rise, and quench time decreased with increasing pressure as expected from the increased heat transfer coefficient (see Figure 3-18). The constant inlet temperature data also shown in Figure 3-18 indicated the same trend with pressure as the constant subcooling data.

3.2.2.5 Peak Power Generation

Figure 3-19 shows heat transfer coefficients for three different power generation rates at 6 in./sec and 2 in./sec flooding rates. Initially the curves are nearly identical. This is as expected since the heat transfer coefficient at the midplane for early times is a function of the steam generation and entrainment at the lower elevations. Although the midplane power differed significantly in these cases, the difference in power generation at the lower elevations was considerably less due to the axial cosine power distribution. At later times, the higher power generation resulted in a higher rod surface temperature and a higher steam generation rate causing the quench front to move more slowly up the bundle. Thus, the midplane heat transfer coefficient was lower as the power generation rate increased.

Temperature rise and turnaround time increased as peak power generation increased. This is reasonable since the heat transfer coefficient necessary to turnaround the clad temperature is greater with higher power generation. This

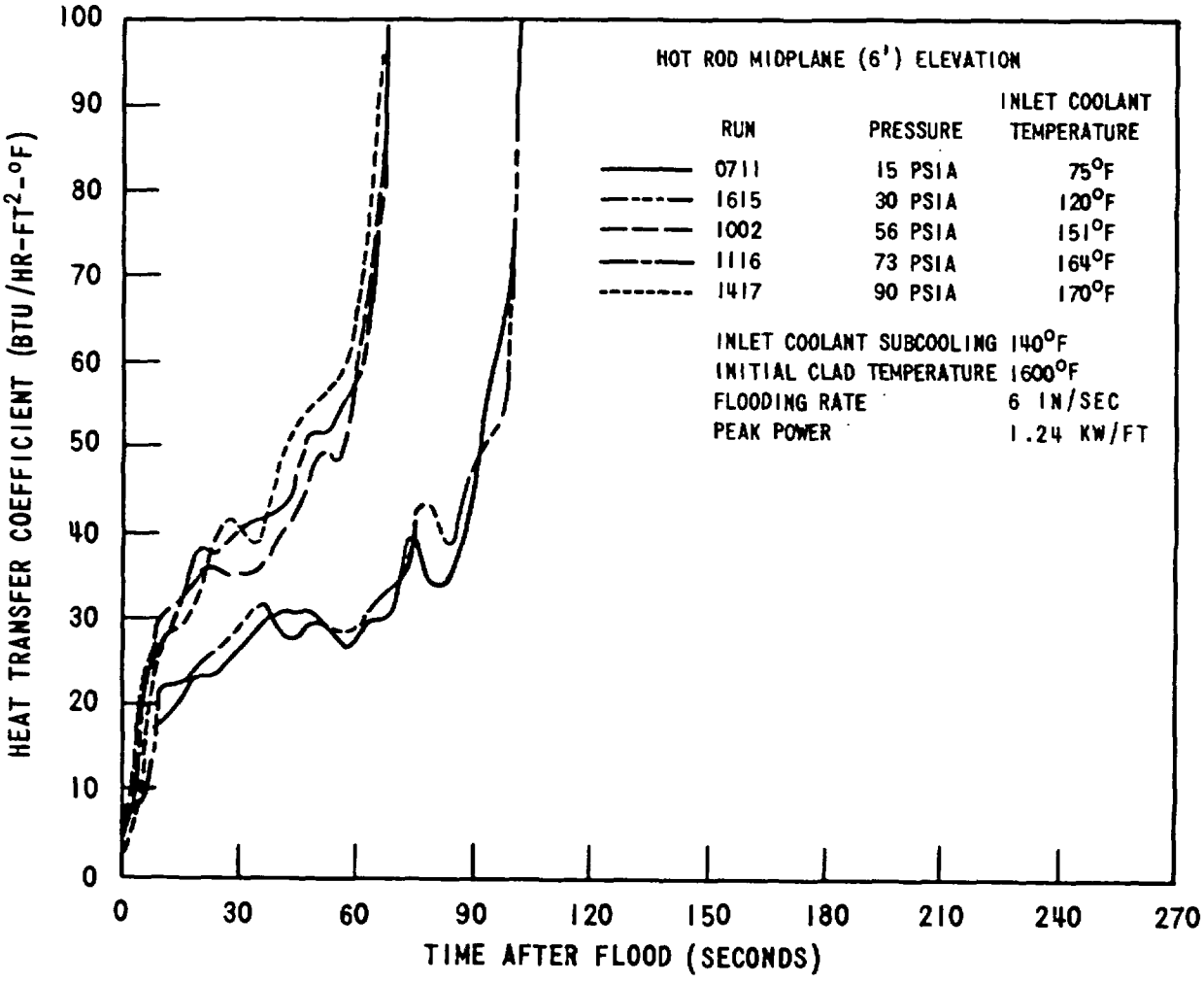

Figure 3-17. Effect of Pressure on Heat Transfer Coefficient at Constant Subcooling

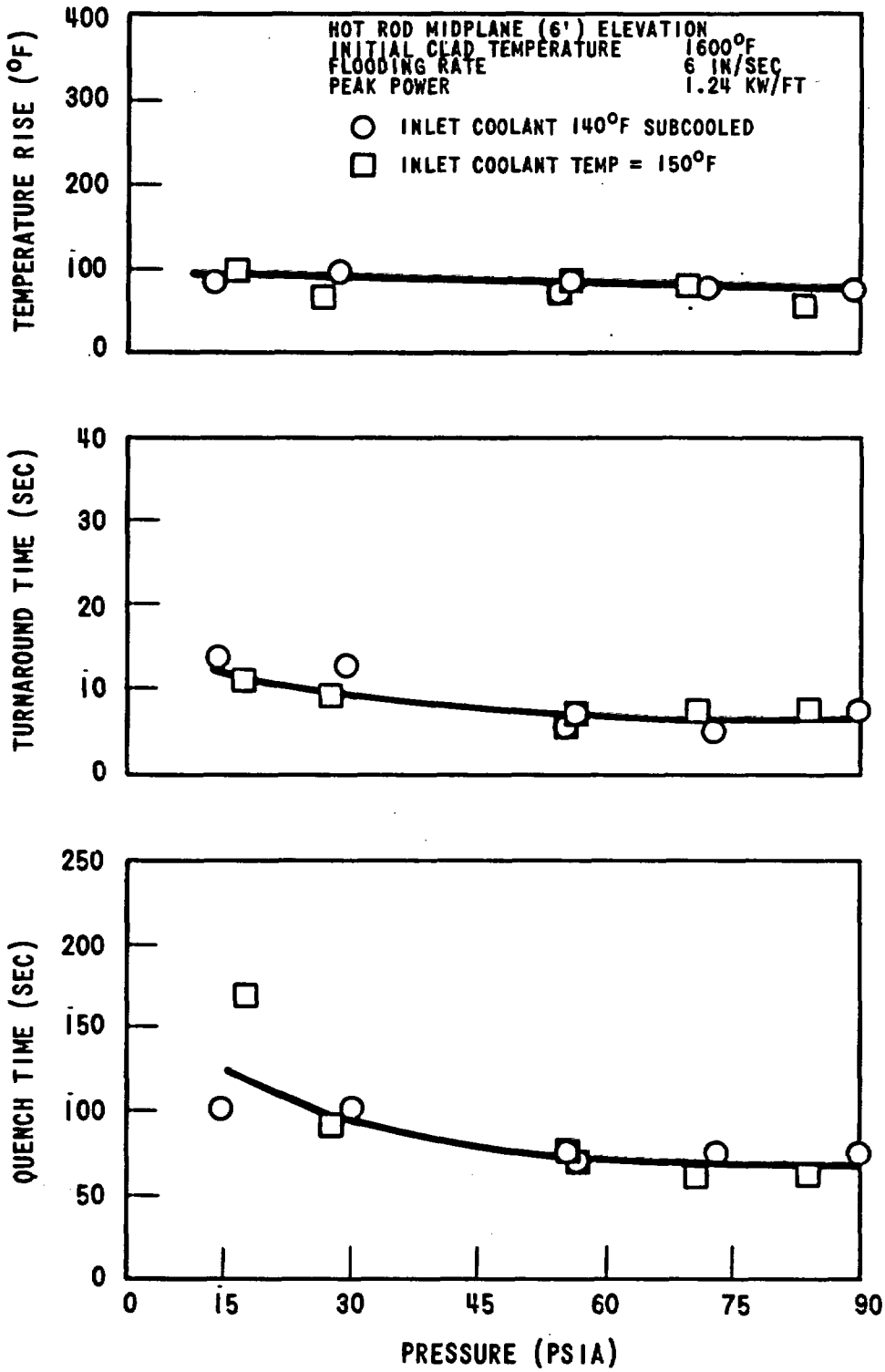

Figure 3-18. Effect of Pressure on Temperature Rise, Turnaround Time and Quench Time

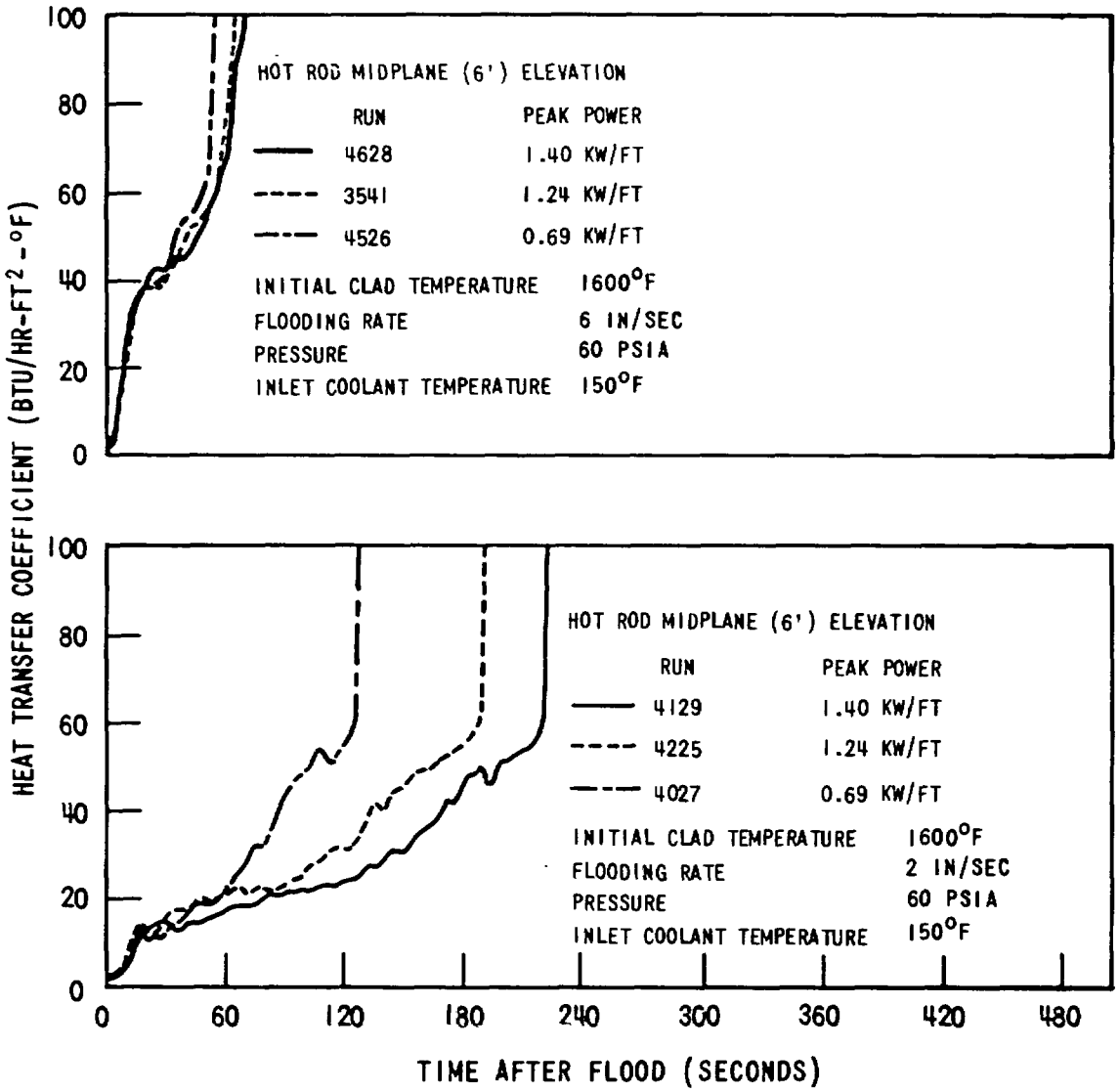

Figure 3-19. Effect of Peak Power on Heat Transfer Coefficient for 6 and 2 in/sec Flooding Rate

is shown in Figure 3-20 for 6 in./sec and 2 in./sec flooding rates. The effect was stronger in the 2 in./sec cases, because the heat transfer coefficient increased more slowly for this flooding rate. Thus, a longer time was required before the turnaround heat transfer coefficient was reached. The quench time increased for increased power generation, since the quench front advanced less rapidly due to the higher steam generation rate.

3.2.2.6 Power Decay Rate

Figure 3-21 shows the three power decay rates investigated. (Note that the initial power is the same in all cases.) Figure 3-22 shows that there is essentially no effect on heat transfer coefficient at low (1.0 in./sec) flooding rates for the range of decay rates tested. This implies that vapor generation rates and entrainment were not significantly different for these three tests. Similarly, at higher flooding rates heat transfer coefficients were not measurably affected by power decay rates in the same range.

Temperature rise, turnaround time, and quench time as a function of power decay rate can be seen in Table 3-5. This table indicates that power decay rate had a significant effect on temperature rise and turnaround time at low (1.0 in./sec) flooding rates and low (1600°F) initial clad temperatures. Since, as discussed above, the heat transfer coefficients were essentially identical, and since they increased very slowly, the temperature rise and turnaround times for these runs were determined primarily by the time required for the power to decay to a sufficiently low level. Absence of a significant effect on quench time is consistent with the implied similarity in vapor generation and entrainment discussed above.

Figure 3-21 indicates that for long periods after flood there is a significant difference in the time required for Curves A, B and C to reach the same decay power. This is not the case for short times after flood. Thus variations in the decay power rate did not have a strong affect on temperature rise and turnaround time in runs with higher flooding rates.

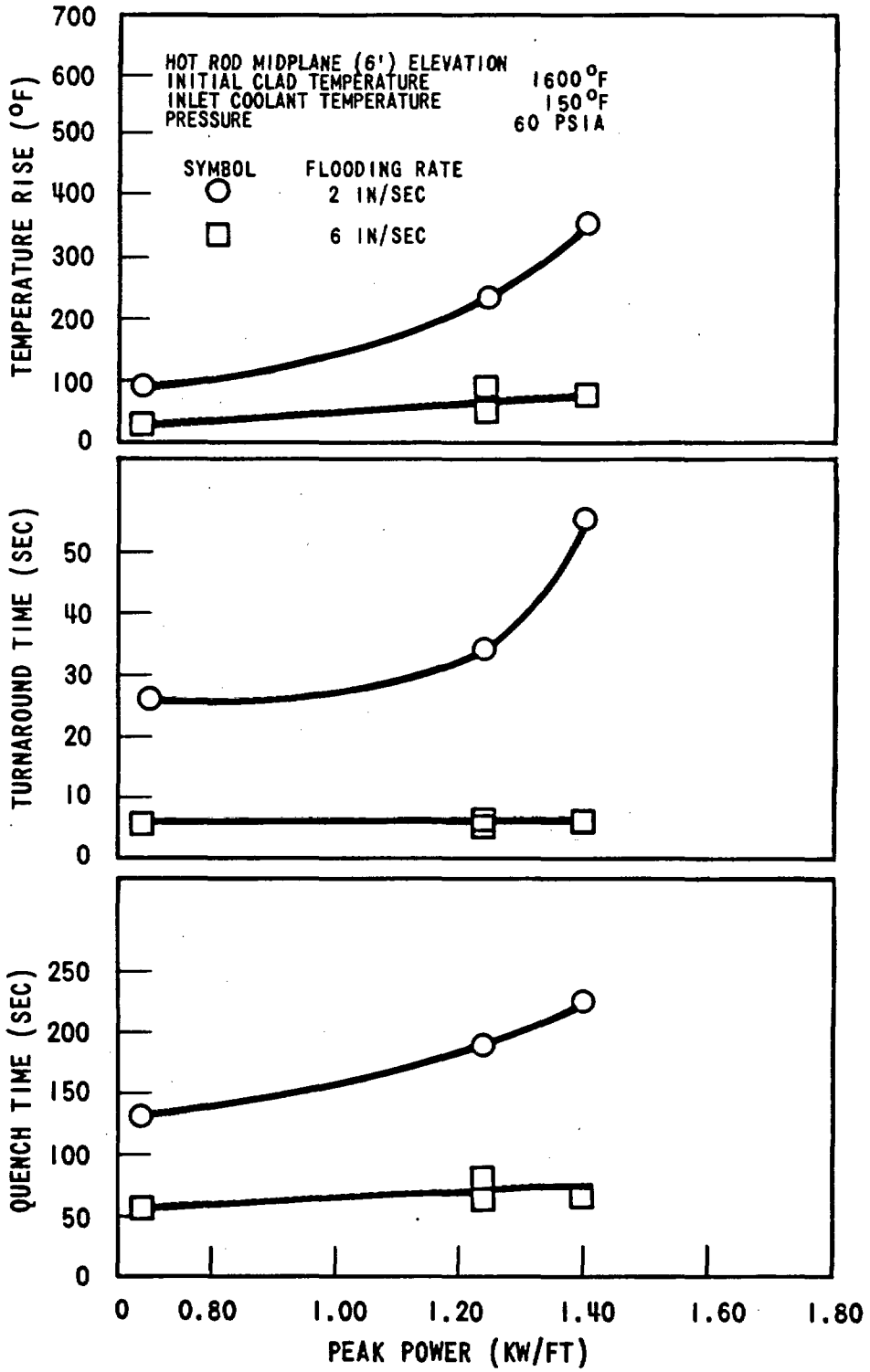

Figure 3-20. Effect of Peak Power on Temperature Rise, Turnaround Time and Quench Time

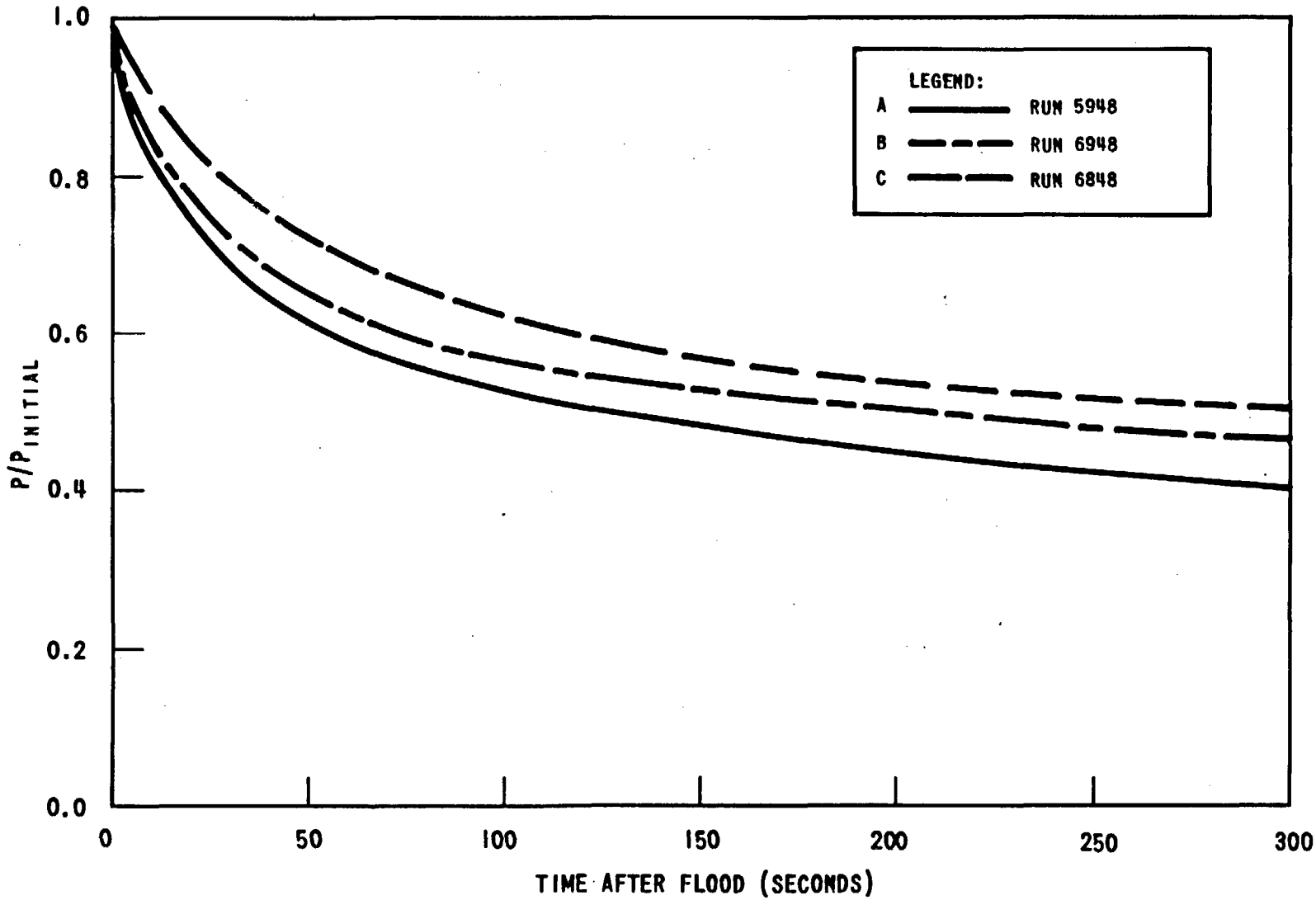

Figure 3-21. Comparison of Power Decay Rates for Runs 5948, 6948, and 6848

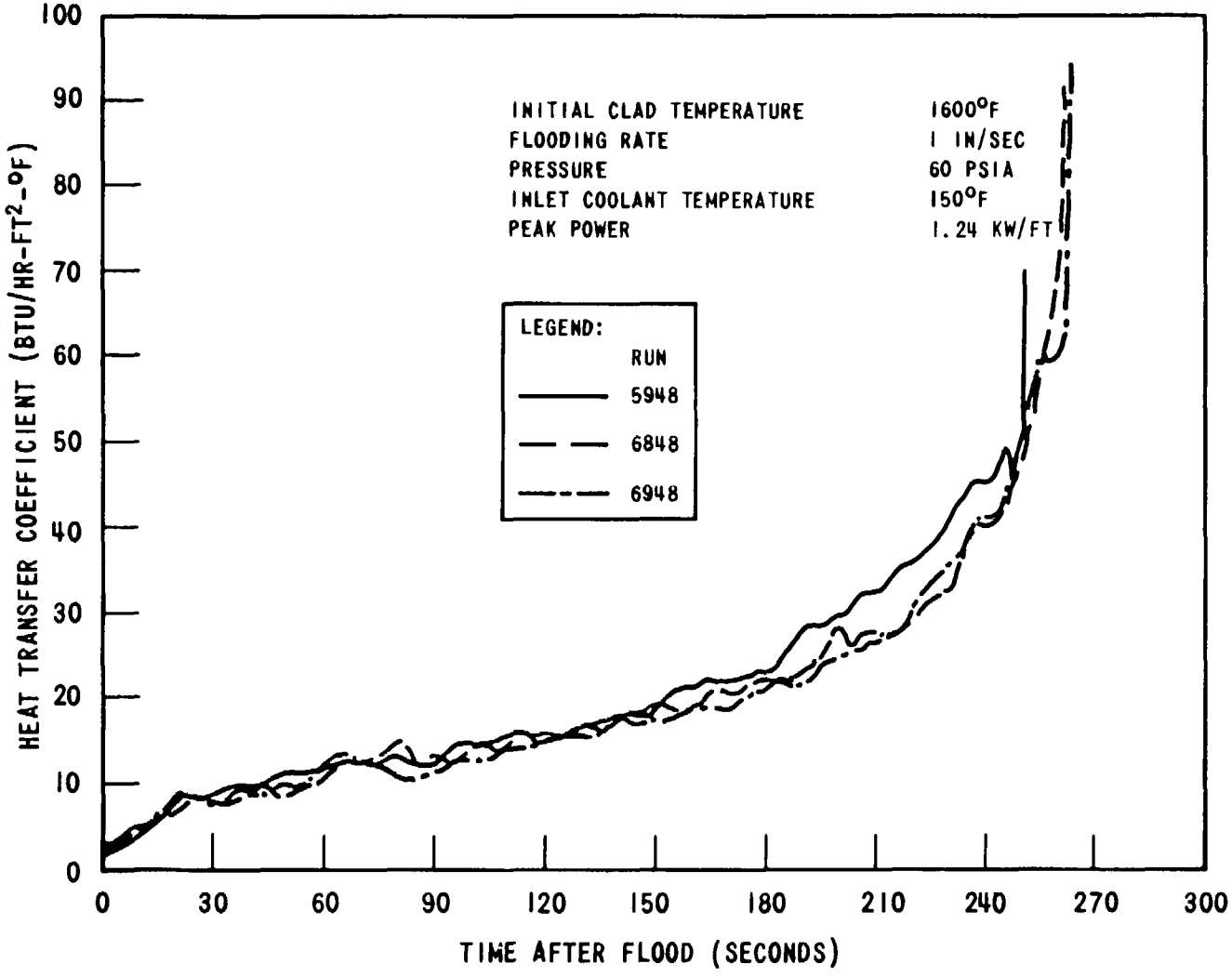

Figure 3-22. Effect of Power Decay Rate on Heat Transfer Coefficient

TABLE 3-5

EFFECT OF POWER DECAY RATE ON TEMPERATURE RISE, TURNAROUND TIME AND QUENCH TIME

Run No.	Power Decay Rate	Relative Power Level	Temperature Rise (°F)	Turnaround Time (sec)	Quench Time (sec)
5948	A	Low	370	66	254
6948	B	Middle	465	95	266
6848	C	High	532	94	265

3.2.2.7 Heat Transfer Behavior with Borated Coolant

One bottom flooding heat transfer test (Run 5730) was conducted with 2000 ppm boric acid in the water coolant. Results of this test are compared with an identical run without boric acid in the coolant in Figure 3-23. It appears that the addition of boric acid resulted in slightly higher heat transfer coefficients. This result is consistent with Reference 6 which reports that addition of up to 4 weight percent of boric acid had a small effect (a 2 percent increase) on pure demineralized water cooling capability. These results show that heat transfer coefficients obtained from tests with no additives in the coolant were slightly conservative.

3.2.3 Heat Transfer Behavior at Different Elevations

Figure 3-24 shows the behavior of typical low and high flooding rate heat transfer coefficients at different elevations. At low flooding rates (2 in./sec or less), the heat transfer coefficient at any given time decreased with increasing elevation. This trend was different for high flooding rate cases (6 in./sec or greater) at early times. For high flooding rates at early times, the heat transfer coefficient at high elevations (6 ft or above) increased with elevation. At later times the trend reversed, and was similar to the low flooding rate behavior.

There were two important competing fluid property effects on heat transfer coefficient with elevation: 1) increasing void fraction with elevation, tended to decrease the heat transfer coefficient; and 2) acceleration or increased velocity of the two-phase mixture with elevation, tended to increase the heat transfer coefficient. At low flooding rates, the first effect dominated. At high flooding rates and early times, the second effect was dominant. The dominance of the second effect at high flooding rates and early time was due to the availability of larger amounts of liquid for evaporation, hence acceleration, of the two-phase mixture above the bundle midplane.

The negative heat transfer coefficient for the 10-foot elevation at early times indicates heat transfer into (rather than out of) the rod. This was caused by the presence of superheated steam having temperatures above the clad temperature at the 10-foot elevation. Data verifying the presence of highly superheated steam is presented in Section 3.6. Negative heat transfer coefficients were generally found at the 10-foot elevation for low flooding rate runs (2 in./sec or less) at early times (from around 5 up to a maximum of about 120 sec after flood).

The variation of temperature rise, turnaround time and quench time with elevation is shown in Figure 3-25. At high flooding rates (6 in./sec and greater), the temperature rise was largest at the 6-foot elevation since it had the highest heat generation rate. As the flooding rate was reduced, the location of the peak temperature rise moved up the bundle. This resulted from the decrease in heat transfer coefficient with elevation for low flooding rate runs, as discussed above. Turnaround time exhibited a similar behavior, increasing with elevation for flooding rates below 6 in./sec.

It should be noted that even in those cases where the largest temperature rise was observed at the 8 or 10-foot elevations, the peak temperature generally occurred at the midplane. This is due to the initial clad temperature profile which resulted from the heater rod cosine power distribution. Although exceptions occurred, these were usually traceable to asymetric clad temperature profiles in which the initial temperatures at the 8 and 10-foot elevations were higher than normal.

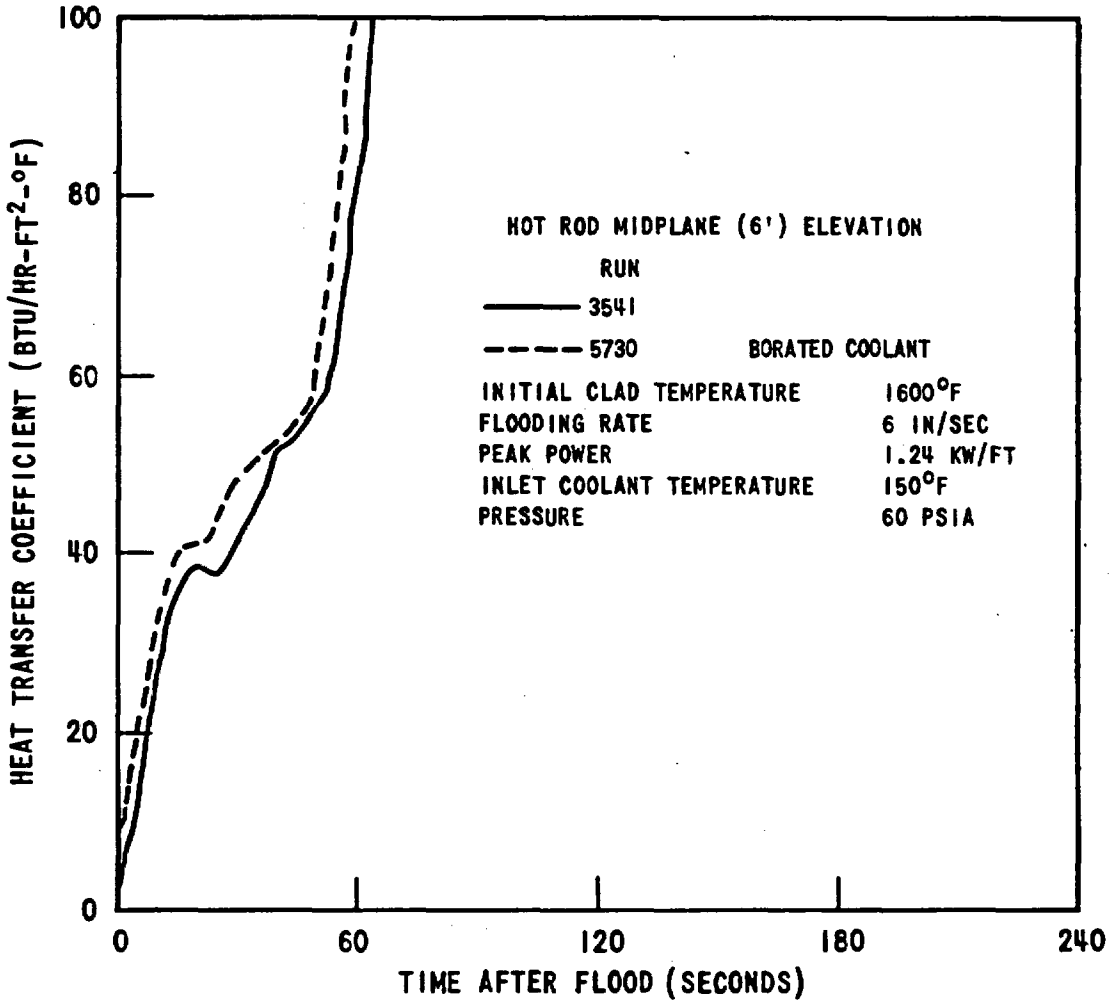

Figure 3-23. Effect of Borated Coolant on Heat Transfer Coefficient

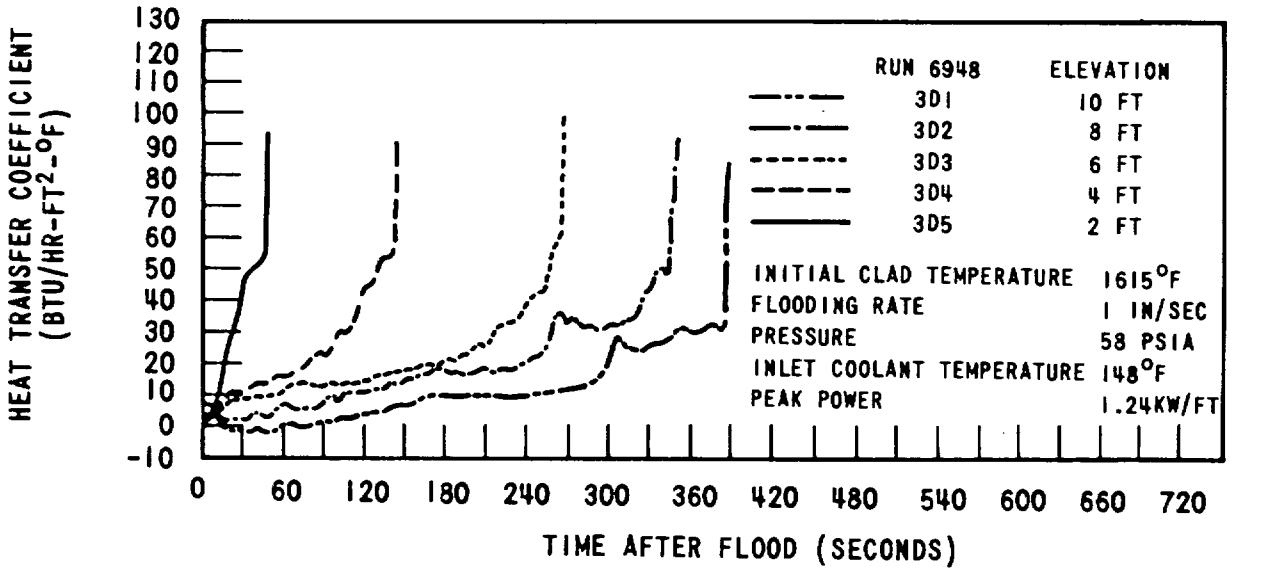

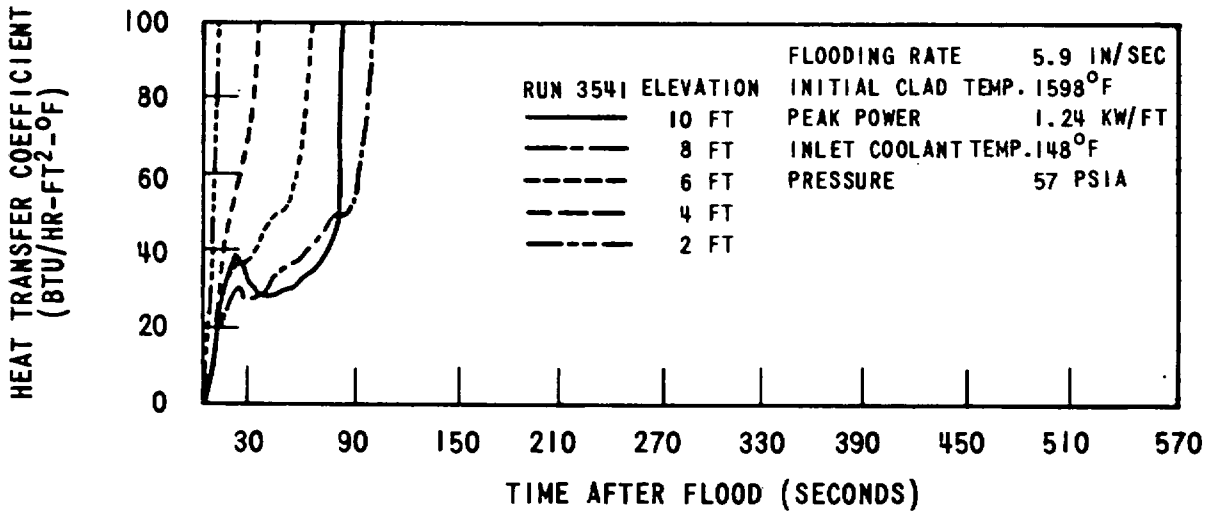

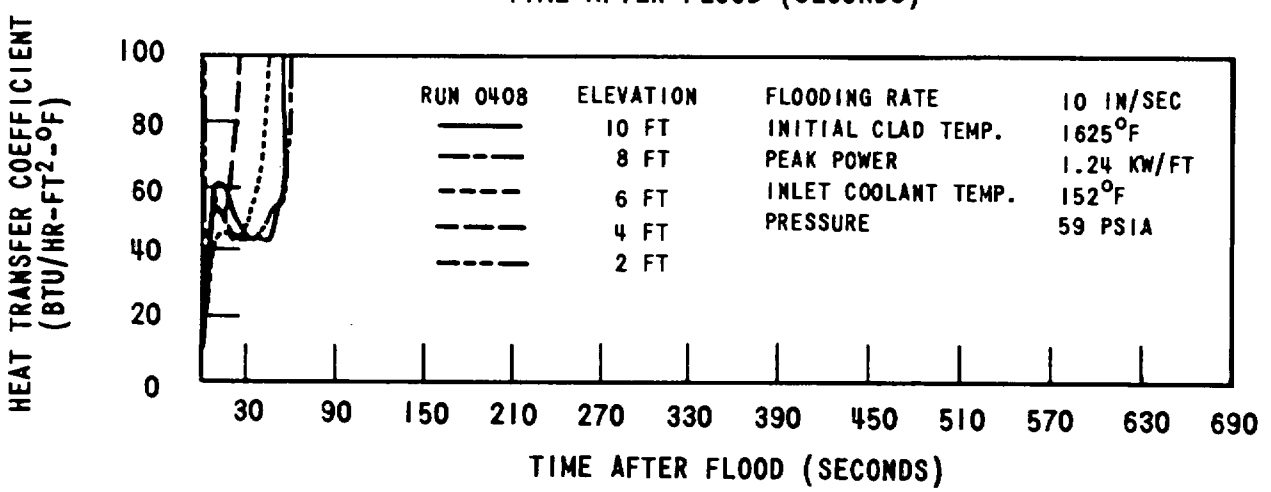

Figure 3-24. Variation of Heat Transfer Coefficient with Elevation for 1, 6, and 10 In Sec Flooding Rates

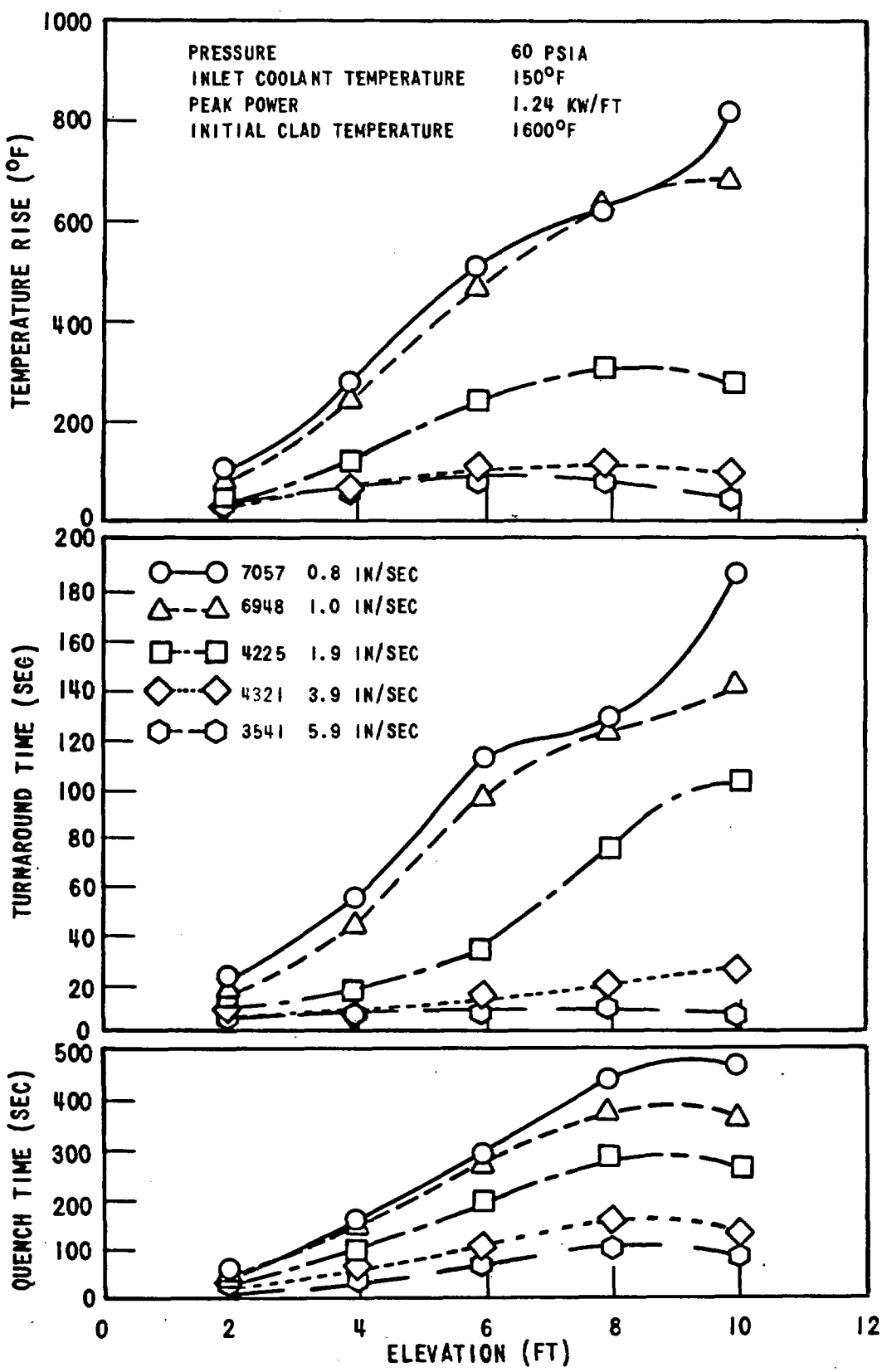

Figure 3-25. Variation in Temperature Rise, Turnaround Time, and Quench Time with Elevation

In general, quench time increased with elevation up to the 8-foot level, then decreased at the 10-foot elevation. At elevations below 10 feet, quenching occurred with the advancement of the quench front. The "early" 10-foot quench was caused by entrained liquid wetting the clad surface prior to arrival of the quench front, because the 10-foot temperature was considerably lower than the 8-foot temperature. This behavior was fairly random in occurrence and can be related to initial 10-foot clad temperature. Also, as indicated by the behavior of run 7057 (0.8 in./sec), the tendency for "early quench" was less at low flooding rates because of the reduced amount of entrained liquid in the test section.

3.2.4 Variable Flooding Rate Tests

3.2.4.1 Variable Flooding Rate Test Results

In an effort to investigate flooding rates more typical of predicted emergency core cooling system behavior, ten variable flooding rate tests were performed. One of these (Run 8463) was run with flow blockage and will be discussed in Section 3.2.5. Figure 3-26 shows the various flooding rates used for these runs. Since in current PWR designs some of the entrained coolant leaving the top of the core could return or fall back into the core as a result of decreasing steam velocities and changes in flow directions, it was decided to also simulate the "fallback" effect in some of the variable flow tests. As discussed in Section 2.3 the test section upper plenum was modified in these cases to permit entrained liquid to fall back into the rod bundle. Also, the upper plenum was heated to 350°F to simulate the heat release from the reactor upper internals. In the non-"fallback" runs, coolant water was collected in the unheated plenum and allowed to drain out of the system.

Figure 3-27 shows typical clad temperature histories at the five thermocouple elevations for 1800 and 2200°F variable flooding rate tests using the curve A flooding rate (Figure 3-26) with "fallback" simulation. It is noted that the temperature rise was quite small in the initial part of the run (high flooding rate) and the cladding cooled quickly until approximately 23 seconds. At this point, the slope of the cooling curve flattened out (except for the 2 and 4 ft elevations) and, in some cases, the temperature began rising again due to the

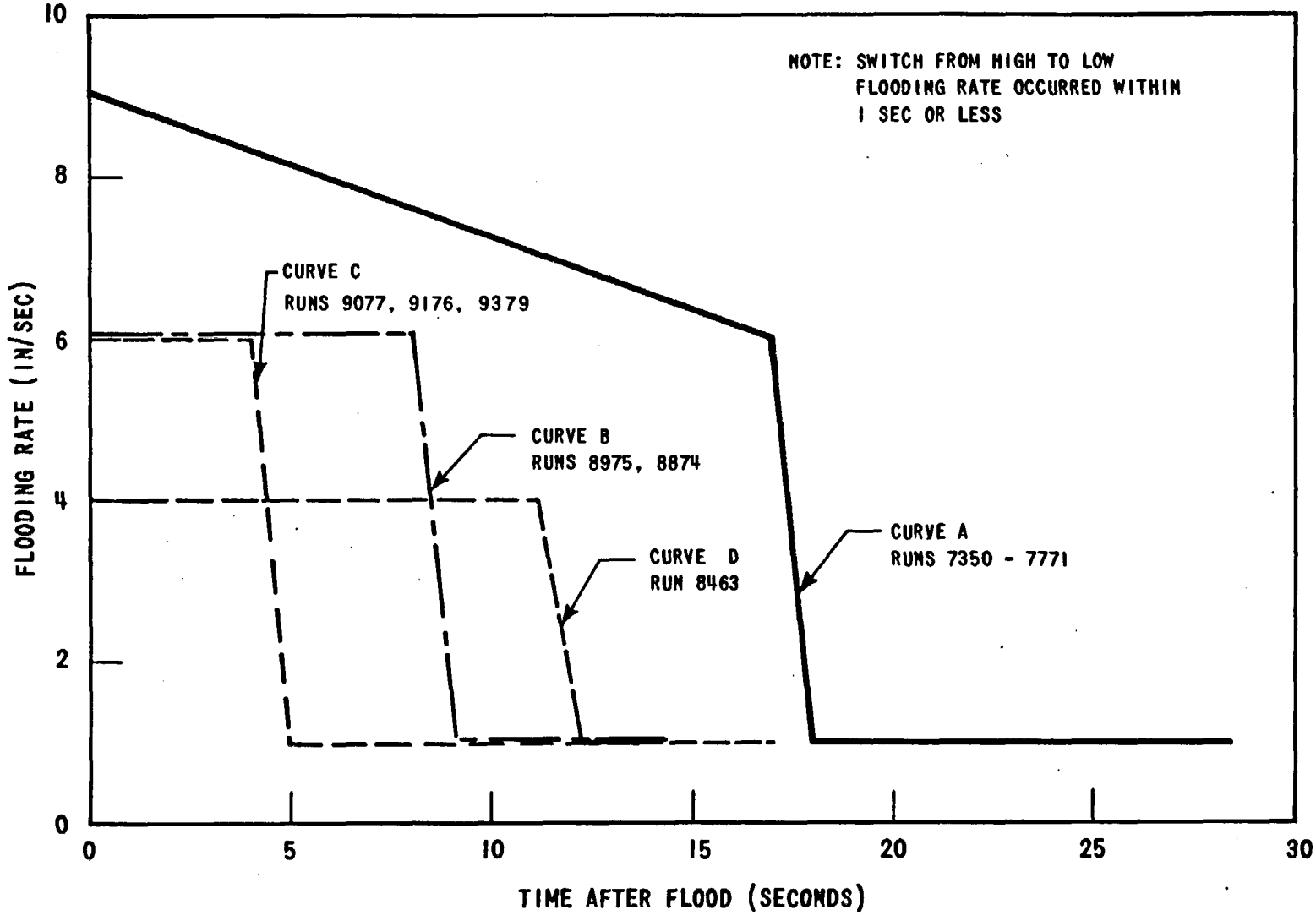

Figure 3-26. Flooding Rates for Variable Flow Tests

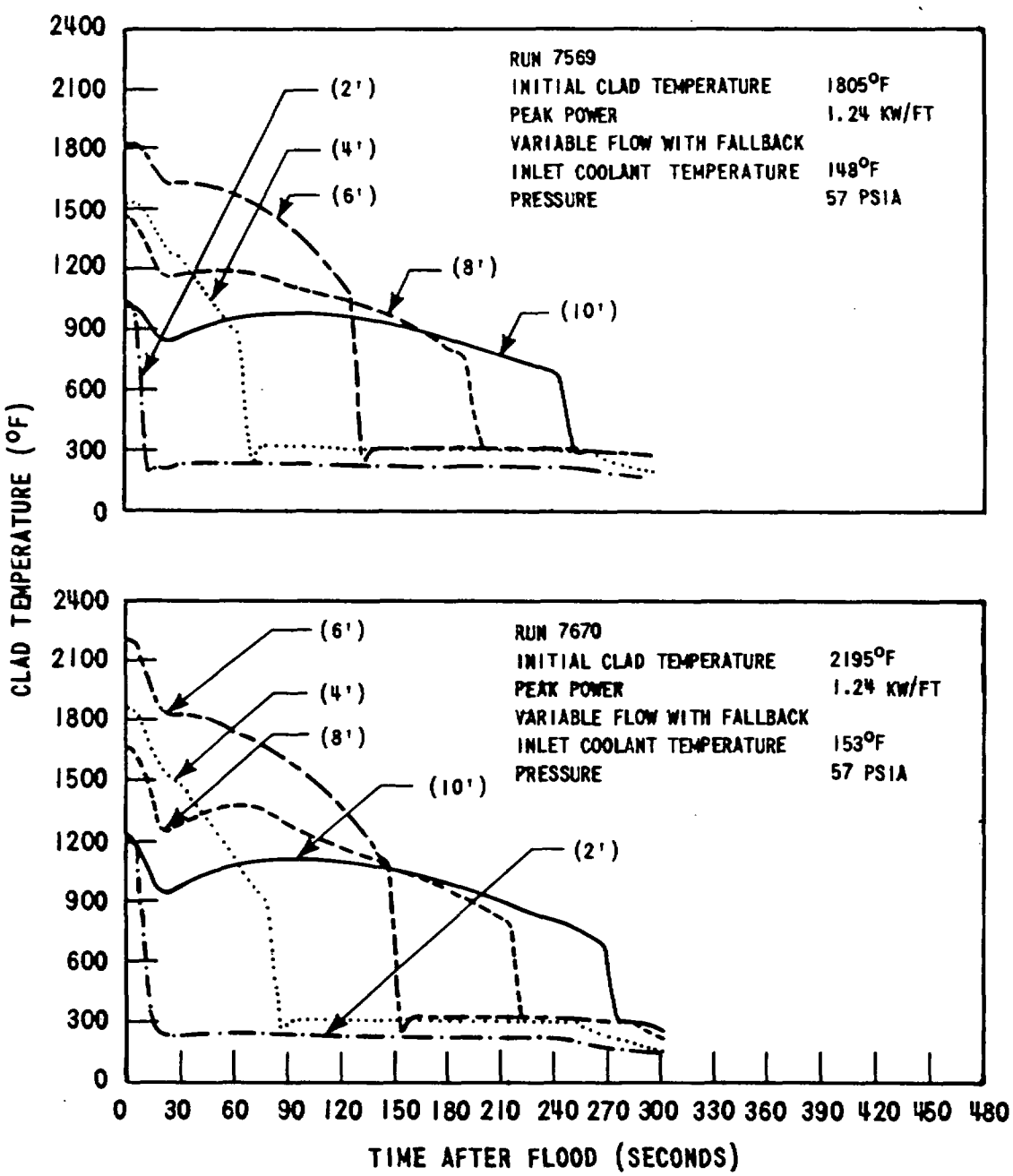

Figure 3-27. Typical Clad Temperature Histories for Variable Flow Tests With Fallback

reduction in flooding rate to 1 in./sec. The corresponding heat transfer coefficients are shown in Figure 3-28. Except for the 2-foot elevation, the heat transfer coefficients peaked at about 14 seconds and dropped to minimum values at approximately 30 seconds. The heat transfer coefficients then increased gradually with time, similar to the behavior observed in the comparable constant flooding rate tests.

Table 3-6 compares midplane temperature behavior for three variable flow "fallback" tests using different flooding rates. Note that as the amount of water supplied to the test section during the high flow portion of the run was increased, the temperature rise and turnaround time decreased in the 1 in./sec part of the test. Quench time also decreased since (1) the quench front level at the time of switch to low flow was higher and (2) increased inlet flow lowered the rod temperature allowing the quench front to advance more rapidly. Figure 3-29 shows typical midplane heat transfer coefficients for these three runs. The heat transfer coefficient increased as the amount of water supplied to the test section during the early high flooding rate portion of the run increased.

TABLE 3-6

EFFECT OF VARIABLE FLOODING RATES ON TEMPERATURE BEHAVIOR

Run No.	Flooding Rate (see Fig. 3-26)	Initial Clad Temperature (°F)	$\Delta T_{rise\ 1}$ (°F)	$t_{turn\ 1}$ (sec)	T_{min} (°F)	t_{min} (sec)	$\Delta T_{rise\ 2}$ (°F)	$t_{turn\ 2}$ (sec)	t_{quench} (sec)
7670	A	2195	25	3	—[a]	—	—	—	148
8975	B	2301	45	4	2181	13	69	36	249
9077	C	2138	42	4	2151	10	100	54	276

[a]Dashes indicate that no second temperature rise occurred in this test)

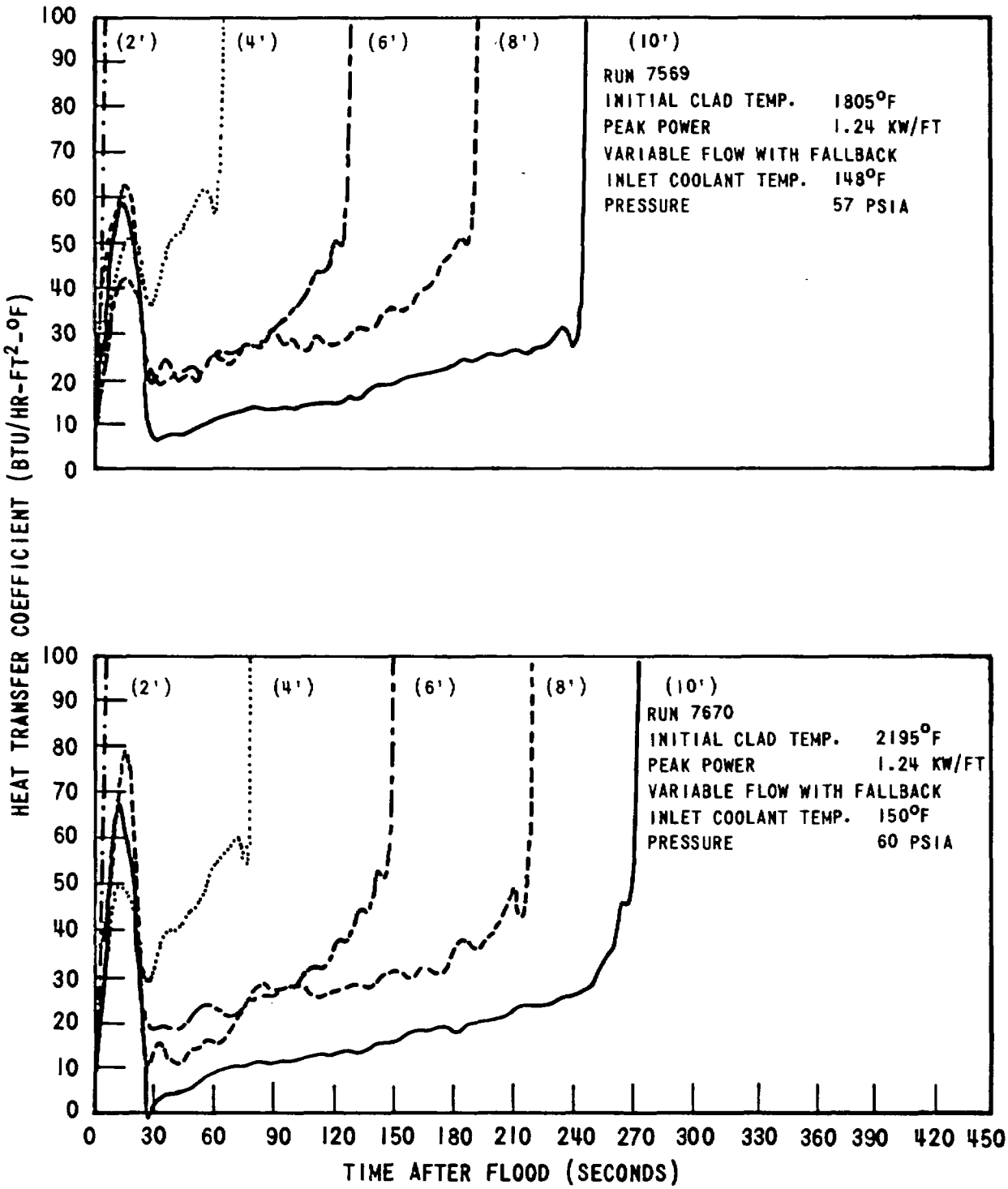

Figure 3-28. Typical Heat Transfer Coefficients for Variable Flow Tests with Fallback

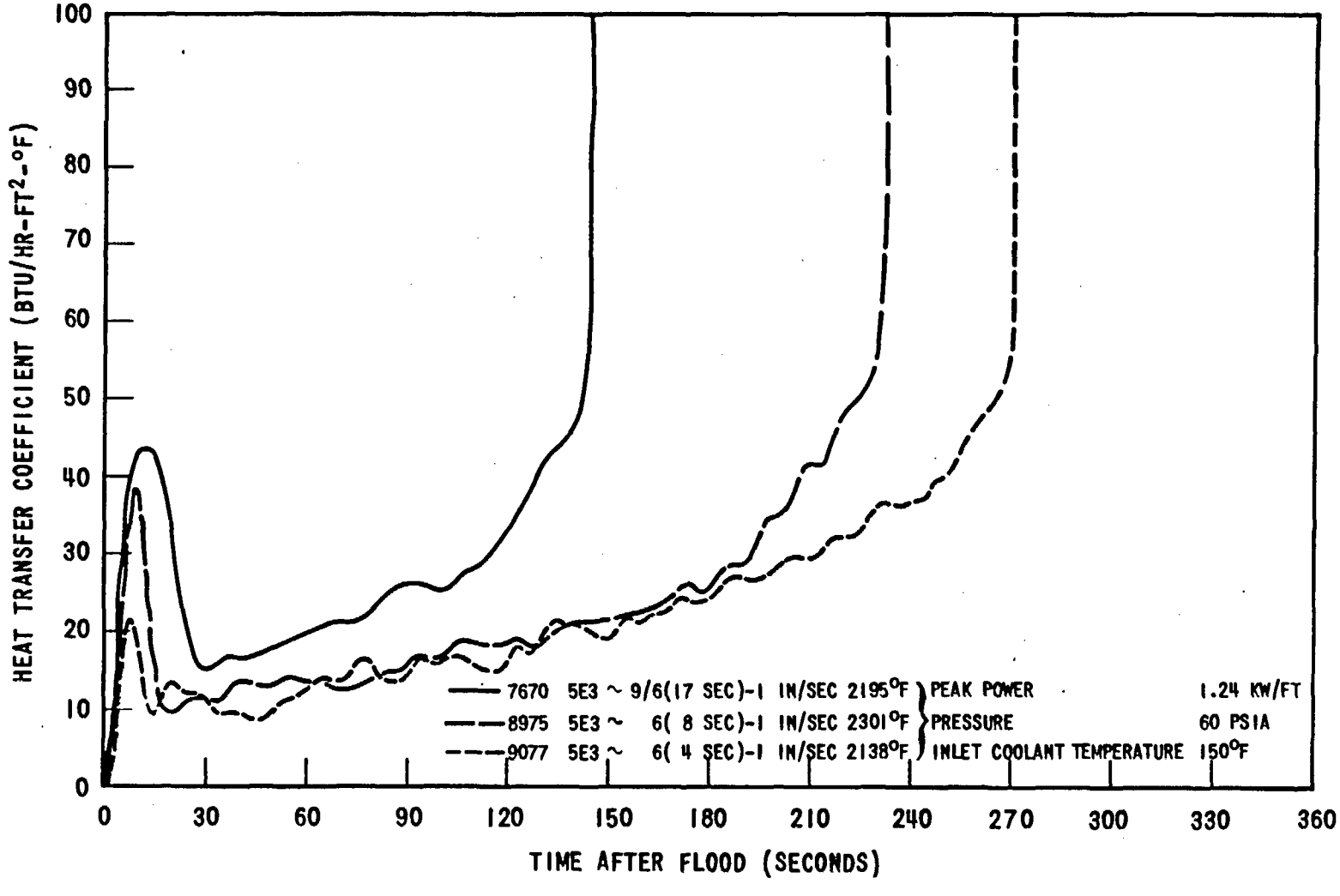

Figure 3-29. Midplane Heat Transfer Coefficients for Three Different Variable Flooding Rates

3.2.4.2 Fallback Effect on Heat Transfer

The Group II Test Report (Reference 3) concluded that water "fallback" reduced second peak midplane temperatures for variable flow rates of 9/6 - 1 in./sec (curve A Figure 3-26). Later tests were performed to determine the effect of "fallback" at a lower initial flooding rate (6 in./sec (4 sec) - 1 in./sec) and also at 1 in./ sec constant flooding rate.

Figures 3-30 through 3-32 show the midplane clad temperature and heat transfer coefficients for the three different flooding rates, with and without "fallback". It can be seen that the "fallback" effect was significant at the 9/6-1 in./sec flooding rate but was small in the 6(4 sec)-1 in./sec and 1 in./sec tests. The increased liquid inventory (retention of more liquid in bundle) at any given time and higher quench front velocity with "fallback" were responsible for the increase in heat transfer coefficient shown in Figure 3-30. As the initial high flow rate and flow time were decreased, these effects became small. This was due to the fact that during the low flow (1 in./sec) part of the run there was very little entrained liquid carryover available to "fallback" into the bundle. Carryover measurement results reported in Section 3-7 show very little carryover for 1 in./sec constant flooding rate runs.

3.2.4.3 Comparison of Constant and Variable Flooding Rate Heat Transfer Results

Figures 3-33 and 3-34 compare midplane heat transfer coefficients for runs with constant and variable (curve A of Figure 3-26) flooding rates with and without "fallback", respectively. As expected, the variable flow heat transfer coefficient was between the 6 and the 10 in./sec curves during the high flow part of the run. For the later low flow part of the run, the heat transfer coefficient of the variable flow runs agreed with those of the comparable 1 in./sec constant flow runs when the time coordinate was shifted using the method of Section 3.3.3.

Figures 3-35 and 3-36 compare midplane heat transfer coefficients for constant and variable flooding rate runs with "fallback" for curves B and C, respectively, of Figure 3-26. During the high flow part of the run, the variable flow heat transfer coefficient followed the 6 in./sec curve and started to drop when the

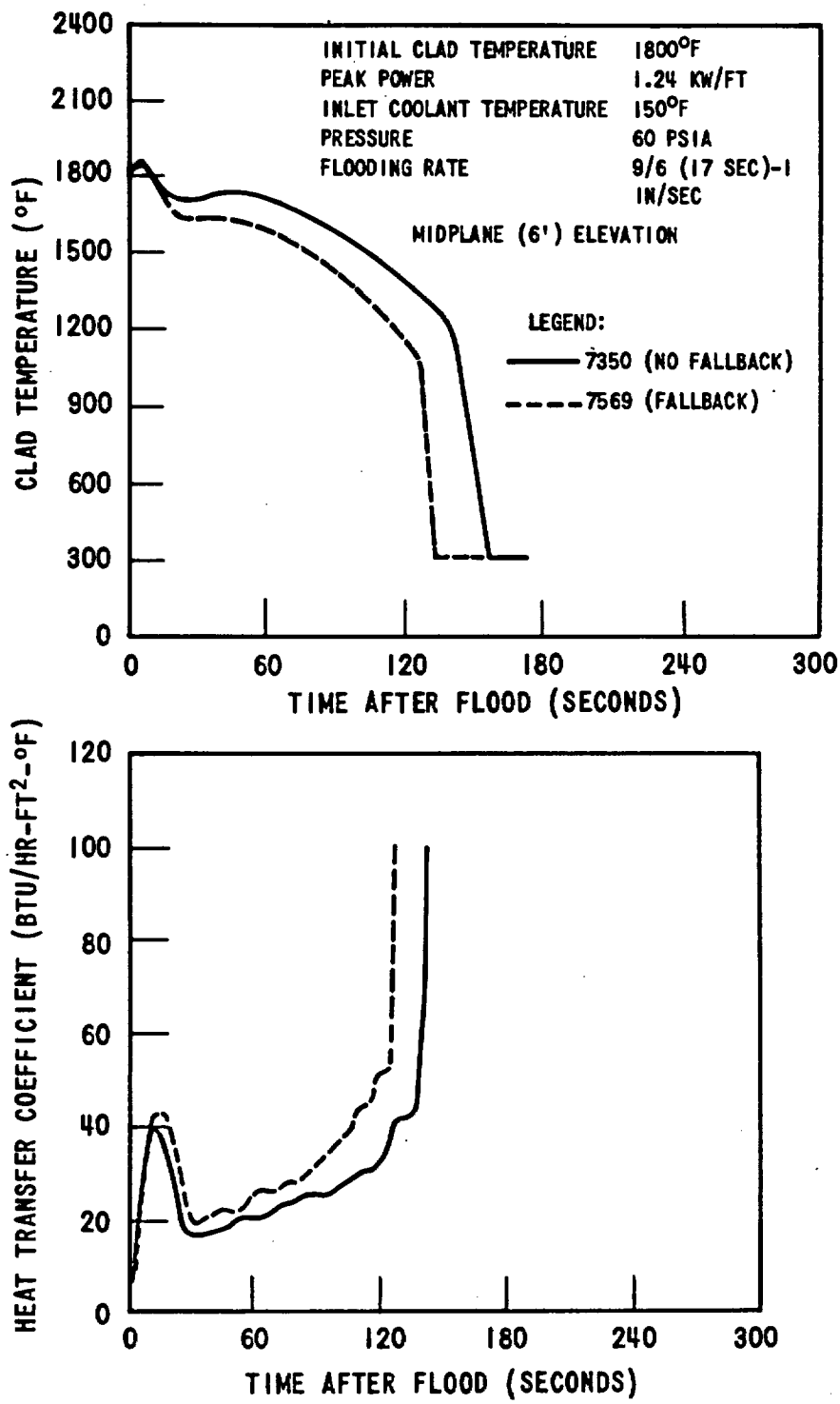

Figure 3-30. Effect of Fallback at 9/6 (17 Sec) - 1 In/Sec Variable Flooding Rate

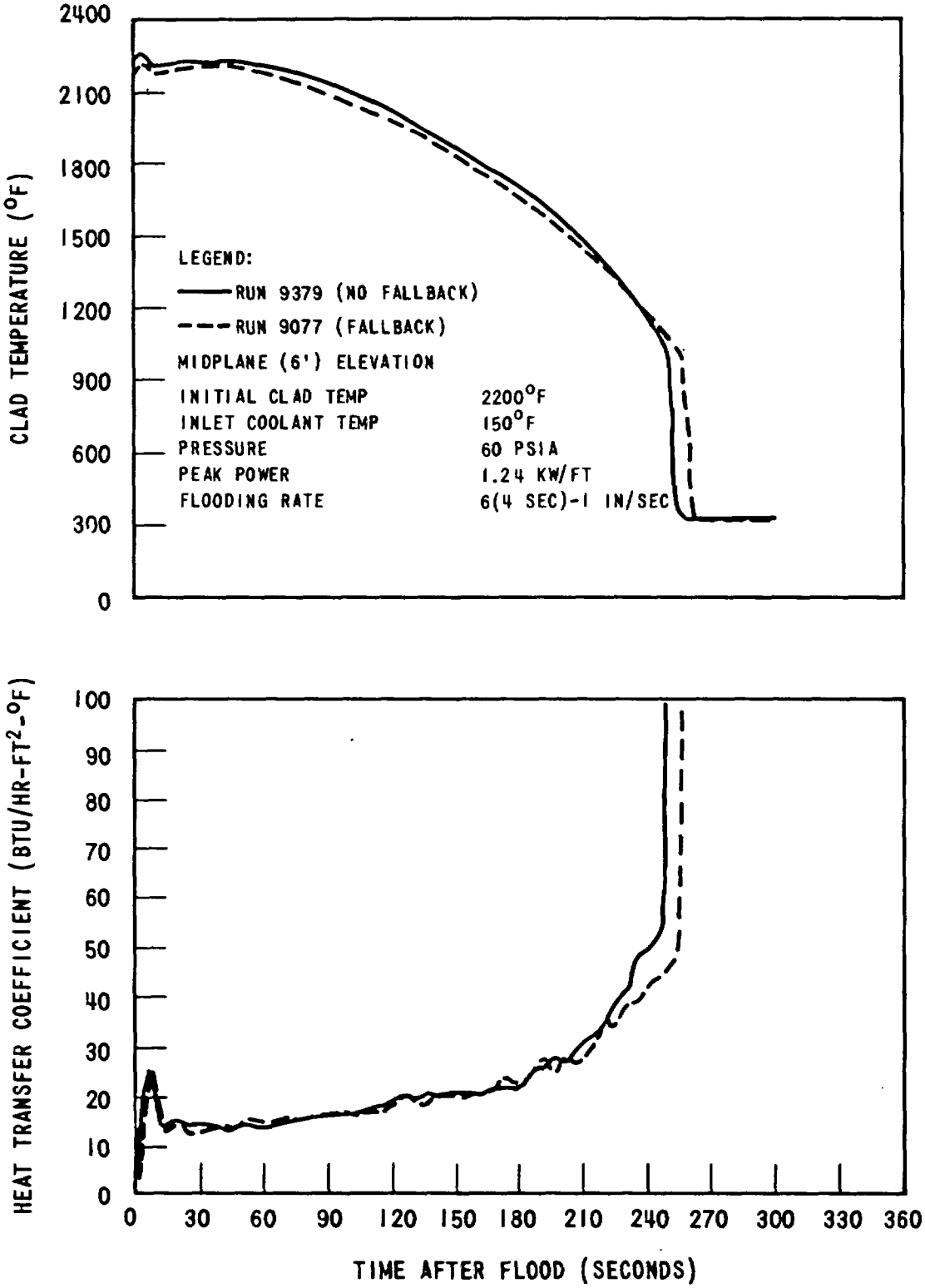

Figure 3-31. Effect of Fallback at 6 (4 Sec)-1 In/Sec Variable Flooding Rate

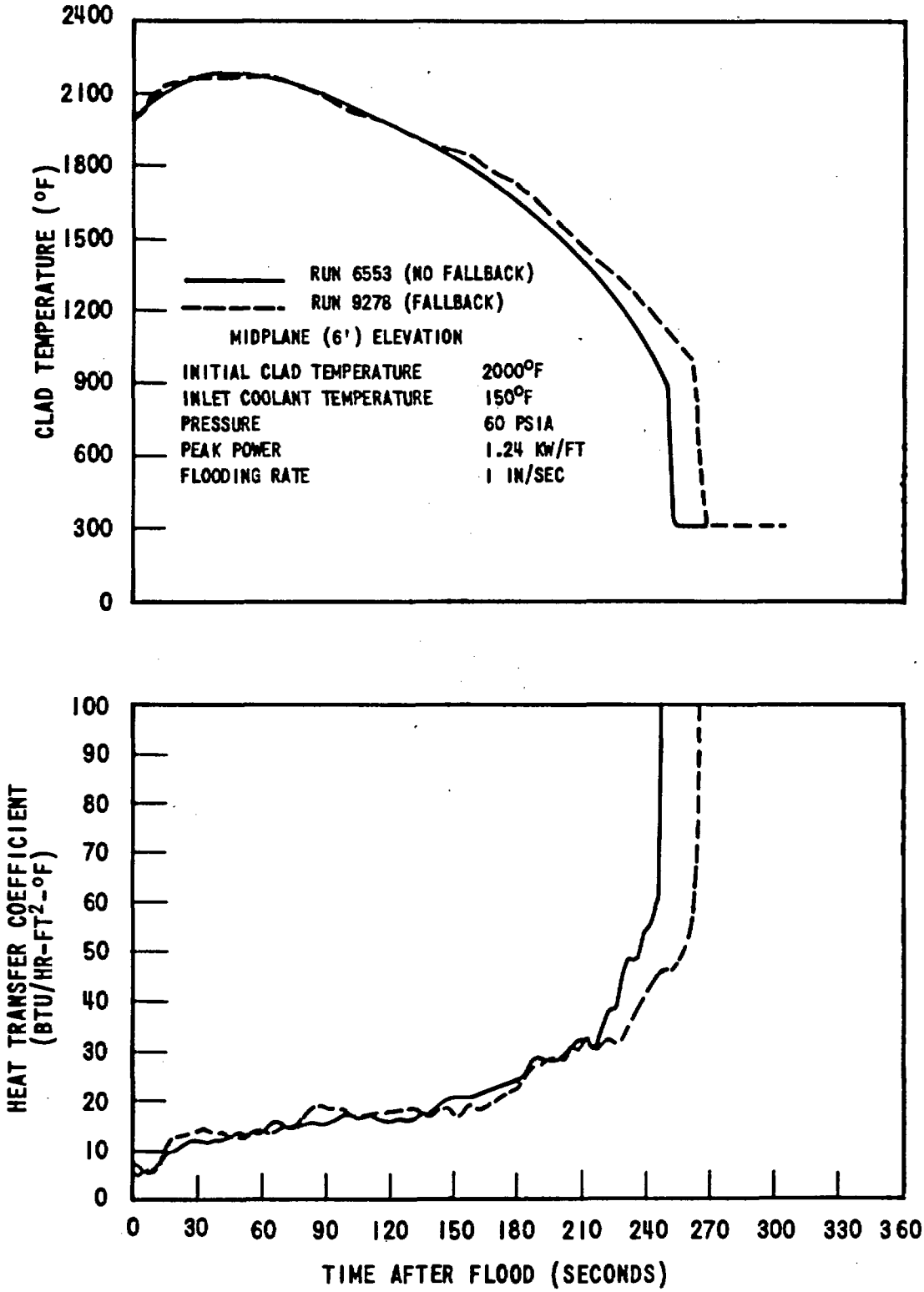

Figure 3-32. Effect of Fallback at 1 In/Sec Flooding Rate

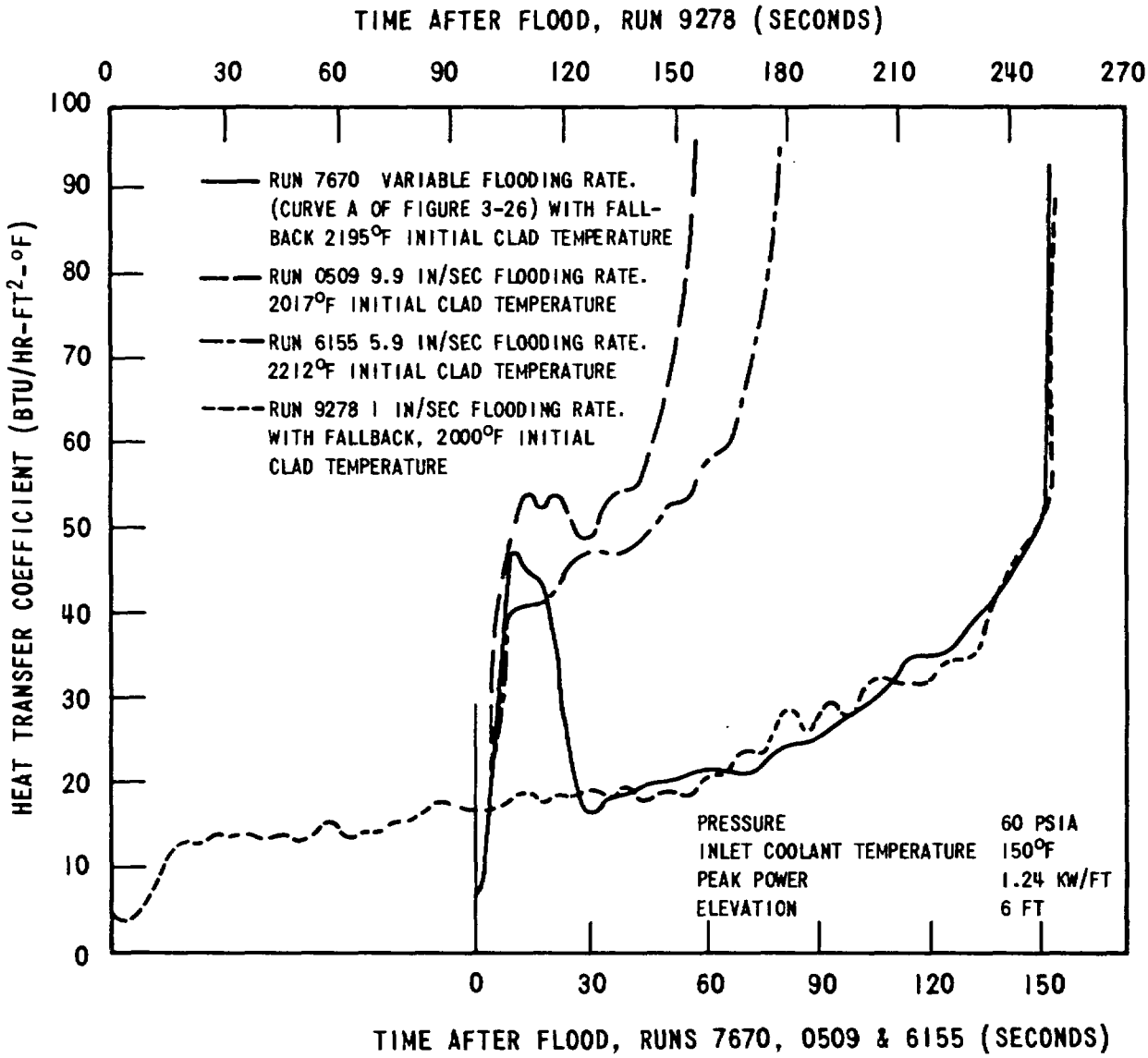

Figure 3-33. Comparison of Heat Transfer Coefficients for Constant and Variable Flooding Rate A Tests with Fallback

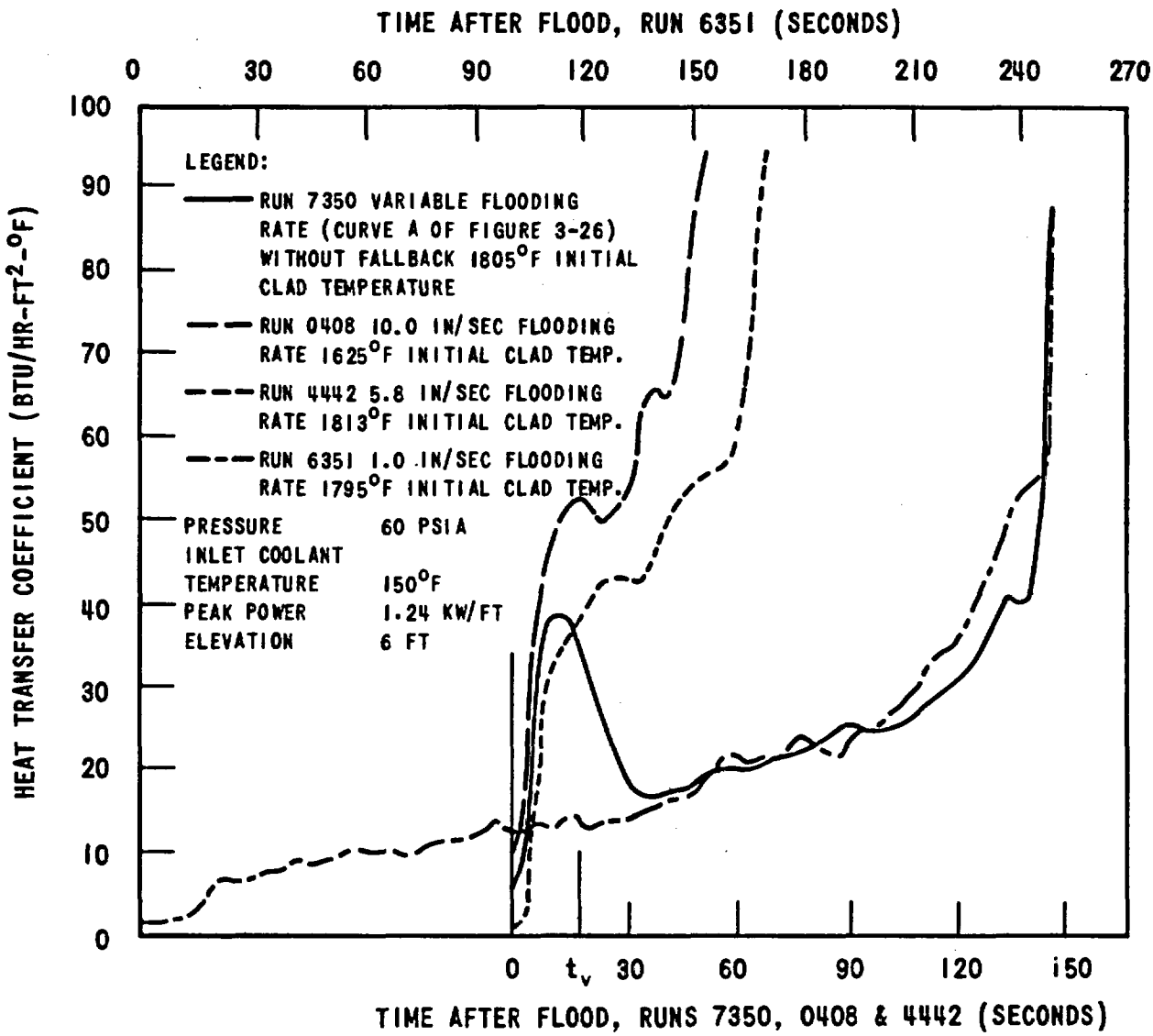

Figure 3-34. Comparison of Heat Transfer Coefficients for Constant and Variable Flooding Rate A Tests Without Fallback

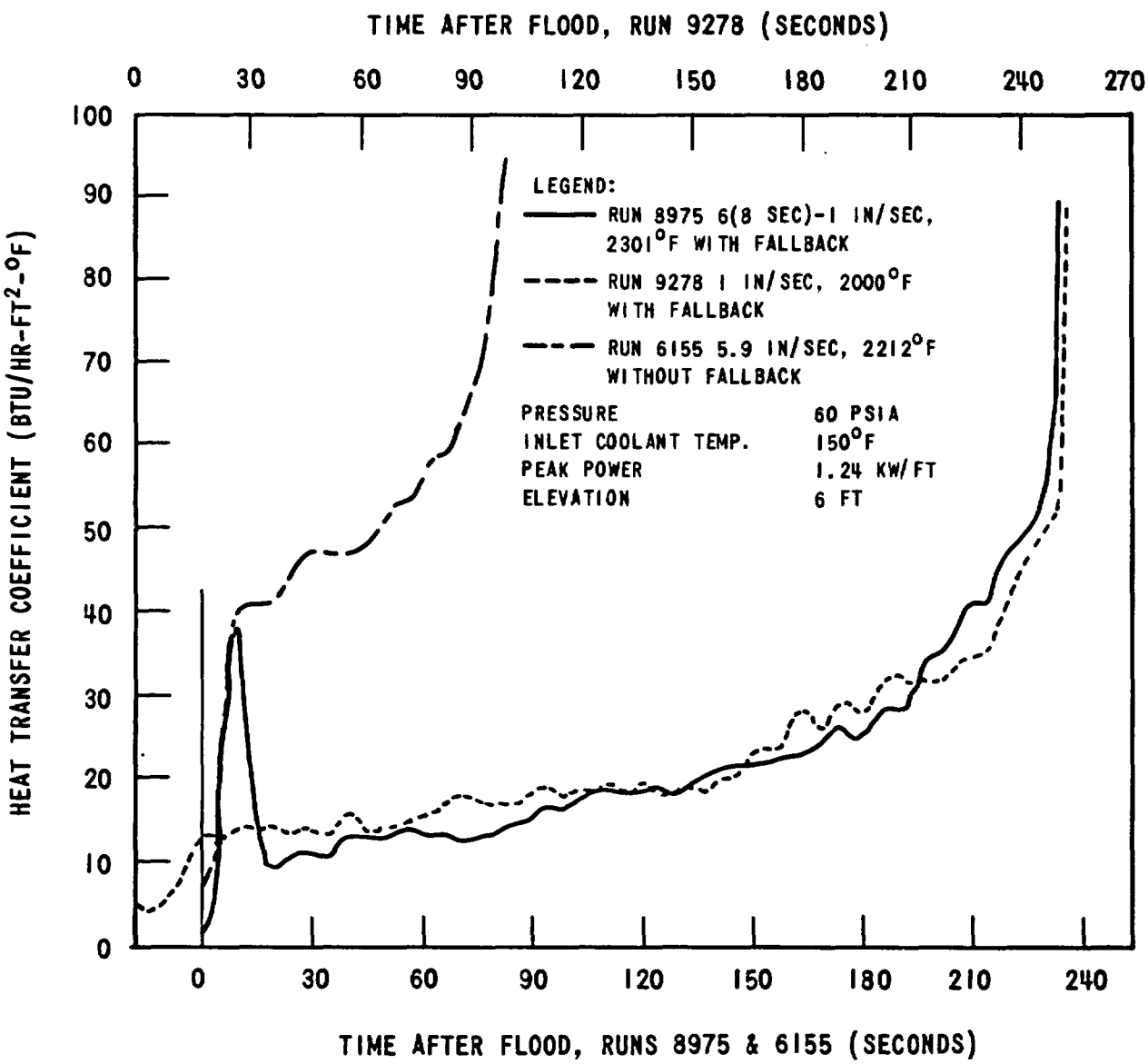

Figure 3-35. Comparison of Heat Transfer Coefficients for Constant and Variable Flooding Rate B Tests with Fallback

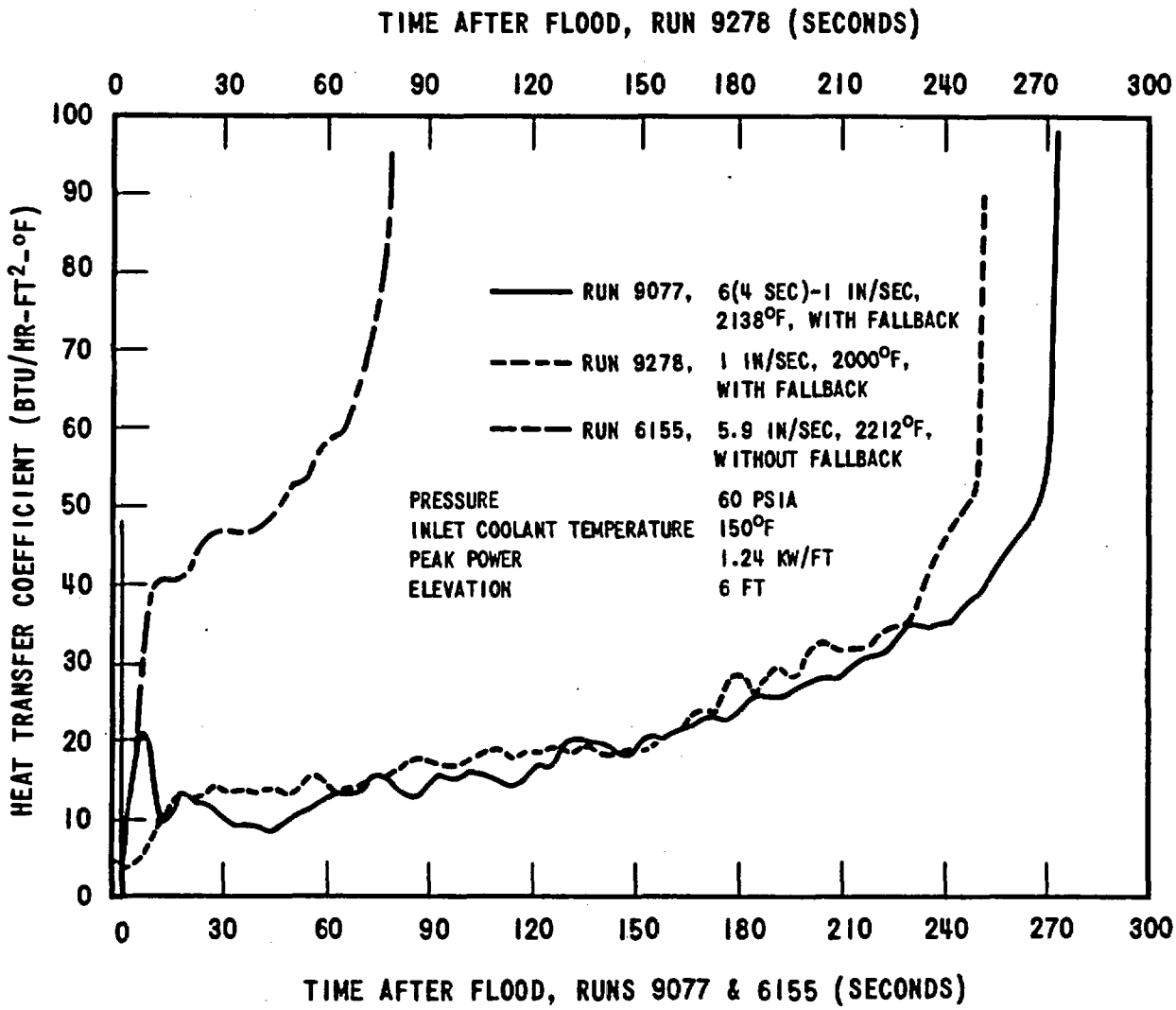

Figure 3-36. Comparison of Heat Transfer Coefficients for Constant and Variable Flooding Rate C Tests with Fallback

flooding rate was reduced to 1 in./sec. For the low flow part of the run, the heat transfer coefficient of the variable flow run was matched with a 1 in./sec constant flow run by a time shift computed using the method of Section 3.3.3. The excellent agreement between constant and variable flow test results in Figures 3-33 through 3-36 shows that the variable flooding rate heat transfer coefficient data is consistent with and predictable by constant flooding rate data.

3.2.5 Flow Blockage Tests

Flow blockage tests were performed in the Group I and Group II test series. The objective of these tests was to simulate subchannel blockage which may occur due to clad swelling and axial rod distortion during a loss of coolant accident and determine its effect on heat transfer. These tests are discussed in detail in References 2 and 3. A more condensed description is presented here.

The blockage was effected by a three-eighths inch thick flat plate approximately one inch below the bundle midplane. In the Group I tests, the plate blocked from 50 percent to 75 percent of the flow area of sixteen central flow channels out of a 49 rod bundle, allowing bypass flow around the plate in the outer channels. A sketch of the plate is shown in Figure 3-37. Flooding rates for these tests were 6, 4, and 2 in./sec. The Group II blockage plate initially blocked 75 percent of the total flow area in the 10 x 10 bundle with no bypass. The blockage of 16 central flow channels could be increased up to 100 percent with the rest of the bundle blocked 75 to 90 percent. This was the most severe blockage configuration investigated. The Group II blockage plate is shown in Figure 3-38. Figure 3-39 is a schematic of the various blockages used in the Group II series. Note that the severity of blockage was increased in going from Blockage Geometry 1 to Blockage Geometry 4. For this series, flooding rates were 4, 1 and 0.6 in./sec. Also, one test was performed using a variable flooding rate. Special thermocouples were installed at 6 ft. 4 in. and 6 ft 8 in. for the Group II flow blockage tests. In both plate designs, blockage was increased by means of special pins inserted into the plate.

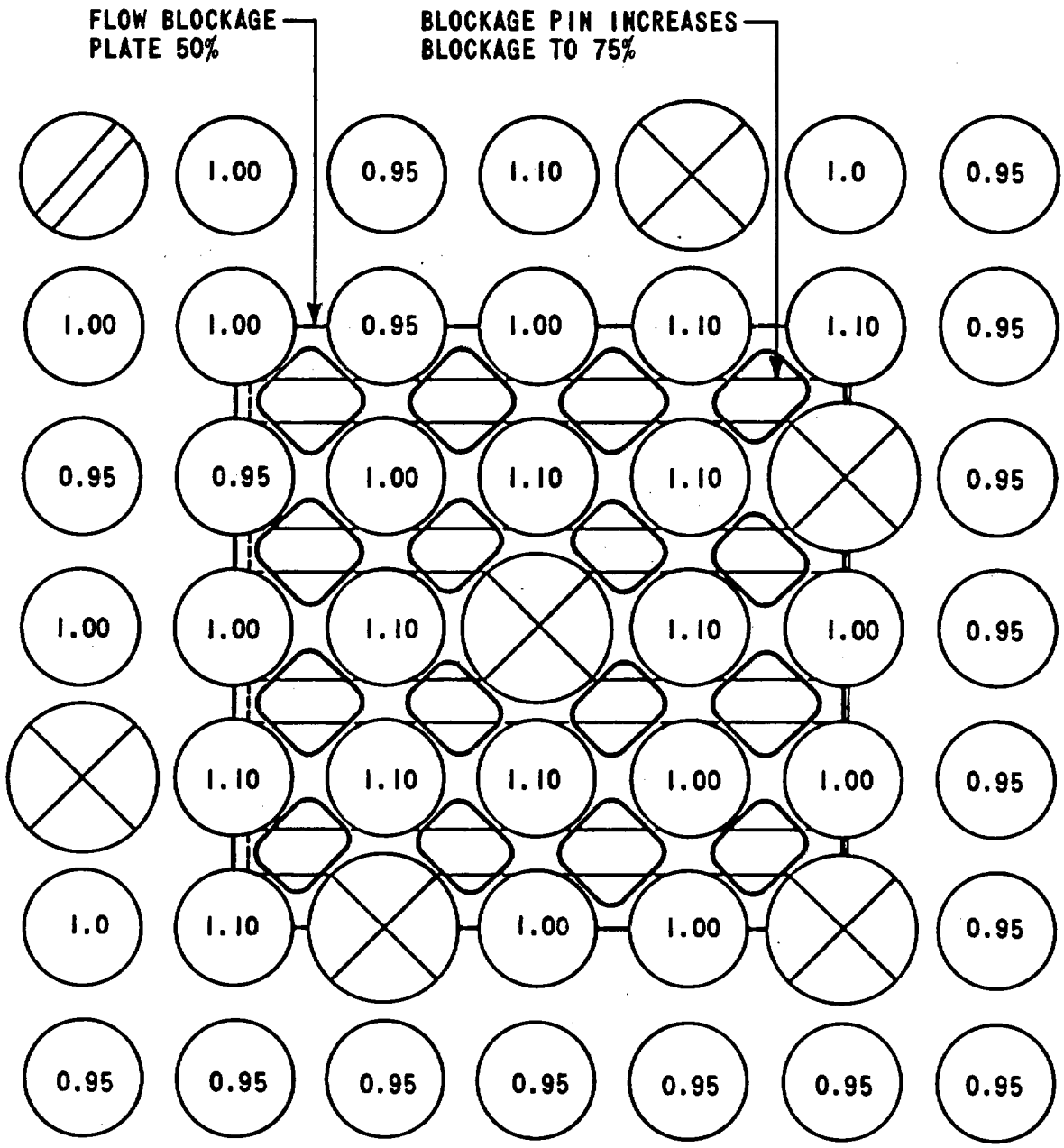

Figure 3-37. Group I Flow Blockage Plate

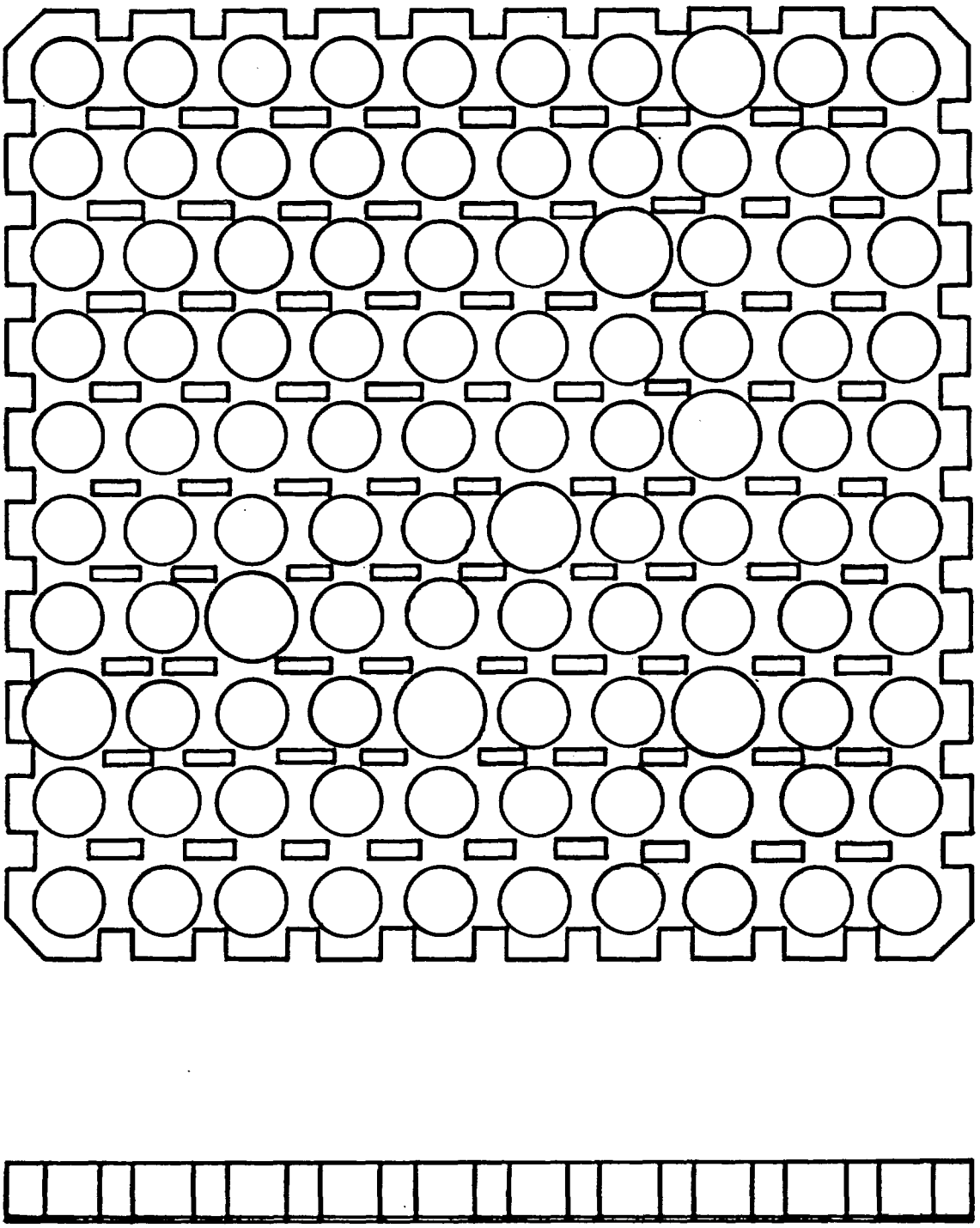

ACTUAL SIZE

Figure 3-38. Group II Flow Blockage Plate

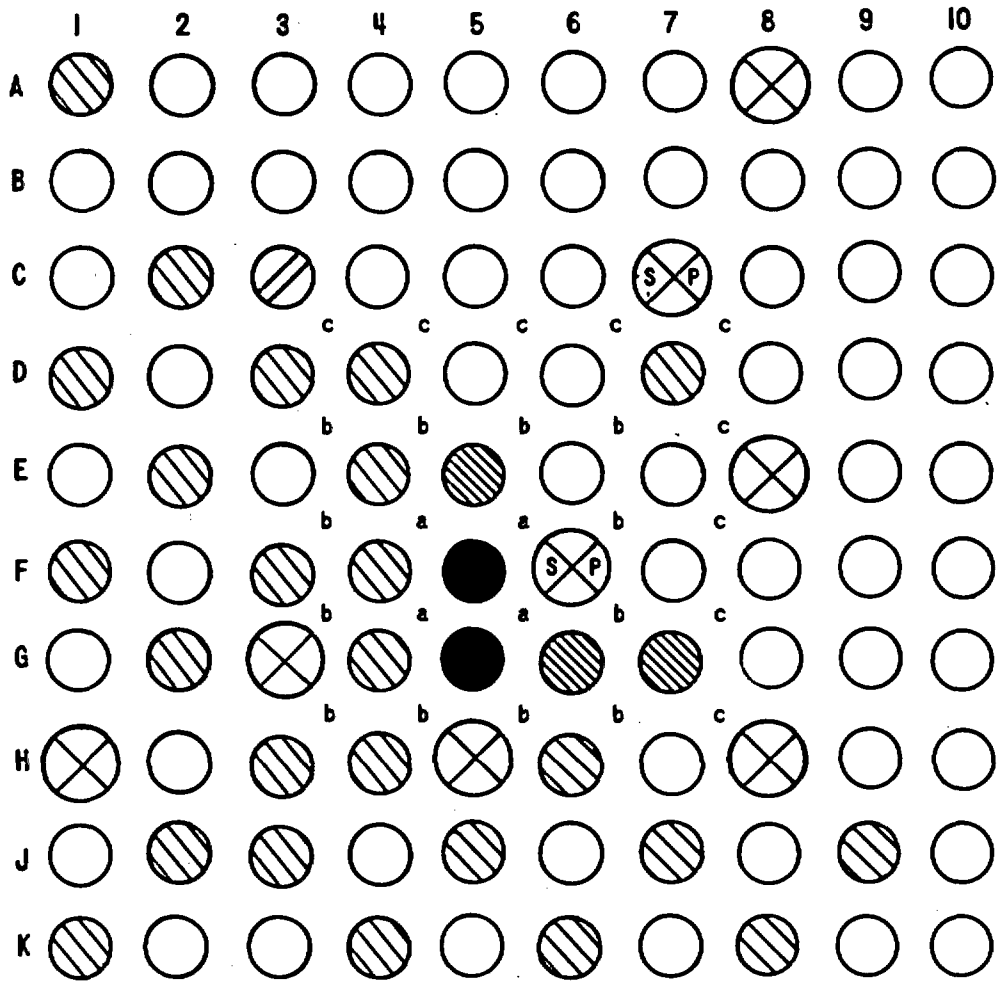

BLOCKAGE GEOMETRY	BLOCKAGE OF FLOW AREA IN CHANNELS DESIGNATED:			
	a	b	c	ALL OTHERS
1	75%	75%	75%	75%
2	90%	90%	90%	75%
3	100%	90%	90%	75%
4	100%	100%	90%	75%

Figure 3-39. Schematic of Group II Flow Blockage Geometries

It should be noted that the effect of using a flow blockage configuration more nearly typical of clad swelling under loss-of-coolant accident conditions has been studied by Idaho Nuclear Corporation as reported in Reference 7. In this investigation, flow blockage was simulated by a flat, perforated plate similar to the blockage plates used in this program and by sleeves patterned after actual swelled areas which occurred on Zircaloy tubing tested under simulated reactor core heat-up conditions. The results of these tests indicated that the geometry of the blockage region (plate versus sleeves) was not a significant factor in the cooling process.

3.2.5.1 Effect of Flow Blockage on Temperature Response

Table 3-1 gives the actual run conditions and test results of the constant flow, flow blockage tests. The variable flow test results are included in Table 3-2 (Run 8463). Temperature response as a function of blockage for all constant flooding rate flow blockage tests is summarized in Table 3-7 along with appropriate zero blockage results. The tests are divided into several sets according to common run conditions. These results are from midplane thermocouples located approximately one inch above the flow blockage plate.

Table 3-7 shows that temperature rises and turnaround times were generally lower in the blockage cases than in the unblocked cases. In the Group II tests the temperature rises and turnaround times were not significantly affected as the severity of the blockage was increased, even in the case of 100 percent blockage of 16 flow channels. However, the Group I tests run with a 6 in./sec flooding rate showed an increase in temperature rise and turnaround time with increased blockage. Midplane quench time was essentially unaffected by flow blockage in the Group II tests; whereas, in the Group I series, midplane quench times were significantly lowered by flow blockage. These differences in behavior are believed to be due to differences in the specific Group I and II flow blockage geometries (bypass vs. no-bypass) and the resultant changes in flow patterns in the vicinity of the blockage plate. In general, the clad temperature results in Table 3-7 indicate that the flow blockage plate improved midplane heat transfer behavior, even for the most severe blockage configurations tested. Additional insight into the test results can be obtained from the heat transfer coefficient data.

TABLE 3-7

MIDPLANE TEMPERATURE RESPONSE FOR VARIOUS FLOW BLOCKAGE CONFIGURATIONS AND TEST CONDITIONS

Run No	Nominal Initial Clad Temperature (°F)	Nominal Flooding Rate (in./sec)	Blockage	Temperature Rise (°F)	Turnaround Time (sec)	Quench Time (sec)
			GROUP I TESTS (Bypass Around Blockage)			
1002	1600	6	0%	70	6	76
2636	1600	6	50% (16 ch. in 7 x 7 bundle)	60	5	54
2838	1600	6	75% (16 ch. in 7 x 7 bundle)	79	7	47
5642	1800	6	0%	67	6	75
2737	1800	6	50% (16 ch. in 7 x 7 bundle)	42	4	56
2939	1800	6	75% (16 ch. in 7 x 7 bundle)	61	5	49
4321	1600	4	0%	107	14	102
3300	1600	4	75% (16 ch. in 7 x 7 bundle)	81	7	62
4225	1600	2	0%	247	35	192
3100	1600	2	75% (16 ch. in 7 x 7 bundle)	131	14	89
			GROUP II TESTS (No Bypass)			
4321	1600	4	0%	107	14	102
7845	1600	4	Geometry 1 (Fig. 3-37)	80	5	119
8054	1600	4	Geometry 2 (Fig. 3-37)	80	5	108
8265	1600	4	Geometry 3 (Fig. 3-37)	90	6	107
8567	1600	4	Geometry 4 (Fig. 3-37)	84	6	113
6948	1600	1	0%	465	95	266
7946	1600	1	Geometry 1 (Fig. 3-37)	193	15	239
8162	1600	1	Geometry 2 (Fig. 3-37)	195	15	242
8366	1600	1	Geometry 3 (Fig. 3-37)	245	17	246
8668	1600	1	Geometry 4 (Fig. 3-37)	220	17	253
6749[a]	1600	0.6	0%	801 (at 107 sec)		
8764[b]	1600	0.6	Geometry 4	720 (at 97 sec)		-

[a]Power scrammed at 107 sec after flood due to 2400°F temperature at 6 ft elevation.

[b]Power scrammed at 97.2 sec after flood due to 2400°F temperature at 8 ft elevation.

3.2.5.2 Effect of Flow Blockage on Midplane Heat Transfer Coefficients

Figures 3-40 and 3-41 present typical inner rod midplane heat transfer coefficients for the Group I and Group II flow blockage tests, respectively. Zero blockage cases are also shown. It is apparent that in all cases the flow blockage caused an improvement in the heat transfer coefficient at the midplane (1 inch downstream of the blockage location). This improvement in midplane heat transfer coefficient was even observed at locations immediately behind the central 100 percent blocked region. The reason for this behavior was that the blockage plate broke up or atomized the entrained liquid droplets as they passed through the plate. Also, flow contraction and expansion increased the turbulence above the plate, and as indicated by the behavior of Runs 8567 and 8668 it is evident that the flow redistributed very rapidly immediately downstream of the blockage region. The droplet atomization gave a much greater liquid surface heat transfer area for a given liquid volume fraction. High speed motion pictures taken through the flow housing midplane window confirmed this is the primary mechanism for improved heat transfer.

3.2.5.3 Effect of Flow Blockage at Other Elevations

To this point it has been shown that flow blockage increases heat transfer at the midplane, or one inch downstream of the blockage location. Reference 2 concluded that heat transfer at other elevations in the bundle was not affected. However, the more severe blockages investigated in Group II and reexamination of the Group I data have revealed effects at other elevations which can be summarized as follows:

1. At 6 ft. 4 in. and 6 ft. 8 in. (special thermocouples in Group II tests) the temperature rise at 4 in./sec flooding rate was about equal to that at the 6 ft elevation. For 1 in./sec, the temperature rise at these elevations exceeded the 6 ft elevation. Also as blockage was increased, temperature rise at 6 ft 4 in. and 6 ft 8 in. increased at 1 in./sec flooding rate, but was always less than that of the 6 ft unblocked case.
2. At 4 ft (2 ft below the blockage location) there was no effect due to blockage except in the 1 in./sec flooding rate tests. In these cases,

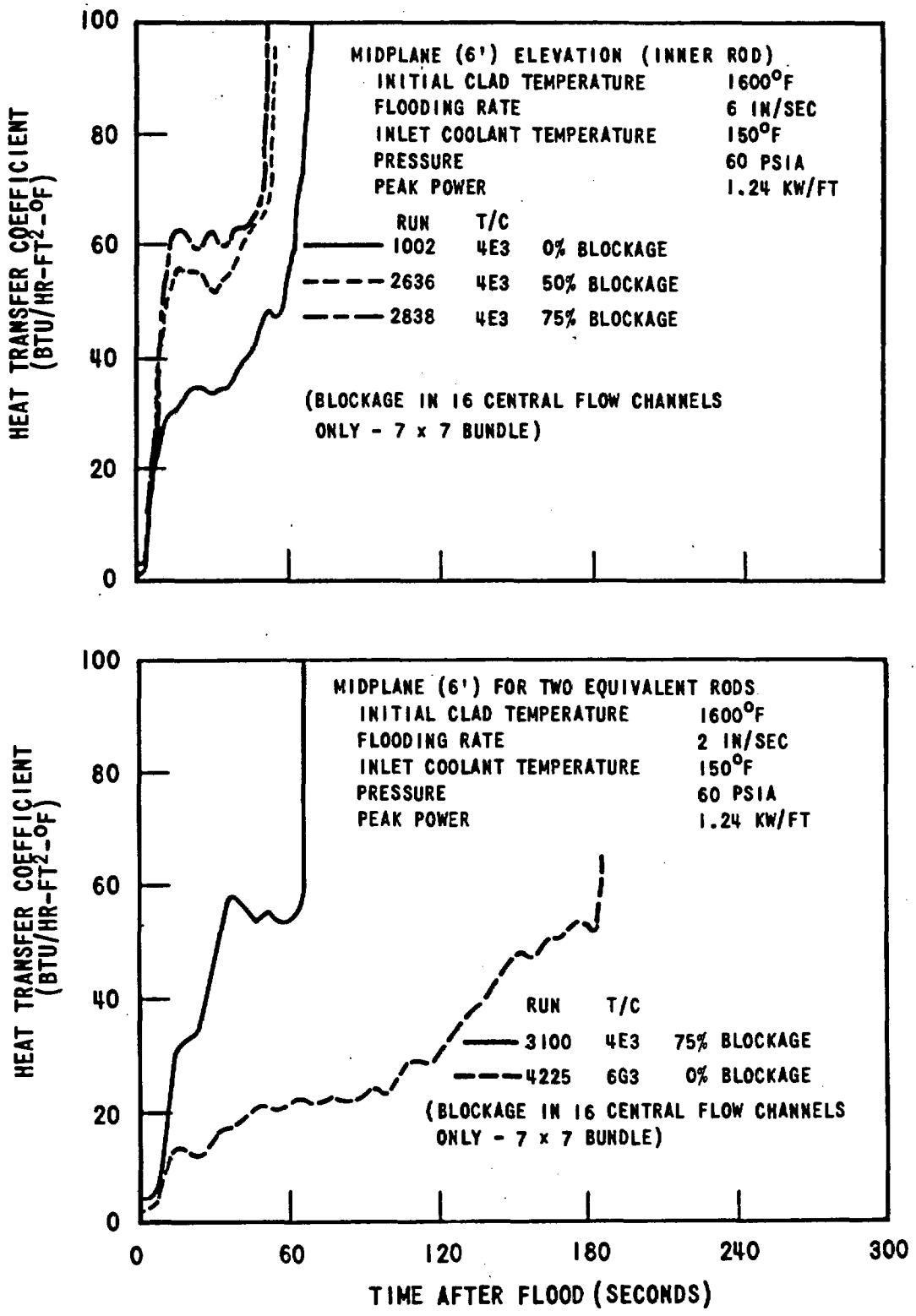

Figure 3-40. Effect of Flow Blockage with Bypass Flow on Midplane Heat Transfer Coefficients

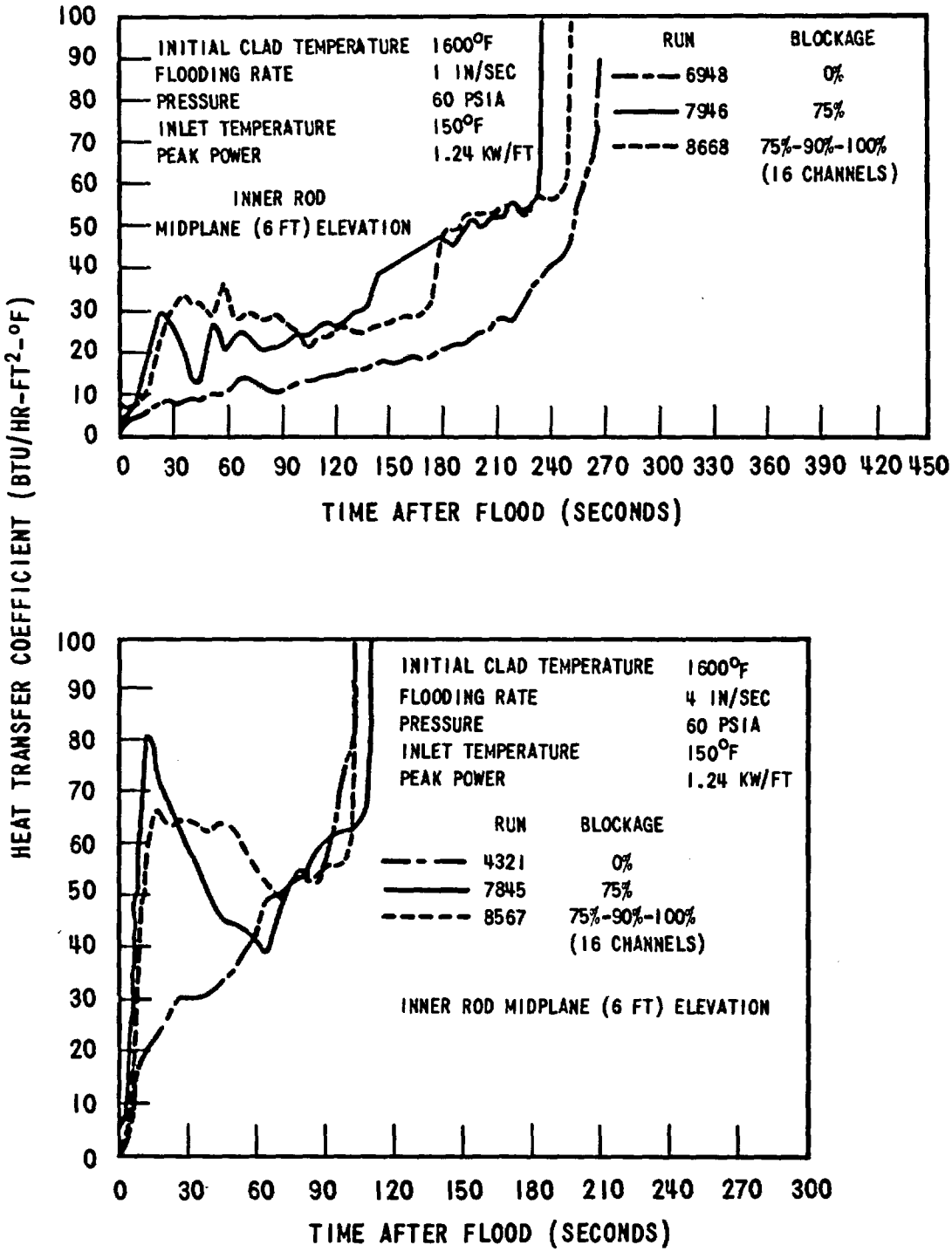

Figure 3-41. Effect of Flow Blockage without Bypass Flow on Midplane Heat Transfer Coefficients

there was improved heat transfer with blockage. This may have been due to the blockage plate keeping some water in the lower part of the bundle. At higher flooding rates, the driving force for the flow was stronger and the two phase mixture was forced through the blocked region.

3. Improved heat transfer was found at the 8 ft and 10 ft elevations, particularly at flooding rates of 4 in./sec or less. The degree of improvement was less, however, as the blockage was increased, unlike the six foot elevation which was generally unaffectd by increased blockage. At the highest blockages tested the temperature rise at the 8 ft elevation was, at worst, on the same order as the unblocked case. The 10 ft temperature rise at the highest blockages sometimes exceeded the unblocked case; however, this elevation is at a relatively low temperature due to the axial power distribution. Thus, there is very little danger of excessive temperatures at the 10 ft elevation due to flow blockage.

Thus, it can be concluded that flow blockage effects extended as far as 2 feet upstream and 4 feet downstream of the blockage location. The effects were most strongly felt in the region just downstream of the blockage.

3.2.5.4 Heat Transfer in the Variable Flooding Rate Test with Flow Blockage

The midplane heat transfer coefficient for the variable flow test with flow blockage was compared with constant flow test results. Figure 3-42 shows the variable flooding rate midplane heat transfer coefficients together with the constant flooding rate data for the same blockage. The method used in comparing these runs is described in Section 3.3.3.

The high flow rate portion of the test shows good agreement with the 4 in./sec constant flow test. After the switch to 1 in./sec, the variable flow test had a higher heat transfer coefficient for about 90 seconds, after which agreement with the 1 in./sec constant flow test was very good. Thus, it is possible to conservatively predict variable flooding rate flow blockage results with flow blockage constant flow data.

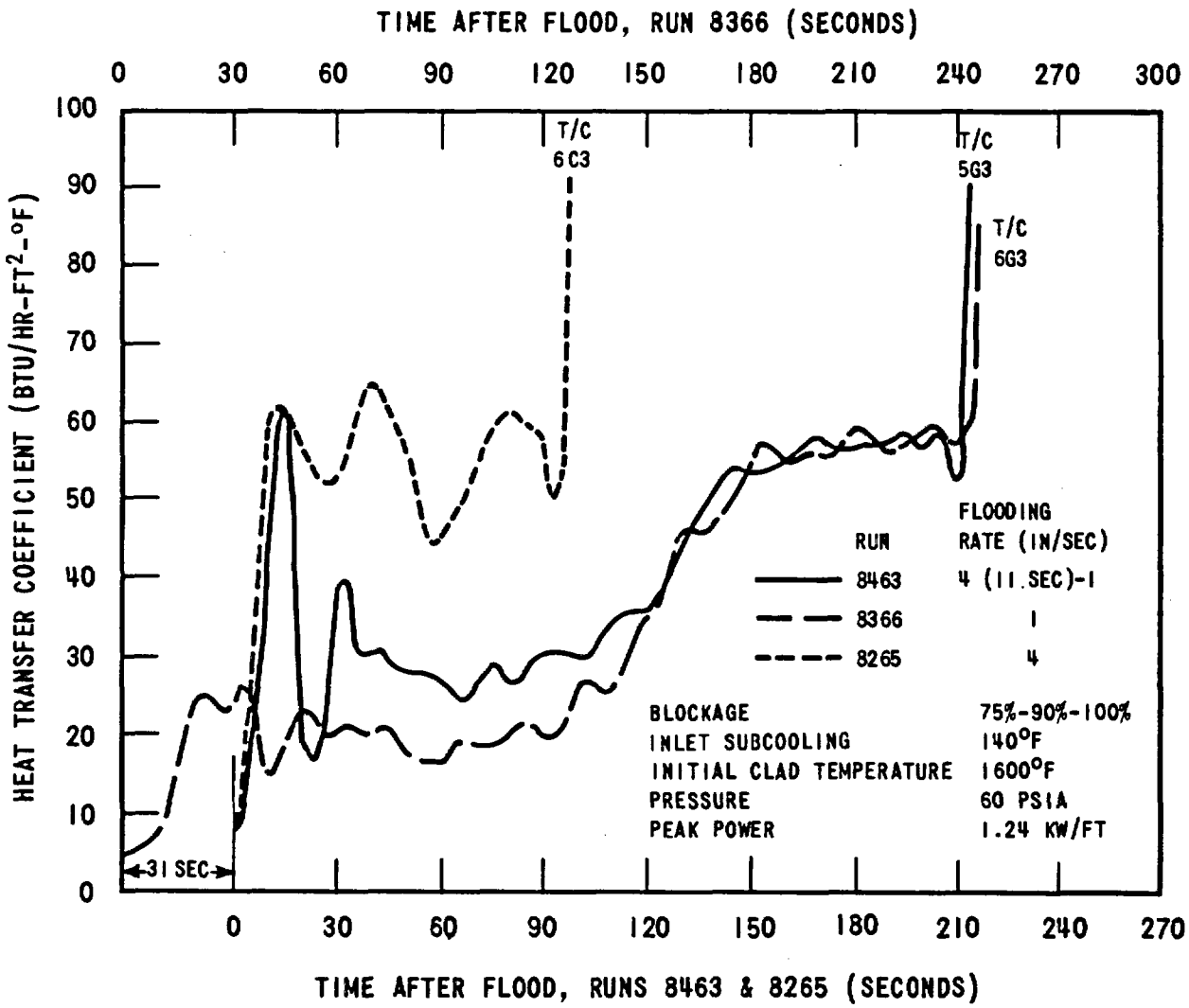

Figure 3.42. Comparison of Variable and Constant Flooding Rate Flow Blockage Heat Transfer Coefficients

3.3 HEAT TRANSFER REGIMES AND CORRELATIONS

3.3.1 Heat Transfer and Flow Regimes

3.3.1.1 Movie Observations

The flow patterns which occur between the FLECHT heater rods have been observed in high-speed (967 frames/sec) movies taken through a 4.6 inch square window at one side of the rod bundle. The various flow regimes, as they might have existed at a given instant in time, are shown in Figure 3-43. However, the boundaries between each regime moved upward with time, and all seven of the regimes were generally not present simultaneously.

The most important of the moving boundaries, the one between the film boiling and transition boiling regimes, is called the quench front. The location of this front can be determined from the cladding temperature history. The time at which the clad temperature began its rapid descent to saturation indicated the arrival of the quench front at that particular location (Figure 3-44). Below the quench front the liquid could wet the heated rod surface, whereas above the quench front it could not.

Figure 3-45 is a photograph of the eight heater rods which were visible through the observation window. The interface between the transition boiling and nucleate boiling regimes can be seen as the division between the light and dark segments of rods 1 through 7 (counting from the left). This line is the trailing edge of that portion of the rod in transition boiling. The transition boiling regime was characterized by an unsteady generation rate of vapor bubbles. Its irregular nature was most clearly evidenced by the large vapor bubbles around rods 3, 6, and 7 in the upper half of the window and around rod 8 near the bottom of the window.

A stable film boiling regime existed just above the quench front, or leading edge of the transition boiling regime. The flow pattern observed in the movies consisted of a thin vapor annulus around the rod surrounded by a continuous liquid phase. The bright line on either side of the heater rod (upper portions of rods 1, 2, 4 and 5 in Figure 3-45) marked the liquid-vapor interface. The wave motion typical of film boiling could be seen at the interface when the movie film was running. The wave velocity was from 5 to 10 times the liquid

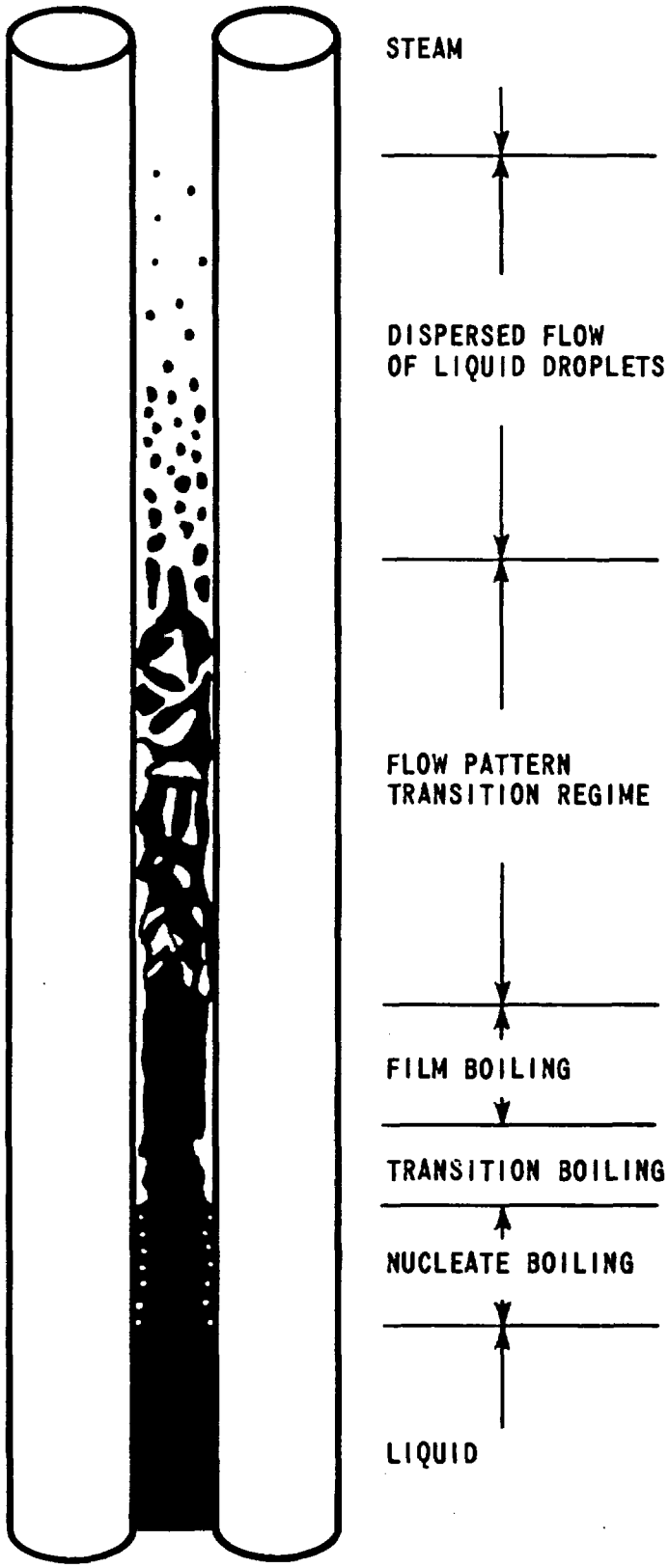

Figure 3-43. Flecht Flow Regimes

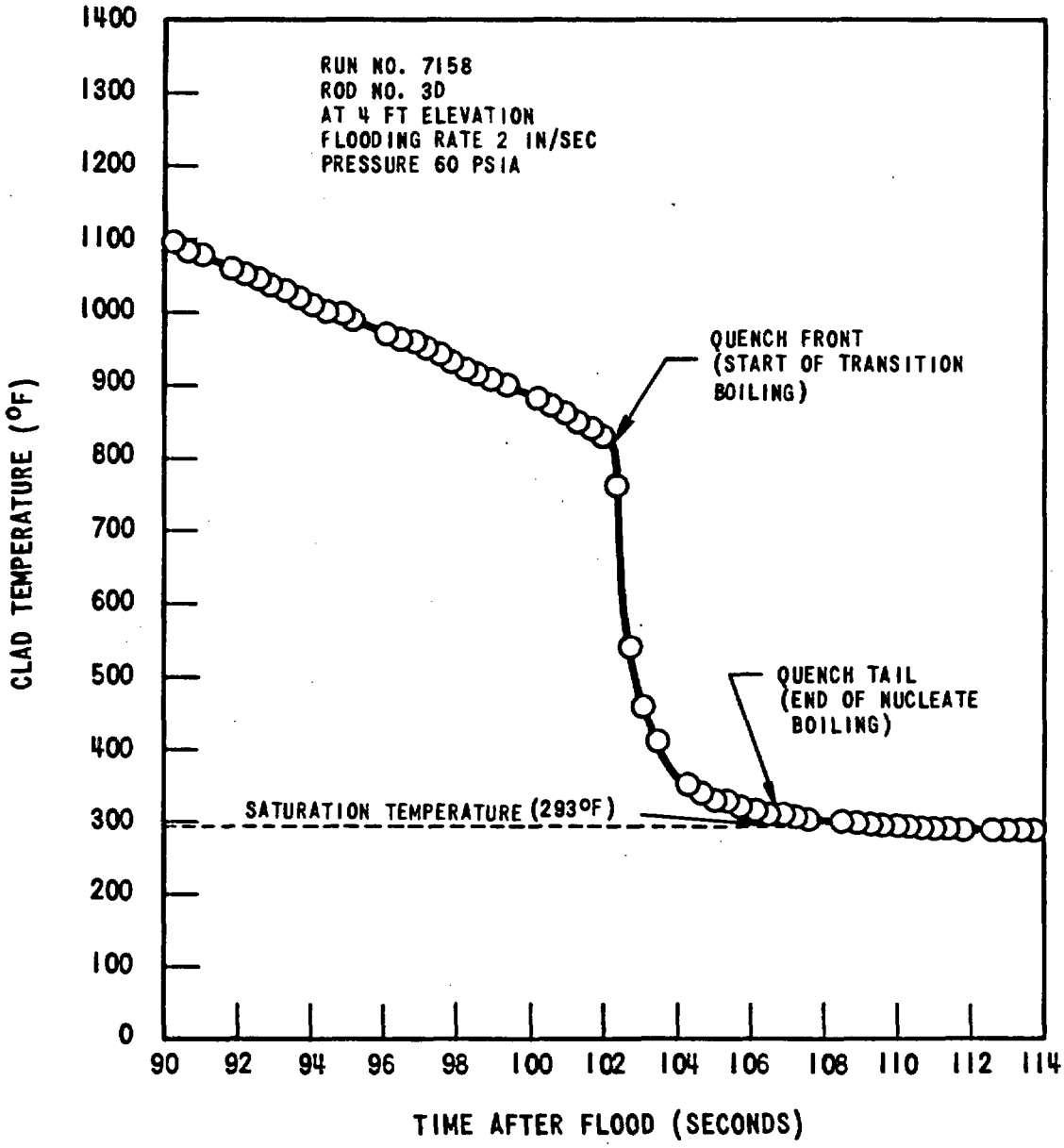

Figure 3-44. Clad Quench Behavior

RUN	3440
TIME	59.26 SEC AFTER FLOOD
ELEVATION	6 FT
INITIAL CLAD TEMPERATURE	1204°F
FLOODING RATE	5.9 IN/SEC
COOLANT TEMPERATURE	155°F
PRESSURE	55 PSIA
PEAK POWER	1.24 KW/FT

Figure 3-45. Nucleate Boiling, Transition Boiling and Film Boiling Regimes

velocity, which equaled the flooding rate (6 in./sec for Run 3440). The wave length was 0.5 inch, or slightly larger than the rod diameter.

The relatively low void fraction and uniform appearance of the vapor layer in Figure 3-45 suggested that the liquid was subcooled and that most of the heat from the rods was absorbed in raising the liquid temperature, at least for the conditions under which the film boiling regime was photographed. The local coolant thermocouple data presented in Section 3.6 also indicated the presence of subcooled liquid above the quench front. Under other conditions, for example low flooding rates and high elevations, calculations indicated that liquid above the quench front was at the saturation temperature.

Just as an unstable transition boiling regime existed between the nucleate and stable film boiling regimes, an unstable flow pattern transition regime existed between the stable film boiling and dispersed flow regimes. In the flow pattern transition regime, the flow changed from mostly liquid, or the continuous liquid phase with vapor film boiling, to mostly steam, or the continuous vapor phase with dispersed droplet flow. In Figure 3-46, rod 8 had started into the flow pattern transition regime. The other 7 rods were still in the dispersed flow regime.

The flow pattern transition regime was highly turbulent, and during its early part two types of behavior were observed. At lower elevations (3 and 6 ft) the entrained droplet flow characteristic of the dispersed flow regime was not visible, but swirls of liquid blown by vapor generated at the rod surface appeared to be moving in all directions. At the higher elevation (9 ft), on the other hand, entrained droplet flow continued to appear between the rods, while the violent motion of the liquid swirls was more confined to the vicinity of the rods (Figure 3-47). The difference in behavior at the higher elevation was evidently the result of increased vapor velocity due to heating.

During the later portion of the transition flow regime, as the continuous liquid phase was approached, unstable film boiling occurred (Figure 3-48).

Flow regimes similar to those of Figure 3-43 were also identified in the FHUST program (Reference 8). However, the transition flow and transition boiling flow regimes were not distinguished. The photographs in Reference 8 show

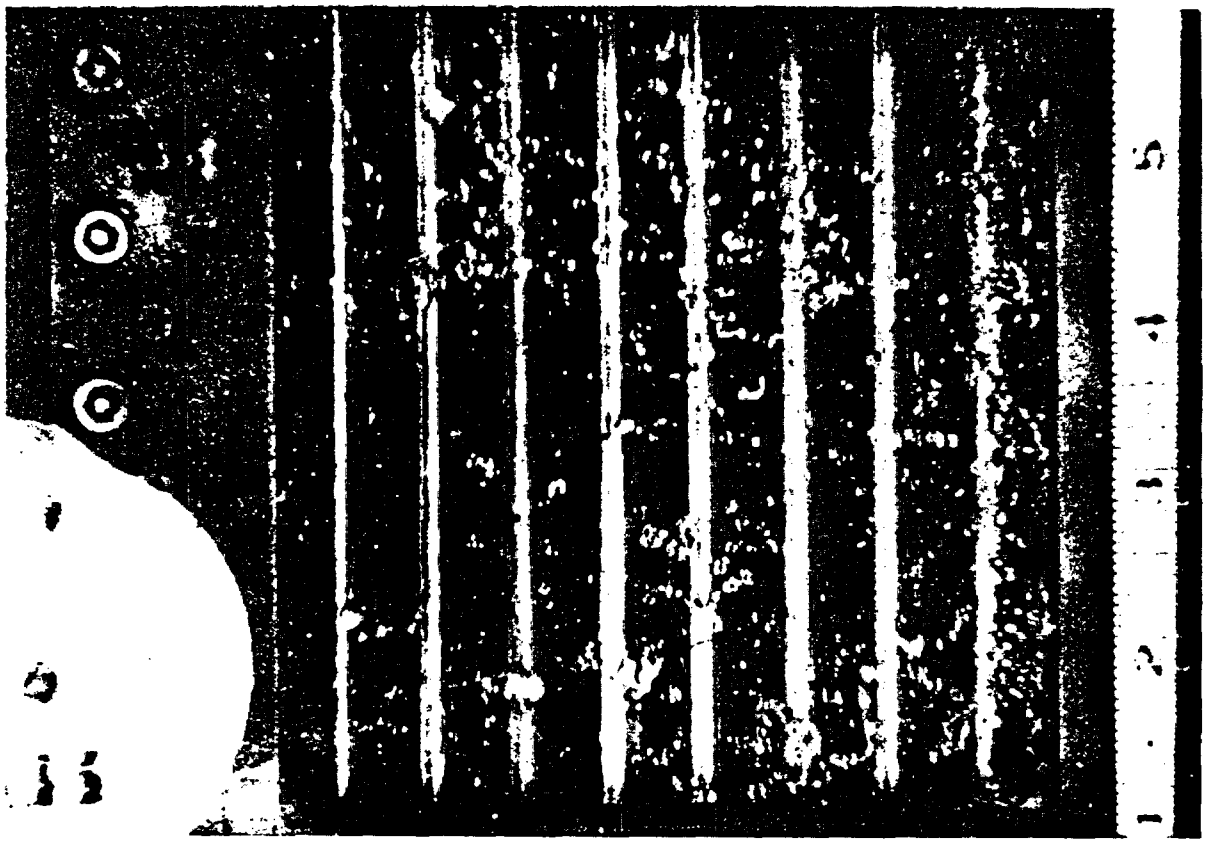

RUN	4442
TIME	12 SEC AFTER FLOOD
ELEVATION	6 FT
INITIAL CLAD TEMPERATURE	1813°F
FLOODING RATE	5.8 IN/SEC
COOLANT TEMPERATURE	154°F
PRESSURE	59 PSIA
PEAK POWER	1.24 KW/FT

Figure 3-46. Dispersed Flow Regime and Start of Transition Flow Regime

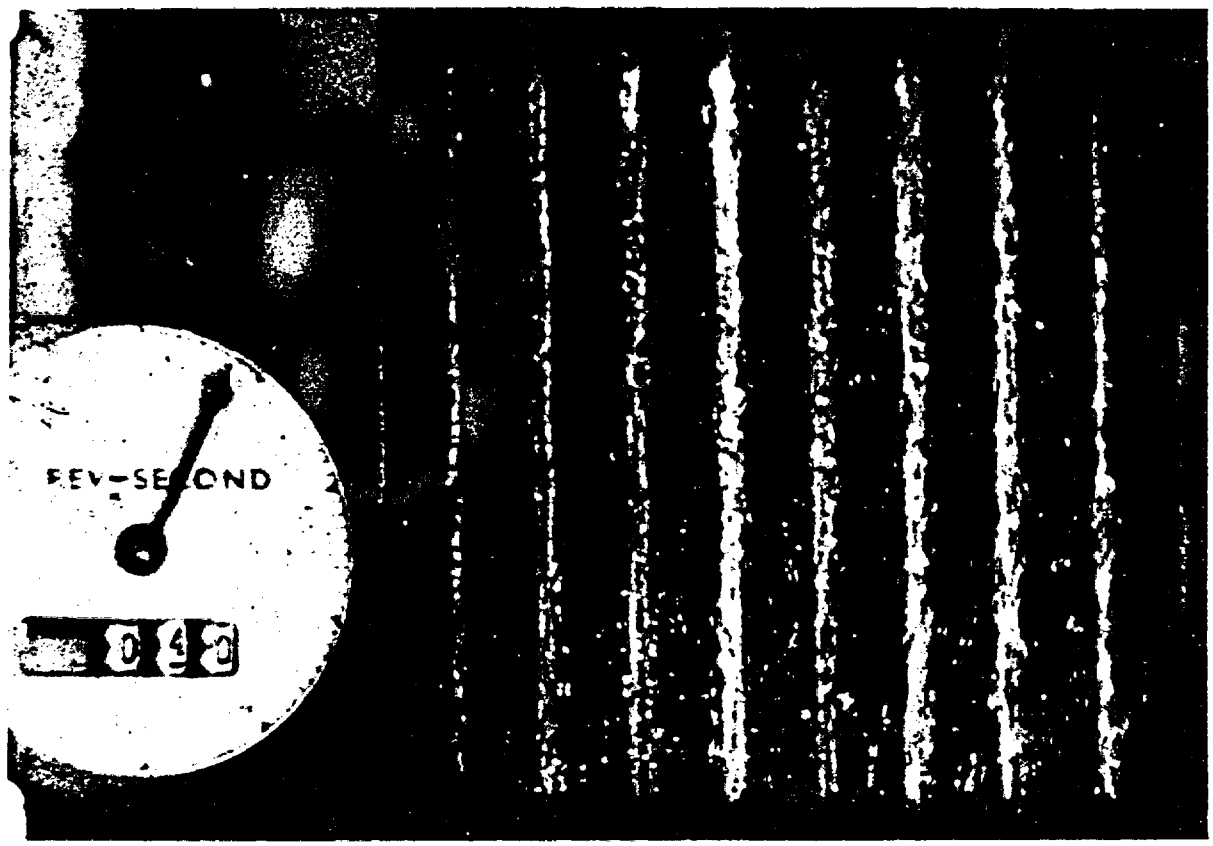

RUN	5642
TIME	40 SEC AFTER FLOOD
ELEVATION	9 FT
INITIAL CLAD TEMPERATURE	1811°F
FLOODING RATE	5.8 IN/SEC
COOLANT TEMPERATURE	152°F
PRESSURE	60 PSIA
PEAK POWER	1.24 KW/FT

Figure 3-47. Transition Flow Regime, Early Part at High Elevation

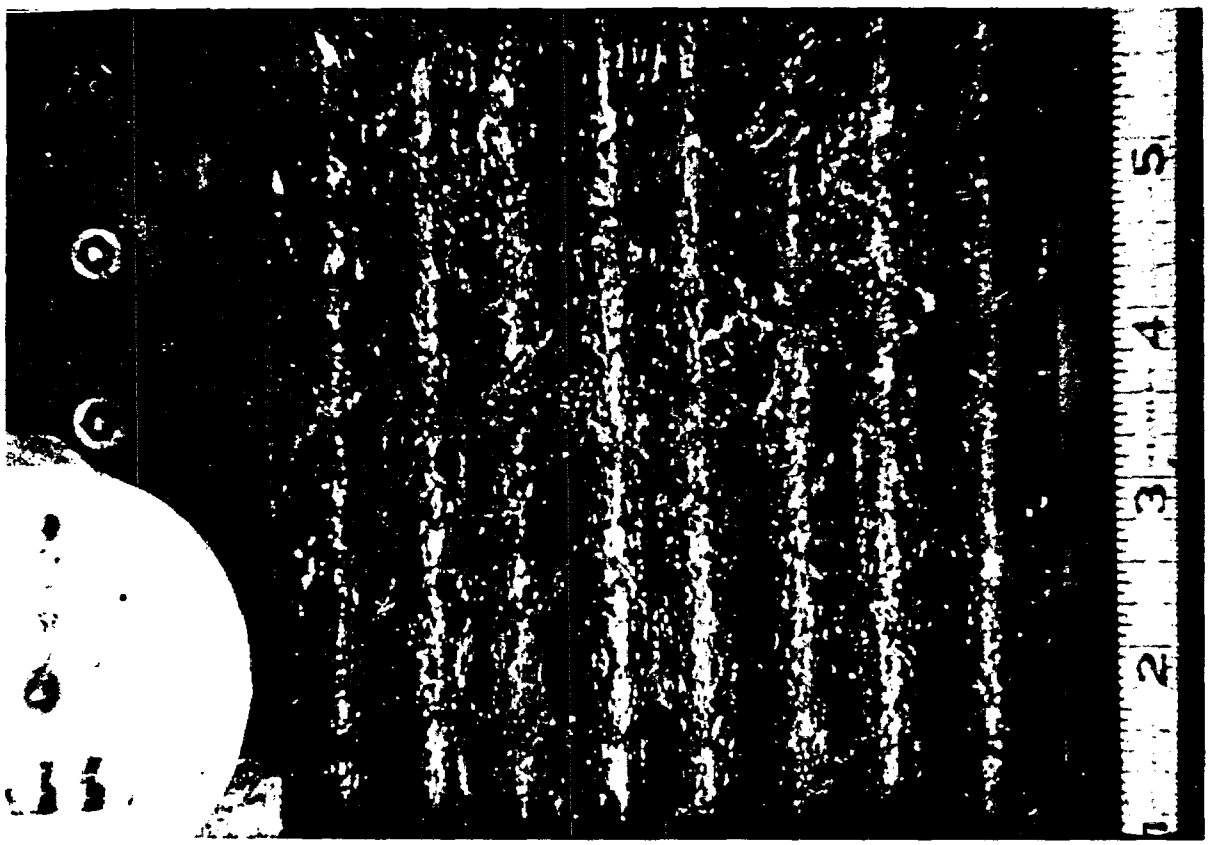

RUN	4442
TIME	50 SEC AFTER FLOOD
ELEVATION	6 FT
INITIAL CLAD TEMPERATURE	1813°F
FLOODING RATE	5.8 IN/SEC
COOLANT TEMPERATURE	154°F
PRESSURE	59 PSIA
PEAK POWER	1.24 KW/FT

Figure 3-48. Transition Flow Regime, Later Part

what would be interpreted, in light of PWR FLECHT experience, as transition flow just below the dispersed flow regime, which was clearly visible. The annular, or stable film boiling regime, on the other hand, cannot be discerned in the figures. The transition boiling regime is also not readily identifiable, although it is well known to exist above the nucleate boiling regime.

An unstable transition flow regime must exist between the vapor continuum (dispersed flow regime) and the liquid continuum (stable film boiling regime). The interface between these two stable continua persisted at a given elevation for a length of time which increased with elevation. Since the FHUST test section was only 2-1/2 feet high, the time in transition flow may have been quite short.

3.3.1.2 Heat Transfer and Flow Regimes

Plots of heat transfer coefficient versus time after flood for several elevations are presented in Figure 3-49. These curves were used as a model in relating the flow regimes described above to heat transfer behavior, since in this case movie and thermocouple data were available at the same elevation. From this comparison it was determined that, as a general rule, the first peak of the heat transfer coefficient curve corresponded to the start of the transition flow regime (end of dispersed flow) and the last valley corresponded to the start of the film boiling regime (end of transition flow regime). The times selected accordingly are shown in Figure 3-49, where the points on the heat transfer coefficient curves have been connected by lines representing the boundaries between the heat transfer regimes indicated. Although not indicated on Figure 3-49, the start of the dispersed flow regime (end of steam flow) was interpreted to be the point at which the heat transfer coefficient first began to rise rapidly and the quench point was taken as the time at which the heat transfer coefficient exceeded 100.

A comparison of the location of the FLECHT flow regime boundaries as seen in the movies and inferred from the plots of heat transfer coefficient behavior is shown in Figure 3-50. It should be noted that boundaries between the flow regimes were often not sharply defined in the movies. Furthermore, the heat transfer coefficient curves were obtained from an instrumented rod at the

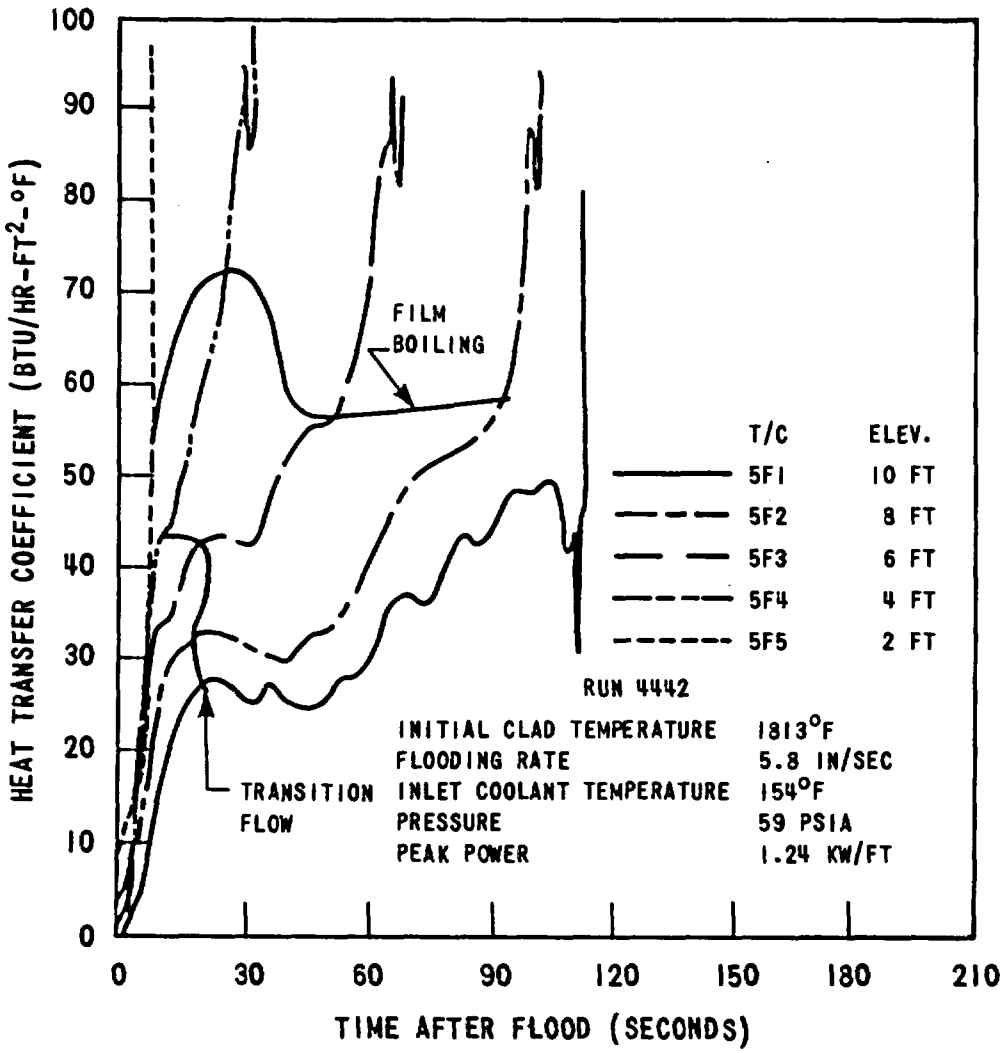

Figure 3-49. Heat Transfer Coefficients at Several Elevations for Run 4442

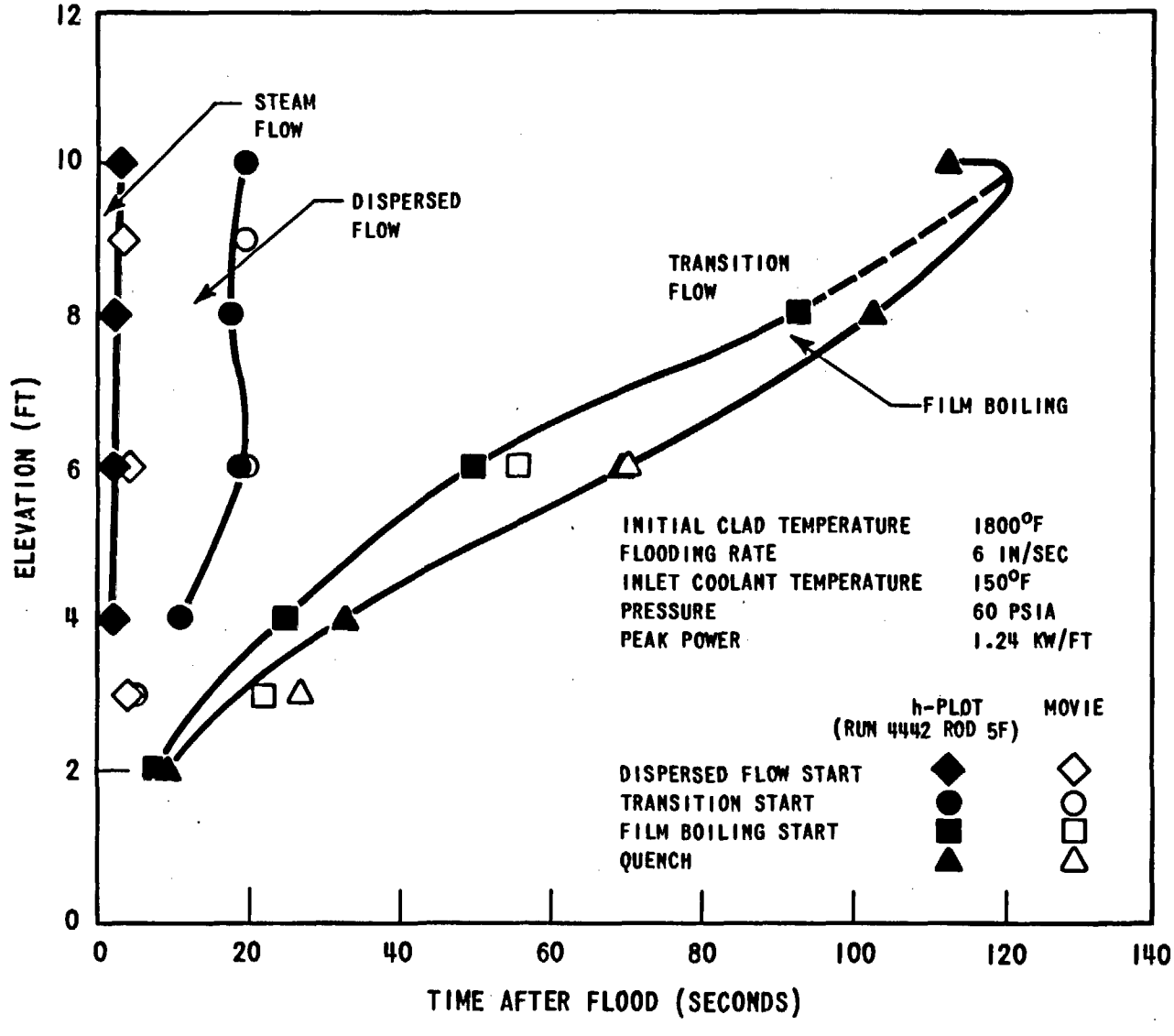

Figure 3-50. Comparison of Heat Transfer and Flow Regimes for FLECHT Runs 3642, 4442 and 5642

center of the bundle while the movies recorded behavior at the outer edge. The general agreement displayed in Figure 3-50 is, therefore, considered to indicate a one-to-one correspondence between the heat transfer regimes of the heat transfer coefficient curves and the flow regimes observed in the movies.

3.3.2 Constant Flooding Rate Heat Transfer Correlations

For empirical correlation purposes, FLECHT heat transfer coefficient behavior at a given elevation prior to quench can be divided into three periods as shown in Figure 3-51. These periods approximately correspond to different flow regimes as observed in the high speed movies. For example; Period I corresponds to the steam and dispersed flow regimes, Period II corresponds to the transition flow regime and Period III corresponds to the film boiling regime. The heat transfer coefficient, h, was correlated as follows for each period.

Period I. $0 < t/t_{q6ft} < (t/t_{q6ft})_2$

$$h = h_1 + [h_{12} - h_1]\,[(1 - e^{-x}) - 0.9xe^{-x^2}]\,[1 - 1.583\,e^{-0.0625V_{in}^2}\,ue^{-u}\,\exp\{-(0.588Z - 3.824)^2\}]$$

where:

t = time after flood in seconds

$$t_{q6ft} = 87.54\,[e^{-0.0107\Delta T_{sub}}\,(1 - e^{-.667V_{in}}) + 3.44\,V_{in}^{-1.205} - 16.75\,e^{-2.5V_{in}}]\,[1 + 0.0000588\,T_{init}]\,[1 + .91\,e^{-0.0345P}]\,Q'^{\,0.544}_{max}$$

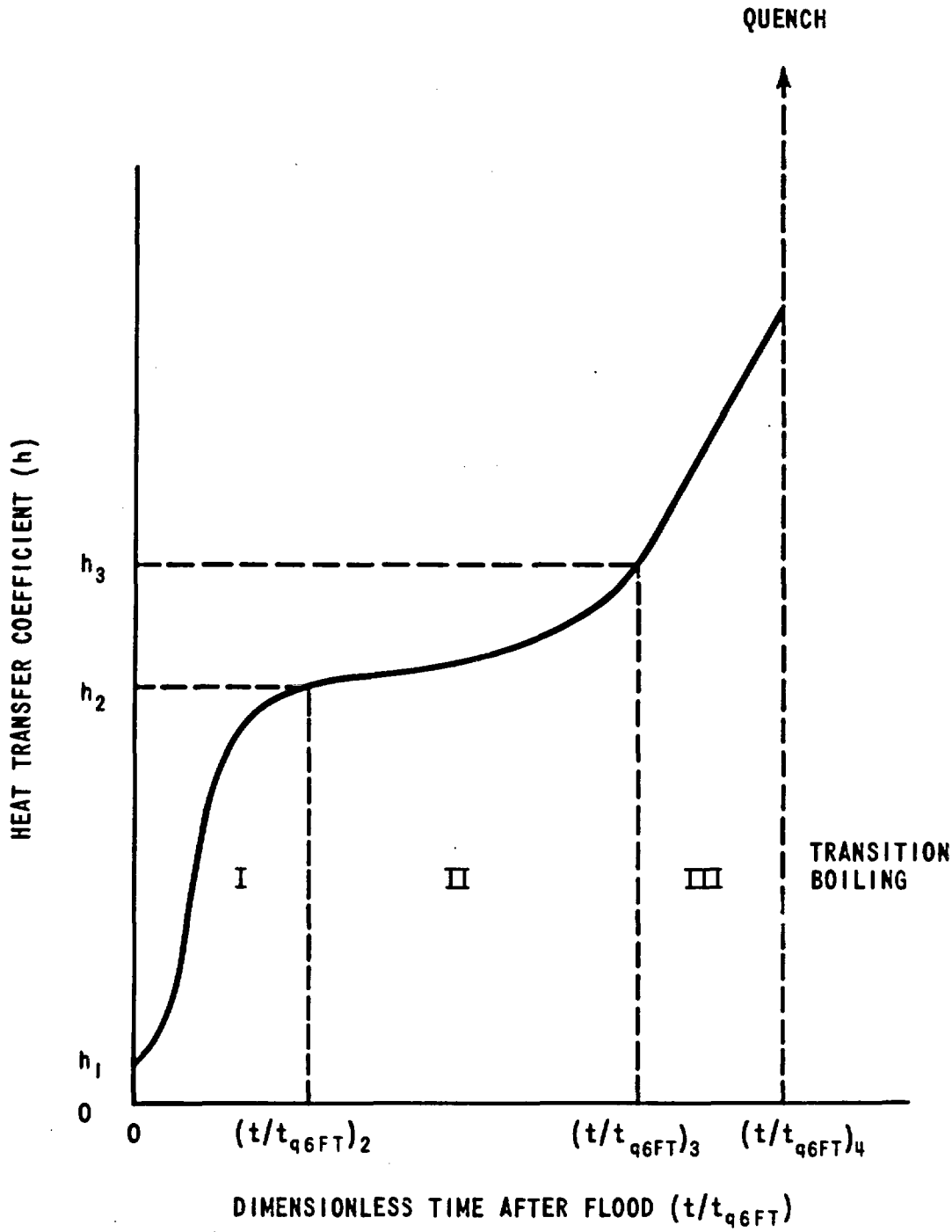

Figure 3-51. Schematic Diagram of FLECHT Heat Transfer Coefficient versus Dimensionless Time

$$(t/t_{q6ft})_2 = 0.62\ [(1 - e^{-0.192Z}) - 0.115Ze^{-0.0368Z^2}]$$

h_1 = the initial heat transfer coefficient (taken as 4 Btu/hr ft^2- ^oF*)

$$h_{12} = h_1 + [35.7 + (22 - 0.00303Z^{4.1})\ (1 - e^{-0.0333P} - 0.3Pe^{-0.011P^2})]\ [1 - e^{-0.2V_{in}}] + 8\ [1 - e^{-V_{in}/0.5}]\ [1 - e^{-B/25}],$$

$$x = 17.6\ [1 + 4.37e^{-.0166\Delta T_{sub}}]\ [1 - \exp\{-(.00075 + .0000272\ (V_{in}-8)^2)\ (T_{init} - 650)\}]\ (t/t_{q6ft})$$

$$u = 9\ (t/t_{q6ft})^2 \Big/ (t/t_{q6ft})_2^2$$

Period II. $(t/t_{q6ft})_2 < t/t_{q6ft} < (t/t_{q6ft})_3$

$$h = h_2 + b_1\ [y^2 + b_2\ (y^2 - b_3y^3)]$$

where:

$$(t/t_{q6ft})_3 = 1.55\ [(1 - e^{-0.205Z}) - 0.154Z\ e^{-0.0421Z^2}]$$

*The initial heat transfer coefficient h_1 should be a function of T_{init} and P. Examination of the data showed a scatter in h_1 from 1 to 8 Btu/hr-ft^2-^oF with no consistent parameter trends. Therefore a mean value of h_1 (4 Btu/hr-ft^2-^oF) was specified.

$$h_2 = h_1 + [h_{12} - h_1]\ [1 - e^{-x_2}) - 0.9\ x_2\ e^{-x_2^2}\ ]$$

$$x_2 = 17.6\ [1 + 4.37e^{-0.0166\Delta T_{sub}}]\ [1 - \exp\{-(0.00075$$

$$+ 0.0000272\ (V_{in} - 8)^2)\ (T_{init} - 650)\}]\ (t/t_{q6ft})_2$$

$$b_1 = [682 - 650\ (1 - e^{4-Z})]\ [1 - \exp\{-0.95\ (1 - 0.0488Z)\ V_{in}\}]\ [1$$

$$- \exp\ \{-0.0238\Delta T_{sub}\}]\ [0.696 + 0.304e^{-B/25}]$$

$$y = (t/t_{q6ft}) - (t/t_{q6ft})_2$$

$$b_2 = 0.5Z\ [1 - e^{-2(Z-3.5)}]\ [1.33\ (1 - e^{-0.0227P}) - 1]$$

$$-2.9\ [1 - e^{-V_{in}/2.5}]\ [1 - e^{-B/25}]$$

$$b_3 = 2.55\ [Z - 3.7]^2\ e^{3.7-Z}$$

Period III. $t/t_{q6ft} > (t/t_{q6ft})_3$

$$h = h_3 + C\ [t/t_{q6ft} - (t/t_{q6ft})_3]$$

where:

$$h_3 = h_2 + b_1\ [y_3^2 + b_2\ (y_3^2 - b_3 y_3^3)]$$

$$C = 420\ [1 - e^{-0.00625b_1}]$$

$$y_3 = (t/t_{q6ft})_3 - (t/t_{q6ft})_2$$

The previous correlations are valid over the following ranges of parameters:

Flooding rate (V_{in})	0.8 - 10 in./sec
System pressure (P)	15 - 90 psia
Inlet coolant subcooling (ΔT_{sub})	16 - 189°F
Initial clad temperature (T_{init})	1200 - 2200°F
Peak power density (Q'_{max})	0.69 - 1.40 kw/ft
Elevation (Z)	4 - 8 ft
Percent Blockage (B)	0 - 75%

The above correlations are also valid for the 10 ft elevation for those cases in which the quench at the 10 ft elevation occurred after the 8 ft elevation quench.

It should be noted that not all possible combinations of the above parameters were covered by the data and predictions for untested parameter combinations should be made with caution. In particular, it was found that heat transfer behavior for cases with flow blockage was quite dependent on the geometry of the blockage tested. The blockage terms included in the above correlations are based on the Group I flow blockage geometries described in Section 3.2.5.

Figures 3-52 through 54 compare measured and predicted heat transfer coefficients at the 6 ft elevation for different flooding rates, pressures, and elevations, respectively. Since the measured heat transfer coefficient oscillated with time while the predicted values follow a smooth curve, it was more reasonable to compare the time integral of the heat transfer coefficient than the instantaneous values. The time integrals of the measured and predicted heat transfer coefficient in the three periods shown in Figure 3-51 were defined as follows:

	Period I	Period II	Period III
Measured:	$\int_{o}^{\tau_2} h_m \, d\tau$	$\int_{\tau_2}^{\tau_3} h_m \, d\tau$	$\int_{\tau_3}^{\tau_4} h_m \, d\tau$
Predicted:	$\int_{o}^{\tau_2} h_p \, d\tau$	$\int_{\tau_2}^{\tau_3} h_p \, d\tau$	$\int_{\tau_3}^{\tau_4} h_p \, d\tau$

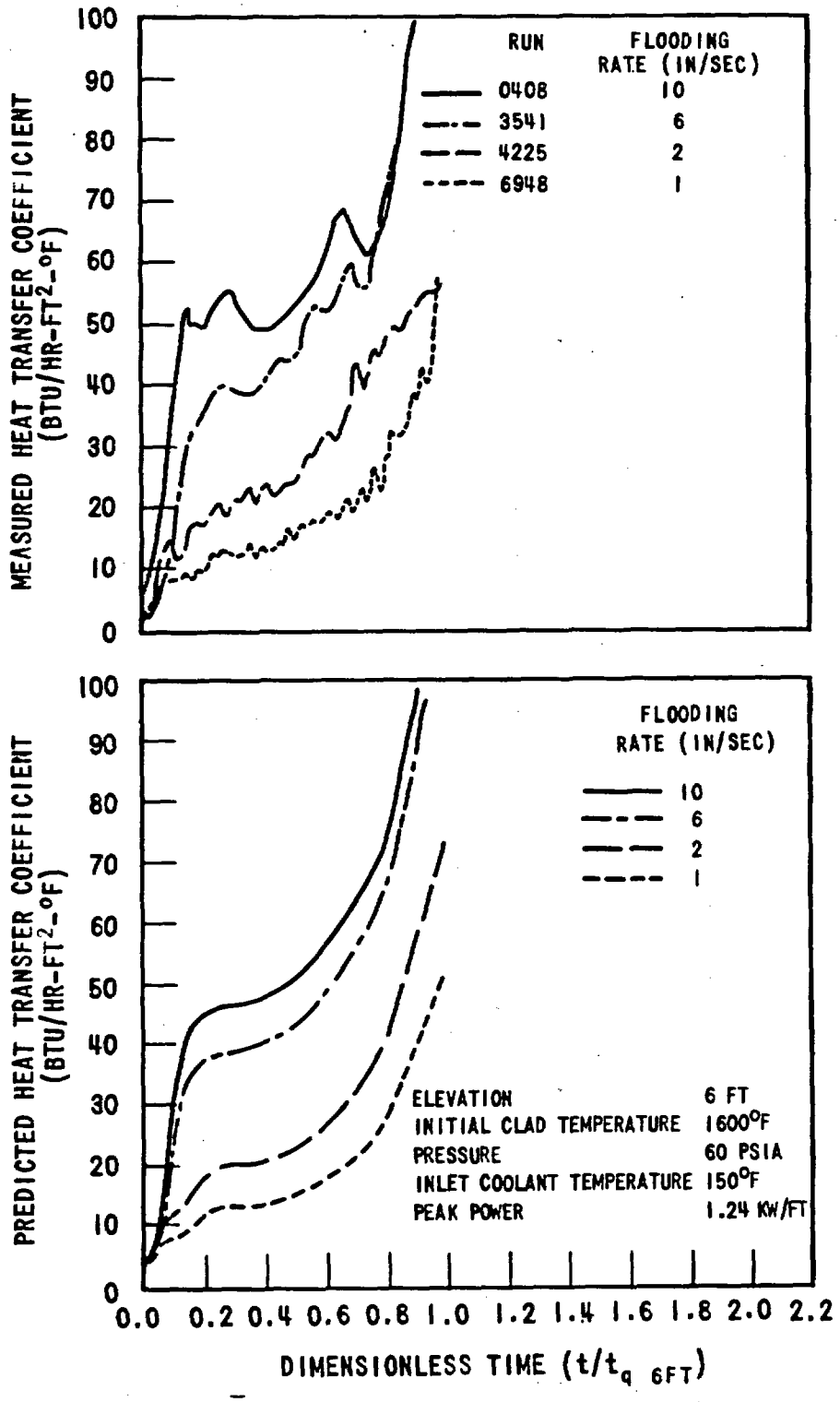

Figure 3-52. The Effect of Flooding Rate on Measured and Predicted Heat Transfer Coefficients

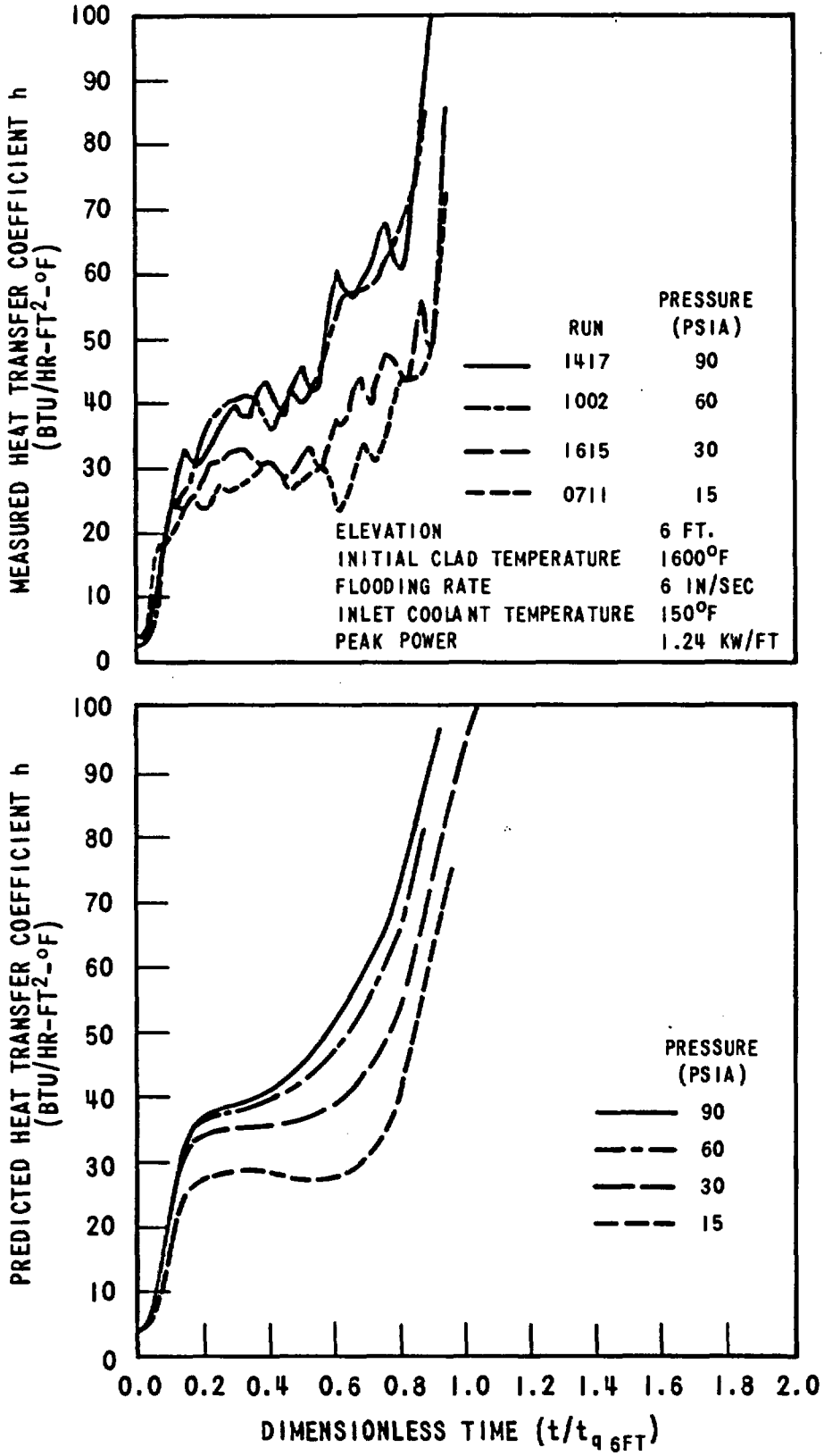

Figure 3-53. The Effect of Pressure on Measured and Predicted Heat Transfer Coefficients

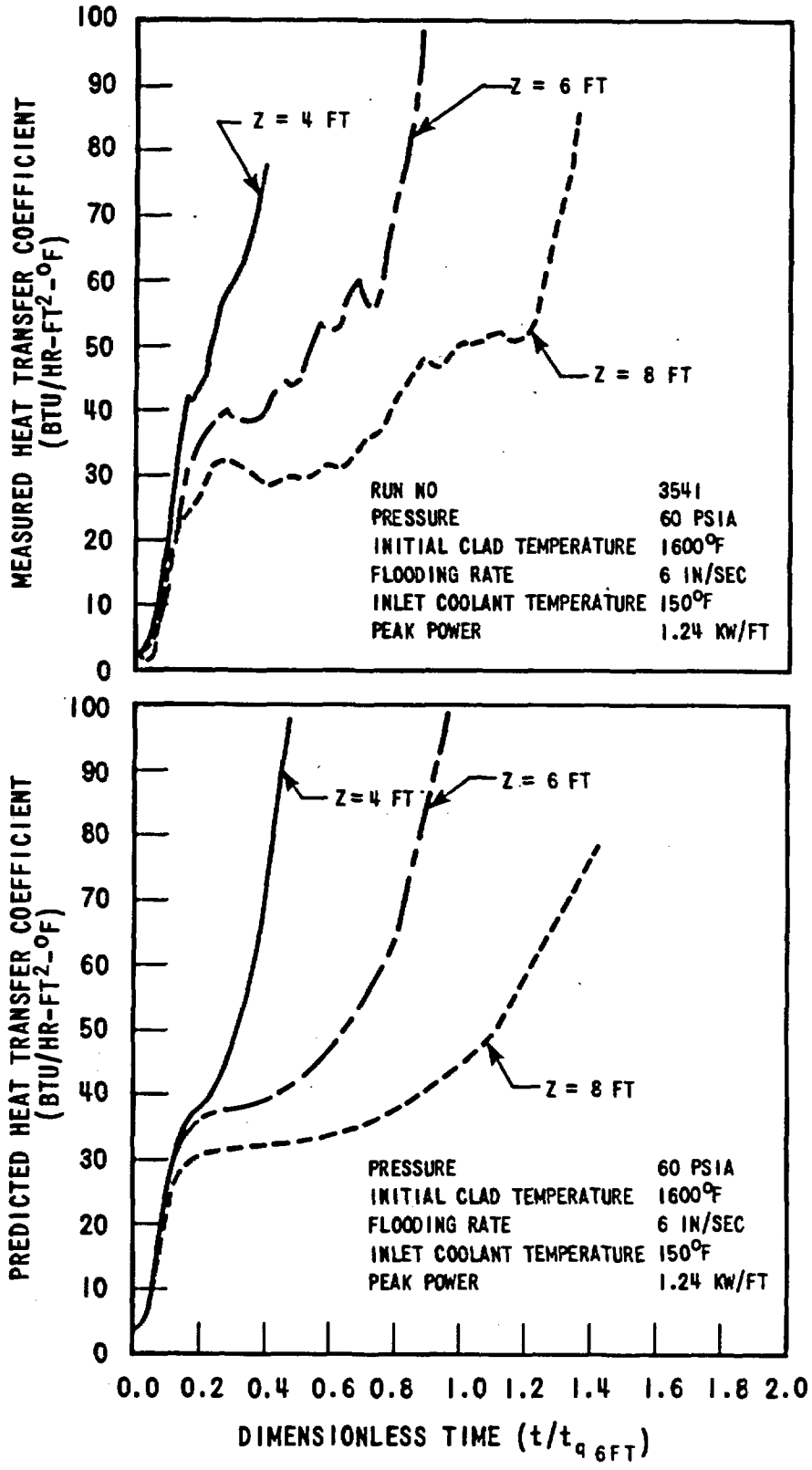

Figure 3-54. The Effect of Elevation on Measured and Predicted Heat Transfer Coefficient

where h_m is the measured heat transfer coefficient, h_p is the predicted heat transfer coefficient, τ is the dimensionless time t/t_{q6ft}, and τ_2, τ_3 and τ_4 are computed from the following equations:

$$\tau_2 \equiv (t/t_{q6ft})_2 = 0.62\ [(1 - e^{-0.192Z}) - 0.115Z\ e^{-0.0368Z^2}]$$

$$\tau_3 \equiv (t/t_{q6ft})_3 = 1.55\ [(1 - e^{-0.205Z}) - 0.154Z\ e^{-0.0421Z^2}]$$

$$\tau_4 \equiv (t/t_{q6ft})_4 = 0.38 \quad \text{for 4 ft elevation}$$
$$= 0.9 \quad \text{for 6 ft elevation}$$
$$= 1.2 \quad \text{for 8 ft elevation}$$

where Z is the elevation (ft).

The results of the comparison of the time integrals of measured and predicted integrated midplane heat transfer coefficients for over forty typical runs are plotted in Figure 3-55. It is seen that the correlation is capable of predicting the data within about $\pm$ 10 percent. The largest deviations appeared in Period I, where the comparison is very sensitive to the exact time due to the rapid rate of change of h with time.

3.3.3 Variable Flooding Rate Correlations

Heat transfer coefficients from variable flooding rate runs such as those shown in Figure 3-26 were also correlated using the equations given in the preceding Section (3.3.2). Consistent with expectations, the first part of a variable flooding rate test having a high initial flooding rate, V_{inH}, followed by a step reduction to a lower flooding rate, V_{inL}, was identical with the constant flooding rate test having the same run conditions and a flooding rate equal to V_{inH}. Thus the constant flooding rate heat transfer coefficient

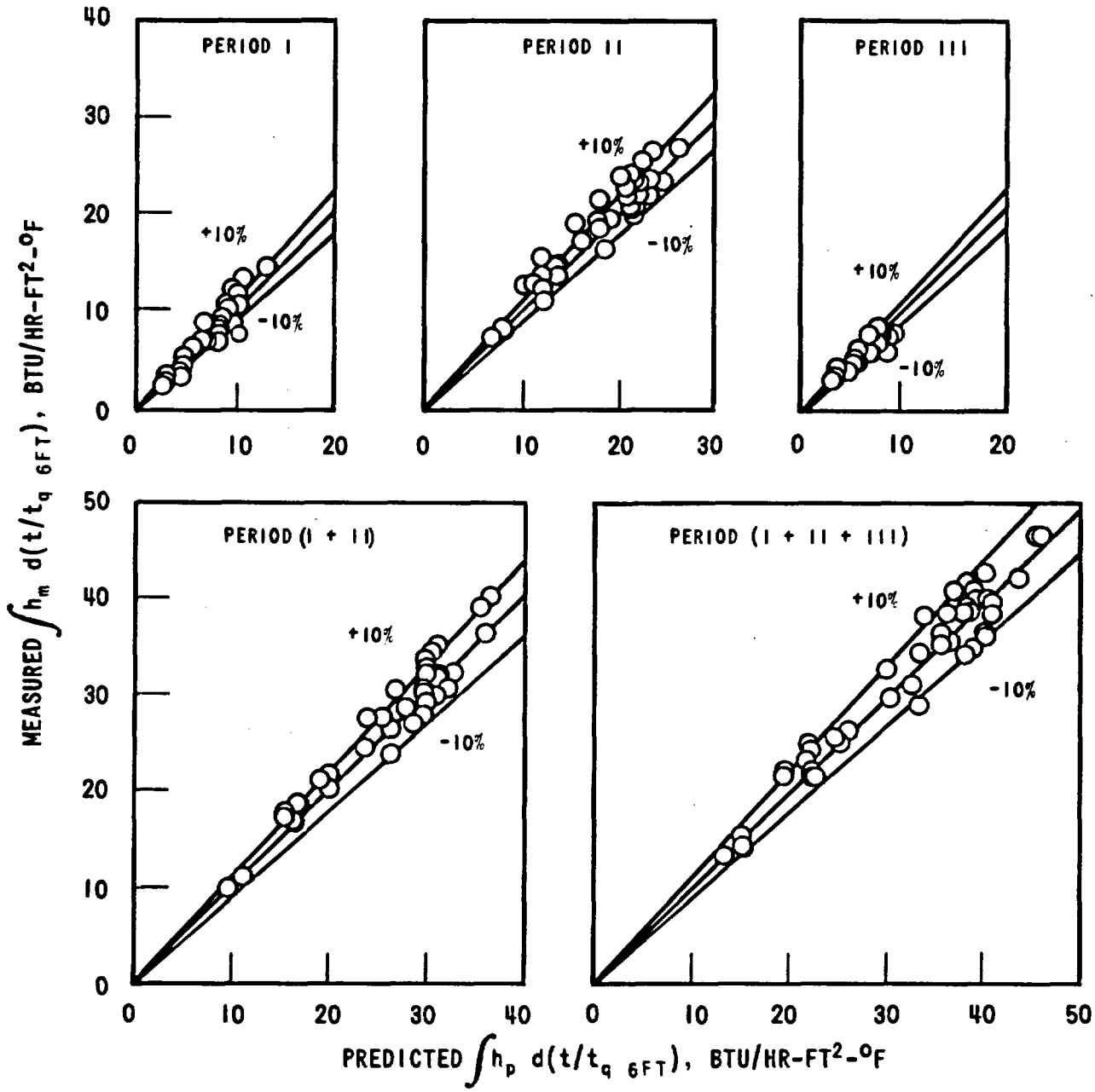

Figure 3-55. Comparison Between Measured and Predicted Integrated Midplane Heat Transfer Coefficients

equations given in Section 3.3.2 were used directly to correlate variable flooding rate test behavior from the start of the test up to the time that the flooding rate drops to V_{inL} ($t = t_v$).

Although actual test flooding rates dropped from the high to the low flooding rate within approximately one second, the drop in heat transfer coefficient to that representative of the lower flooding rate was more gradual. Examination of the test data indicated that the rate of decrease of the heat transfer coefficient after the "step" reduction in flooding rate at $t = t_v$ was approximately equal to the rate of increase from the start of flood, $t = 0$, to the time that the peak heat transfer coefficient was obtained, usually at $t = t_v$. Hence the method used for $t > t_v$ was to draw a symmetrical curve about $t = t_v$, or about the peak h, until the heat transfer coefficient dropped to the value computed by the method discussed below for the low flooding rate part of the test.

Heat transfer coefficients during the low flooding rate portion of a variable flow run were correlated using the constant flooding rate equations by determining the corresponding time (t_c) in the comparable constant flooding rate run ($V_{in} = V_{inL}$) that accounted for the previous history in the variable flooding rate run. In other words, allowance was made for the fact that at t_v, more coolant had been injected into the bundle than would have been had the flooding rate been a constant V_{inL} from $t = 0$ to $t = t_v$. The magnitude at this time shift ($t_c - t_v$) was therefore a function of ξ, or the excess amount of water introduced into the bundle from $t = 0$ to $t = t_v$ as compared to a constant flooding rate run with $V_{in} = V_{inL}$.

$$\xi = \int_0^{t_v} (V_{inH} - V_{inL})/V_{inL} \, dt \qquad (1)$$

Figure 3-56 shows a schematic representation of the use of ξ to compare constant and variable flooding rate heat transfer coefficients. It can be seen that equating the magnitude of the time shift to ξ provided approximate but not exact agreement between the two runs. The ξ agreement was not exact because of the differences in "carryover" of entrained liquid and coolant efficiency during the high flooding rate portion of the variable flooding rate run as compared to the constant flooding rate run.

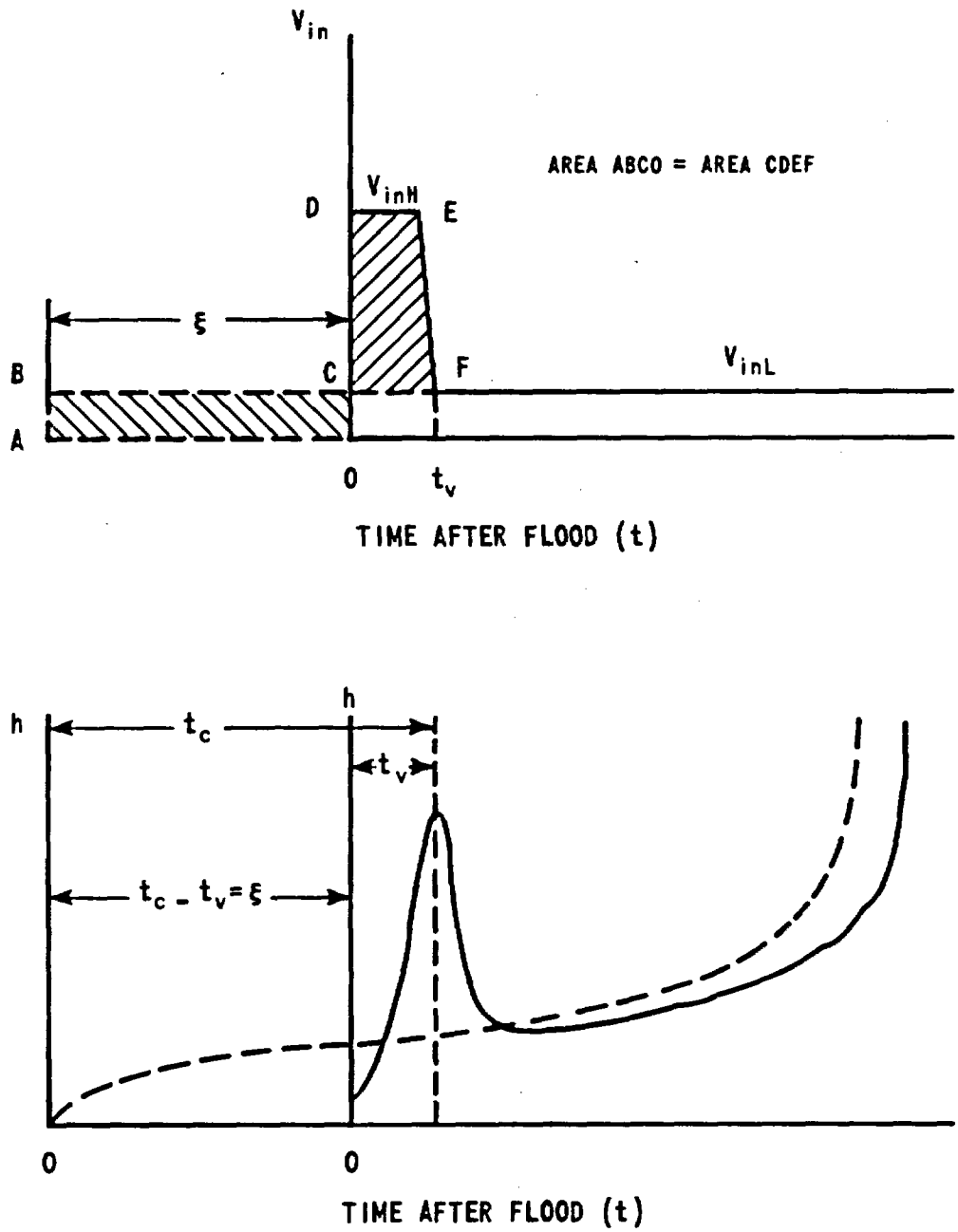

Figure 3-56. Schematic Representation of the Use of ξ to Compare Constant and Variable Flooding Rate Heat Transfer Coefficients

Examination of the variable flooding rate data along with limiting case considerations, which indicated that the maximum value of the time shift for a given elevation was the difference in quench times between two constant flooding rate runs with flooding rates equal to V_{inH} and V_{inL}, resulted in the following expression for the magnitude of the time shift. (See Appendix D for derivation.)

$$\Delta t_{vc} \equiv t_c - t_v = 224\ [1 - (1 + 0.01528\xi)\ \exp\{-0.01389\xi\}]$$

$$+ [2.2Z^{2.13} - 100]\ [1 - \exp\{-0.01416\xi\}$$

$$-0.1331\xi\ \exp\{-0.0002\xi^2\}] \qquad (2)$$

The variable Z is the elevation in feet (applicable for the 4, 6, and 8 ft elevations). Equation (2) applies when V_{inL} = 1 in/sec and t_v is small in comparison with the quench time of the constant flooding rate run with $V_{in} = V_{inH}$. Examples of the application of Equation (2) to compare variable and constant flooding rate heat transfer coefficients, with and without "fallback", are shown on Figures 3-33 through 36. Figure 3-57 shows that the method also produced good agreement between measured and predicted heat transfer coefficients.

As discussed in Appendix D, the magnitude of the time shift was expected to be slightly larger than that predicted by Equation (2) for cases where V_{inL} was greater than 1 in./sec or for flow blockages runs with V_{inL} = 1 in./sec. The following equation was therefore developed for use in such cases:

$$\Delta t_{vc} \equiv t_c - t_v = (0.214Z - 0.386)\ \xi$$

$$= (0.214Z - 0.386)\int_0^{t_v} (V_{inH} - V_{inL})/V_{inL}\ dt \qquad (3)$$

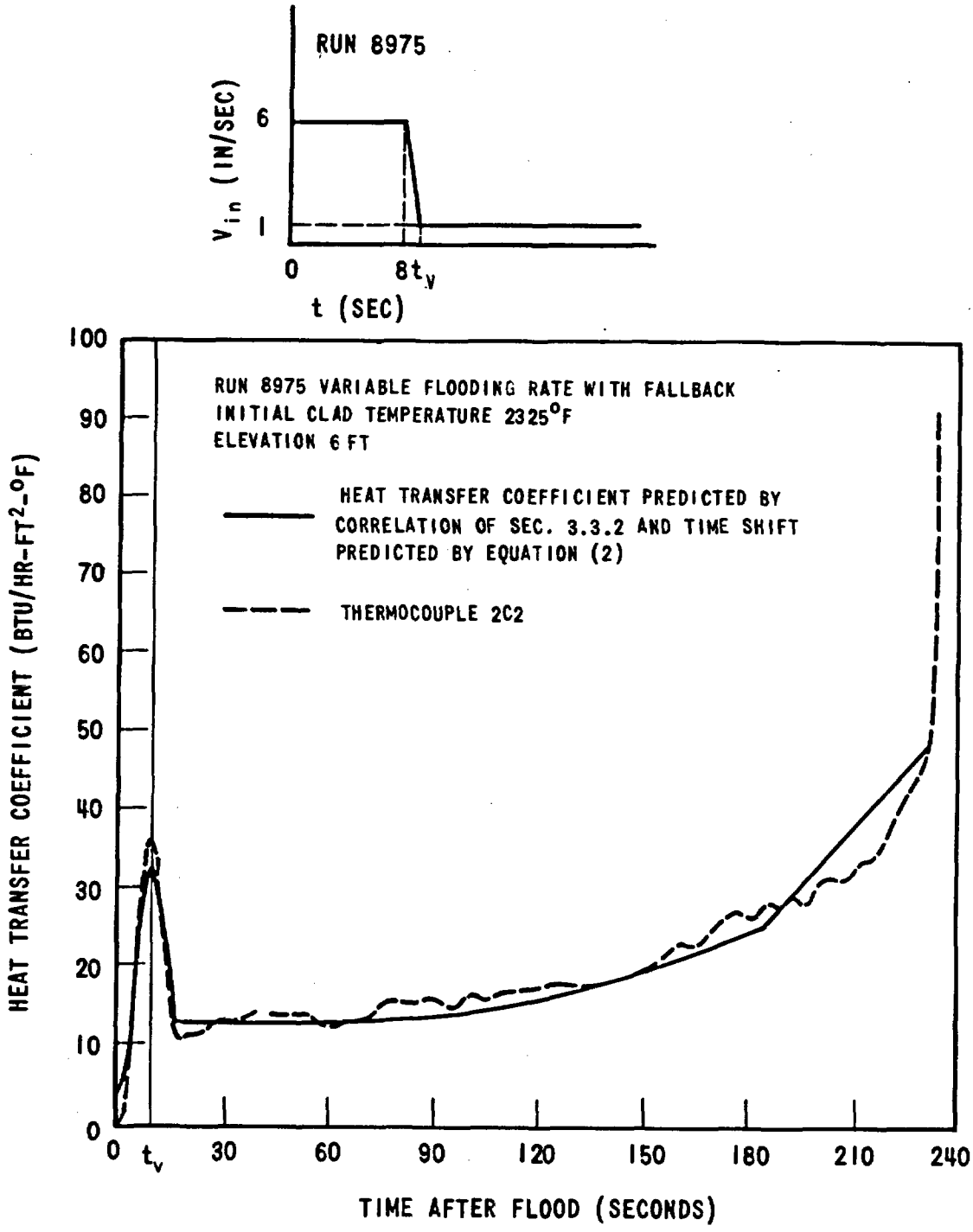

Figure 3-57. Comparison Between Measured and Predicted Heat Transfer Coefficients for a Variable Flooding Rate Run

Equation (3) is valid for small ξ as long as t_v is small in comparison with the quench time of the constant flow run with $V_{in} = V_{inH}$. An example of the application of this equation to compare constant and variable flow blockage test results is shown in Figure 3-42.

Note that the above techniques have been verified only for cases where the initial clad temperatures of the constant and variable flooding rate runs were not too far different, i.e., within approximately $\pm 200°F$.

In summary, variable flooding rate heat transfer coefficients were correlated as follows:

1. Compute the matching time (t_c) of the low flooding rate run from Equations (2) or (3) as appropriate.
2. Using the high flooding rate V_{inH} and the correlations of Section 3.3.2 compute the heat transfer coefficients from $t = 0$ to t_v.
3. Using the low flooding rate V_{inL} and the correlations of Section 3.3.2 compute the heat transfer coefficients from $t = t_v$ to quench. Shift the time scale to the left by ($t_c - t_v$) such that t_c in the constant flooding rate case corresponds to t_v in the variable flooding rate case.
4. Draw a curve from $t = t_v$ downward symmetrically with respect to the curve computed from step 2 and join the curve computed by step 3.

In cases where the flooding rate, V_{inH}, of the high flooding rate period was not constant (e.g. Curve A of Figure 3-26), step 2 of the above computational procedure was modified by inclusion of a time shift procedure similar to those discussed above.

First, a fictitious time, t_1'', was computed for each value of t_1 from t_0 to t_v, using the following equation:

$$t_1'' = t_1 + (0.214Z - 0.386) \int_0^{t_1} (V_{inH} - V_{inH_1})/V_{inH_1} \, dt.$$

where t_1 and V_{inH_1} are any combination of time and flooding rate from the variable flooding rate curve. The heat transfer coefficient at time t_1 was then obtained by substituting $t_1 = t_1''$ and $V_{in} = V_{inH_1}$ in the correlations of Section 3.3.2.

3.4 GROUP III ZIRCALOY CLAD TEST RESULTS

3.4.1 Test Results

The purpose of the Group III tests was to compare the heat transfer behavior of Zircaloy clad and stainless steel clad heater rods.

Four Zircaloy clad tests were performed, two of which were in the so-called "early" Group III test series. Test conditions and hot rod midplane transient temperature results for these four runs are shown in Table 3-3. Several materials and/or fabrication problems associated with the use of Zircaloy clad heater rods occurred in these tests. The influence of these problems on interpretation of the heat transfer results is discussed below.

3.4.1.1 "EARLY" Group III Tests - Runs 2443 and 2544

Runs 2443 and 2544 were conducted with a nominal initial temperature of 2000°F and flooding rates of 10 and 4 in./sec, respectively. In both cases the heater rods appeared to perform satisfactorily during heatup and temperature turnaround; however, the cooldown and particularly the quench behavior at the midplanes of the highest temperature rods were degraded. An example of "degraded" quench is shown in Appendix A, Figure A-2. The degraded temperature response was due to a gap which formed between the cladding and the boron nitride heater insulation (which contained the thermocouple junction). Formation of the gap was caused by internal gas pressure buildup resulting from reaction of impurities on the boron nitride and the increase in heater rod temperature. At elevated temperature the strength of Zircaloy 4 is relatively low and swelling can occur with only modest internal pressures. This problem was successfully avoided in later tests by outgassing the boron nitride prior to heater fabrication as discussed in Appendix A. As a result of the clad swelling some of the midplane heat transfer data obtained from the "early" Group III runs is considered unreliable.

3.4.1.2 Later Group III Tests - Runs 8874 and 9573

Run 8874 was performed with a nominal initial temperature of 2325°F and a flooding rate of 6 in./sec for eight seconds followed by a step reduction to 1 in./sec. Five heater elements failed during the test, at 9.6, 18.5, 19.3, 29.3 and 55.5 seconds after flood. Post-test examination revealed significant rod bowing at the bundle midplane and evidence of electrical arcing between the heater clad and resistance element on all failed rods. There was also evidence of arcing between failed heater rods and adjacent stainless steel guide tubes and of Zircaloy-stainless steel eutectic reactions. The eutectic may have been formed after arcing started. Possible causes of the initial failure were heater rod bowing, eutectic reaction, and the high temperatures imposed by the test conditions. Electrical arcing in the initially failed rod most likely caused the subsequent failures in adjacent heaters. Because of the number of heater element failures which occurred during this run, data beyond the first eighteen seconds should be used with caution.

Examination of the time-temperature history of Run 8874 indicated generally consistent and reliable behavior for all instrumented rods. However, heat transfer coefficients for the first ten seconds after flooding were higher than anticipated. For example, based on an average of seven inside rods, the peak heat transfer coefficient was approximately 36 percent higher than an equivalent stainless steel test. It is believed that this improvement in heat transfer behavior was due to hydrogen evolved by the Zircaloy-water reaction at the clad surface and differences in the material properties (e.g. wetability and emissivity) of Zircaloy and stainless steel. It is also possible that rod bowing and distortion may have caused a flow blockage effect, i.e., the heat transfer coefficient may have been improved by entrained droplet breakup and atomization in the distorted portion of the rod bundle.

The heat-up rate for Run 8874 was compared against the three other Group III tests and was found to be from 0 - 14 percent low at the midplane. Although the trend was not consistent within each power zone, the effect of an assumed reduction in peak power generation on calculated heat transfer coefficients was never-the-less investigated. It was found that a 10 percent reduction in peak power (1.116 as opposed to 1.24 kw/ft) reduced the peak heat transfer coefficient

by only about 2 Btu/hr-ft^2-°F, still leaving about a 31 percent difference between the peak Zircaloy and stainless steel heat transfer coefficients. The reduction in heat transfer coefficients during the latter part of the run (from about thirty seconds to quench) were also reduced by about 2 Btu/hr-ft^2-°F, but were still consistently greater than for the comparable stainless steel test.

The final PWR-FLECHT Zircaloy bundle test, Run 9573, was conducted with a nominal initial cladding temperature of 2000°F and a flooding rate of 1 in./sec. For this test, the stainless steel guide tubes were replaced with Zircaloy guide tubes and the freedom of the heater rods for vertical expansion was increased. Cladding temperatures were predicted to reach 2400°F after about 30 seconds, at which time heater element failures were expected to occur.

During the test, heater element failures started at 18.2 seconds; sixteen elements failed by 30 seconds and all but nine of the forty-two heater elements had failed when power was shut off at 55.5 seconds. At the time of the initial failures, midplane clad temperatures were in the range of 2200 - 2300°F. The only prior indication of excessive temperatures was provided by the 7 ft steam probe, which exceeded 2500°F at 16 seconds (2 seconds prior to start of heater element failure).

Post-test bundle inspection indicated a locally severe damage zone within approximately ±8 inches of a Zircaloy grid at the 7 ft elevation. The heater rod failures were apparently caused by localized temperatures in excess of 2500°F. Possible causes of the high temperatures include metal-water reaction of (a) the Zircaloy grid, (b) the Zircaloy steam probe or (c) a eutectic solution of the steam probe stainless steel and Zircaloy components. The remainder of the bundle was in excellent condition, however, and there was very little rod bowing compared to Run 8874.

Analysis of the test results showed that heat transfer coefficients for the first eighteen seconds were generally lower than for a comparable stainless steel test. However, the data from this period is suspect and has therefore not been considered in comparing stainless steel and Zircaloy heat

transfer behavior. In addition to the short time involved, anomalous (negative) heat transfer coefficients were observed at the bundle midplane for 5 of 14 thermocouples during this period. These may have been related to the high steam probe temperatures measured at the 7 ft elevation. Data beyond the first eighteen seconds was not valid due to the large number of heater rod failures.

It should be noted that the heater element failures which occurred in Runs 8874 and 9573 were not related to the behavior of reactor fuel during a loss-of-coolant accident. The failures referred to were failures of the heater rod internal electrical resistance element. Failure of this element resulted in either a loss of power to the heater rod or, more commonly, arcing from the resistance element to the clad. Aside from the regions in which heater rod failures took place, the clad was generally in excellent condition throughout the remainder of the bundles, including the peak temperature midplane regions. Additional information regarding the post-test condition of the cladding from all four Group III tests can be found in Appendix B.

3.4.2 Comparison to Stainless Steel Results

3.4.2.1 Comparison of Zircaloy and Stainless Steel Temperature Response

Figure 3-58 shows midplane temperature rise, turnaround time and quench time as a function of flooding rate for Zircaloy and stainless steel clad tests. The temperature rise and turnaround time were greater for the Zircaloy tests than the stainless steel tests. This was expected since the heat capacity of a Zircaloy clad rod was approximately 15 percent lower than that of a stainless steel clad rod. Also, the Zircaloy-water reaction provided an additional heat source at the rod surface, which contributed to the higher Zircaloy temperature rises. Quench times for the Zircaloy clad tests were shorter than the stainless steel tests. This was primarily due to the higher midplane quench temperatures and lower heat capacity of the Zircaloy clad rods.

Quench temperatures for comparable Zircaloy and stainless steel clad tests which were determined using the methods described in Appendix E are shown in Figure 3-59. Recognizing that the shape of the curves plotted should not be

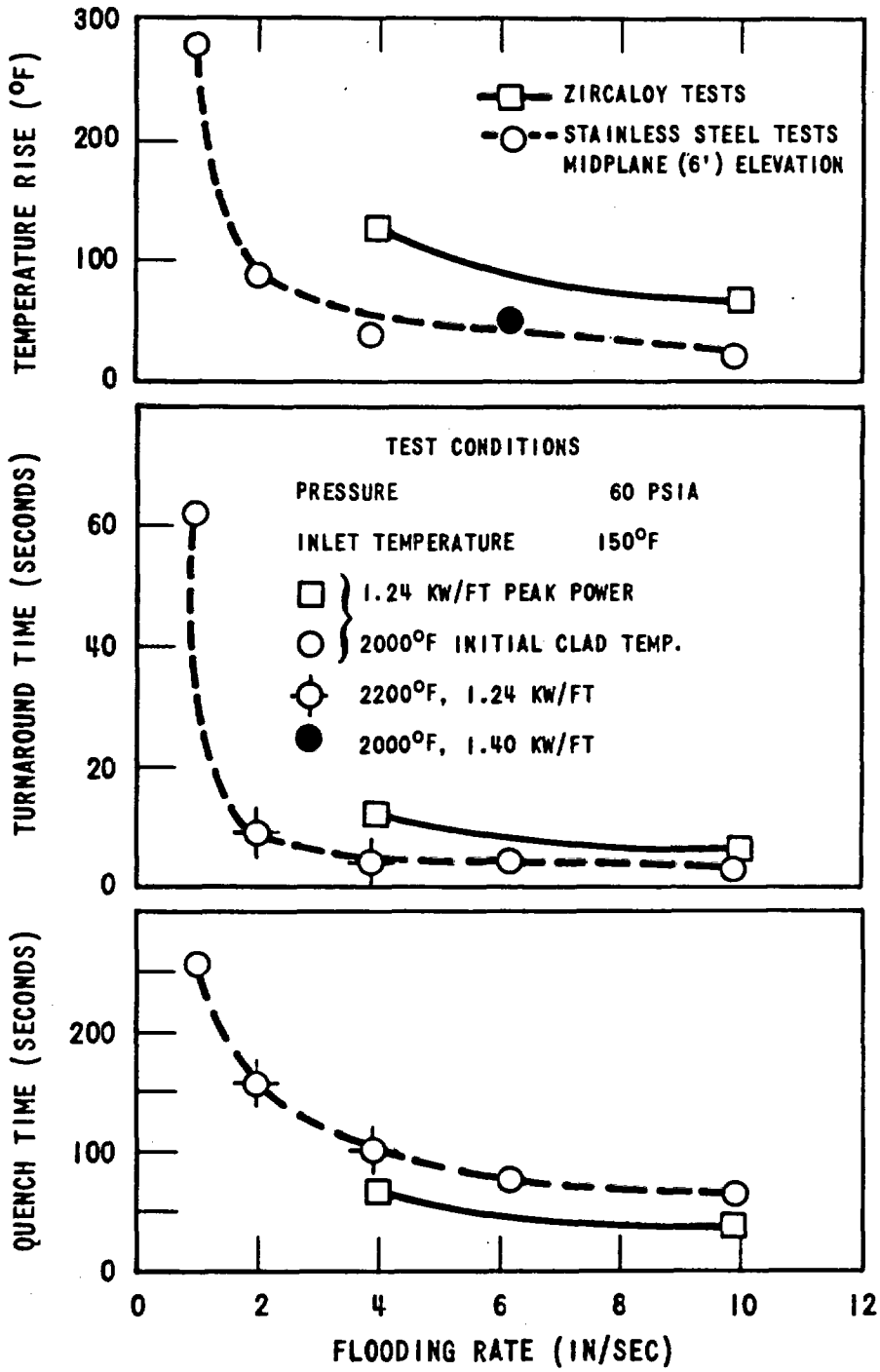

Figure 3-58. Comparison of Zircaloy and Stainless Steel Clad Temperature Response

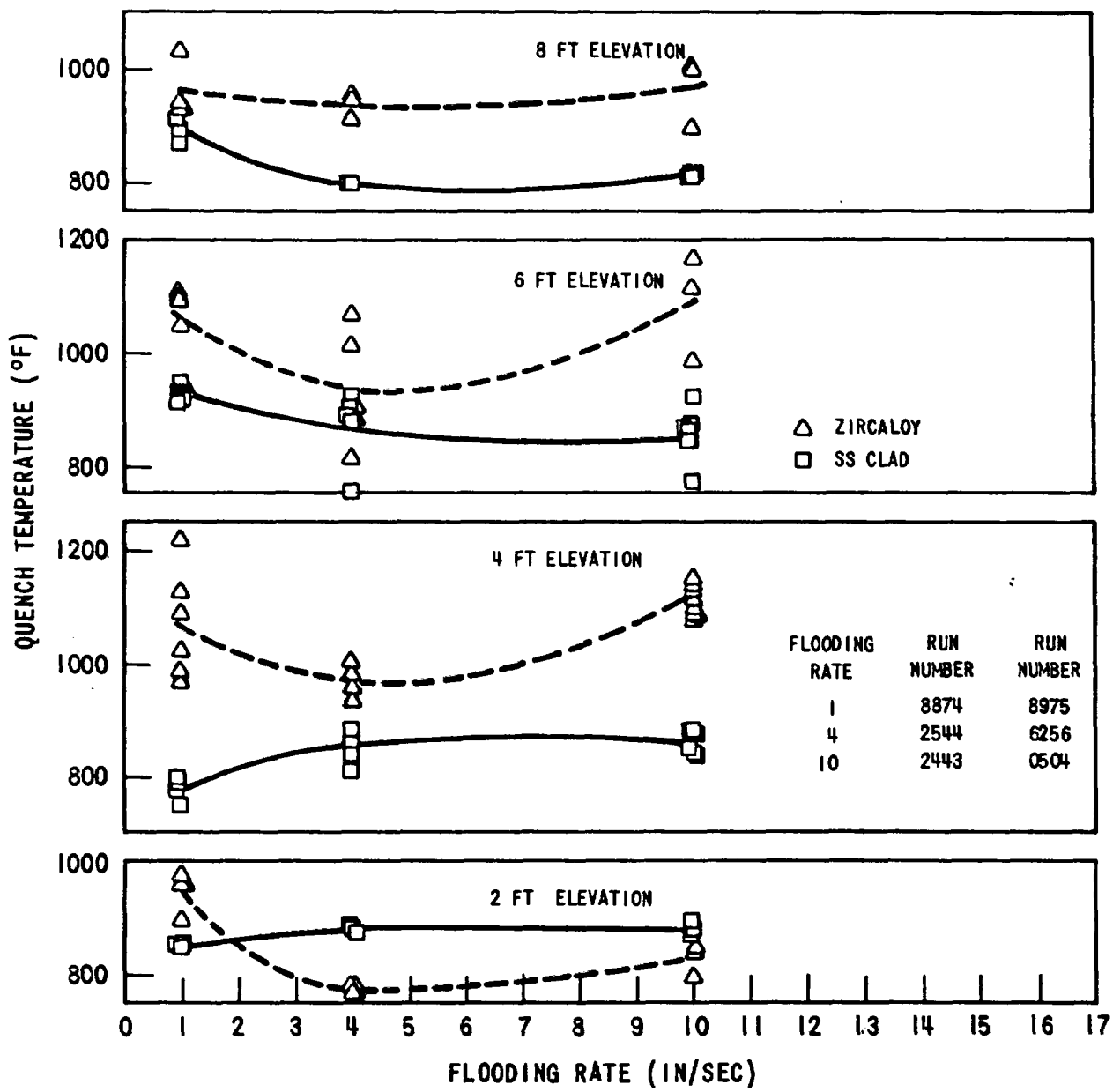

Figure 3-59. Comparison of the Quench Temperature Between Zircaloy and Stainless Steel Clad

taken too literally, the data shows that the quench temperature of the Zircaloy clad was consistently higher than that of the stainless steel by about 100°F to 200°F at the 4, 6, and 8 ft elevations. For the 2 ft elevation, however, the reverse was true for flooding rates above 2 in./sec.

Plum reported in Reference 9 that the quench temperature of Zircaloy clad is about 800°F and is slightly lower than that of stainless steel. This discrepancy with the data shown in Figure 3-59 may be explained by differences in the peak temperatures for the two sets of experiments. The peak temperature in Plum's experiments was 1800°F, while in the present tests the peak temperatures were all above 2000°F. It appears that the greater amount of oxide formed at the higher temperatures increases the quench temperature. Since the peak temperatures at the 2 ft elevation did not exceed 1800°F this would also explain the low Zircaloy quench temperatures at the 2 ft elevation in the present tests.

Table 3-8 compares the hot rod midplane temperature behavior of a Zircaloy variable flooding rate run with an equivalent stainless steel test. This data is consistent with the constant flooding rate data. The temperature rise in the high and low flooding rate portions of the runs were larger for the Zircaloy run. The Zircaloy case cooled down to a lower T_{min}, however, due to the lower heat capacity and higher heat transfer coefficient. Also, the quench time was shorter in the Zircaloy bundle for the reasons discussed above.

3.4.2.2 Comparison of Zircaloy and Stainless Steel Heat Transfer Coefficients

Comparisons of Zircaloy and stainless steel heat transfer coefficients are shown in Figures 3-60 through 62. In general, the Zircaloy heat transfer coefficients appeared to be somewhat greater than the stainless steel coefficients. This difference may be related in part to the differences in Zircaloy and stainless steel quench behavior discussed in Section 3.4.2.1 and as shown in Figures 3-63 through 3-65.

TABLE 3-8

COMPARISON OF ZIRCALOY AND STAINLESS STEEL CLAD
VARIABLE FLOODING RATE TEST RESULTS

Run No.	T_{init} (°F)	T_{max} (°F)	$\Delta T_{rise\ 1}$ (°F)	$t_{turn\ 1}$ (sec)	T_{min} (°F)	t_{min} (sec)	$T_{max\ 2}$ (°F)	$\Delta T_{rise\ 2}$ (°F)	$t_{turn\ 2}$ (sec)	t_{quench} (sec)
8874(Zirc)	2297	2360	63	4	2060	12	2147	87	40	204
8975(SS)	2301	2346	45	4	2181	13	2250	69	36	249

Test Conditions: Flooding Rate - 6 (8 sec) - 1 in/sec; Inlet Coolant Temp - 150°F, Pressure - 60 psia, Peak Power - 1.24 kw/ft

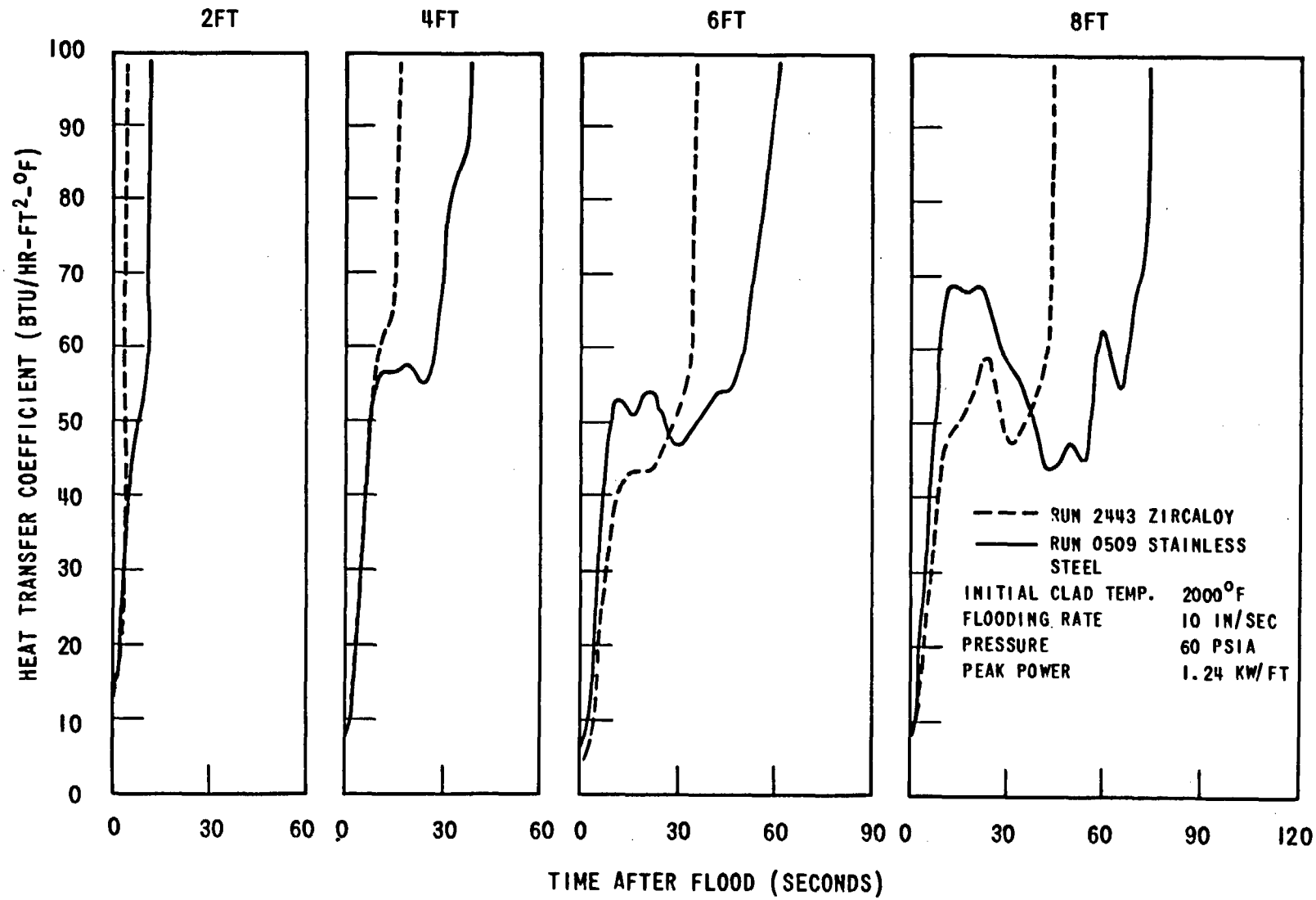

Figure 3-60. Comparison of Zircaloy and Stainless Steel Clad Heat Transfer Coefficients at 10 In/Sec

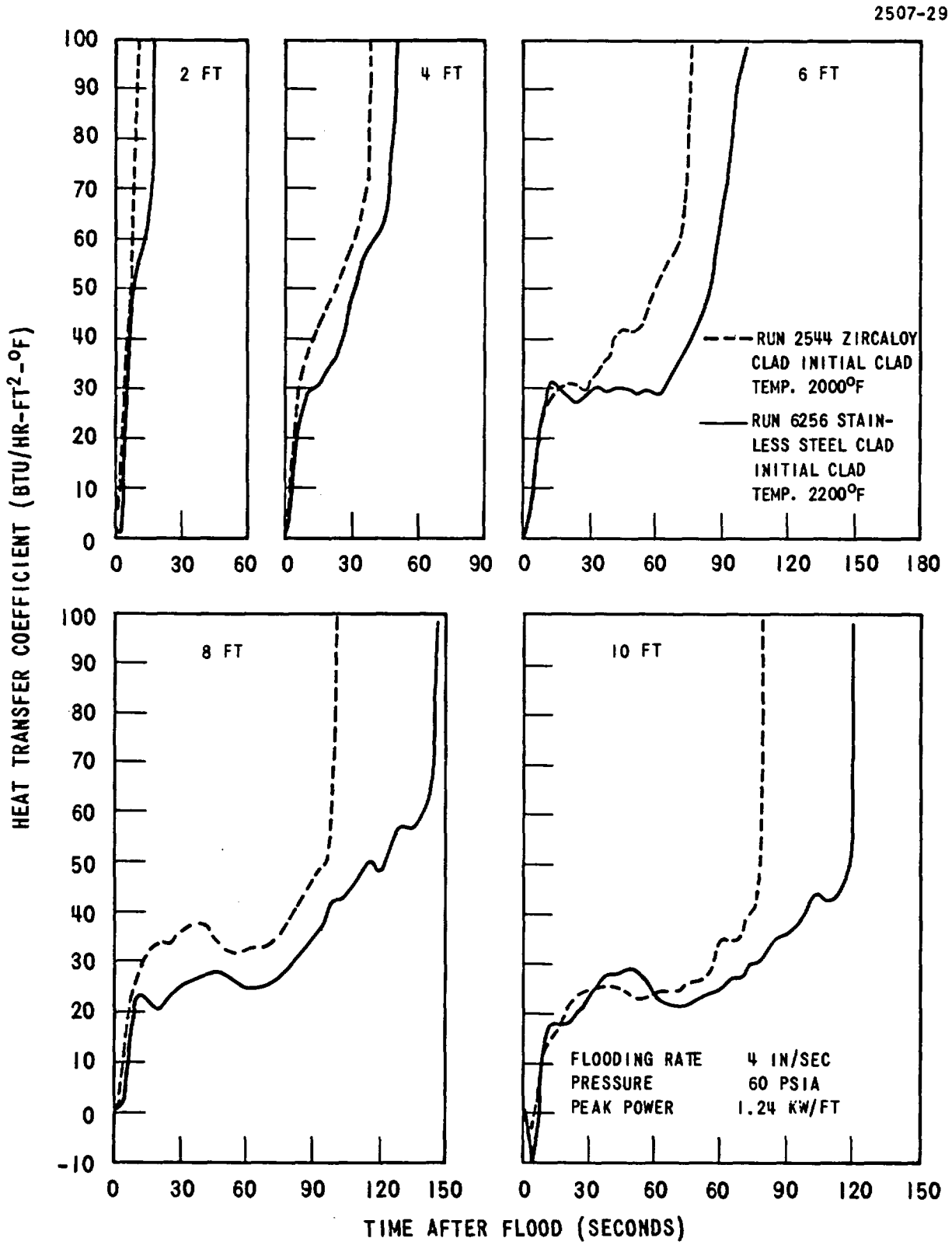

Figure 3-61. Comparison of Zircaloy and Stainless Steel Clad Heat Transfer Coefficients at 4 In/Sec

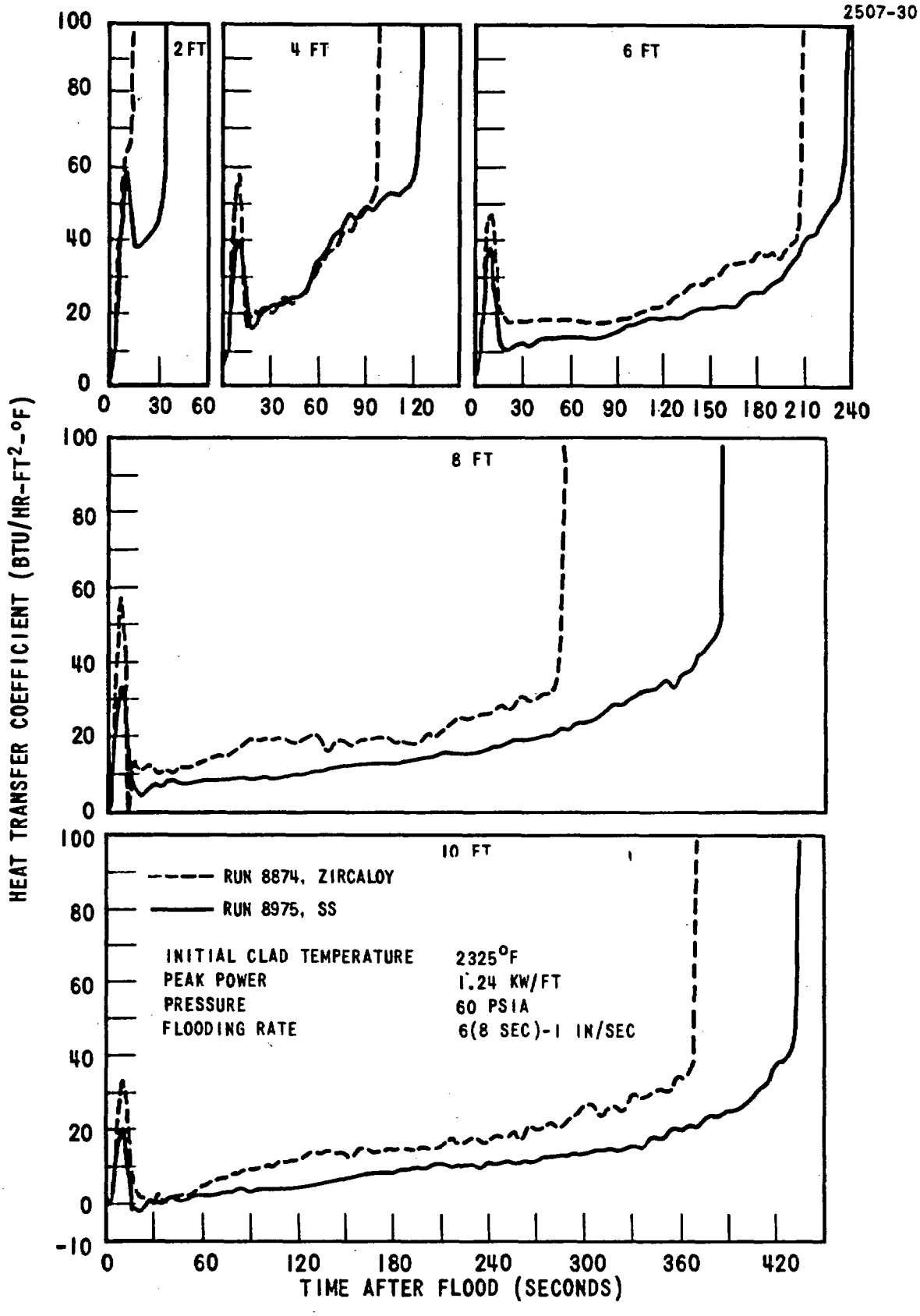

Figure 3-62. Comparison of Zircaloy and Stainless Steel Heat Transfer Coefficients at 6 (8 Sec)-1 In/Sec)

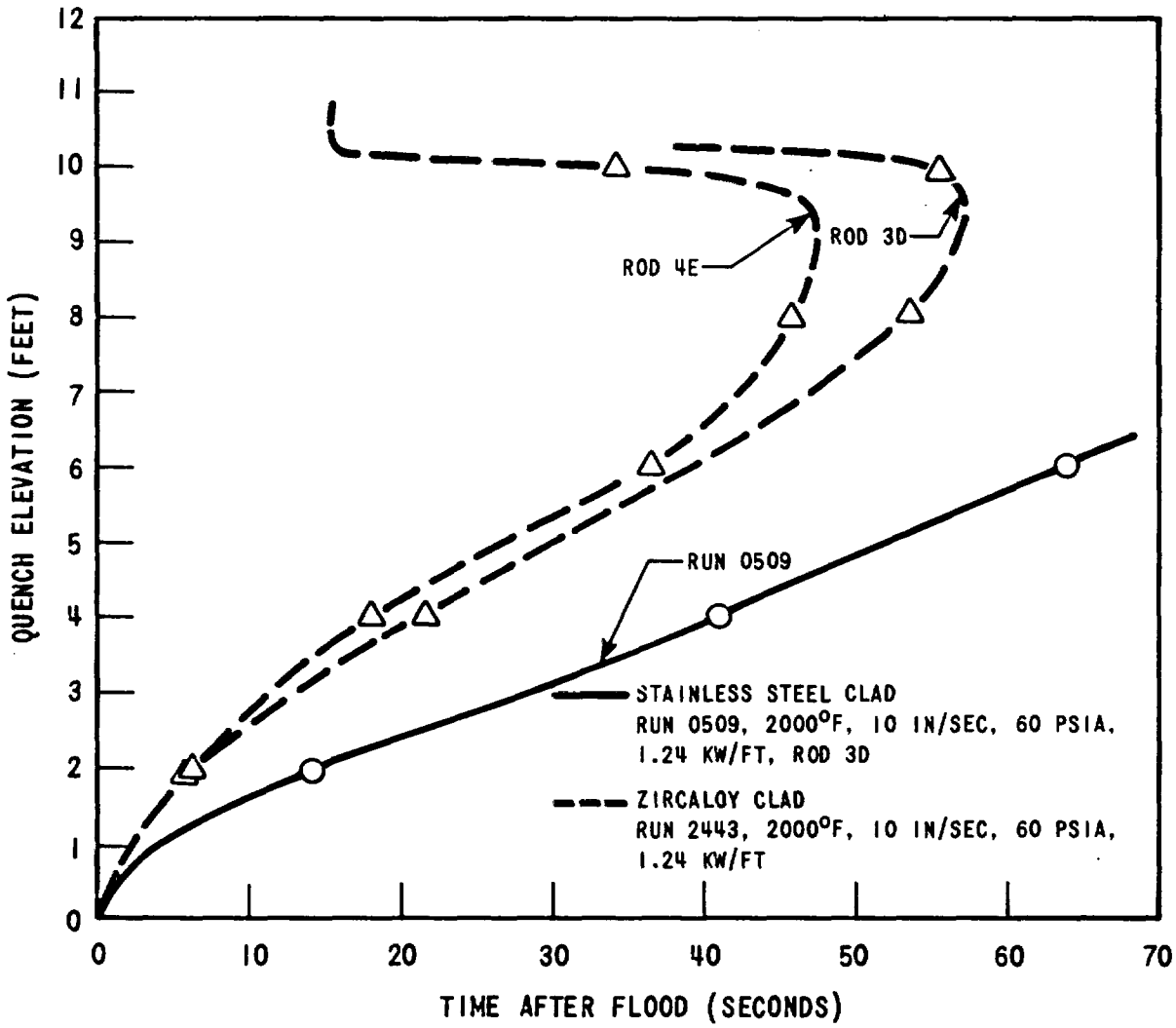

Figure 3-63. Comparison of Zircaloy and Stainless Steel Quench Behavior, 10 In/Sec

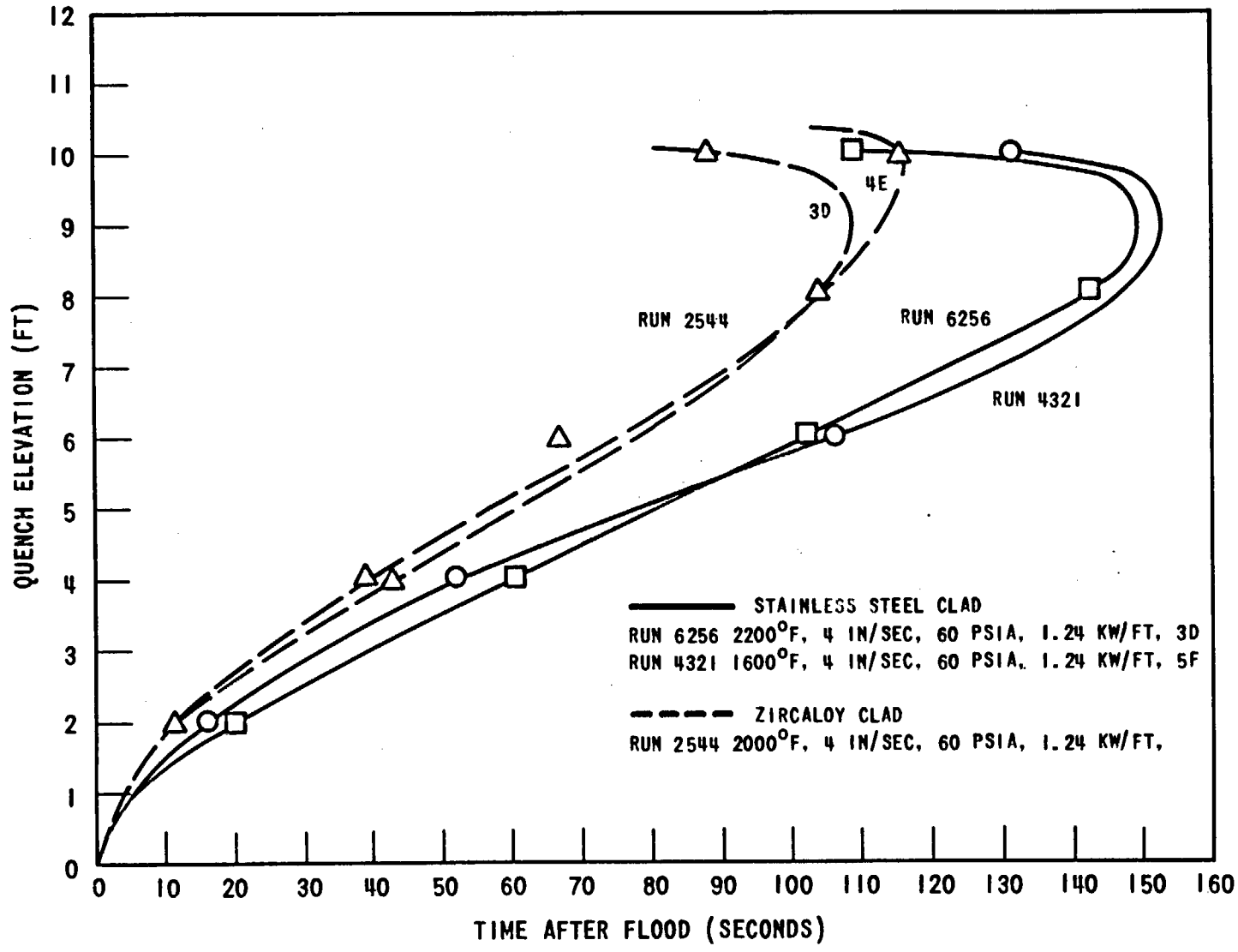

Figure 3-64. Comparison of Zircaloy and Stainless Steel Quench Behavior, 4 In/Sec

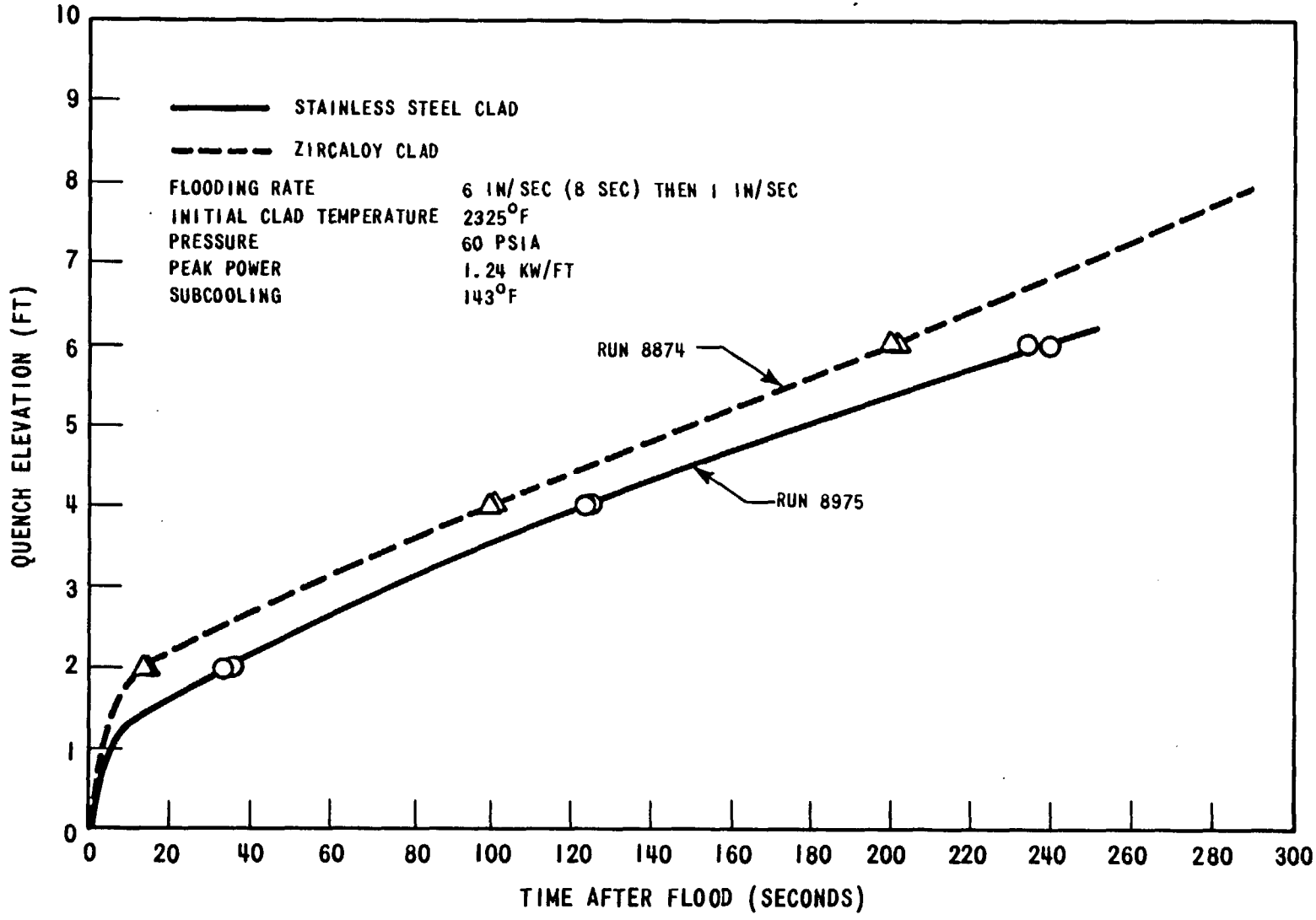

Figure 3-65. Comparison of Zircaloy and Stainless Steel Clad Quench Behavior, 6(8 Sec)-1 In/Sec

2507-116

Figures 3-63 through 3-65 show that in all cases the quench front velocities for the tests with Zircaloy clad were greater than for the tests with stainless steel clad. The effect of this difference in quench front velocities as a possible explanation for the higher Zircaloy transfer coefficients, can be explained in terms of the flow regimes identified in Section 3.3.1 as follows:

> Film boiling starts at the quench front. Above the quench front, the thickness of the vapor film and velocity of the vapor increase. As the vapor film thickness and velocity increase, the liquid-vapor interface becomes more and more unstable, and eventually the flow pattern changes to the transition flow regime. For greater quench front velocities, the boundaries between these regimes may be higher in elevation at any given point in time. Therefore, when the Zircaloy clad rods were in the stable film boiling regime, the stainless steel clad rods may have still been in the transition flow regime. Since heat transfer coefficients for the film boiling regime are greater than those for the transition flow regime, this would result in higher Zircaloy heat transfer coefficients. Hence a given elevation in a Zircaloy clad test could pass through the various flow and heat transfer regimes at a faster rate than a comparable stainless clad test resulting in a more rapidly increasing heat transfer coefficient with time.

In addition to the above differences in flow behavior, it is believed that the production of hydrogen by the Zircaloy-water reaction and differences in the emissivity of the Zircaloy probably were partly responsible for the improved Zircaloy heat transfer coefficients, particularly during the early part of Run 8874. Calculations using the Dittus-Boelter single phase heat transfer correlation showed that the presence of hydrogen in the convective film near the rod surface results in increased heat transfer coefficients. This is due to the higher thermal conductivity and heat capacity and lower viscosity of a steam hydrogen mixture compared to pure steam.

Although the measured Zircaloy heat transfer coefficients appeared to be generally larger than the stainless steel coefficients, the amount and consistency of the data did not permit a quantitative assessment of the magnitude of the effect. Hence, it is recommended that stainless steel heat transfer coefficients be used as a conservative representation of Zircaloy behavior. If desired, estimates of Zircaloy heat transfer coefficients can be obtained from stainless steel data by decreasing the stainless steel quench time by

amounts estimated from Figures 3-63 through 65. This would compress the stainless steel data into a shorter time period for each elevation, resulting in a higher heat transfer coefficient at any instant in time.

3.5 PRESSURE TRANSDUCER RESULTS

3.5.1 Radial Pressure Drop

Radial pressure drop measurements were made by means of two pressure taps located at the start of the heated length, with one in a guide tube and the other in the housing wall. Figure 3-66 shows a typical radial pressure difference for a 10 x 10 run. There was essentially no measurable radial pressure gradient in the bundle. This means that at this elevation the radial flow was quite small and the difference between the flooding velocity at the inside and outside of the bundle was negligible.

3.5.2 Axial Pressure Drop

3.5.2.1 Axial Pressure Drop in Constant Flooding Rate Tests

The effect of flooding rate and initial clad temperature on axial pressure drop is shown in Figure 3-67. As can be seen in the upper portion of the figure, an increase in flooding rate resulted in a larger pressure drop at all points in time. Estimates of elevation head as a function of time based on the quench front elevation and density of the liquid-vapor mixture above the quench front indicate that the measured axial pressure drop is primarily a function of elevation head, i.e. friction and momentum effects are relatively small. Thus, as the flooding rate was increased, the elevation head and hence the pressure drop at any point in time became greater.

The lower portion of Figure 3-67 shows that initial clad temperature had a negligible effect on axial pressure drop. Since the flooding rate was uniform for the three cases shown, this indicates that at a 1 in./sec flooding rate the initial clad temperature did not have a significant effect on friction and momentum pressure drop terms. This is consistent with the small effect of initial clad temperature on heat transfer coefficient at 1 in./sec, which was shown in Figure 3-10.

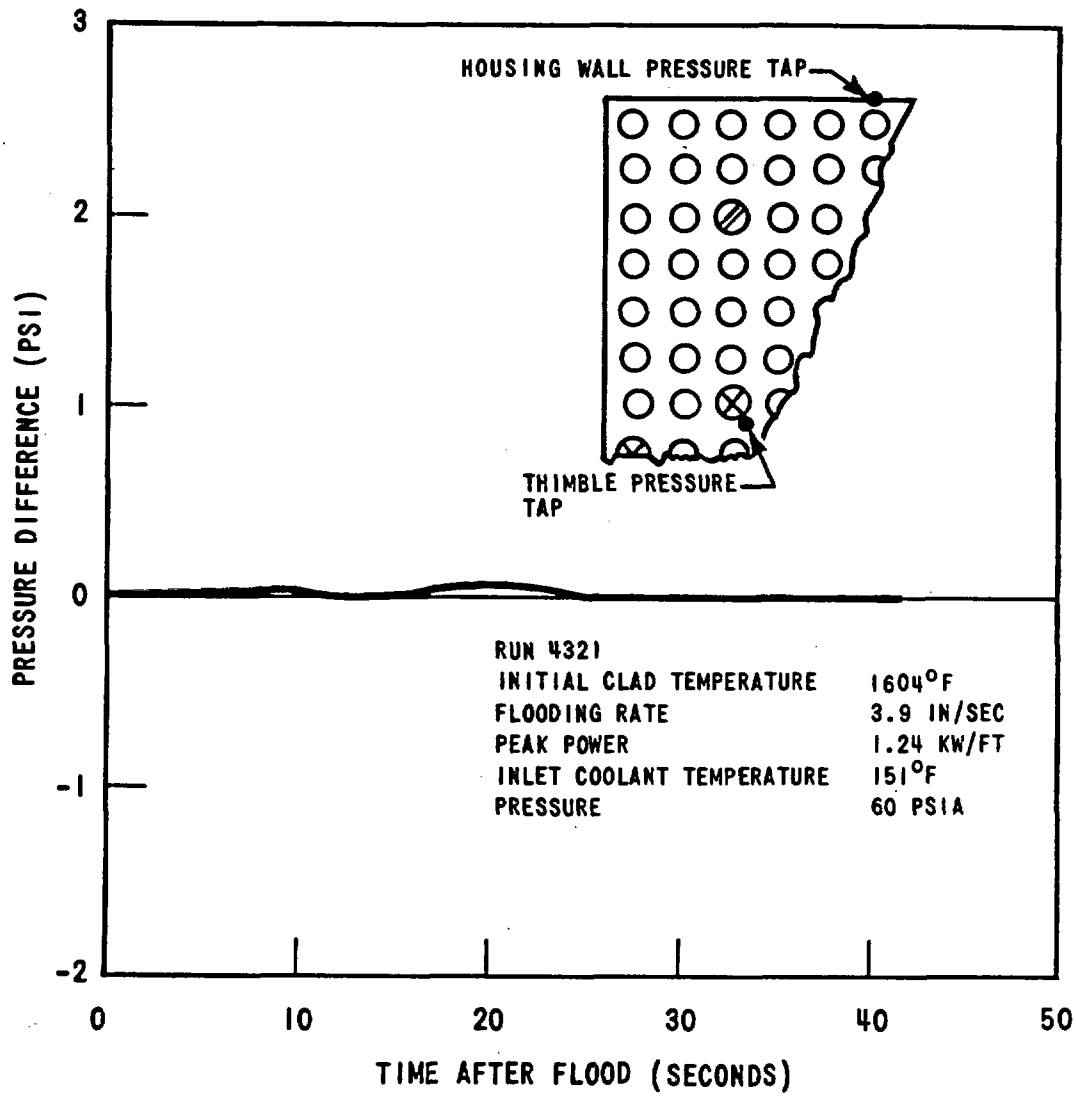

Figure 3-66. Bundle Radial Pressure Difference Between Thimble Tap and Housing at Bottom of Heated Length

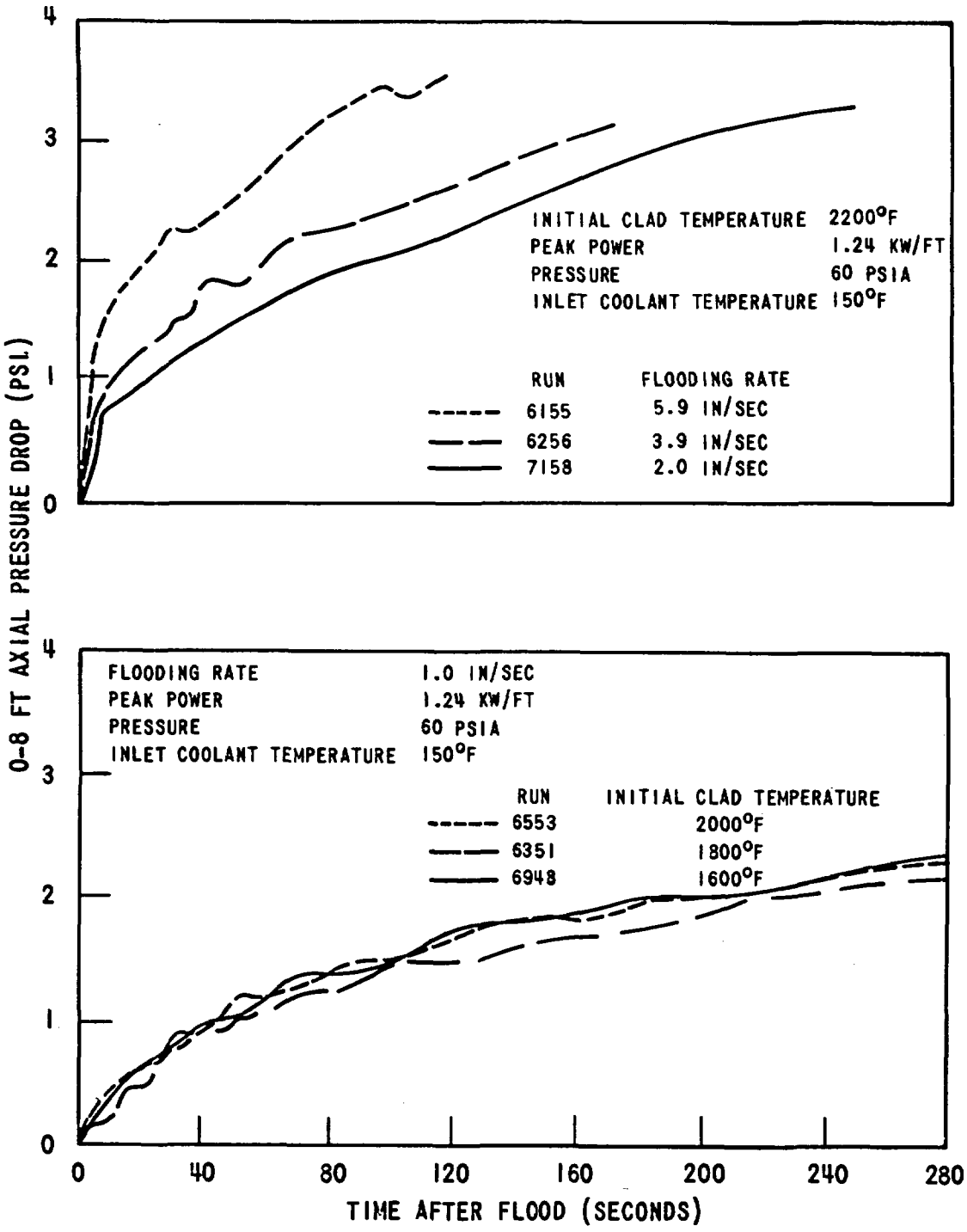

Figure 3-67. Effect of Flooding Rate and Initial Clad Temperature on Axial Pressure Drop

3.5.2.2 Axial Pressure Drop in Variable Flooding Rate Tests

Figure 3-68 compares axial pressure drops for constant and variable flooding rate tests without "fallback". The variable flow pressure drop increased more rapidly than the 6 in./sec test and then dropped to a level which reflected the elevation head at the time the flooding rate underwent a step reduction to 1 in./sec. Thereafter, the variable flow pressure drop increased at a rate which resembled the 1 in./sec test, indicating the strong dependence of pressure drop on flooding rate.

A comparison of the pressure drop in variable flooding rate tests with and without "fallback" is shown in Figure 3-69. As can be seen, the pressure drop was similar for cases with and without "fallback" in both the high and low flooding rate portions of the tests.

3.5.2.3 Axial Pressure Drop in the Flow Blockage Test

Figure 3-70 shows the axial pressure drop for runs with 0 percent, 75 percent uniform and sixteen-channel 100 percent flow blockage at a 1 in./sec flooding rate. The blocked runs had a higher pressure drop by 0.1 to 0.3 psi, which is as expected due to the flow obstruction created by the blockage plate. Increasing the blockage in the center 25 channels of a 10 x 10 assembly which has already been 75 percent blocked did not significantly affect the pressure drop.

3.6 LOCAL COOLANT AND GUIDE TUBE TEMPERATURES

Several different methods were used to measure local coolant and guide tube temperatures in the FLECHT tests. Originally, bare thermocouples were used. "Steam probes" consisting of a thermocouple in a guide tube surrounded by a radiation shield were then added in the Group I 10 x 10 and Group II 7 x 7 bundles. These are described in Section 2.1.2. During heatup and after flooding, the bare thermocouples were strongly influenced by radiation from adjacent heater rods. The measurements were therefore considered reliable only after the thermocouples quenched to saturation. The original "steam probe" offered little improvement over the bare thermocouple.

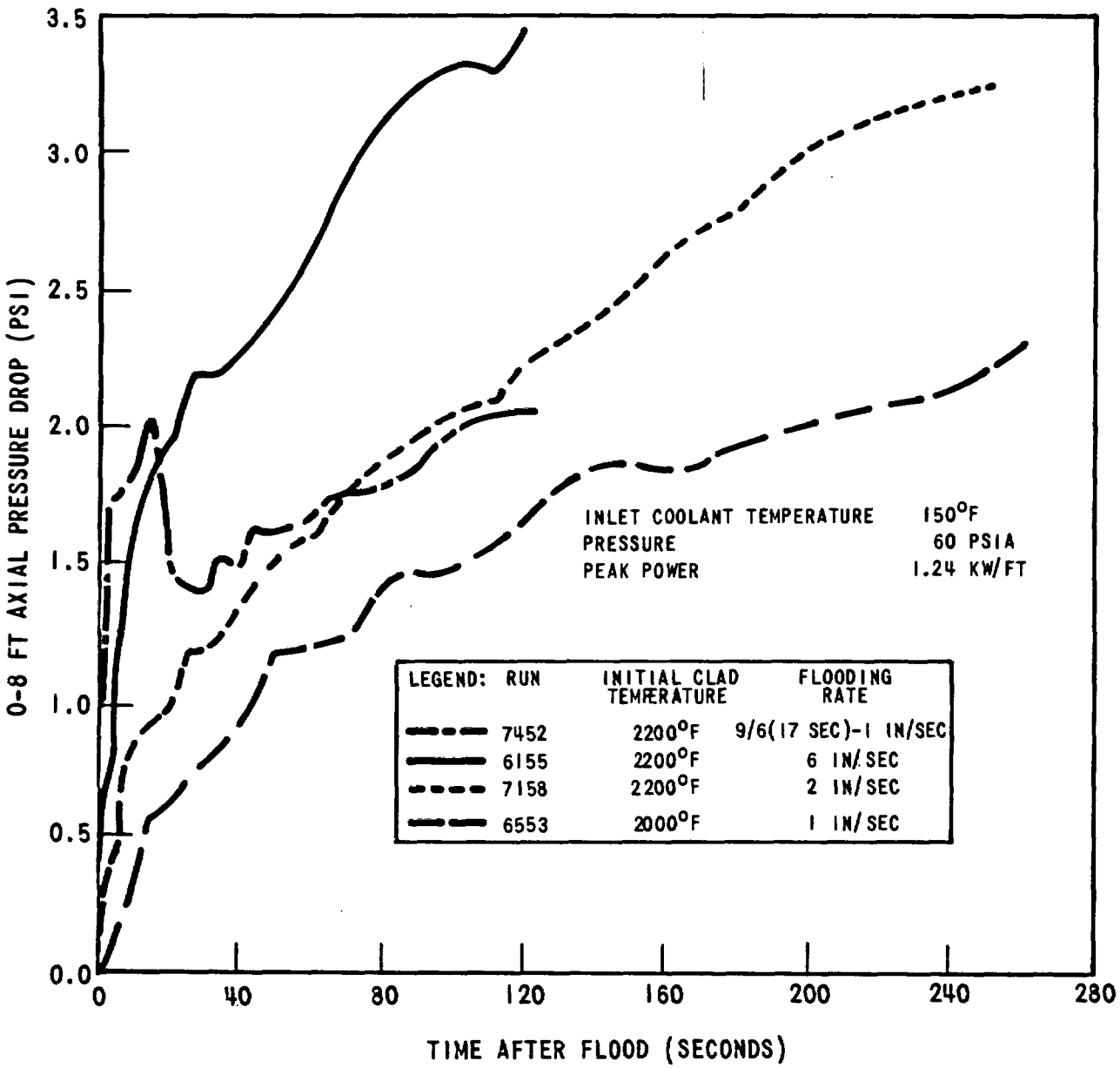

Figure 3-68. Comparison of Axial Pressure Drop for Constant and Variable Flooding Rate Tests

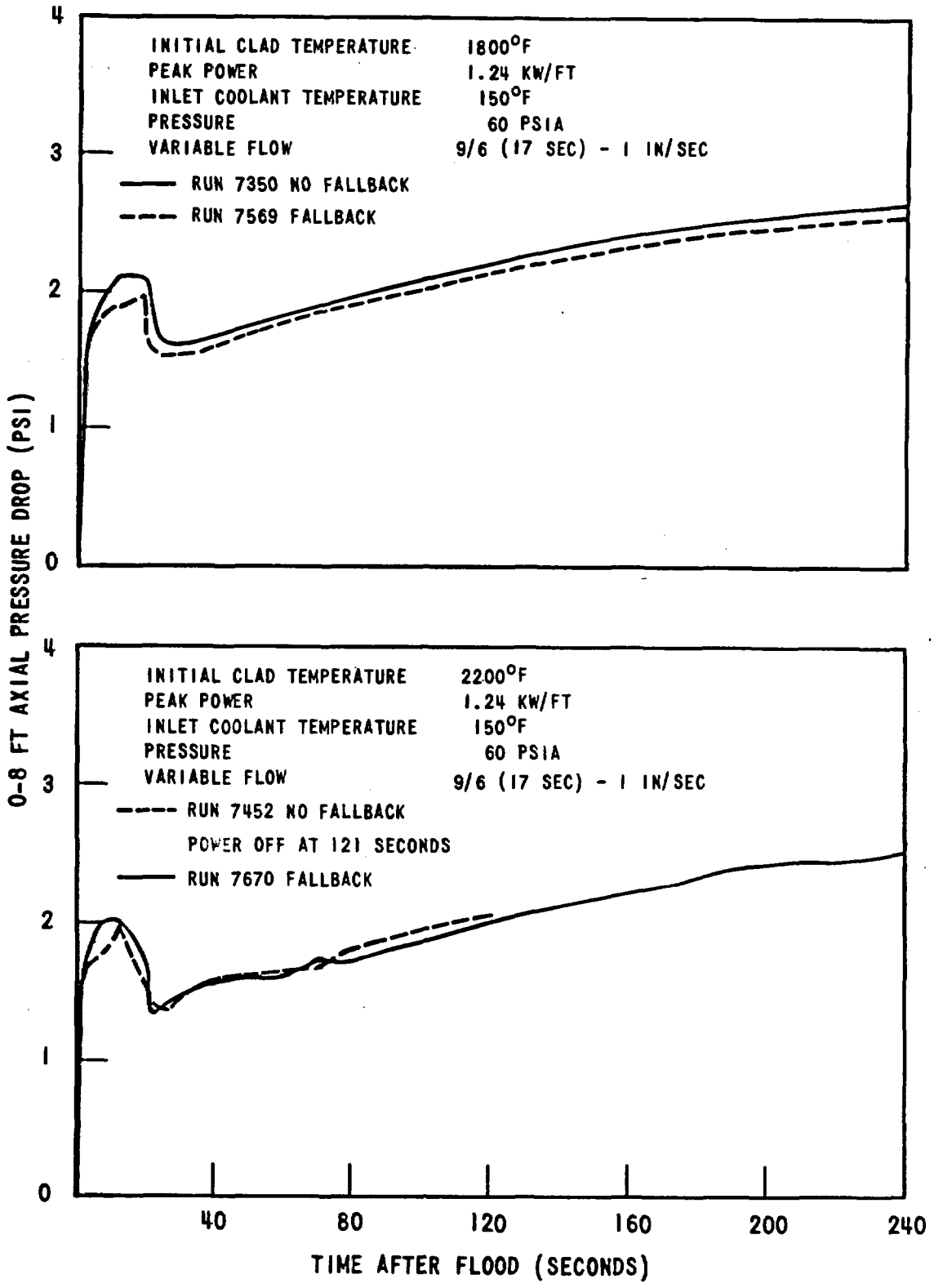

Figure 3-69. Effect of Fallback on Axial Pressure Drop

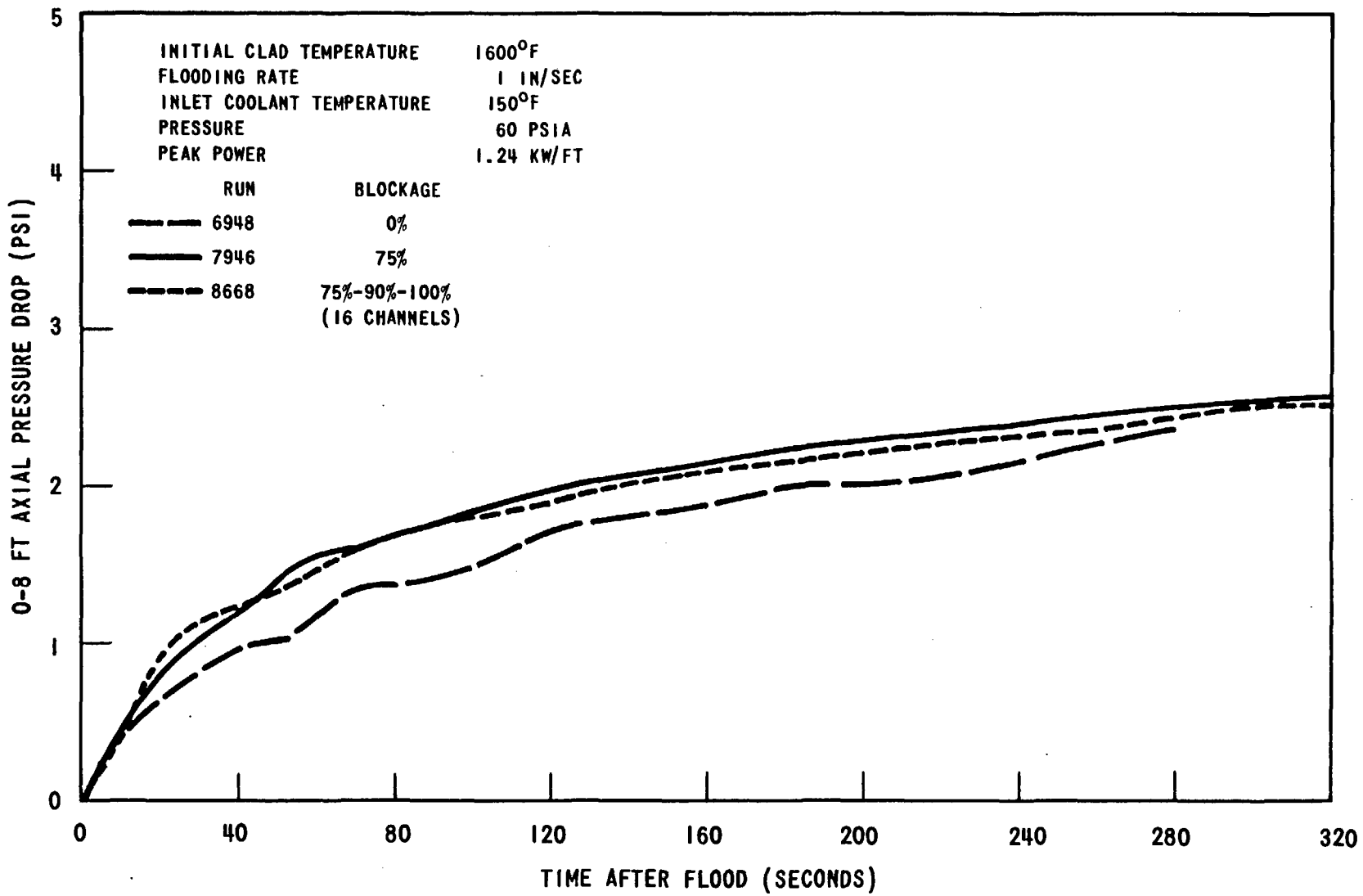

Figure 3-70. Effect of Flow Blockage on Axial Pressure Drop

The "steam probes" were redesigned at the time of the Group II flow blockage tests to include a flow bleed system which would assure adequate steam flow past the thermocouple, thereby reducing radiation effects. In addition, bare thermocouples were installed in the bundle above the heated length and at the outlet pipe. These instruments provided generally reliable and consistent data.

Typical behavior of the local coolant and guide tube thermocouples and the original "steam probes" is shown in Figure 3-71. The temperatures are shown only after the thermocouples quenched down to saturation temperature. Good agreement was obtained between the local coolant, guide tube, and "steam probe" thermocouples at the same elevation. The figure also shows the time of the 2, 4, 6, and 8 ft heater rod quench. As discussed in Section 3.3.2, calculations and movie observations indicated the presence of subcooled liquid in the film boiling regime just above the quench front for high flooding rates and 140°F inlet subcooling. The measured local coolant temperatures at the 4, 6, and 8 ft elevations were consistent with this observation in that temperatures dropped below saturation before the arrival of the heater rod quench front. However, for flooding rates of 2 in./sec and lower the local coolant data indicated that at the time of the 6 ft heater rod quench the coolant temperature at the 6 ft elevation was at saturation.

Figures 3-72 and 3-73 show coolant temperatures and typical 8 and 10 ft clad temperatures during the flow blockage tests with 100 percent blockage of sixteen channels at 4 in./sec and 1 in./sec, respectively. Figure 3-74 shows modified "steam probe" data for a typical variable flooding rate test without flow blockage. A summary of the coolant temperature data from the Group II flow blockage tests and some later unblocked tests is presented in Table 3-9.

The above figures and table show that superheated steam was present in the bundle prior to the initiation of flooding. Thermocouples TE-19 and TE-50 read near saturation during this period because they were in the upper plenum and were reading the temperature of the steam from the pressurizer. The amount of initial superheat increased with initial clad temperature, but lagged the clad temperature by several hundred degrees. During the run, superheated steam was found to be present for long periods of time, indicating that the coolant was a non equilibrium mixture of superheated steam and liquid droplets.

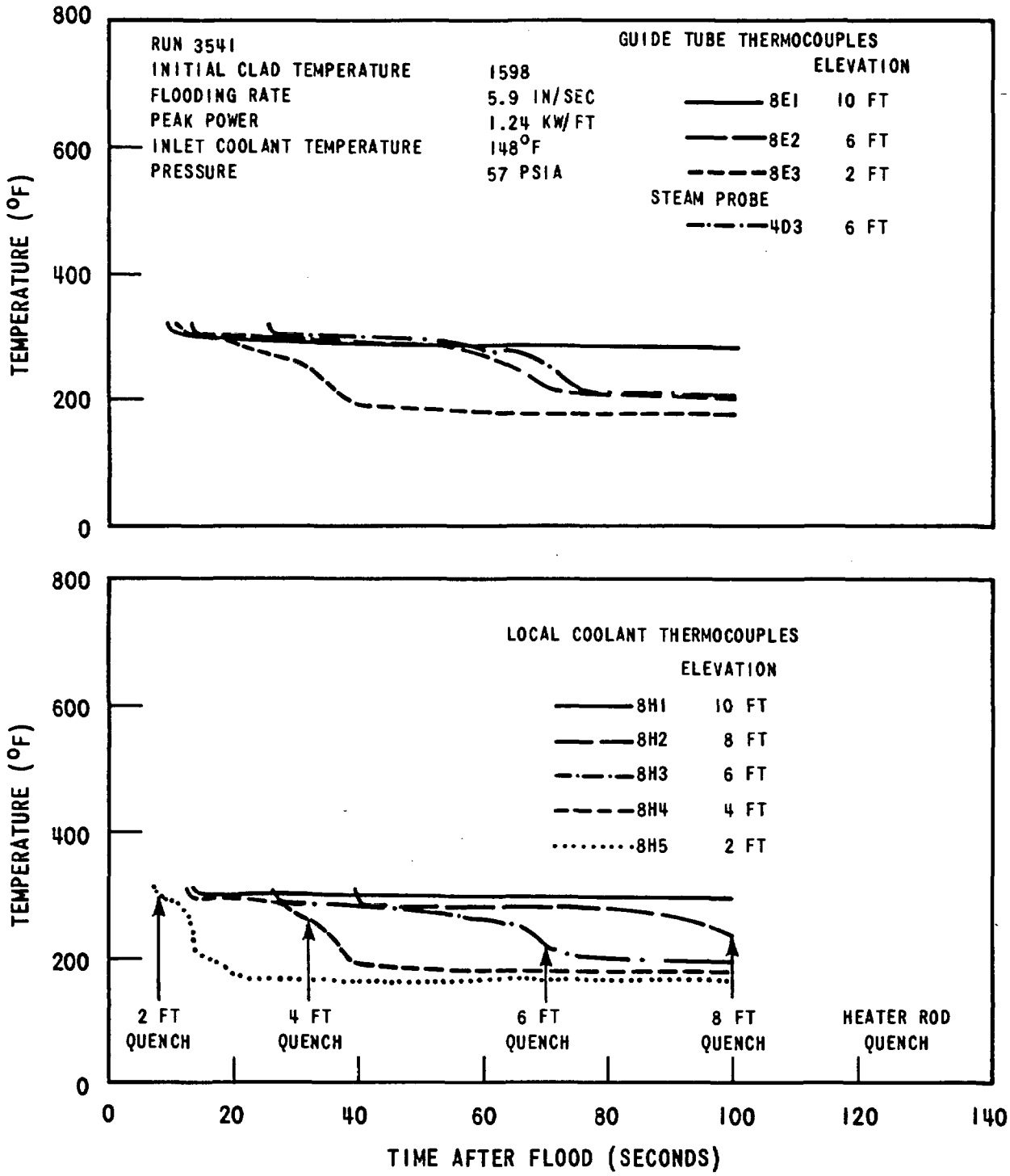

Figure 3-71. Local Coolant, Steam Probe and Guide Tube Wall Temperatures versus Time for Reference Run Conditions

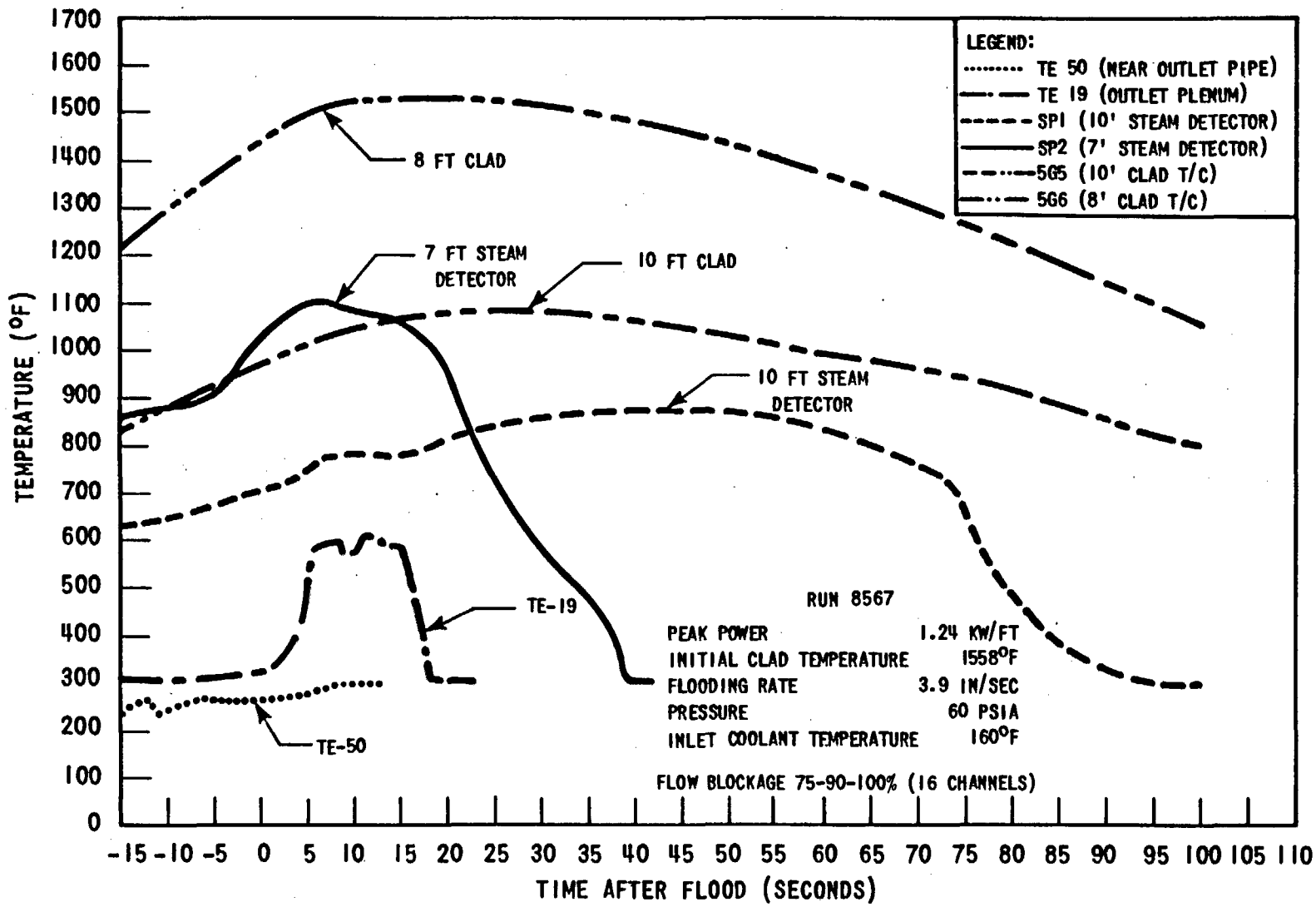

Figure 3-72. Measured Steam and Clad Temperatures for 4 In/Sec Flow Blockage Run

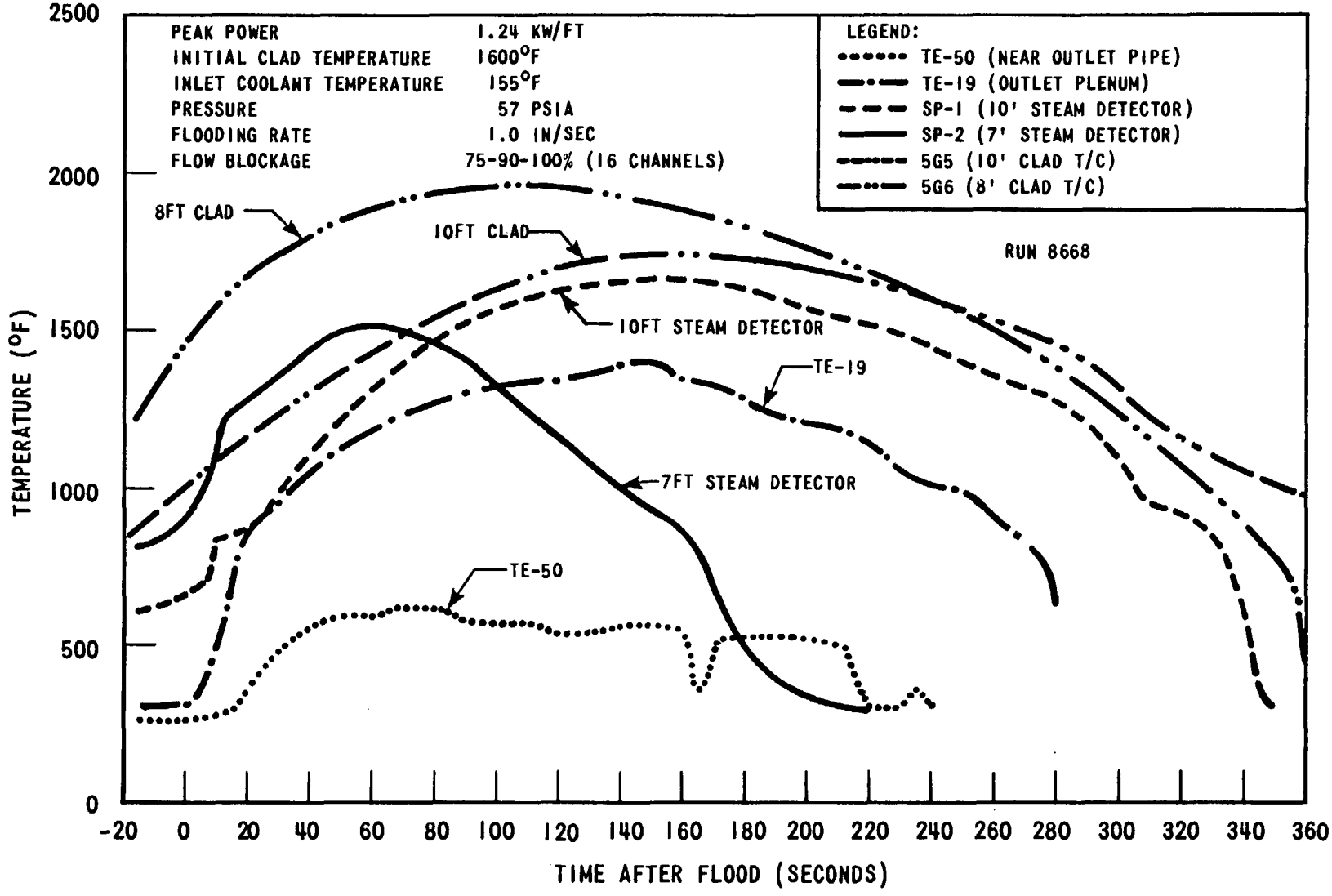

Figure 3-73. Measured Steam and Clad Temperatures for 1 In/Sec Flow Blockage Run

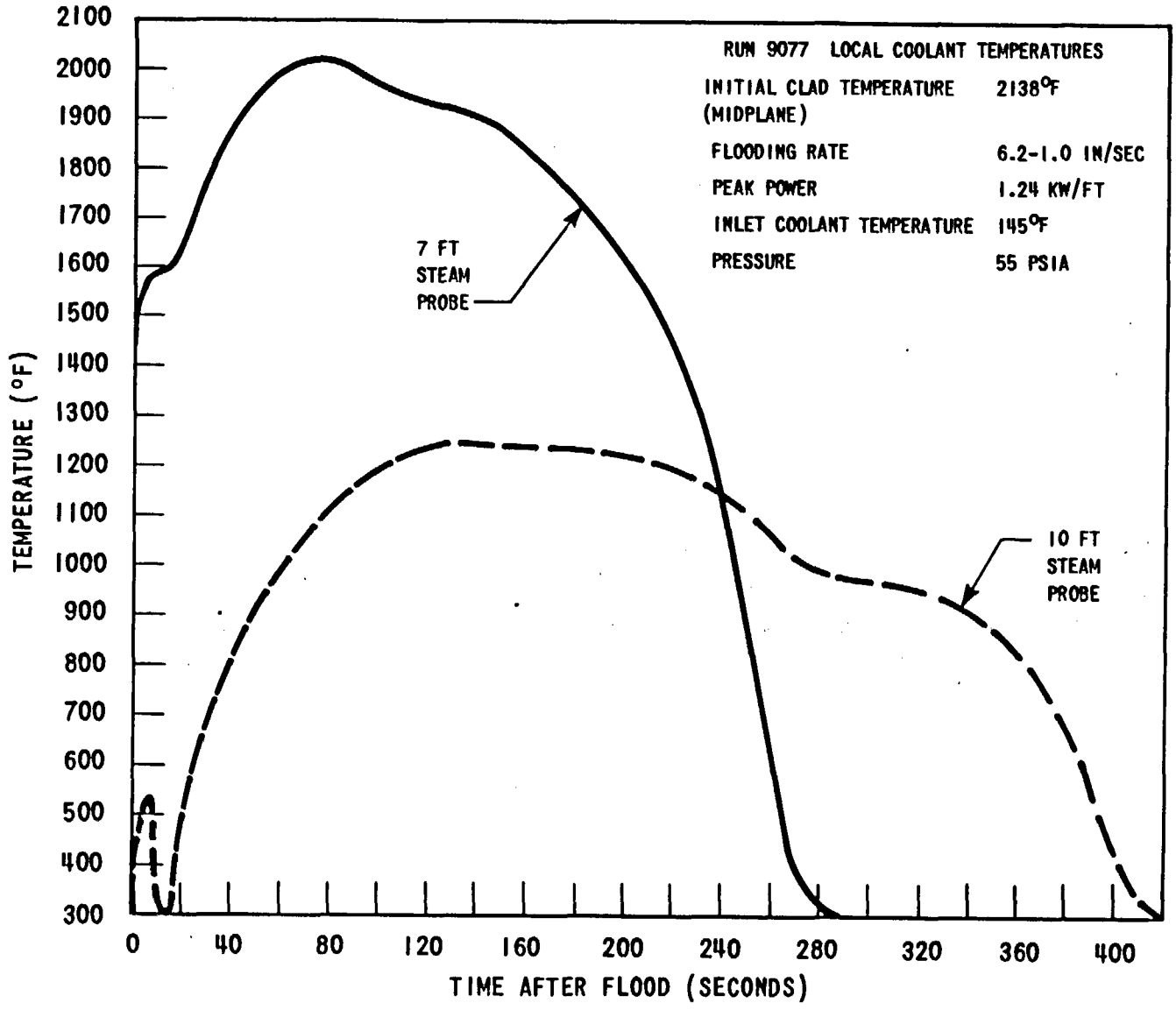

Figure 3-74. Measured Steam Temperatures for Variable Flooding Rate Test Without Blockage

TABLE 3-9

SUMMARY OF COOLANT TEMPERATURE DATA

Run No.	Run Conditions		Coolant T/C	Peak Temp (°F)	t_{peak} (sec)	time above 300°F (sec)
	GROUP II FLOW BLOCKAGE (4 in./sec Tests)					
7845	Initial Temperature	1600 °F	SP1 (10')	675	12	46
(75% Blockage)	Pressure	55 psia	SP2 (7')	970	8	35
	Inlet Coolant Temperature	151 °F	TE-19	515	8	17
	Peak Power	1.24 kw/ft	TE-50	300	15	0
8054	Initial Temperature	1570 °F	SP1 (10')	705	8	69
(75-90% Blockage)	Pressure	56 psia	SP2 (7')	835	13	42
	Inlet Coolant Temperature	158 °F	TE-19	530	10	12
	Peak Power	1.24 kw/ft	TE-50	300	10	0
8265	Initial Temperature	1600 °F	SP1 (10')	740	23	77
(75-90-100%	Pressure	57 psia	SP2 (7')	955	14	44
-4 Channels)	Inlet Coolant Temperature	156 °F	TE-19	620	15	20
	Peak Power	1.24 kw/ft	TE-50	300	9	0
8567	Initial Temperature	1558 °F	SP1 (10')	875	45	98
(75-90-100%	Pressure	60 psia	SP2 (7')	1100	8	41
-16 Channels)	Inlet Coolant Temperature	160 °F	TE-19	615	15	21
	Peak Power	1.24 kw/ft	TE-50	300	9	0
	GROUP II FLOW BLOCKAGE (1 in./sec Tests)					
7946	Initial Temperature	1595 °F	SP1 (10')	1360	166	313
(75% Blockage)	Pressure	58 psia	SP2 (7')	1450	78	203
	Inlet Coolant Temperature	150 °F	TE-19	1015	90	167
	Peak Power	1.24 kw/ft	TE-50	525	90	54
8162	Initial Temperature	1595 °F	SP1 (10')	1380	150	290
(75-90% Blockage)	Pressure	57 psia	SP2 (7')	1455	61	189
	Inlet Coolant Temperature	151 °F	TE-19	1150	128	165
	Peak Power	1.24 kw/ft	TE-50	560	86	55
8366	Initial Temperature	1580 °F	SP1 (10')	1530	159	329
(75-90-100%	Pressure	58 psia	SP2 (7')	1530	51	209
-4 Channels)	Inlet Coolant Temperature	150 °F	TE-19	1270	152	243
	Peak Power	1.24 kw/ft	TE-50	625	80	159
8668	Initial Temperature	1600 °F	SP1 (10')	1660	149	345
(75-90-100%	Pressure	57 psia	SP2 (7')	1505	57	213
-16 Channels)	Inlet Coolant Temperature	155 °F	TE-19	1390	152	282
	Peak Power	1.24 kw/ft	TE-50	615	72	202
	UNBLOCKED TESTS					
8874	Initial Temperature	2297 °F	SP1 (10')	1005	94	236
(Flooding Rate:	Pressure	64 psia	SP2 (7')	1975	4	199
6.0 (8 sec) - 1.0 in/sec)	Inlet Coolant Temperature	141 °F	TE-19	1050	79	177
	Peak Power	1.24 kw/ft	TE-50	475	108	43
9077	Initial Temperature	2138 °F	SP1 (10')	1225	123	418
(Flooding Rate:	Pressure	55 psia	SP2 (7')	2020	68	276
6.2 (4 sec) - 1.0 in/sec)	Inlet Coolant Temperature	145 °F	TE-19	----	---	---
	Peak Power	1.24 kw/ft	TE-50	----	---	---
9278	Initial Temperature	2028 °F	SP1 (10')	1150	144	420
(Flooding Rate:	Pressure	58 psia	SP2 (7')	2130	85	283
1.0 in/sec)	Inlet Coolant Temperature	148 °F	TE-19	----	---	---
	Peak Power	1.24 kw/ft	TE-50	----	---	---

The presence of superheated steam during the run was consistent with the negative heat transfer coefficients calculated by the DATAR code for the 10 ft elevation in some runs. The peak steam temperature and the time of superheat observed tended to increase with decreasing flooding rate and increased blockage.

3.7 LIQUID CARRYOVER RESULTS

Measurements of entrained liquid carryover were made by continuously draining the trapped water from the upper plenum and collecting it in catch vessels. At the completion of a test the water in the catch vessels was weighed to determine the carryover as a percentage of the total inlet flow. For the last three tests in the program (Runs 9379, 9480 and 9573) the collecting system was modified as follows to measure carryover as a function of time:

> The catch vessels were replaced by a heated and insulated vertical 3 in. Sch. 80 pipe placed next to the test section. The drain pipe from the upper plenum was connected to the collection pipe and a baffle was placed in front of the steam exit in the upper plenum to separate out any entrained liquid. A pressure transducer was connected to the lower end of the pipe to measure the elevation head in the pipe as a function of time with the output recorded on a visicorder.

Figure 3-75 shows typical test results obtained with the modified system along with the total volume of water supplied to the test section and an estimate of the amount of water remaining in the bundle below the quench front. The run shown is a variable flow test with an initial clad temperature of 2200°F and a flooding rate of 6 in./sec for four seconds followed by a step reduction to 1 in./sec. Only about 10 percent of the water supplied to the bundle was entrained and carried out of the flow housing throughout the run. A carryover fraction of 10 percent was also found in a 1 in./sec constant flooding rate test as shown in Figure 3-76. This run was not considered valid because of heater rod failures; however, the carryover data was probably not affected significantly.

Since the data obtained with the modified carryover measurement system was not consistent with previously reported data (Reference 3), the reliability of the two sets of data was checked by performing a heat balance on the test

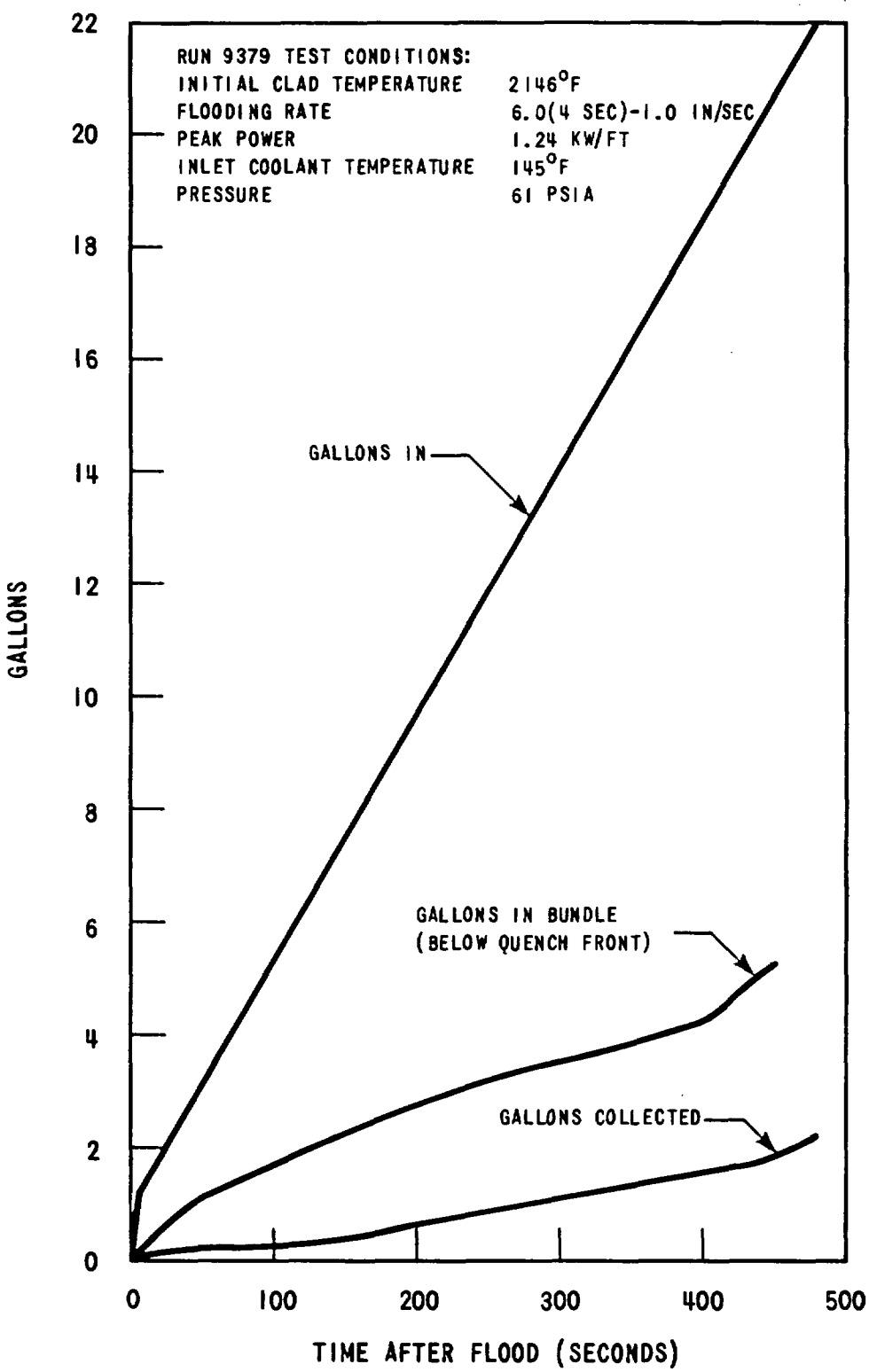

Figure 3-75. Liquid Carryover Data Run 9379 - Variable Flooding Rate Test

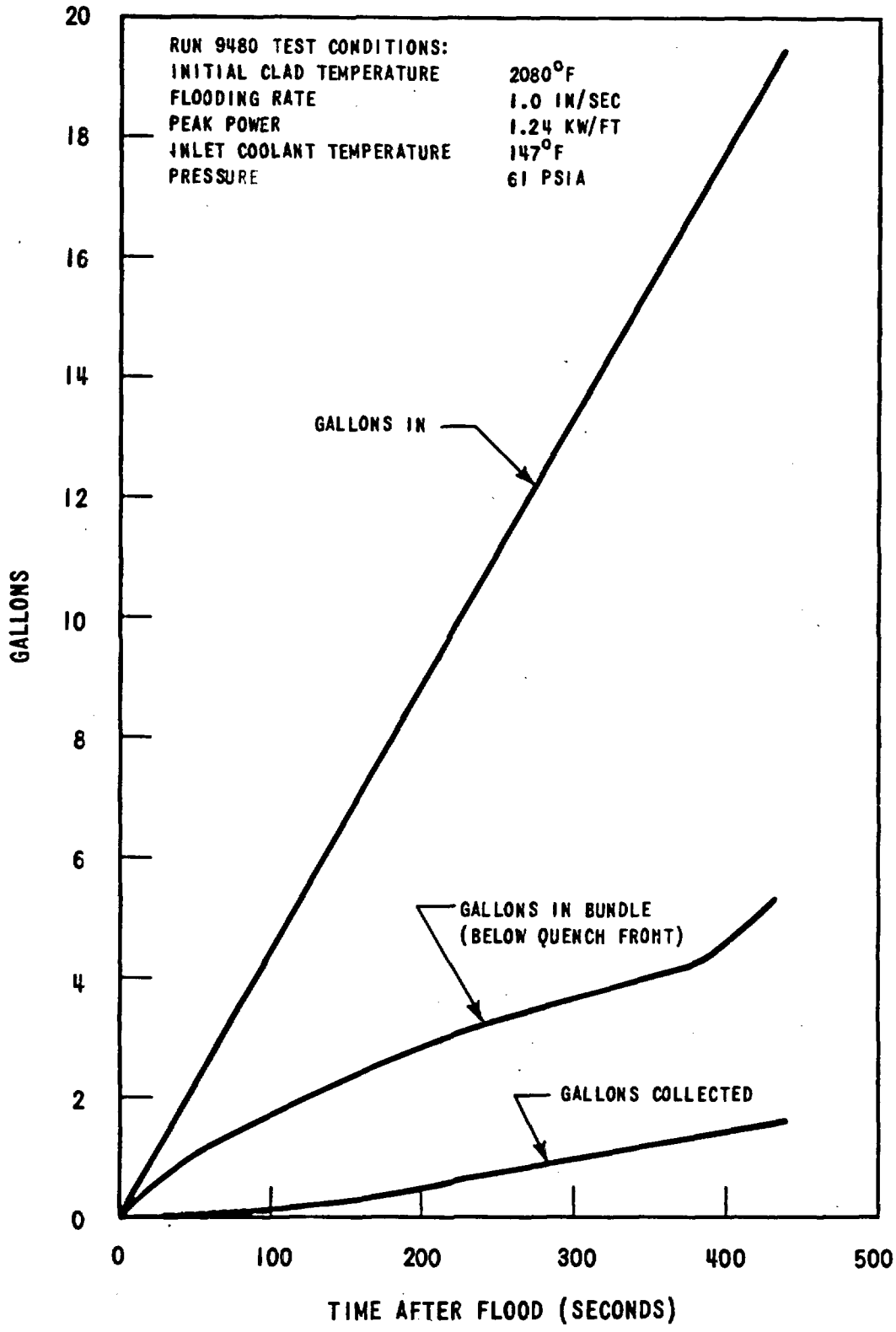

Figure 3-76. Liquid Carryover Data Run 9480 - 1 IN/SEC Flooding Rate Test

section. This analysis revealed that 10 percent of the coolant supplied to the flow housing, or approximately 2.5 gallons, was a reasonable amount of carryover for a 1 in./sec test. An unreasonably high effluent steam temperature was required for the amount of carryover reported in Reference 3 for similar conditions (50 percent).

Review of the design of the original carryover measurement system revealed the probable cause of the previously reported data. In the original system the catch tanks were large, uninsulated vessels, which were vented to the outlet steam pipe. Thus, it was possible that the outlet steam pipe acted as an aspirator, causing steam to flow into the catch vessels and condense. This would increase the measured amount of carryover, consistent with the earlier data.

Consideration of the above information led to the conclusion that the previously reported carryover data was not valid. The current data indicates that at a flooding rate of 1 in./sec carryover represents approximately 10 percent of the coolant supplied to the flow housing throughout the run. The amount of carryover is expected to increase with flooding rate.

Another indication of the carryover fraction was obtained from the quantity $(V_{in}-V_q)/V_{in}$; where V_{in} is the flooding rate and V_q is the quench front velocity. This quantity indicates the fraction of inlet flow which is evaporated and entrained at the quench front, but not necessarily carried out of the bundle. In general, the fraction ranged from 0.85 to 0.90 in the 4 and 6 in./sec tests, and from 0.77 to 0.81 in the 0.8, 1 and 2 in./sec tests, showing a slight increase with flooding rate.

SECTION 4

RELATION OF FLECHT RESULTS TO REACTOR LOCA ANALYSIS

4.1 ASSUMPTIONS AND LIMITATIONS OF FLECHT TESTS

As in most experimental programs, certain compromises and simplifying assumptions were necessary in order to achieve PWR FLECHT objectives in a timely and efficient manner. These can be summarized most conveniently under the following headings:

1. Use of separate effects approach.
2. Use of electrically heated rods to simulate the performance of reactor fuel.
3. Use of a limited number of heater rods to simulate the behavior of the reactor core hot assembly.
4. Other differences between FLECHT tests and reactor behavior during a loss-of-coolant accident.

The following subsections discuss the principal assumptions and limitations of the PWR FLECHT tests with respect to each of the above categories.

4.1.1 Separate Effects

The PWR FLECHT program investigated the reflooding phase of the loss-of-coolant accident. Behavior prior to core reflooding, during subcooled and saturated blowdown and adiabatic heatup, was not investigated or simulated in the PWR FLECHT tests. Instead the tests were designed to simulate calculated reactor conditions at the end of blowdown, with the core completely uncovered and heating up, with the level of water in the inlet plenum rising as a result of accumulator and other emergency core cooling system pump discharges and with the level of water just at the bottom of the active core.

Validity of the separate effects approach depends on the ability to accurately calculate and reproduce conditions at the start of the particular phase being

investigated. To overcome the uncertainty in calculated reactor conditions at the start of core reflooding and to account for the effects of differences in reactor designs on these conditions, the PWR FLECHT program was planned as a multi-parameter investigation. Thus, the system pressure, flooding rate, inlet coolant subcooling, initial clad temperature, flow blockage, and peak power were systematically varied over a wide range. Although a full factorial investigation of all parameter effects was not performed, it is believed that the test results provide an adequate basis for analyzing reactor performance under almost any realistically conceivable set of conditions.

As noted above, ability to reproduce prescribed reactor conditions at the start of reflooding was also vital to the validity of the separate effects approach. In general, the equipment and procedures used permitted simultaneous attainment of all desired initial test conditions within very close tolerance bands. This can be very difficult, particularly in transient testing, and achieving this objective should be considered one of the principal accomplishments of the PWR FLECHT program.

Although prescribed reactor conditions were accurately reproduced, it is worth noting that initial steam temperatures (within the bundle) were not controlled in the PWR FLECHT tests. Reactor loss-of-coolant accident calculations indicate that in some cases steam temperatures at the start of reflooding may be within 100°F of the clad temperature. As discussed in Section 3.6, PWR FLECHT steam temperatures were in the superheat range at the start of flooding, but were generally several hundred degrees below the clad temperature. This could be expected to have some effect on the value of the initial heat transfer coefficient; however, it is not believed to have had a significant effect on subsequent test behavior.

4.1.2 Electrically Heated Rods

Figure 4-1 shows a comparison of the temperature response of boron nitride-stainless steel (BN-SS), boron nitride-Zircaloy (BN-Zr) and uranium dioxide-Zircaloy (UO_2 - Zr) rods for 6 and 2 in./sec flooding rates. The curves were generated by a conduction code using heat transfer coefficients obtained from stainless steel PWR FLECHT tests. The gap coefficients for the BN

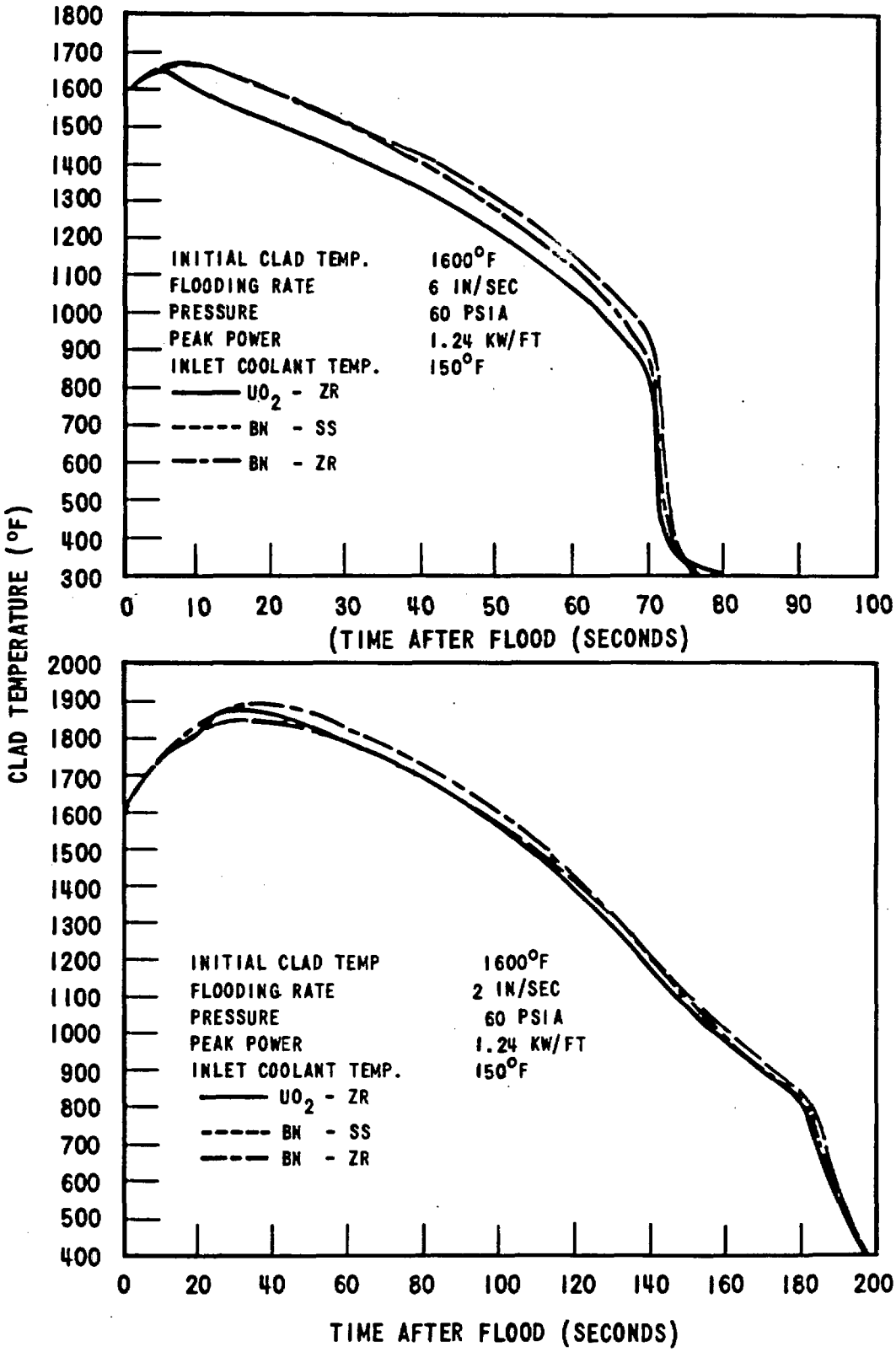

Figure 4-1. Comparison of Thermal Response of PWR-FLECHT and Reactor Fuel Rods

and UO_2 cases were 10,000 and 500 Btu/hr-ft^2-°F, respectively. Initial temperature distributions were assumed to be uniform in the BN cases, whereas a 59°F difference between peak pellet and initial clad temperature was used in the UO_2 cases. Metal-water reaction was predicted in the Zircaloy cases using the Baker-Just parabolic rate equation (Reference 4). The BN-SS curves are generally representative of the behavior of Group I and II PWR FLECHT heater rods and were found to be in good agreement with the measured temperature response for the same run conditions. The BN-Zr curves are representative of the behavior of Group III PWR FLECHT rods while the UO_2 -Zr curves are representative of reactor fuel rod response, assuming the BN-SS heat transfer coefficients apply.

Although there is general similarity in the temperature response of the three different cases considered, the peak temperatures are different. Further, it is expected that at lower flooding rates and/or higher initial clad temperatures, where metal-water reaction would be more significant, the differences between the three cases could be even larger. This difference in behavior indicates the inadvisability of using PWR FLECHT transient clad temperature response to quantitatively characterize reactor fuel pin behavior during loss-of-coolant accidents. However, it was never expected that the simulation provided by FLECHT heater rods would be close enough for this purpose (e.g. see Figure A-1). Instead, the objective of the program has always been to simulate the behavior of reactor fuel close enough to provide valid heat transfer coefficients which could then be used to analyze reactor thermal response during a loss-of-coolant accident. It is believed that the similarity shown in Figure 4-1 is more than adequate for this purpose.

4.1.3 Number of Heater Rods

Due to an average cost of approximately $500 per heater rod it was obviously desirable to minimize the size of PWR FLECHT test assemblies. Therefore it was decided that a PWR FLECHT test assembly should simulate the behavior of a portion of the "hot" assembly in a reactor core. Boundary effects were one area of significant concern in this regard. However, as discussed in Section 3.2.1.3, it was found that proper specification of flow housing

temperatures would allow the test assembly to behave as though it was part of a larger array.

It should be noted that no attempt was made to simulate core-wide radial flow effects in the PWR FLECHT tests. Typical reactor loss-of-coolant accident calculations indicate that the coolant flow at the midplane of the "hot" assembly with 50 percent flow blockage would be approximately 75 percent of the core average (Reference 10). Therefore, it is important to recognize the need to take the radial flow distribution into account in using FLECHT data for reactor loss-of-coolant accident analyses.

4.1.4 Other Differences

The PWR FLECHT tests differed from the reactor case in two other respects which are worth noting. First, the rate of coolant delivery to the test section was fixed rather than determined by system effects. This was consistent with the separate effects approach discussed previously. The wide range of flooding rates tested and the demonstrated capability to correlate variable flooding rate results with constant flooding rate test data (Section 3.3.3) provide a means for analyzing system effects on reactor behavior.

Aside from the flow blockage tests, the geometry of the PWR FLECHT test assembly as well as the radial and axial power distributions were not varied throughout the program. The uniformity of measured heat transfer coefficients across the interior of the 7 x 7 and 10 x 10 assemblies suggests that minor variations in assembly geometry or radial power distribution should not have a significant effect on heat transfer behavior. Variations in the axial power distribution would be more significant; however, the worst combination of peak power level and axial profile from a loss-of-coolant accident standpoint, generally occurs when the axial power distribution is peaked at the midplane. Thus, the PWR FLECHT test results should provide the information needed for "worst case" loss-of-coolant accident analyses.

4.2 APPLICATION OF FLECHT RESULTS TO REACTOR LOCA ANALYSIS

Despite the assumptions and limitations discussed above, the PWR FLECHT

program has important implications for reactor loss-of-coolant accident analysis. From an overall standpoint the results of this program are significant in that they have verified the basic assumptions used in current loss-of-coolant accident calculations. Current practice predicts essentially adiabatic heatup of the reactor fuel until the steam velocity in the core becomes great enough to cause entrainment. Following the onset of entrainment, the core is assumed to be cooled by a two phase flow of entrained liquid droplets and steam. The test results reported in Section 3 show less than adiabatic heatup rates during the initial stage of reflooding and are fully consistent with the entrainment model. In particular the effectiveness of bottom flooding and the importance of entrainment as a heat transfer mechanism have been demonstrated.

More specifically, the results of this program are significant in that when properly used, they can improve the accuracy of reactor loss-of-coolant accident analyses. In using the heat transfer coefficient data or correlations presented herein, it is important that the coolant temperature be taken as saturation, even though superheat conditions are know to exist. In addition, since the initial steam temperature in the reactor case may not be the same as in the PWR FLECHT tests, it is suggested that the initial heat transfer coefficient be adjusted to reflect initial reactor conditions.

With regard to application of the PWR FLECHT heat transfer correlations in reactor loss-of-coolant accident analyses, it should be noted that the correlations presented in Section 3.3.2 are conservative in several respects. These correlations do not take any credit for the effects of "fallback" or borated coolant, and are based on stainless steel clad data. The degree of conservatism introduced by absence of these effects will depend on the specific case being analyzed.

Perhaps the most important application of the results of this program will be the development and testing of models and correlations which can predict loss-of-coolant accident transient heat transfer coefficients and clad temperature behavior as a function of calculated local coolant properties. Such models would allow the available data to be extrapolated with greater confidence and could be used to explore emergency core cooling system performance margins which were beyond the capabilities of PWR FLECHT heater rods.

SECTION 5

CONCLUSIONS

5.1 SYSTEM PARAMETER EFFECTS ON HEAT TRANSFER

In general, the effect on heat transfer coefficient of varying system parameters was clearly discernable, with flooding rate being by far the most influential parameter investigated. More specifically, the effect of each parameter was as follows:

Initial Clad Temperature - Increasing the initial clad temperature increased the heat transfer coefficient in 6 and 2 in./sec tests for short periods after flooding. At later times, the heat transfer coefficient decreased with increasing initial clad temperature. At 1 in./sec, the effect of initial clad temperature was less significant than at higher flooding rates.

Flooding Rate - Increasing the flooding rate resulted in a significant increase in heat transfer coefficient throughout the entire run.

Inlet Coolant Subcooling - Decreasing inlet coolant subcooling resulted in increased heat transfer coefficients at early times and lower heat transfer coefficients at later times.

Pressure - Increasing the system pressure resulted in an increase in heat transfer coefficient.

Peak Power Generation - Increasing peak power generation did not affect the heat transfer coefficient at early times, but resulted in reduced heat transfer coefficients at later times.

Power Decay Rate - Changes in the power decay rate did not affect the heat transfer coefficient for the decay rates tested.

Borated Coolant - Addition of 2000 ppm of boric acid to the coolant resulted in a small increase in heat transfer coefficient.

5.2 ELEVATION EFFECTS

In general, heat transfer coefficients decreased with elevation from the start of the heated length. At high flooding rates and short times after flooding the heat transfer coefficients at 6 ft and higher increased with elevation.

5.3 VARIABLE FLOODING RATE TEST RESULTS

Variable flooding rate test results were consistent with and predictable by use of the constant flooding rate data and/or correlations.

Entrained liquid "fallback" increased heat transfer coefficients in high initial flow variable flooding rate tests (e.g., 9/6 (17 sec)-1 in./sec). At a variable flooding rate of 6 in./sec (4 sec)-1 in./sec or lower the "fallback" effect was small.

5.4 FLOW BLOCKAGE TEST RESULTS

In general, flow blockage at the midplane was found to improve heat transfer. This was due to increased turbulence and atomization of entrained liquid droplets as the flow passed through the blockage region. More specifically, it was observed that:

1. flow blockage significantly increased midplane heat transfer coefficients for all blockages tested, including 100 percent blockage of sixteen adjacent flow channels surrounded by 75 and 90 percent blockage of the remaining flow channels.
2. flow redistributes very rapidly downstream of the blockage, as indicated by increased heat transfer effectiveness as close as one inch downstream of the sixteen 100 percent blocked channels.
3. midplane flow blockage increased heat transfer coefficients as far as 2 ft upstream and 4 ft downstream of the blockage location.
4. as blockage was increased, the improvement in heat transfer at the 8 and 10 ft elevation decreased. However, for the most severe blockage tested, the temperature rise at the 8 ft elevation was, at worst, on the same order as the unblocked case.

5.5 HEAT TRANSFER REGIMES AND CORRELATIONS

The following flow regimes have a distinct influence on reflood heat transfer coefficients: steam flow, dispersed flow, transition flow, film boiling, transition boiling, and nucleate boiling. Of these, the unstable transition flow regime generally persisted for the longest period of time at the mid-plane and above.

Empirical correlation of FLECHT constant and variable flooding rate heat transfer coefficients as a function of system parameters resulted in good agreement (± 10 percent) between the correlations and the data.

5.6 ZIRCALOY-STAINLESS STEEL COMPARISON

Heat transfer coefficients for Zircaloy clad appeared to be somewhat greater than for stainless steel. The difference is believed due to observed differences in quench behavior, differences in clad emissivity and possibly the effects of hydrogen produced by the Zircaloy-water reaction. Because the amount and consistency of the data did not permit a quantitative assessment of the magnitude of the difference, it is recommended that stainless steel clad heat transfer coefficients be used as a conservative representation of Zircaloy behavior.

5.7 PRESSURE TRANSDUCER DATA

There was essentially no measurable radial pressure drop in the bundle. The axial pressure drop increased with increasing flooding rate and flow blockage, but was essentially unaffected by changes in initial clad temperature and "fallback".

5.8 LOCAL COOLANT DATA

Superheated steam temperatures were measured in the bundle prior to and after the start of flooding. Peak steam temperatures and the time of superheat increased with decreasing flooding rate and increasing flow blockage. At flooding rates of 4 in./sec, or greater, and 140°F inlet subcooling, the data

suggested that the coolant just above the quench front was subcooled. At lower flooding rates and the same inlet subcooling the coolant in this region was at the saturation temperature.

5.9 LIQUID CARRYOVER

At a flooding rate of 1 in./sec, carryover represents approximately 10 percent of the coolant supplied to the flow housing. The amount of carryover is expected to increase with flooding rate.

Using quench front and inlet flow velocities, the fraction of inlet flow which is evaporated and entrained above the quench front, but not necessarily carried out of the bundle was determined. This fraction ranged from 0.85 to 0.90 in the 4 and 6 in./sec tests and from 0.77 to 0.81 in the 0.8, 1 and 2 in./sec tests.

5.10 APPLICATION TO REACTOR LOCA ANALYSIS

PWR FLECHT test results have verified the basic assumptions used in current reactor loss-of-coolant accident analyses. In particular, the effectiveness of bottom flooding and the importance of entrainment as a heat transfer mechanism have been demonstrated.

Properly used, PWR FLECHT test results can improve the accuracy of reactor LOCA analysis. The heat transfer correlations which were developed are conservative in that they do not take any credit for the effects of "fallback" or borated coolant and are based on stainless steel clad data.

5.11 MATERIALS EVALUATION

The Baker-Just parabolic rate equation appears to provide a satisfactory basis for determining the overall extent of metal-water reaction. However, the formation of an oxide film and an oxygen containing α-zirconium layer beneath the oxide film should be accounted for in determining the metal-water reaction energy release and oxide film thickness.

In the investigations reported here, the extent of metal-water reaction was basically homogeneous with no major variations in oxide film thickness at given cross-sectional locations in a fuel rod.

The amount of hydrogen absorption was a low proportion (less than 10 percent) of the available hydrogen resulting from the metal-water reaction.

Even though the specimens examined reached temperatures as high as 2545°F, there was no evidence of clad shattering or failure as a result of being exposed to typical loss-of-coolant accident environments.

SECTION 6

REFERENCES

1. Cermak, J. O. et. al, "PWR FLECHT Final Test Plan," WCAP-7288, January, 1969.

2. Cermak, J. O. et. al, "PWR Full Length Emergency Cooling Heat Transfer (FLECHT) Group I Test Report," WCAP-7435, January, 1970.

3. Cadek, F. F. et. al, "PWR FLECHT (Full Length Emergency Cooling Heat Transfer) Group II Test Report," WCAP-7544, September, 1970.

4. Baker, L. Jr. and Just, L.C., "Studies of Metal-Water Reactions at High Temperatures: III Experimental and Theoretical Studies of the Zirconium-Water Reaction," ANL-6548, May, 1962.

5. Davis, R. F., "The Physical Aspect of Steam Generation at High Pressures and the Problem of Steam Contamination," INSTN. Mech. Engrs., 1940.

6. McCullough, C. R. et. al, "Investigation of the Use of Aqueous Solutions as Emergency Coolants," SNE-50, March, 1969.

7. Davis, P. R. "Experimental Studies of the Effect of Flow Restrictions in a Small Rod Bundle Under Emergency Core Coolant Injection Conditions," TRANS. Am. Nucl. Soc. 13, 158 (1970).

8. Jensen, R. T., "Experimental Results of the Fuel Heatup Simulation Tests (FHUST) - Emergency Core Cooling Test Series," IN-1390, September, 1970.

9. Plum, J. L., "Performance Evaluation of Stainless Steel and Zircaloy - Clad Electrically Powered Heaters," IN-1378, June 1970.

10. Carolina Power and Light Company, H. B. Robinson Unit No. 2 Plant, FSAR Ammendment No. 7, Docket No. 50-261, November 1968.

APPENDIX A

HEATER ROD DEVELOPMENT

A.1 OBJECTIVES

The objectives of the PWR FLECHT heater rod development program were to provide instrumented electrical heaters which would:

1. Simulate the thermal performance of PWR fuel during a loss-of-coolant accident.
2. Have a diameter and heated length typical of full scale commercial PWR fuel, with stainless steel clad for Group I and II testing and Zircaloy 4 clad for Group III testing.
3. Be capable of operation without failure at temperatures up to 2100°F for Group I and "early" Group III testing and 2400°F for Group II and Group III testing.
4. Be capable of operation without failure at a peak power of up to 1.4 kw/ft with a stepped cosine power distribution as shown in Figure 2-3 of this report.
5. Be capable of undergoing repeated quench cycles without failure.
6. Provide accurate and reliable data regarding clad temperature as a function of time at several elevations.

A.2 HEATER ROD DESIGN

A brief description of the heater rod design developed to meet the above objectives is contained in Section 2.1 of this report. As illustrated in Figure 2-4, the heater rod is sixteen feet long with a diameter of 0.422 inch and has an active heated length of twelve feet. Type 347 stainless steel was used as the clad for Group I and II and Zircaloy -4 clad was used for Group III.

The resistance element for Group I and "early" Group III tests was Nichrome V; Kanthal A-1 was used for Groups II and III. The desired stepped cosine power

distribution was achieved by varying the number of turns per unit length along the heated length. For example, there were 165 turns per foot in the peak power region and an average of 100 turns per foot over the length of the heater, yielding a peak to average heat flux of 1.65. The power distribution was flattened at each end because it was not practicable to build these heaters with less than forty-eight turns per foot.

Power tie-in was accomplished at both ends of the rod through solid nickel conductors connected to the resistance element. The heater insulation was boron nitride swaged to a density of approximately 2 gm/cm. Silicone oil impregnated mica wafers were used to seal the heater rod ends against moisture.

Heater rod instrumentation was accomplished by means of thermocouples located along the inside wall of the cladding. Chromel alumel thermocouples within a forty mil stainless steel sheath containing magnesium oxide insulation were used. Typically, three or five thermocouples were installed during fabrication of the heater with the junctions located as indicated in Table 2-1. The thermocouple junctions were non-grounded in order to minimize electrical noise pick-up from high temperature leakage currents.

A.3 GROUP I HEATER ROD DEVELOPMENT

Group I heaters were required to withstand approximately 40 quench cycles with peak temperatures up to 2100°F and peak powers up to 1.40 kw/ft, (10.2 kw total power). Nichrome V, with a melting temperature of 2550°F, was selected as the resistance element for these heaters because its electrical resistance is relatively independent of temperature and because prior experience indicated it would be able to provide the desired lifetime. The development program was aimed at proving fabrication techniques, thermocouple type and installation, and heater and thermocouple performance under quench conditions. The basic heater and thermocouple mounting techniques were developed and proof-tested in a series of five short length heaters (two feet long to five feet long). Finally, full length heaters were built, inspected and quench tested. Performance of the Group I heaters was well within expectations; in subsequent FLECHT testing there were no heater failures in a series of 50 tests with peak temperatures up to 2100°F.

A.3.1 Insulation Selection

Boron nitride was selected as the insulation material for FLECHT heaters because it has a substantially higher thermal conductivity than altenate materials such as alumina or magnesia. Thus, for a given clad temperature, the resistance element temperature is lower with boron nitride than with the other materials which were considered. In addition, concern about Zircaloy-ceramic reactions as a possible cause of Group III heater failure at elevated temperature was a factor in the preference for boron nitride. Subsequent BWR FLECHT experience has shown that reactions between Zircaloy and alumina can take place at temperatures as low as 1500°F and can result in heater rod failure.*

A comparison of the thermal response of a boron nitride FLECHT heater rod with a UO_2 fuel rod is shown in Figure A-1. The clad temperature drops more rapidly for the UO_2 rod than the boron nitride rod because of the higher thermal conductivity and the higher density-specific heat product of the boron nitride. However, this difference in behavior is not expected to have a significant effect on measured heat transfer coefficients.

A.3.2 Thermocouple Arrangement

Several thermocouple arrangements were considered:

1. External sheathed thermocouples mounted in grooves within the cladding to be held in place when the groove is subsequently closed during swaging.
2. External thermocouples spot welded to the cladding.
3. Internal thermocouples with the junction spot welded to the wall of the cladding and insulation of the bare lead wire achieved by the "wetting" action of the boron nitride.
4. Internal mounting of sheathed thermocouples. The thermocouples are located along the inner wall during heater assembly and held in place by the compacted boron nitride.

*Graber, M. J., Zelezny, W. F., Schmunk, R. E., "A Metallurgical Evaluation of Simulated BWR Emergency Core Cooling Tests", IN-1453, February 1971.

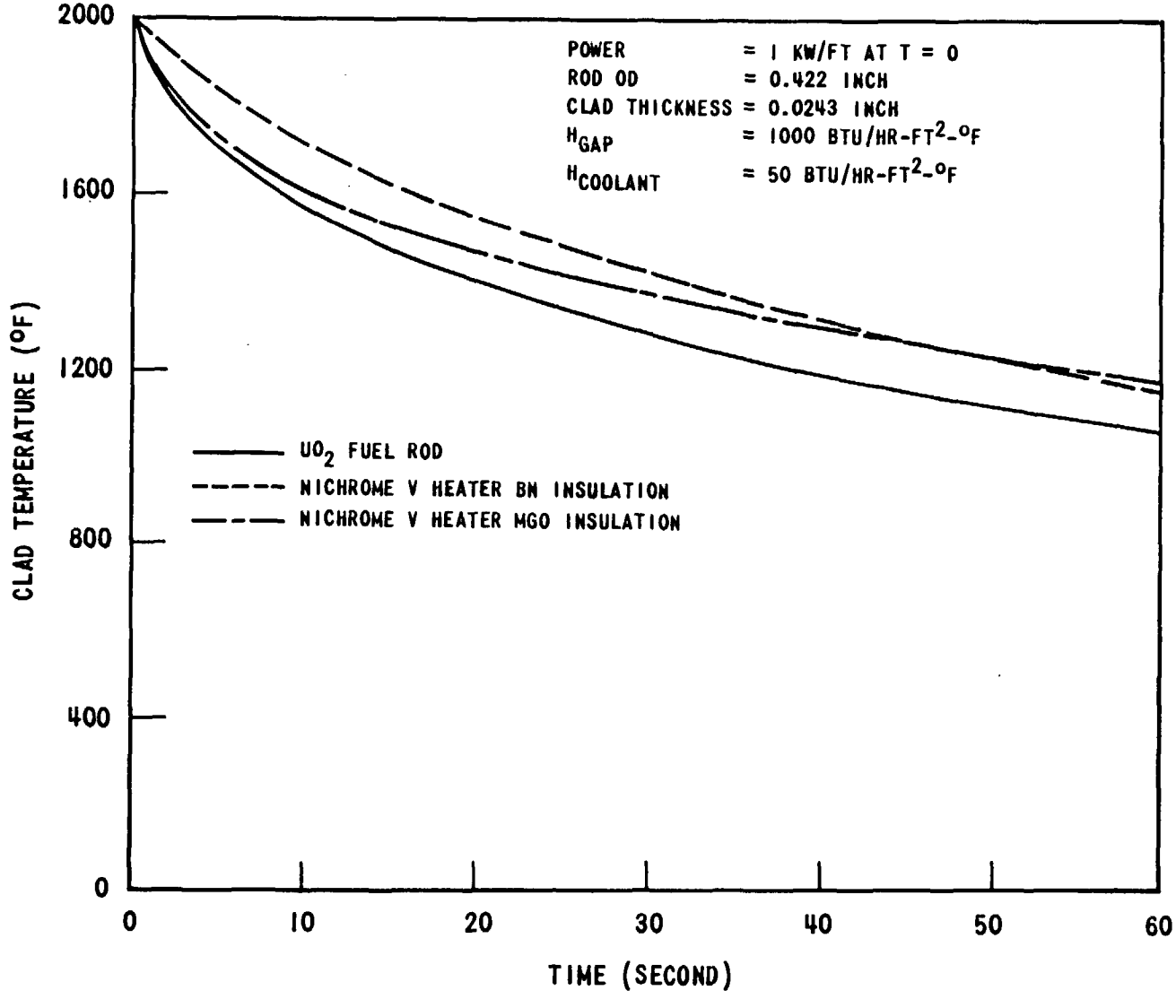

Figure A-1. Temperature Response of SS Clad Heater Rods

The fourth method, internal mounting of sheathed thermocouples, was selected for the full length FLECHT heaters. The first method, sheathed thermocouples in external grooves, was rejected because it was reported elsewhere that the thermocouple wires would break or come out of the grooves during quenching. The second case, external thermocouples, worked reasonably well, but was rejected because temperature traces were erratic during flooding. In addition, with the FLECHT bundle designed for pressurized operation additional seals would be required for the external thermocouples, while with internal thermocouples additional seals are not required. The third method, welded internal thermocouples could not be built. The "wetting" action of the boron nitride did not prevent grounding of the bare thermocouple wire to the cladding. The internal thermocouple finally selected, chromel alumel within a 0.040 inch sheath and non-grounded junction, was thoroughly proof-tested in quench testing as discussed below.

A.3.3 Testing of Short-Length Heaters

The short length heaters were flood-tested under conditions corresponding to the projected FLECHT program. The flood-testing was accomplished with the heater centered within a vertical tube. A teflon stopper was fitted into the lower end of the tube with penetrations for the heater and water inlet. The test procedure was to apply full power, allow the heater to reach temperature, initiate flooding, continue flooding until the heater was quenched and finally turn off power and flow. Time-temperature, power and flooding rate data characterized each run.

The heater failures were always in the nichrome resistance element and always occurred during cooling of the heater at temperatures less than the peak temperature of the run. The ability of the heaters to withstand many cycles of quenching was well established in the flood testing (See Table A-1). Heater number 3 did not fail after 40 quench cycles to 1750°F; heater number 4 failed after 48 cycles, 8 of them at greater than 2000°F.

TABLE A-1

ABILITY OF HEATERS TO WITHSTAND QUENCHING

Heater No.	No. of Test Runs	Thermocouple Location	Range of Peak Temperature
1	1	Internal	2070
2	29	External	1000-2000
3	40	Internal	1000-1750
4	48	Internal	1000-2200
5	12	Internal	1600-2200

The internal chromel alumel thermocouples with non-grounded junctions performed very well in all tests giving well defined heat-up rates, temperature turnaround shortly after flooding and sharp temperature decrease as the heater quenched (transition from film boiling to nucleate boiling). The external thermocouple used in heater number 2 performed reasonably well, but temperature traces were erratic during flooding probably caused by water impinging on the lead wire with resulting conduction heat loss in the vicinity of the junction.

A.3.4 Full Length Heater Testing

Two full length heaters were built, inspected and flood tested prior to release of the production order for Group I heaters. The heaters were well within specifications on length, diameter, thermocouple location, coil centering and power distribution. The power distribution was determined by a count of turns per unit length on X-rays from each of the stepped zones. The turns ratios were within 2 percent of requirements in all cases.

These heaters were each flood tested in a series of six tests with start-of-flood temperatures ranging from 1800°F to 2200°F. The heaters survived testing up to 2150°F, but failed in flooding at 2200°F.

A.4 "EARLY" GROUP III HEATER ROD EXPERIENCE

The Zircaloy heaters used in early Group III testing were an extension of the Group I design except that cladding was Zircaloy-4 instead of Type 347

stainless steel. There was no development testing (flood testing) of these Zircaloy heaters because the temperature requirements (up to 2100°F) were the same as in Group I testing.

The performance of the heaters was generally satisfactory in the heat-up and temperature turnaround phases of the 2000°F FLECHT tests, however, the mid-plane thermocouple response was unexpectedly sluggish during cool-down, especially during quenching. In addition, the mid-plane thermocouples in several cases did not drop to system saturation temperature following quenching, but instead remained several hundred degrees higher. See Figure A-2 for a comparison of one of these "degraded" quenches with a normal quench.

The cause of the degraded cooling behavior was a heat transfer gap which developed between the Zircaloy cladding and the boron nitride core of the tubular heater when operated at temperatures greater than 1700°F. At high temperature, outgassing of the boron nitride led to sufficient internal pressure to cause swelling of the Zircaloy-4 cladding (Zircaloy-4 has substantially less high temperature strength than the Type 347 stainless steel used in Group I cladding). See Table A-2 for the relationship between peak operating temperature, mid-plane swelling and mid-plane temperature following quenching. Rod 3D, which swelled to 0.460 in. had a mid-plane temperature following quench of 1203°F, in contrast to rod 7G which at 0.428 in. operated at 234°F. Peak temperature of 3D was 2065°F, while 7G did not exceed 1491°F.

A.4.1 Single Rod Heat Transfer Tests

Following Run 2443, tests were performed on a new, unused single Zircaloy heater from the same batch used in early Group III testing. This heater was subjected to flooding tests at progressively increasing initial temperature. Before and after each flooding test, a steady state test at low temperature was performed to determine whether the steady state operating behavior was altered as a result of the flooding tests. In addition, the outside diameter of the rod was measured after each flooding test to investigate cladding growth.

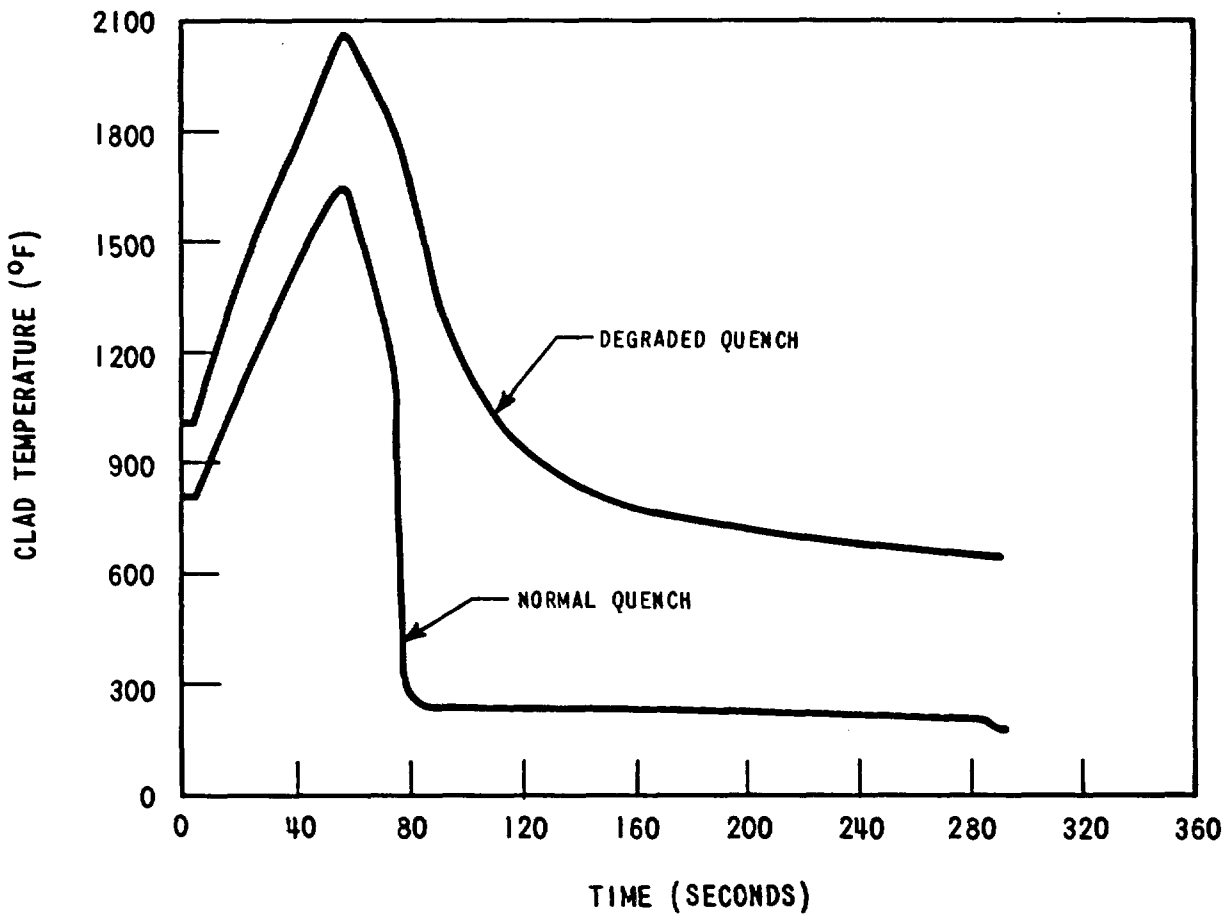

Figure A-2. Flecht Run 2443 - Comparison of Normal and Degraded Quenches

TABLE A-2

MID-PLANE DIAMETER AND MID-PLANE TEMPERATURE FOLLOWING QUENCH AFTER HEATING TO VARIOUS TEMPERATURES, RUN NO. 2443

Heater Rod	Peak Temperature Reached During Test Run (°F)	Mid-Plane Temperature Following Quench (100 Sec After Flooding) Nominal 235°F (°F)	Mid-Plane Diameter After Test Nominal 0.422 in. (in.)
2B	1870	291	0.442
5B	1910	474	0.440
2C	1890	402	0.452
3C	1960	463	0.447
1D	1685	350	0.442
2D	2005	688	0.452
3D	2095	1203	0.460
2E	1960	363	0.438
3E	2065	783	0.448
4E	1970	281	0.444
5E	1895	263	0.441
1F	1695	239	0.431
2F	1875	444	0.449
4F	1885	376	0.444
1G	1615	235	0.434
7G	1491	234	0.428

The flooding tests were performed at 1600°F, 1800°F, and 2000°F. During the 1600°F run, the mid-plane thermocouple quenched normally. The quench from 1800°F displayed a slight amount of degradation; it was somewhat slower than at 1600°F. The 2000°F run had a greatly degraded quench which was similar to the cooldown behavior of the Zircaloy bundle test.

The steady state tests showed a marked increase in the heat transfer resistance at the mid-plane thermocouple elevation after the 1800°F flooding run. This increase in heat transfer resistance is explained by a gap developing between the Zircaloy cladding and the boron nitride core as shown by mid-plane diameter measurements tabulated below:

EVENT	OD AT MID-PLANE (in.)
New Heater	0.422
After 1600°F	0.432
After 1800°F	0.438
After 2000°F	0.464

A.4.2 Boron Nitride Outgassing

The outgassing characteristics of the boron nitride were determined by mass spectrographic quantitative analysis of gases released as the boron nitride was heated in vacuum. In addition, the gas composition from within heater 4C (Run 2443) was determined. The gas composition found in heater 4C was consistent with outgassing analysis of boron nitride specimens provided by the manufacturer. The quantity of gas released was sufficient to explain the swelling of the heaters during Run 2443.

The gas composition within the swelled region of heater 4C was as follows:

Hydrogen	17%
Nitrogen	69%
Methane	1.5%
Carbon Monoxide	10%
Carbon Dioxide	1%

This heater was non-instrumented, but probably reached 2100°F, based on symmetry in the heat transfer assembly with heater 3D. (Heater 3D had a peak temperature of 2095°F and mid-plane swelling to 0.460 in., mid-plane diameter of 3D swelled to 0.465 in.).

Quantitative mass spectrographic analysis was performed on a specimen of BN powder provided by the manufacturer. The specimen was outgassed for approximately five minutes at 500°F, 1000°F, 1500°F and 2000°F respectively. Results were as follows on two identical specimens:

TOTAL GAS RELEASE

Temperature (°F)	Gas Release Specimen #1 (cc - atm/gm)	Gas Release Specimen #2 (cc - atm/gm)
500	0.010	0.034
1000	0.038	0.029
1500	0.030	0.031
2000	0.072	0.145
	0.151	0.239

GAS COMPOSITION AT EACH TEMPERATURE

500°F	Specimen #1 (%)	Specimen #2 (%)
Nitrogen	5.6	8.8
Water	85.0	81.0
Carbon Dioxide	3.1	2.7
Hydrocarbons	2.9	4.8

1000°F	Specimen #1 (%)	Specimen #2 (%)
Nitrogen	4.8	8.9
Water	26.0	15.0
Hydrogen	4.6	8.0
Carbon Dioxide	24.0	18.6
Hydrocarbons	40.0	41.0
Carbon Monoxide		7.2

1500°F	Specimen #1 (%)	Specimen #2 (%)
Nitrogen	4.7	8.7
Hydrogen	51.0	47.0
Carbon Dioxide	24.0	8.6
Carbon Monoxide	7.4	9.4
Hydrocarbons	12.0	23.0

2000°F	Specimen #1 (%)	Specimen #2 (%)
Nitrogen	37.0	16.0
Hydrogen	30.0	55.0
Carbon Monoxide	32.0	28.0

The volume of gas released, approximatley 0.2 cc - atm. per gram of boron nitride, would produce 90 psia at 2000°F in the annular void in heater 4C. This pressure is sufficient to cause the observed swelling of the Zircaloy tubing at 2100°F.

The specifications for the boron nitride used in Group II heaters, Kanthal elements with stainless cladding, were expanded to include a requirement for high temperature outgassing prior to assembly of the heaters. The specification required outgassing of the boron nitride at 1800°F for four hours under vacuum. In addition, the boron nitride was to be held at approximately 400°F during all subsequent operations when it could contact the atmosphere (for example, filling the heater tube).

A.5 GROUP II HEATER ROD DEVELOPMENT

The Kanthal tubular heater with stainless steel cladding was required to withstand repeated quenching with peak temperatures up to 2400°F. The basic heater construction and power distribution was the same as the Group I heaters. The development program was aimed at proving satisfactory short term performance of chromel alumel thermocouples at the high temperatures, and satisfactory heater and thermocouple performance during quench tests from 2400°F. Performance of the Group II heaters was highly satisfactory; there were no heater failures in a full series of FLECHT tests at temperatures up to 2400°F, although three heaters failed in a later test series within a bundle constructed with heaters used in previous testing.

A.5.1 Resistance Element Selection

Kanthal A-1 was selected as the resistance element for these heaters because its electrical resistance is relatively constant with temperature. Originally it was thought that molybdenum, with a melting point of 4,750°F, might be required for the Group II and III heater rods. However, the electrical resistivity of molybdenum is very temperature dependent; its resistivity at 2500°F is approximately eight times that observed at 70°F. Thus, when the

Kanthal heater bench tests discussed below gave favorable results, it was decided to specify Kanthal as the resistance element for the Group II and III heater rods.

A.5.2 Thermocouple Calibration

The calibration of the thermocouples (chromel alumel within 0.040 inch stainless sheath and non-grounded junction) was checked at temperatures up to 2400°F and the measured temperatures were in exact agreement with the standard at 2200°F and within one percent at 2400°F. Even after exposure to 2400°F for 15 minutes there was no substantial shift in calibration. Results were as follows:

Standard Temperature (°F)	Chromel Alumel #1 (°F)	Chromel Alumel #2 (°F)
2002	2006	2004
2188	2188	2186
2428	2406	2405
(hold at 2400°F for 15 minutes, then cool to 1600°F and reheat)		
1640	1643	1641
2007	2007	2006
2204	2191	2190
2403	2381	2380

A.5.3 Part and Full Length Heater Testing

Three Kanthal stainless development heaters were tested, the first heater was five feet long with a uniform heated length, the other two were full length prototypes. The five foot heater survived a series of quench tests ranging from 2200°F to 2400°F peak temperature, then failed during a sixth test at 2480°F. The full length prototypes each survived a series of nine quench tests with peak temperatures from 2200°F to 2450°F. The heaters were satisfactory for further use following this testing.

The diameter of the Kanthal heaters increased by 0.010 in. at mid-plane, but there was no change in the length at the end of the nine quenches. The increase in diameter was caused by expansion of the boron nitride at elevated temperatures, and not by internal gas pressure. This was evident because all

quench curves were sharp with a return to system saturation temperatures; there were no degraded quenches like those associated with cladding separation in early Group III testing.

A.6 GROUP III HEATER ROD DEVELOPMENT

The Group III heater was required to operate for only one quench cycle at temperatures up to 2400°F. Each Group III test assembly was used only once in order to properly simulate the effect of metal-water reaction on clad behavior during a loss-of-coolant accident and to permit a post-test metallographic examination of the thickness of the Zirconium oxide produced (see Appendix B).

The construction of the Zircaloy Kanthal heater was the same as the Group II heaters except that the sheathed thermocouples were coated with alumina (approximately 0.003 inch thick) in order to prevent metallurgical reaction between the thermocouple sheath and Zircaloy cladding. The boron nitride was outgassed at 2200°F instead of the 1800°F specification for Group II heaters; the higher outgassing temperature was employed to minimize the possibility of swelling of the Zircaloy at elevated temperature. Performance of the Group III heaters in the two tests performed appeared to be satisfactory; the severity of the test conditions and performance of other test assembly components apparently were responsible for the heater rod failures which occurred. For example, in the final Group III test, several heaters failed during flooding while the mid-plane temperatures were only 2200-2300°F. The heaters apparently failed because of higher temperatures that developed above the mid-plane region which were most likely caused by steam reaction with a Zircaloy grid. There was no evidence of the swelling problem encountered in the "early" Group III tests in either of these tests.

The Group III development program again consisted of quench testing full length heaters. Four sets of two heaters each were tested (Table A-3). The failure of the first set of heaters appeared related to swelling and high temperature regions occurring at locations away from the mid-plane thermocouple. In order to prevent any formation of heat transfer gaps, the outgassing temperature was increased to 2200°F and the final tests were run with external pressure (60 psia)

as in FLECHT run conditions. The final two heaters each performed satisfactorily in two quench tests from 2250°F and 2350°F. The mid-plane swelling (0.017 inch) was caused by high temperature expansion of the boron nitride; all quench curves were sharp with a return to system saturation temperature.

TABLE A-3

QUENCH TESTING OF GROUP III HEATERS

Heater Number	BN Outgassing Temperature (°F)	External Pressure During Test	Peak Temperature (°F)	Mid-Plane Swelling (In.)	Length Increase (In.)	Comments
1A	1800	Atmospheric	2200 2220	0.015 0.017	1 1-1/4	Heater failed 45 seconds after start-of-flooding in second test when mid-plane temperature was 1750°F. Failure region was swelled, 8-1/2 inches below mid-plane.
1B	1800	Atmospheric	2380 thermocouple failure	0.010	1	Failure 12 seconds after start-of flooding in swelled area 8 inches below mid-plane.
2A	1800	Atmospheric	2325	0.015	3/4	Failure 22 seconds after start-of-flooding in swelled area 3 inches above mid-plane.
2B	1800	60 psia 60 psia 60 psia 60 psia 60 psia	2100 2200 2300 2400 2450	0.010 0.012 0.013 0.016 not measured	3/4 1 1-1/2 1-3/4	Failure after 2450°F start-of-flooding, failure region not evident from external appearance.
3A	2200	60 psia	2400	0.015	1-1/2	No heater failure.
3B	2200	60 psia	2400	0.012	1-1/4	Failure 10 seconds after 2400°F start-of-flooding, swelled region 8 inches above mid-plane.
4A	2200	60 psia	2250 2350	not measured 0.017	 1-1/2	No heater failure.
4B	2200	60 psia	2250 2350	not measured 0.018	 1	No heater failure.

APPENDIX B

MATERIALS EVALUATION

F. D. Kingsbury
J. F. Mellor
A. P. Suda

B.1 INTRODUCTION

In order to properly analyze FLECHT Group III heat transfer data, information regarding the amount of energy released during a test by the metal-water reaction was required. The purpose of the materials evaluation portion of the FLECHT program was to determine the extent of metal-water reaction in the Group III tests and compare it with the predictions of an analytical model. Information regarding the effect of emergency core cooling system operation on fuel element integrity was also to be obtained.

The specific objectives of this task were to:

1. Determine the extent of metal-water reaction as a function of test conditions and bundle location.
2. Determine whether the reaction is homogeneous.
3. Determine the axial distribution of hydriding subsequent to the metal-water reaction and emergency core cooling.
4. Determine whether the hydrogen distribution is influenced by the oxygen solution and to what extent.

This appendix summarizes the results of the metallographic analysis of the Zircaloy clad heater rods from the four Group III tests. The data from Runs 2443, 2544, and 8874 were obtained by Westinghouse and the data from Run 9573 was obtained by Idaho Nuclear Corporation. An earlier publication (WCAP-7444) reported on results from the two "early" Group III tests (Runs 2443 and 2544) together with results of the materials characterization of as-fabricated Group III heater rod cladding.

B.2 SPECIMEN SELECTION, PREPARATION, & EXAMINATION

Actual test conditions and transient temperature data for the Four Group III tests are presented in Table B-1. The transient temperature data reported was obtained from the midplane thermocouple (six foot elevation) on the hottest rod. The turnaround time reported (t_{turn}) represents the elapsed time from the start of flooding to the time the peak heater rod temperature (T_{peak}) is reached.

TABLE B-1

GROUP III TEST RESULTS

	"Early" Group III			
Run Number	2443	2544	8874[a]	9573
Initial temperature (°F)	2035	2017	2297	1970
Flow rate (in./sec)	10.0	4.0	6.0 (for 8 sec)-1.0	1.1
Peak Power (kw/ft)	1.24	1.24	1.24	1.24
Inlet temperature (°F)	150	150	141	140
Pressure (psia)	56	58	64	61
Peak heater rod temperature	2102	2144	2361	2320[b]
Turnaround time (sec)	6	12	4	--

[a] with fallback

[b] at 18 seconds

As can be seen from Table B-1, the peak temperatures for the two "early" Group III tests were only 42°F apart. Due to the similarity in peak temperatures for these two runs it was decided to concentrate the metallographic examination on the bundle used for Run 2443 (Zircaloy Bundle No. 1) and to take only a limited number of samples from the bundle used for Run 2544 (Zircaloy Bundle No. 2). Thirteen specimens were therefore taken from Bundle No. 1 and two from Bundle No. 2.

Fifteen specimens were taken from the bundle used for Run 8874 (Zircaloy Bundle No. 3) and three from the bundle used for Run 9573 (Zircaloy Bundle No. 4). Table B-2 gives the radial and axial location within the bundles of the specimens taken. With one exception, the specimen locations were chosen to correspond to thermocouple locations within the heater rods. The time temperature histories for typical high temperature locations are presented in Appendix C. It should be noted that for those thermocouples which exhibited "degraded" quench behavior, (see Appendix A), the temperature data presented in Appendix C probably is somewhat higher than the actual cladding temperature.

The specimens selected as discussed above were prepared for metallographic determination of oxide film thickness, hydrogen content and distribution, and grain size in accordance with standard procedures. These detailed, step-by-step procedures were given in Appendix B of WCAP-7444.

B.3 RESULTS OF METALLOGRAPHIC EXAMINATIONS

B.3.1 Metallographic Structure

In the "early" Group III bundles (Runs 2443 and 2544), the sections taken represented rod locations which had been both below and above the transformation temperature from the $\alpha + \beta$ to the β phase. There are, therefore, marked differences in the type of microstructure dependent upon prior thermal history. The sections examined from Runs 8874 and 9573 were, without, exception, taken from rod locations which had been above the transformation temperature and, consequently, differences in microstructure were of degree rather than type.

The following microstructures were observed in the specimens examined:

1. For a peak temperature of 900°F, surface oxidation was minimal and the microstructure was basically the same as the as received material. (See Figure B-1.)
2. For peak temperatures above 1000°F, but below the $\alpha + \beta$ transformation temperature, even where the time above 1000°F was relatively

TABLE B-2

METALLOGRAPHIC SPECIMEN LOCATIONS

Heater Rod Number	Section Location	T_{peak} (°F)	t_{turn} (sec)
	ZIRCALOY BUNDLE NO. 1 - RUN 2443		
3C	2 feet below midplane	1550	1.0
3C	rod midplane	1960	4.5
3C	2 feet above midplane	1520	2.5
3D	2 feet below midplane	1610	2.0
3D	rod midplane	2100	6.0
3D	2 feet above midplane	1580	2.5
3E	2 feet below midplane	1635	1.5
3E	rod midplane	2065	4.5
3E	2 feet above midplane	1560	2.5
2E	2 feet below midplane	1580	2.0
2E	rod midplane	1960	3.5
2E	2 feet above midplane	1530 (estimated)	2.5 (estimated)
2E	4 feet above midplane	900	3.5
	ZIRCALOY BUNDLE NO. 2 - RUN 2544		
5B	rod midplane	2145	12.0
4E	rod midplane	2100	7.0
	ZIRCALOY BUNDLE NO. 3 - RUN 8874		
3C	2 feet below midplane	2013	3.0
3C	rod midplane	2365	4.0
3C	2 feet above midplane	2089	3.0
3D	2 feet below midplane	2086	3.0
3D	rod midplane	2357	3.0
3D	2 feet above midplane	2089	3.0
3E	rod midplane	2326	2.0
2B	rod midplane	2270	3.0
2C	rod midplane	2321	3.0
2D	rod midplane	2264	3.0
2E	rod midplane	2273	4.0
2F	rod midplane	2361	4.0
1F	rod midplane	2093	4.0
4F	rod midplane	2058	3.0
5E	rod midplane	2259	3.0
	ZIRCALOY BUNDLE NO. 4 - RUN 9573		
2E	rod midplane	2384	57.0
4F	rod midplane	2457	56.0
4E	rod midplane	2545	57.0

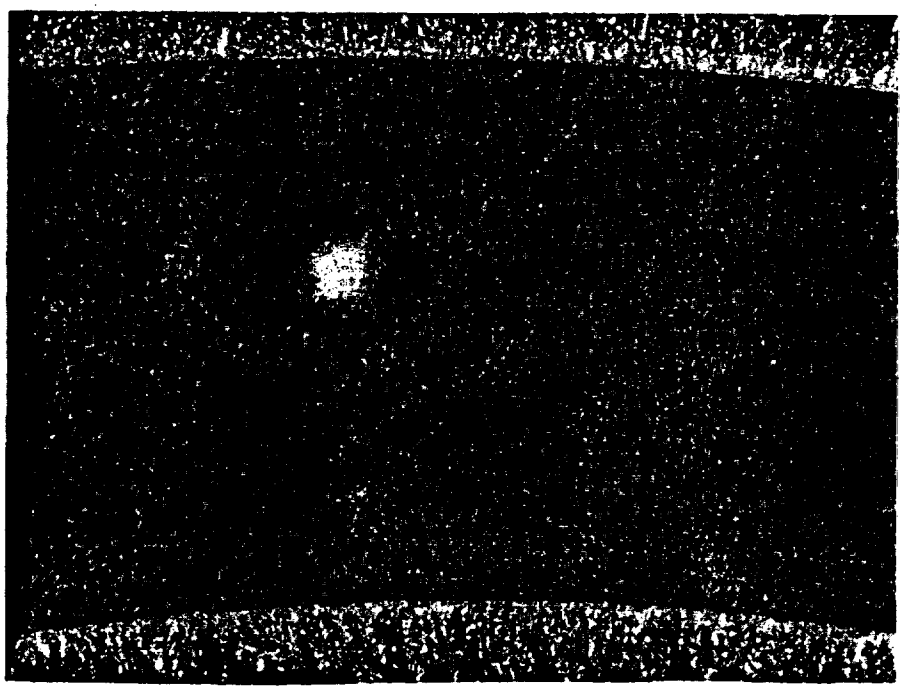

NEGATIVE 12868-3 ROD NO. 2E, BUNDLE NO. 1 100X
4 FEET ABOVE MIDPLANE
GRAIN SIZE - ASTM 10

Figure B-1. Microstructure of a Rod Section Heated to 900°F

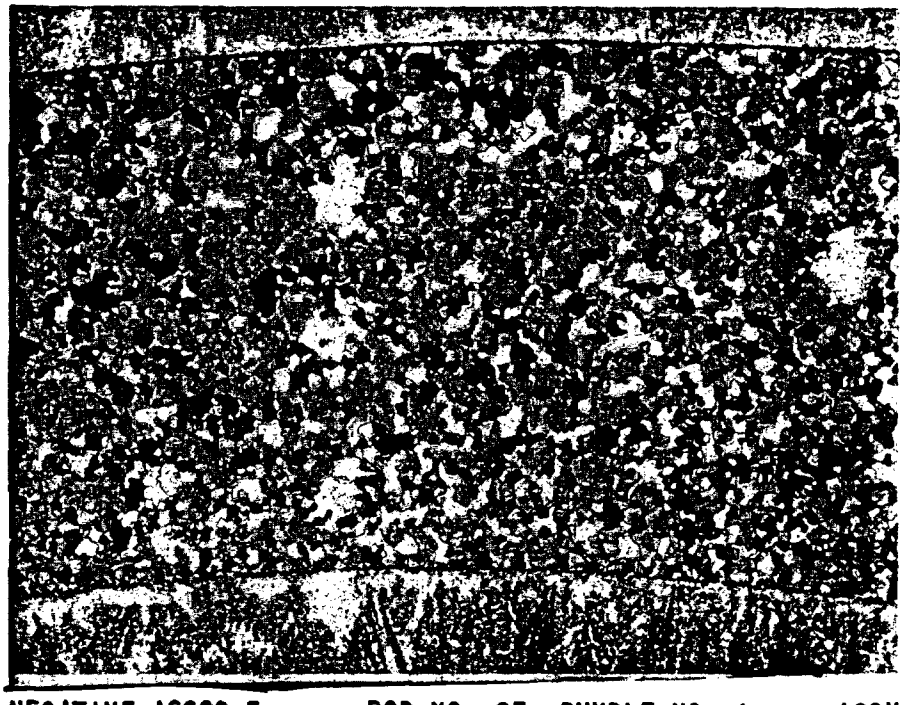

NEGATIVE 13033-5 ROD NO. 2E, BUNDLE NO. 1 100X
2 FEET ABOVE MIDPLANE
GRAIN SIZE - ASTM 9

Figure B-2. Microstructure of a Rod Section Heated to 1500°F

short, grain growth of Zircaloy was rapid. As seen in Figure B-2, a visibly larger and more clearly defined grain structure was evident. The extent of oxidation was still minor.

3. For peak temperatures above the transformation temperature from the $\alpha + \beta$ to the β phase, rapid grain growth occurred. Under the relatively rapid cooling conditions typical of reflooding, the prior β phase reverted back to the α phase in the form of elongated platelets of the "basket weave" or "Widmanstetten" type (See Figure B-3.) This "prior-β phase" microstructure was observed in the peak temperature specimens from Runs 2443, 2544 and in all of the specimens from Run 8874. The extent of oxidation in such specimens was measurable (>0.1 mil).
4. For specimens where the test temperature was high enough and the time at test temperature was of sufficient duration to permit significant oxidation and consequent thermal diffusion of oxygen into the rod surface, another microstructure was found between the surface oxide and prior-β phase. This was the oxygen-enriched α-zirconium layer, with a thickness comparable to that of the oxide film, as seen in Figure B-4. The α layer shows a single grain structure as evidence of substantial grain growth at the test temperature.

The presence of the α-zirconium layer seen in Figure B-4 is explained by the zirconium-oxygen phase diagram shown in Figure B-5. The phase diagram shows that the transformation temperature between the $\alpha + \beta$ and β phases is increased significantly by the presence of oxygen. Where the oxygen level in the base metal is approximately 1000-1500 ppm (i.e., the "normal" range for Zircaloy) the transformation temperature is approximately 1800°F. At about ten atom percent oxygen, the transformation temperature is in excess of 3600°F.

B.3.2 Oxide Thickness

The results of oxide film thickness measurements on rods from the "early" Group III bundles (Runs 2443 and 2544) are shown in Table B-3. Results of both oxide film thickness and α-zirconium thickness on rods from Run 8874 are shown in Table B-4 together with the limited data reported for Run 9573.

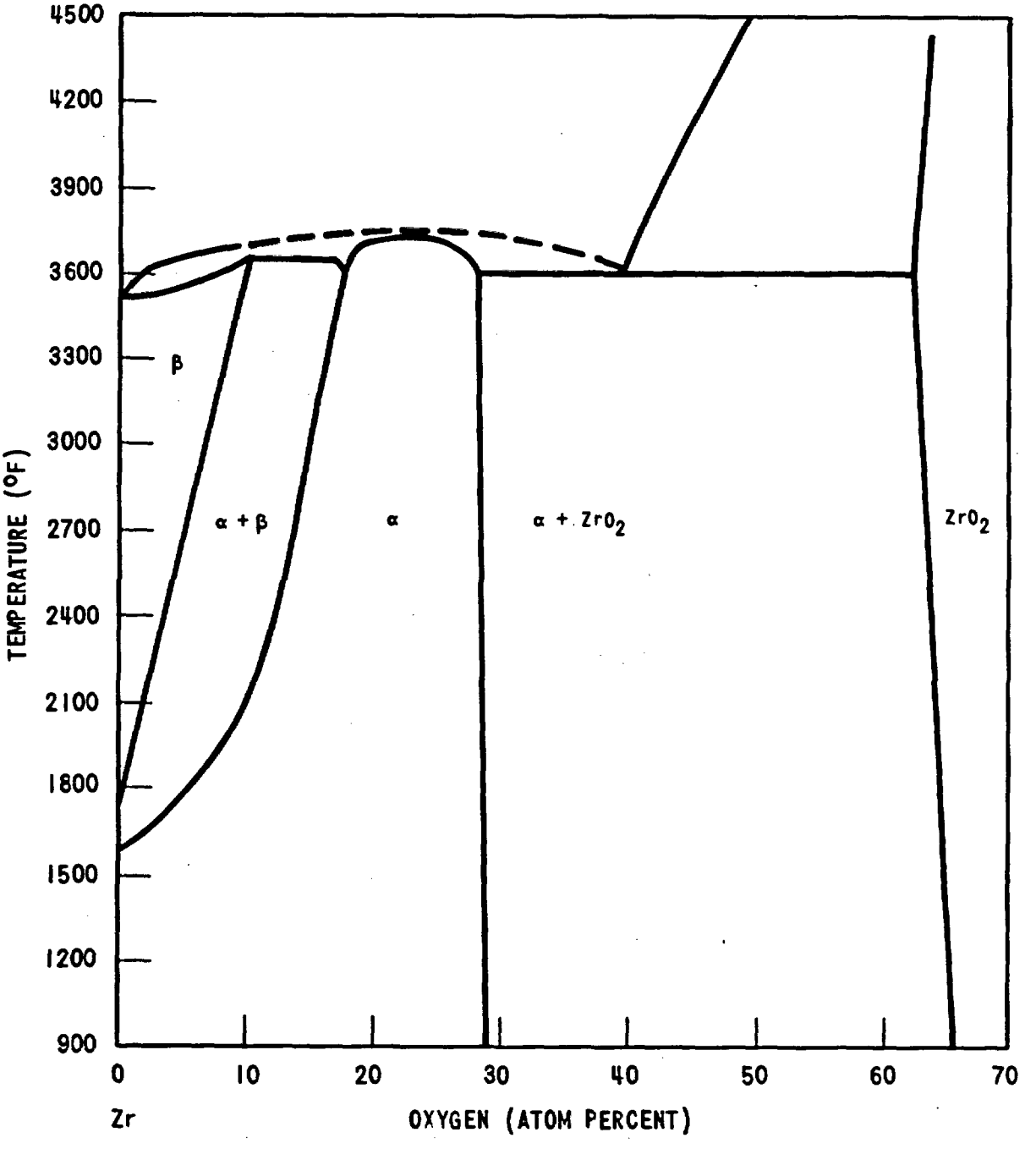

Figure B-5. Zirconium - Oxygen Phase Diagram [1]

Negative 12,867-5 ROD NO. 2E, BUNDLE NO. 1 100X MIDPLANE

Figure B-3. Microstructure of Rod Section from Bundle No. 1 Heated to 1960°F

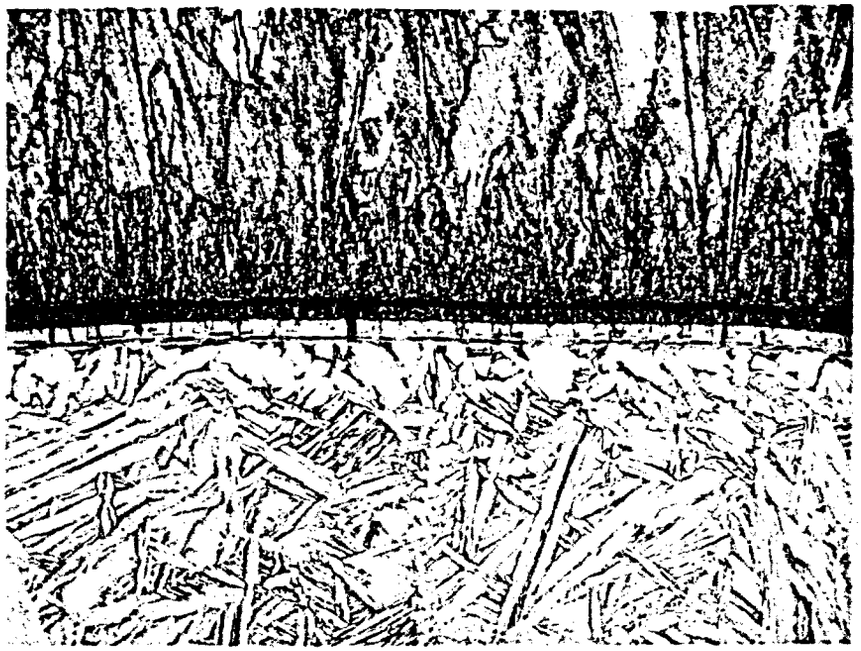

Negative 13,759 ROD NO. 3C-3, BUNDLE NO. 3 250X MIDPLANE

Figure B-4. Microstructure of a Rod Section From Bundle No. 3 Heated to 2365°F

TABLE B-3

OXIDE FILM THICKNESS FOR BUNDLES 1 & 2

Thermocouple Designation	Section Location	Peak Temperature (°F)	Calculated Oxide Thickness (mils)	Maximum Measured Oxide Thickness (mils)	Grain Size ASTM #
1st Bundle Run 2443					
(2E3)	2 feet below rod midplane	1580	0.00	<.1	9
(2E2)	Rod midplane	1960	.36	.35	Basket weave
-	2 feet above midplane	1530[a]	0.00	<.1	9
(2E1)	4 feet above midplane	900	0.00	0	10
(3C4)	2 feet below midplane	1550	0.00	<.1	9
(3C3)	Rod midplane	1960	.37	.35	Basket weave
(3C2)	2 feet above midplane	1520	0.00	<.1	9
(3E4)	2 feet below midplane	1635	0.00	<.1	9
(3E3)	Rod midplane	2065	.59	.4	Basket weave
(3E2)	2 feet above midplane	1560	0.00	<.1	9
(3D4)	2 feet below midplane	1610	0.00	<.1	9
(3D3)	Rod midplane	2100	.87	.55	Basket weave
(3D2)	2 feet above midplane	1580	0.00	<.1	9
2nd Bundle Run 2544					
(5B2)	Rod midplane	2145	1.36	.6	Basket weave
(4E3)	Rod midplane	2100	.75	.3	Basket weave

[a]Estimated.

TABLE B-4

QXIDE FILM AND α - ZIRCONIUM THICKNESS FOR BUNDLES 3 & 4

Thermocouple Designation	Section Location	Peak Temperature °F	Calculated Oxide Thickness, mils.	Measured Oxide Maximum Thickness, mils.	α-Zirconium Layer Maximum Thickness, mils.
		BUNDLE 3, RUN 8874			
3C3	Midplane	2365	--	1.23	0.98
2F2	Midplane	2361	1.96	1.21	0.97
3D3	Midplane	2357	--	1.14	1.41
3E3	Midplane	2326	1.83	1.09	1.27
2C2	Midplane	2321	1.82	1.26	1.32
2E2	Midplane	2273	1.70	1.14	1.33
2B2	Midplane	2270	1.65	1.01	1.20
2D2	Midplane	2264	1.49	1.07	1.02
5E3	Midplane	2259	1.40	0.90	1.00
1F2	Midplane	2093	0.86	0.82	0.85
3D2	2' Above Midplane	2089	0.85	0.64	0.75
3C2	2' Above Midplane	2086	1.06	0.62	0.74
3D4	2' Below Midplane	2086	0.68	0.55	0.65
4F2	Midplane	2058	0.59	0.45	0.56
3C4	2' Below Midplane	2013	0.44	0.46	0.59
		BUNDLE 4, RUN 9573			
2E2	Midplane	2384	2.45	1.75	--
4F2	Midplane	2457	2.88	1.75	--
4E3	Midplane	2545	3.77	2.25	--

It was apparent that the oxide film thicknesses observed in the specimens from Run 8874 were more uniform (Figures B-6, B-7) than in the earlier reported series (Figure B-8). There was also no evidence in Run 8874 of oxide cracking due to radial strain as noted in the prior work (Figure B-9). In both test series there was no evidence of oxide loss by spallation outside of the region of heater rod failure.

B.3.3 Hydrogen Uptake

In none of the metallographic sections examined in either the earlier or more recent test series was there any positive evidence of hydride precipitation. Analysis of a number of sections for hydrogen revealed overall hydrogen levels in the range 50-85 ppm with no perceptible correlations with respect to the extent of metal-water reaction. The fraction of the hydrogen generated in the metal-water reaction which is absorbed into the cladding is very low (i.e., less than 10 percent). The absence of visually precipitated hydride at the levels analyzed is not unusual for Zircaloy cooled rapidly from the β phase field.

B.3.4 Microhardness Measurements

Diamond pyramidal microhardness measurements were taken on 13 tube cross-sections traversing from the oxide/metal interface through the oxygen rich α-zirconium layer into the "prior β" phase. Results from three sections on a single rod (3C Run #8874) are shown in Figure B-10 and may be taken as representative of the general hardness pattern observed. The α-zirconium layer shows a very high hardness (>1200 DPH) at the oxide/α-zirconium interface which decreases down to approximately 600 DPH at the "visible" boundary between the α-zirconium and the "prior β" regions. The base hardness of the prior β region is approximately 200 DPH. It can be noted that the greater inward diffusion of oxygen at the higher peak test temperatures influences the hardness gradient markedly.

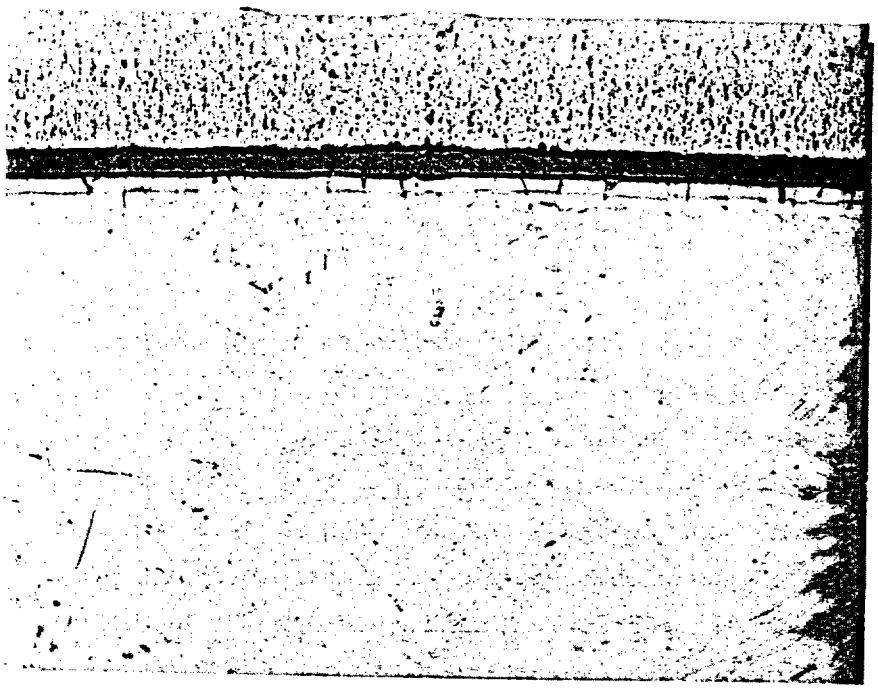

13,770 ROD NO. 3C BUNDLE NO. 3 250X

Figure B-6. Oxide Film Two Feet Above Midplane

13,764 ROD NO. 3E BUNDLE NO. 3 250X

Figure B-7. Oxide Film at the Midplane

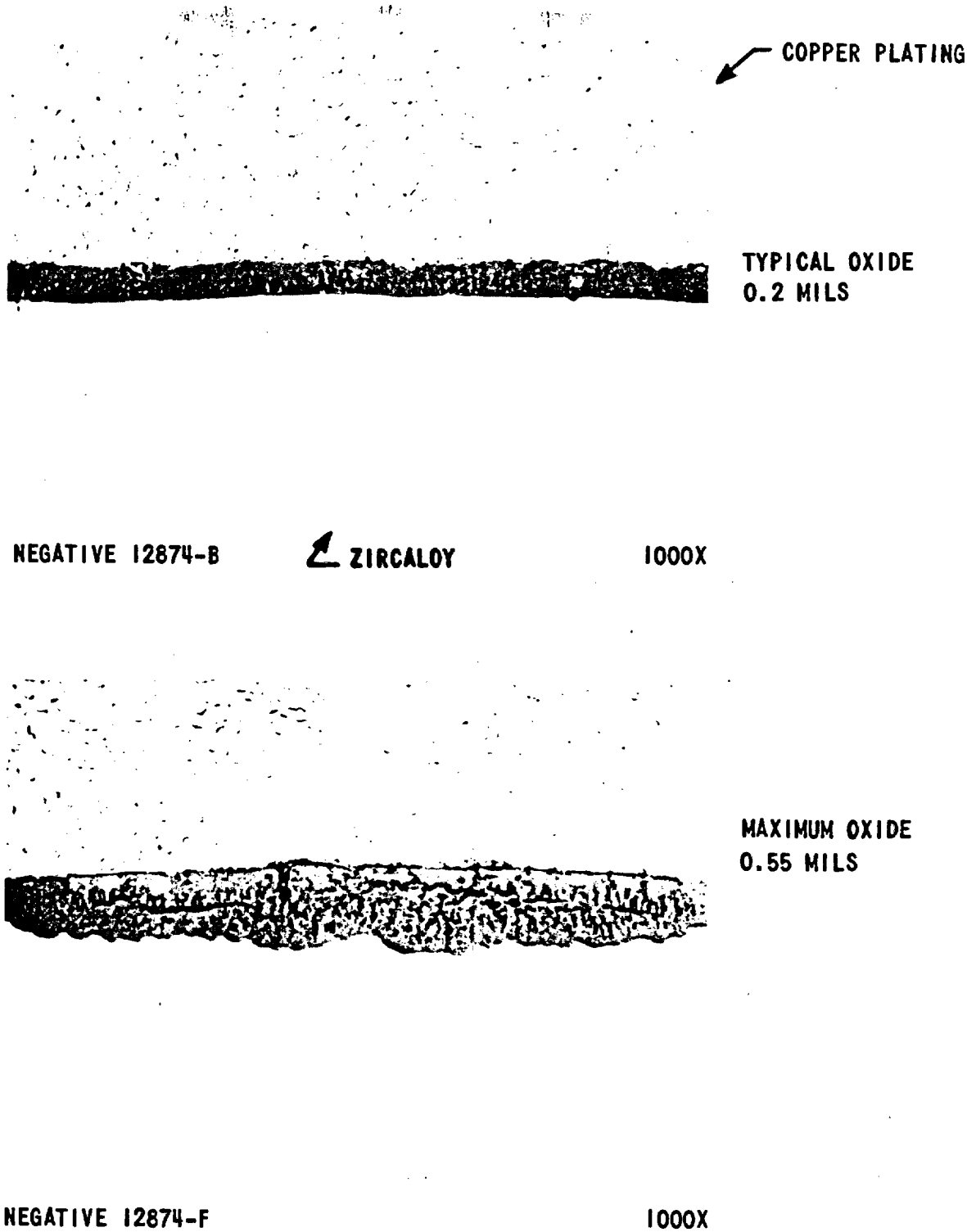

Figure B-8. Photomicrograph of Zirc-Oxide Film on Rod No. 3D - Midplane Bundle No. 2

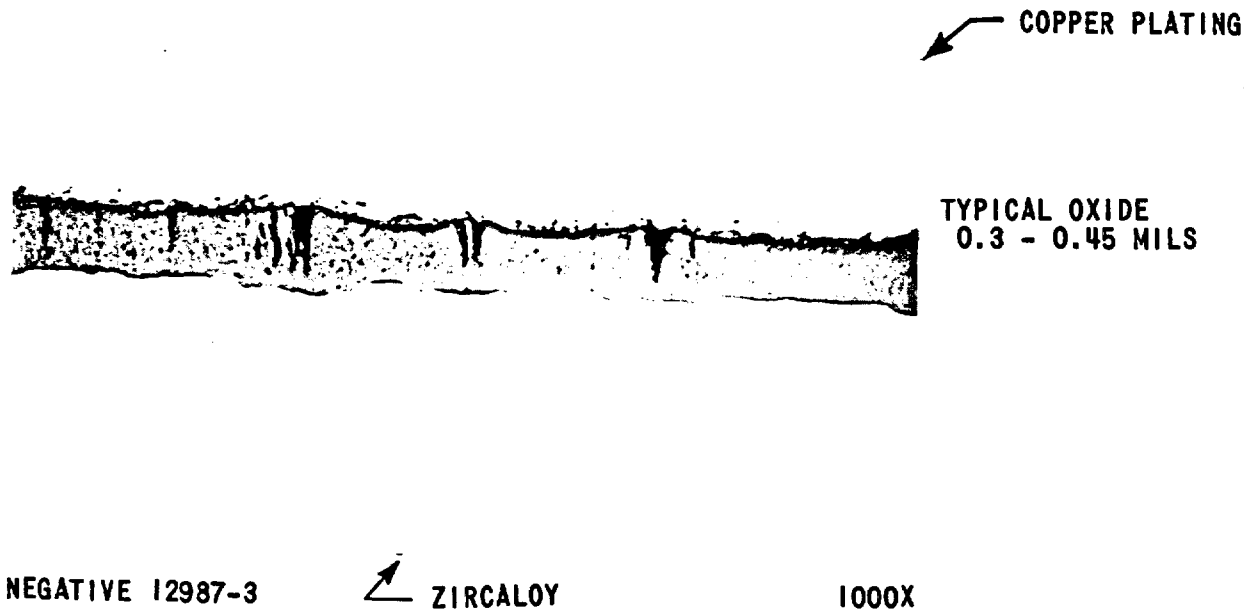

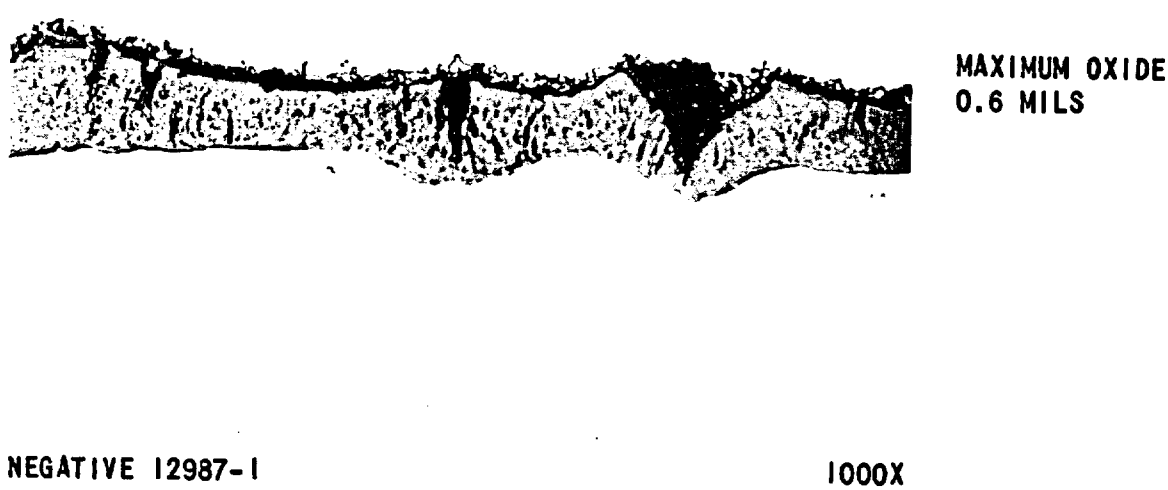

Figure B-9. Photomicrograph of Zirc-Oxide Film on Rod No. 5B Midplane Bundle No. 2

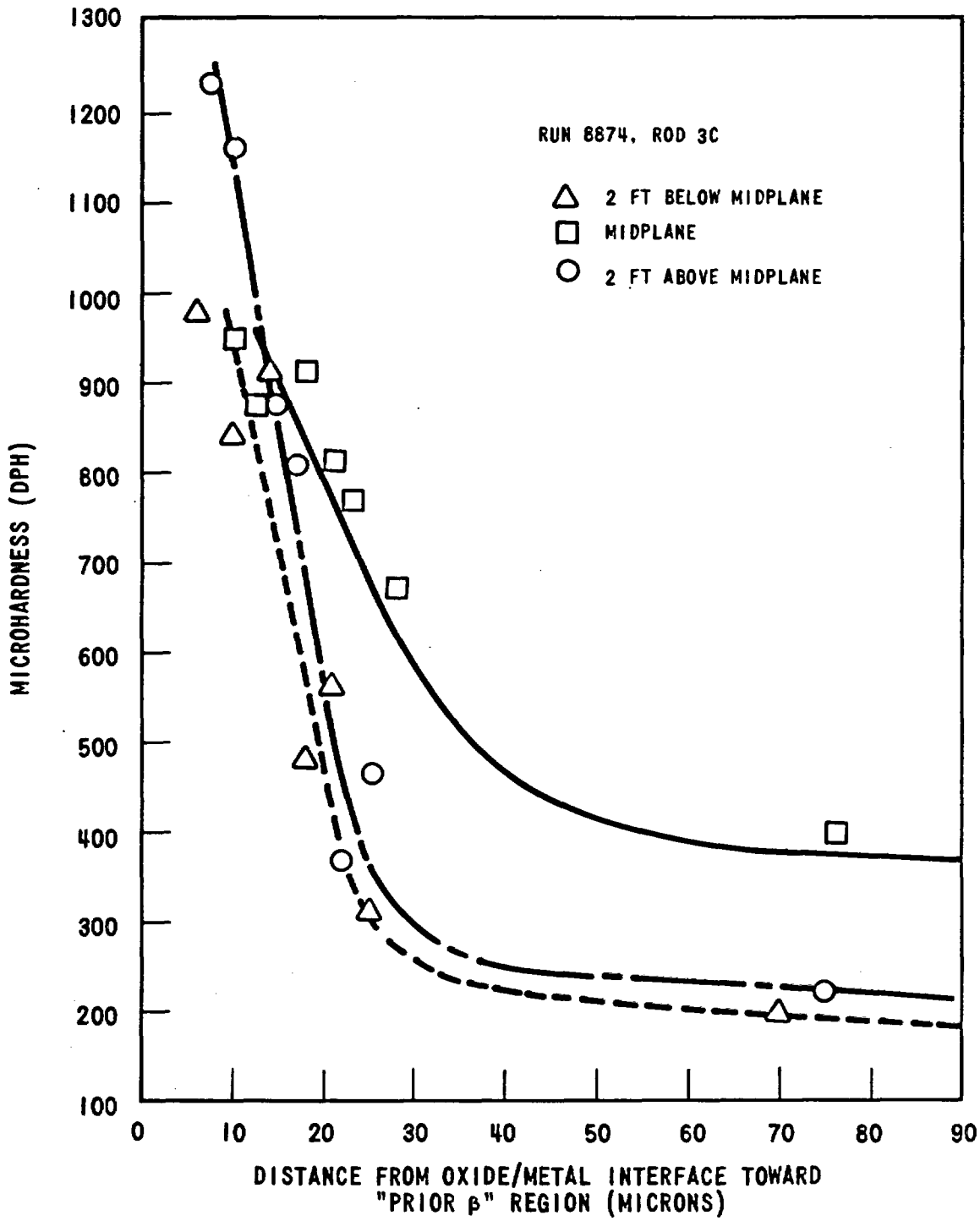

Figure B-10. General Hardness Pattern Observed

B.3.5 Materials Characterization

The metallurgical properties of as-fabricated heater rods were evaluated in order to provide background information relevant to the overall FLECHT program and to assist in interpretation of the post-test materials evaluation results.

The evaluation included tensile and burst tests and determination of texture, grain size, and hydride orientation.

B.3.5.1 Tensile and Burst Test Results

The results of the tests are shown in Table B-5. As anticipated, there was a substantial reduction in strength at elevated temperatures.

The tensile test results are consistent with the method of manufacture of the heater rods, the texture observed, and reported data on the strength and ductility of Zircaloy-4. The strength values of the burst tests at 725°F were slightly lower than anticipated -- there is generally 15-20 percent greater strength in the biaxial test compared with the uniaxial tensile test.

B.3.5.2 Texture

Inverse pole figures representing the texture of the as-fabricated heater rods are shown in Figure B-11. The pole figures show a high concentration of basal (0001) poles in the tangential compared to the radial direction in the tube. This type of texture is invariably obtained when the final stages of fabrication involve a reduction of the tube diameter without a corresponding reduction in the tube wall thickness. The effect of this texture is to induce radial hydride formation in a hydrided tube and to influence the relative uniaxial/biaxial strength ratios at least at temperatures <750°F.

B.3.5.3 Grain Size

The grain size of the as-received tube was very fine and approximated ASTM 11 (non-ferrous).

TABLE B-5

MECHANICAL PROPERTIES TESTS

Test No.	Test Temperature (°F)	0.2 percent Offset (psi)	Ultimate Strength (psi)	Ductility (percent)
Tensile Test				
No. 1	RT	83,800	92,950	8.5
No. 2	RT	85,275	95,200	7.9
No. 3	RT	86,350	97,000	10.7
Mean	RT	85,142	95,050	9.03
No. 4	725	45,150	46,600	a
No. 5	725	45,450	48,200	a
No. 6	725	44,660	47,750	13.6
No. 7	725	44,940	47,300	6.6
No. 8	725	46,460	48,750	6.0
Mean	725	45,332	47,720	8.73
Burst Test				
No. 1	725	41,520	50,760	29
No. 2	725	47,280	51,660	10
No. 3	725	46,710	47,790	14.5
Mean	725	45,170	50,070	17.8

[a]Broke outside gauge marks.

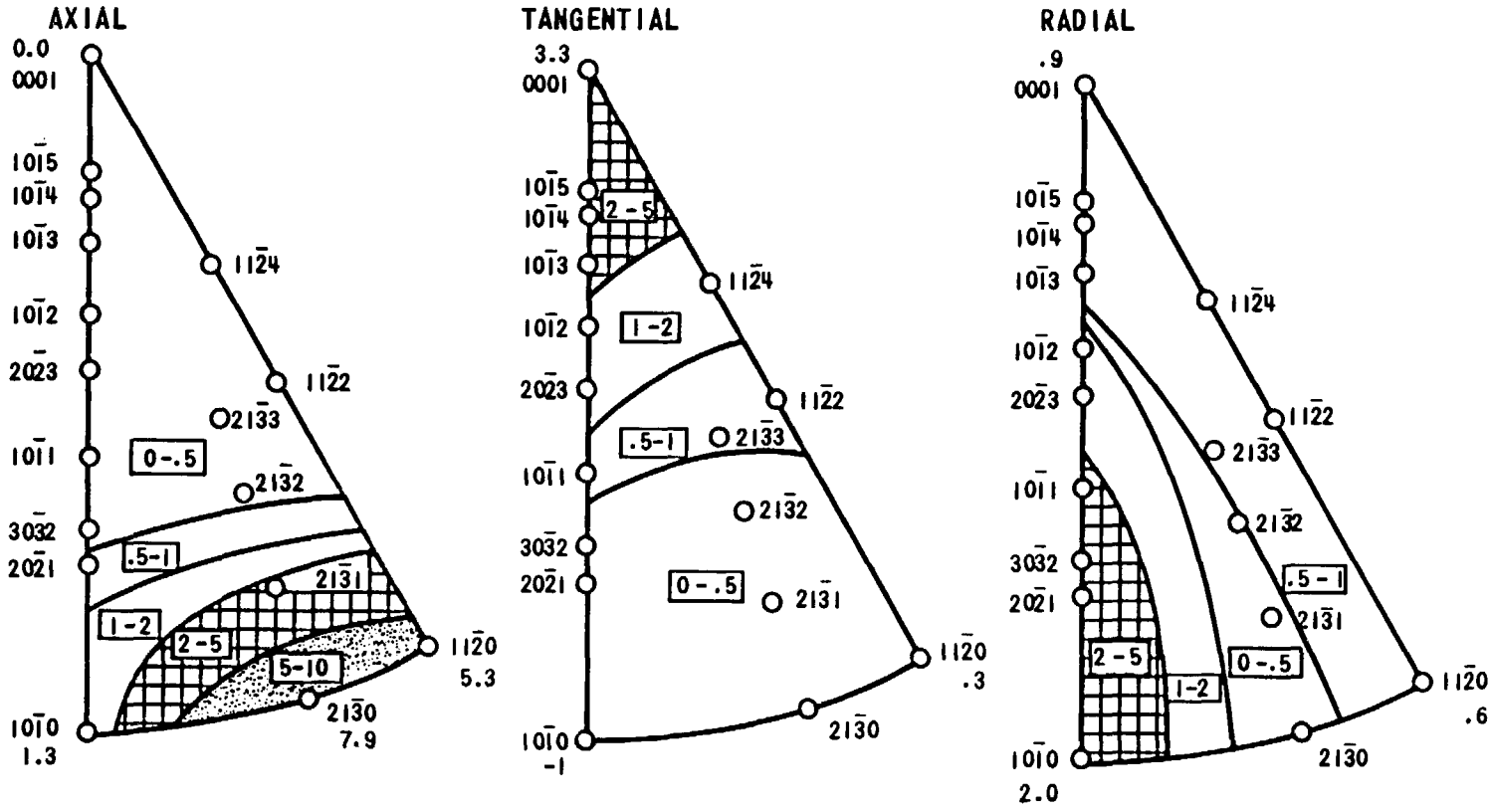

Figure B-11. Inverse Pole Figure for As-Fabricated Heater Rod

B.3.5.4 Hydride Orientation

In samples of tubing hydrided in concentrated LiOH to a level of 150 ppm total hydrogen, the resultant room temperature hydride orientation was radial to the tube axis.

This result is consistent with the texture analysis, because hydrides preferentially precipitate on habit planes adjacent to the basal plane of the tube. Since the basal planes (which are perpendicular to the tangentially oriented basal poles) are radially oriented, the radial hydride precipitation can be anticipated.

At high temperatures, the hydrogen solubility is substantial and the effect of orientation non-existent. Furthermore, precipitates forming at higher hydrogen levels tend to seek out other preferential sites (that is grain boundaries) with the result that hydride orientation becomes random/radial. The exact distribution site of hydride precipitate is also markedly influenced by the rate of cooling.

B.4 DISCUSSION OF RESULTS

B.4.1 Metal-Water Reaction

Tables B-3 and B-4 presented calculated and measured oxide thickness data from the four Group III tests performed. A comparison of this data is shown in Figure B-12. It is evident that the calculated thicknesses are consistently high, with the error increasing with increasing oxide thickness. The principal reason for this difference is discussed below.

The calculated oxide thickness data given in Tables B-3 and B-4 were obtained using the Baker and Just [2] parabolic rate equation and the detailed temperature-time output of the thermocouples located at the sections examined. As discussed in Section 3.1, these calculations were performed by the DATAR computer code. The output of the code was expressed as a fraction of the metal reacted, which was then converted into a calculated oxide thickness by assuming that ZrO_2 was the only reaction product.

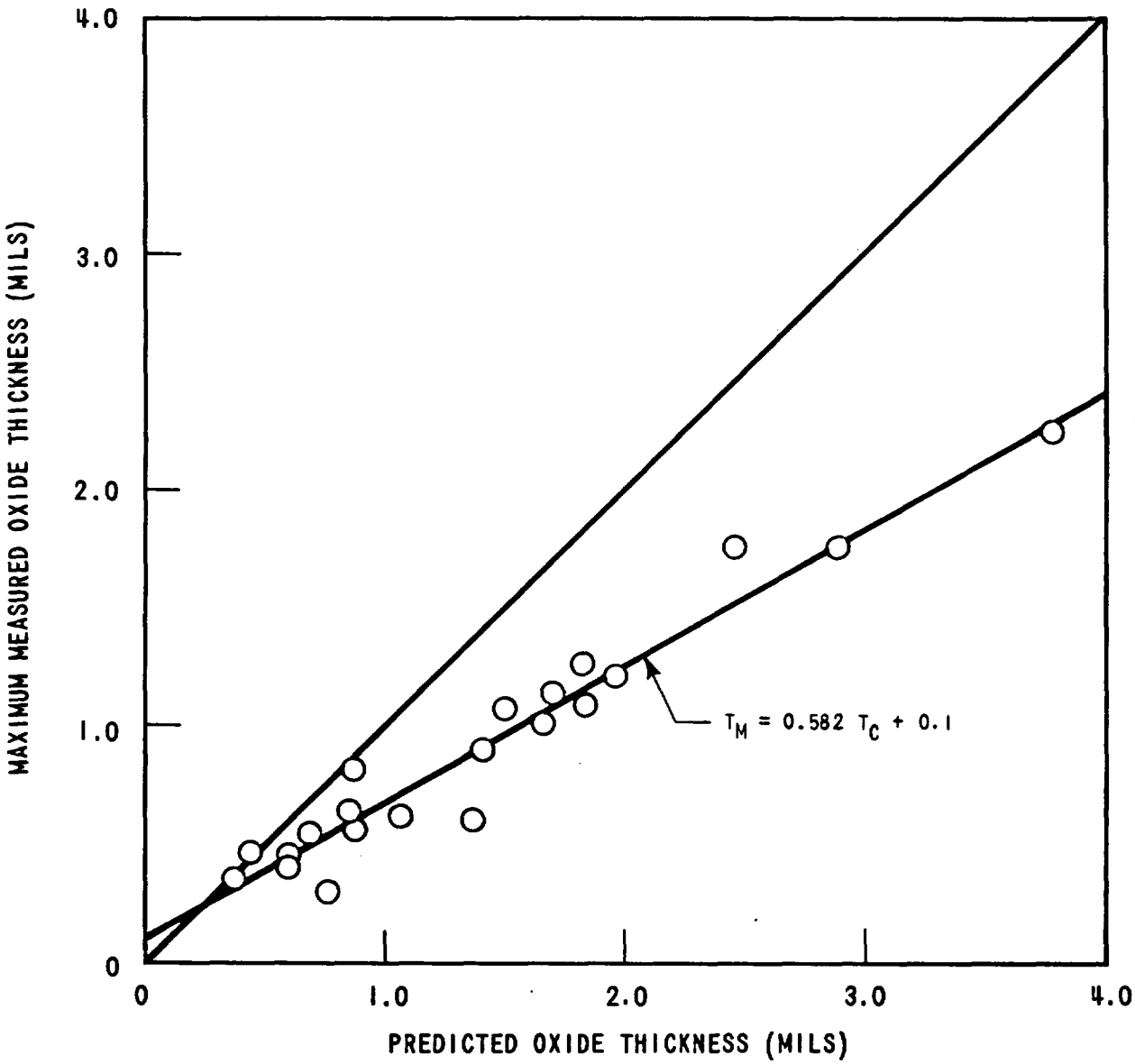

Figure B-12. Comparison of Measured versus Predicted Values of Oxide Thickness

The α -zirconium thickness and microhardness data presented above provide an explanation for the difference between measured and calculated oxide thicknesses. This data shows that in addition to the formation of ZrO_2, oxygen diffuses into the Zircaloy to form an interstitial solid solution. Since the Baker-Just parabolic rate equation was based on measurements of metal-water reaction evolved hydrogen, its use to calculate oxide thicknesses should take oxygen diffusion into account. This distinction is of importance, however, only at temperatures where the rate of diffusion of oxygen into the metal is large relative to the diffusion of the oxidizing species through the surface oxide layer.

Hesson, et al, [3] simulated clad-steam reactions following loss-of-coolant accidents and estimated the extent of dissolved oxygen relative to the total oxidation reaction. In the temperature range 1400-1600°C, the extent of oxygen dissolved was one-third to one-half the oxygen which formed a measurable oxide film. In the tests reported here, a similar proportion of dissolved oxygen is required to obtain agreement with the Baker-Just parabolic rate equation.

Kerns and Chirigos [4] determined the diffusivity of oxygen in α-zirconium using microhardness measurements. Their analysis was based on Mudge's [5] finding that there is an approximate linear relationship between microhardness and oxygen content in the range 0 to 2.4 percent oxygen. While a complete quantitative confirmation was outside the scope of this work, it is possible to demonstrate qualitatively that the extent of dissolved oxygen estimated on the basis of the microhardness measurements reported in Section B.3.4 is consistent with the over prediction of oxide film using the Baker-Just equation.

A least squares fit of the data plotted in Figure B-12 provided the following correlation between measured and calculated oxide thicknesses:

$$T_m = 0.582\ T_c + 0.1$$

where T_m is the measured oxide thickness in mils, and T_c is the calculated oxide thickness in mils, assuming that ZrO_2 is the only reaction product.

Figure B-13 shows a comparison of measured oxide and α-zirconium layer thicknesses. This figure indicates that for the specimens examined in this study the thicknesses of the two layers are approximately equal.

Since the above correlations are based on a limited amount of data, caution should be exercised in applying them to other test conditions. In this context one should note the absence of an α-zirconium layer beneath the oxide film in the specimens from Runs 2443 and 2544. This shows that one cannot assume an α-zirconium thickness equal to the oxide thickness for all conceivable metal-water reaction time-temperature parameters.

The formation of reaction products other than ZrO_2 should be considered in loss-of-coolant accident analyses. In determining metal-water reaction energy release, current practice is to assume that ZrO_2 is the only reaction product. Since only about 58 percent of the reacted oxygen shows up as ZrO_2, with the remainder going into solid solution, the metal-water reaction energy release term should be modified to account for formation of both reaction products.

B.4.2 Hydrogen Uptake

Although hydrogen analyses were limited to a few selected samples, the absence of visual hydride needles in the microstructures examined and the low hydrogen values determined quantitatively were persuasive evidence that hydrogen uptake was a low proportion of the potentially available hydrogen from the metal-water reaction.

While it was not confirmed in these tests, it would be anticipated from the work of Brown and Hardie [6] that hydrogen precipitation would be influenced by oxygen diffusion, and the α-zirconium layer (and of course the oxide film) would contain little or no hydrogen. Excluding the tests of Run 9573, for which hydrogen data was not available, the maximum observed thickness of ZrO_2 plus α-zirconium in this work was less than 2.7 mils, or approximately 12 percent of the initial clad thickness. Therefore, the concentration of hydrogen in the remaining thickness of the clad would be scarcely detectible given the variance, the hydrogen content observed, and the limits of analytical accuracy.

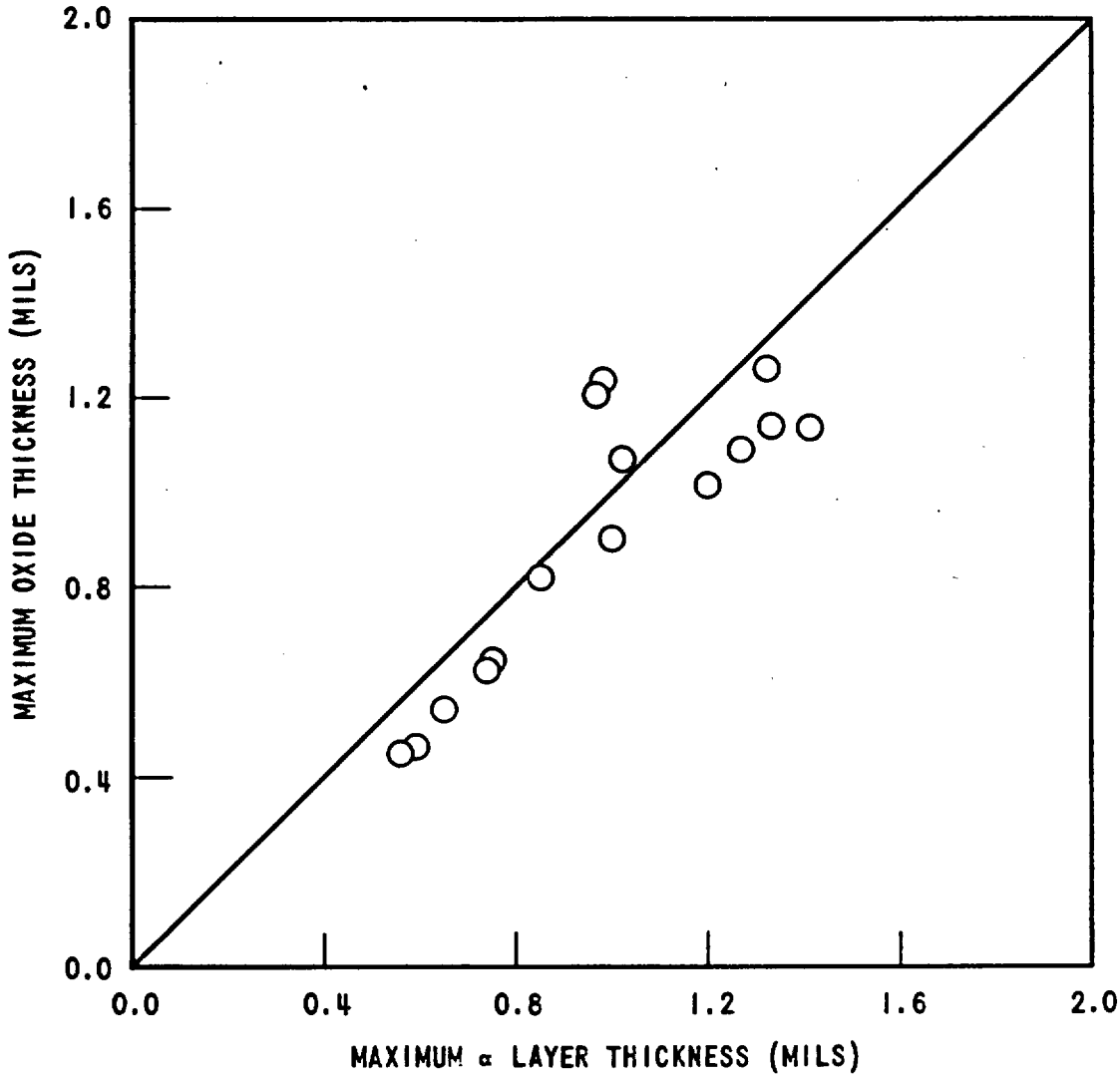

Figure B-13. Comparison of Maximum Oxide and α Zirconium Layer Thickness

B.5 CONCLUSIONS

The Baker-Just parabolic rate equation appears to provide a satisfactory basis for determining the overall extent of metal-water reaction. However, the formation of an oxide film and an oxygen containing α-zirconium layer beneath the oxide film should be accounted for in determining the metal-water reaction energy release and oxide film thickness.

In the investigations reported here, the extent of metal-water reaction was basically homogeneous with no major variations in oxide film thickness at given cross-sectional locations in a fuel rod.

The amount of hydrogen absorption was a low proportion (less than 10 percent) of the available hydrogen resulting from the metal-water reaction.

Even though the specimens examined reached temperatures as high as 2545°F, there was no evidence of clad shattering or failure as a result of being exposed to typical loss-of-coolant accident environments.

REFERENCES

1. R. H. Meservey and R. Herzel, "Brittle Behavior of Zircaloy in an Emergency Core Cooling Environment", IN-1389, September 1970.

2. L. Baker, Jr., and L. C. Just, "Studies of Metal-Water Reactions at High Temperatures: III Experimental and Theoretical Studies of the Zirconium-Water Reaction", ANL-6548, May 1968.

3. J. C. Hesson, R. O. Ivins, R. E. Wilson, K. Nishio and C. Barnes. Jr., "Laboratory Simulations of Cladding-Steam Reactions Following Loss-of-Coolant Accidents in Water-Cooled Power Reactors", ANL-7609, January 1970.

4. J. J. Kearns and J. N. Chirigos, "The Use of Microhardness in the Determination of the Diffusivity of Oxygen in Alpha Zirconium", WAPD-TM-306, February 1962.

5. W. L. Mudge, "Mechanical Properties and Microstructure of Annealed Zirconium", WAPD-T-46, June 1953.

6. A. Brown and D. Hardie "The Effect of Dissolved Oxygen on the Solubility of Hydrogen in Alpha Zirconium", J. Nucl. Mater. 4, 110-12, 1961.

APPENDIX C

FLECHT DATA SUMMARY SHEETS

FLECHT RUN SUMMARY SHEET

RUN NO. 2443

DATE 6/18/69

A. RUN CONDITIONS

Bundle Size and Clad	7 x 7 - Zr4
Initial Clad Temperature	2035 °F
Flooding Rate	10.0 in/sec
Peak Power	1.24 kw/ft
Decay Power	Curve A Figure 3-21
Inlet Coolant Temperature	150 °F
Pressure	56 psia
Flow Blockage	0 %

B. HOUSING TEMPERATURES

Elevation (ft)	Initial Temperature (°F)	Temperature at Quench Time of Hot Rod Midplane (37 Sec)
3	476	314
6	576	358
9	492	298

Initial T_{avg} Actual = 457 °F

FLECHT RUN SUMMARY SHEET

RUN NO. 2443 (Cont'd)

DATE 6/18/69

C. HEATER THERMOCOUPLE DATA

T/C Number	Initial Temp. (°F)	Max. Temp. (°F)	Temp. Rise (°F)	Turnaround Time (Sec.)	Quench Temp. (°F)	Quench Time (Sec.)
3D1	868	886	18	4	590	53
3D2	1560	1581	21	2	760	53
3D3	2035	2102	67	6	Degraded Quench*	
3D4	1599	1609	10	2	1017	21
3D5	865	891	26	2	840	6
2D2	1951	2004	53	5	Degraded Quench*	
1D2	1671	1672	1	0	1255	34
3E3	2004	2064	60	4	Degraded Quench*	
4E1	861	881	20	4	685	34
4E2	1494	1519	25	4	908	46
4E3	1920	1969	49	4	1281	37
4E4	1549	1565	16	3	1185	18
4E5	864	890	26	2	836	6
5E3	1874	1893	19	2	1341	34

* Hotter rods did not quench normally due to clad swelling

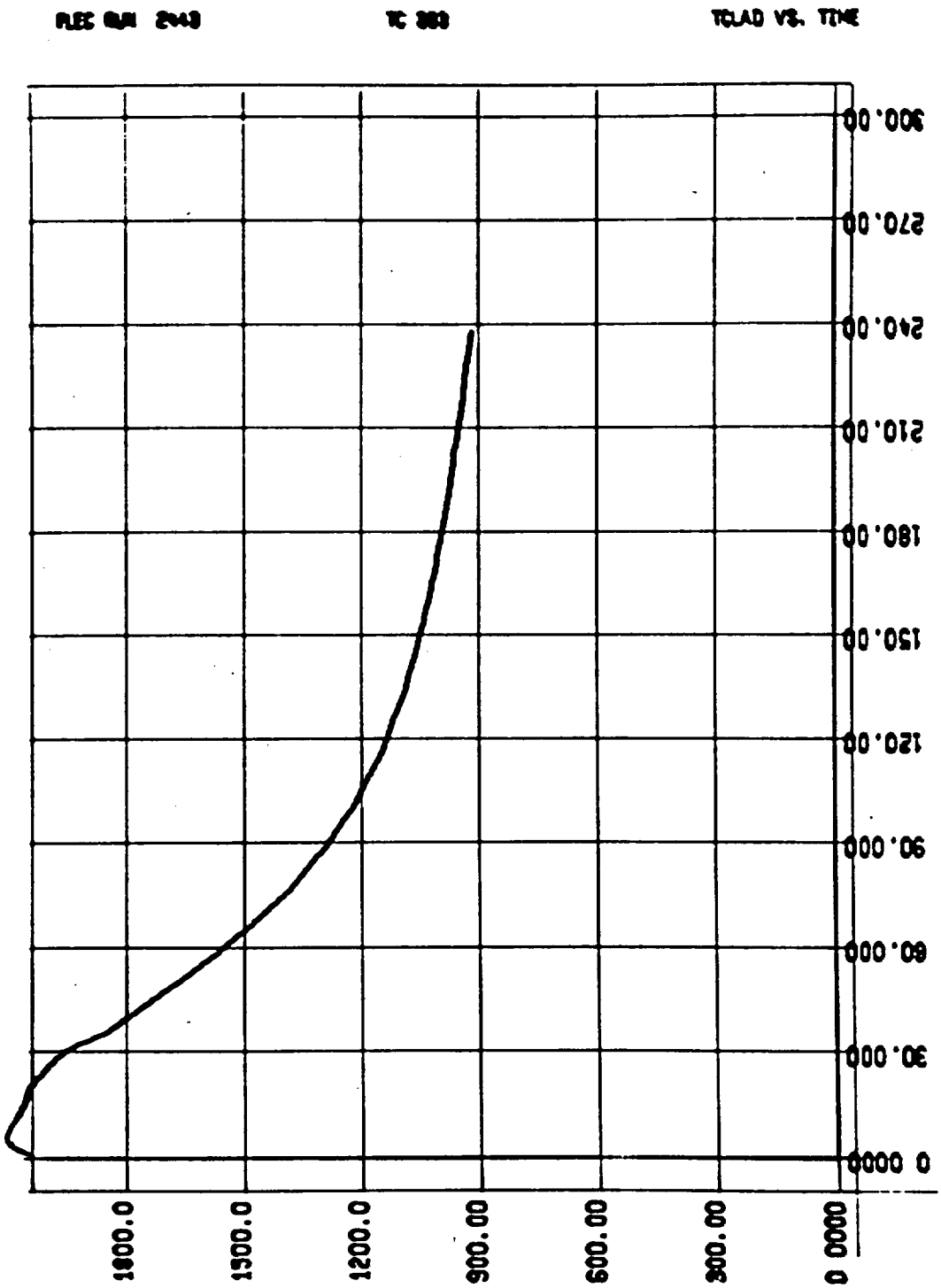
FLEC RUN 2043
TC 303
TCLAD VS. TIME
1800.0
1500.0
1200.0
900.00
600.00
300.00
0.0000
0.0000
30.000
60.000
90.000
120.00
150.00
180.00
210.00
240.00
270.00
300.00

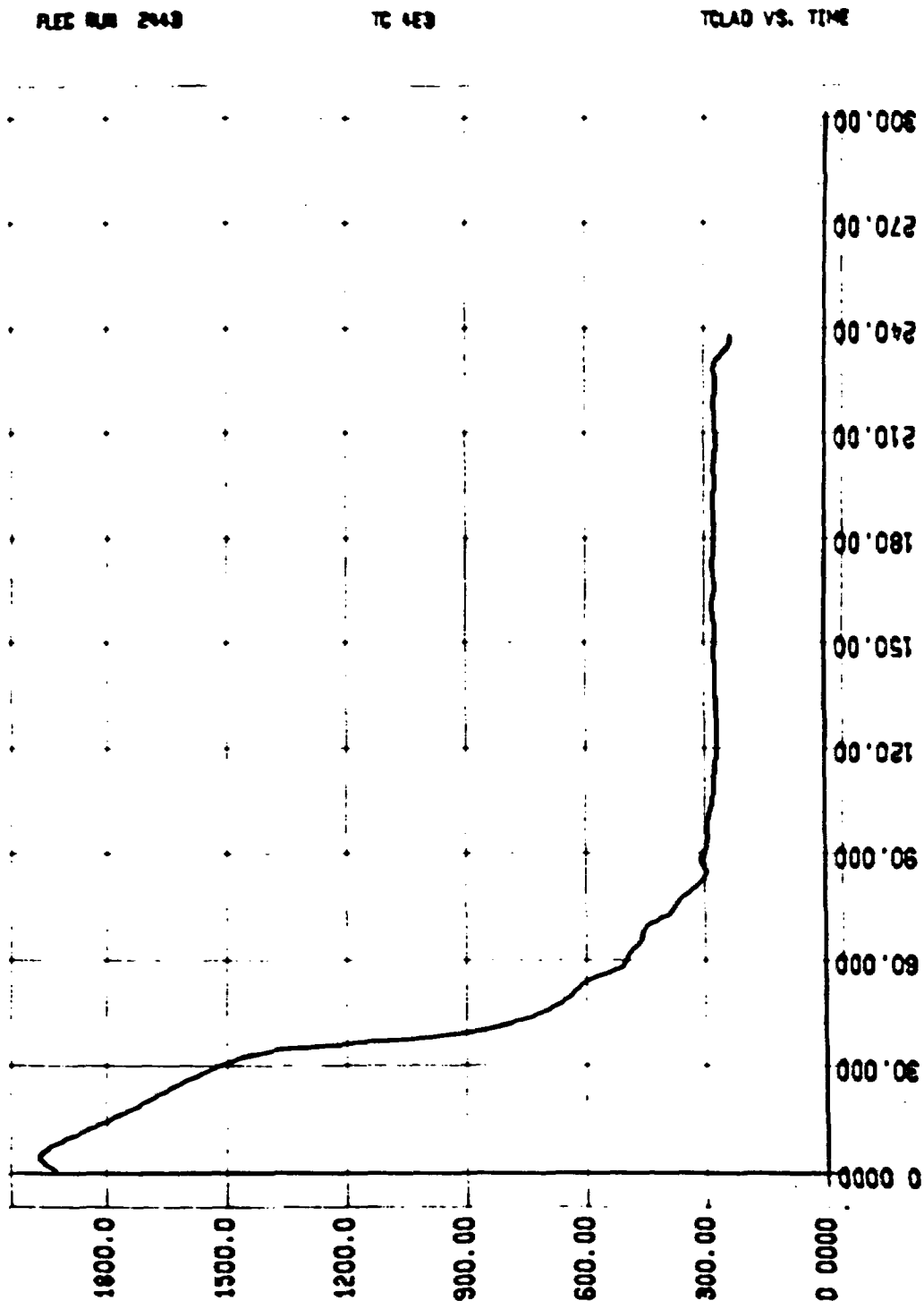
FLEC RUN 2943
TC 4E3
TCLAD VS. TIME
1800.0
1500.0
1200.0
900.00
600.00
300.00
0.0000
0.0000
30.000
60.000
90.000
120.00
150.00
180.00
210.00
240.00
270.00
300.00

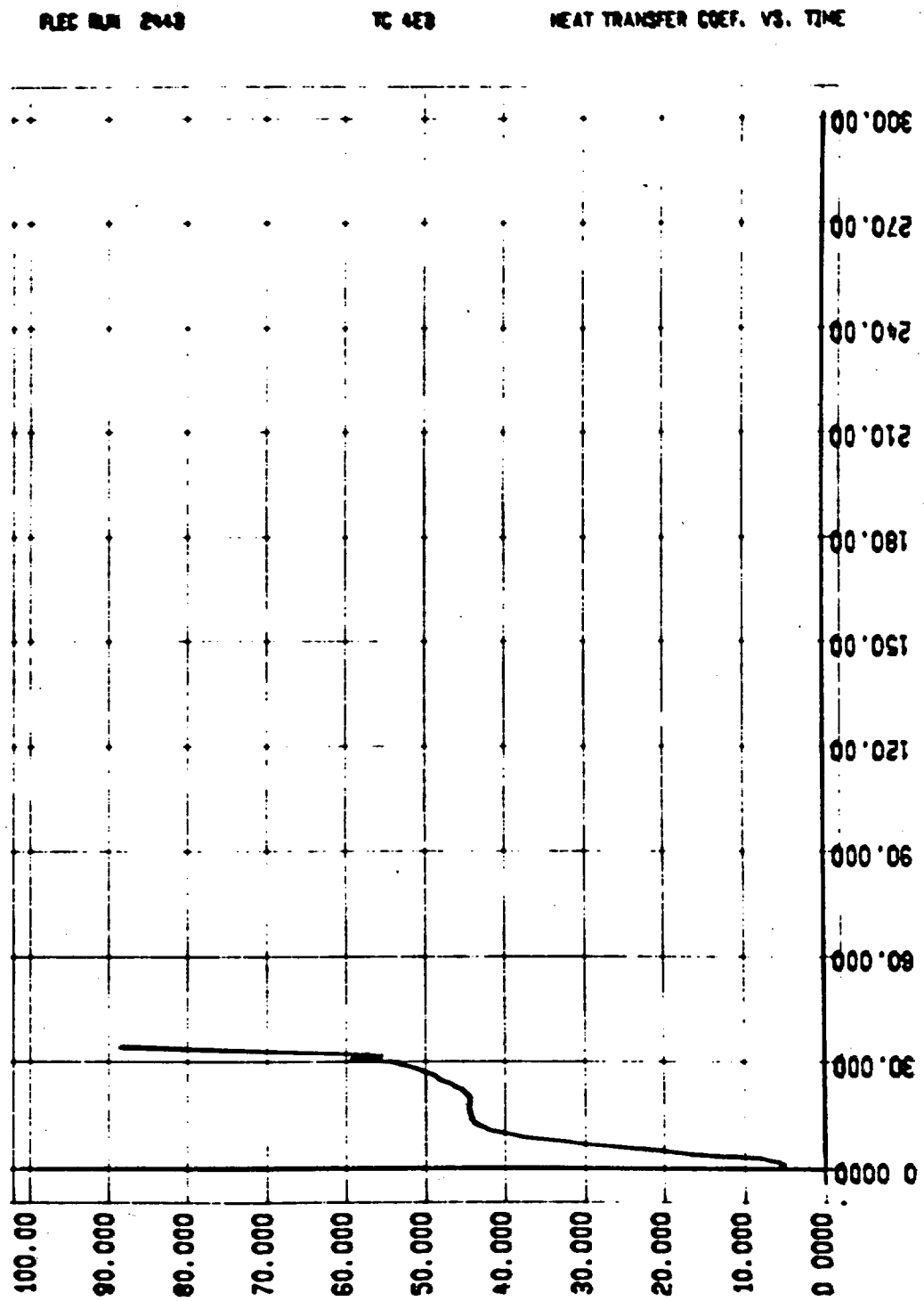
FLEC RUN 2943
TC 4E3
HEAT TRANSFER COEF. VS. TIME
100.00
90.000
80.000
70.000
60.000
50.000
40.000
30.000
20.000
10.000
0.0000
0.0000
30.000
60.000
90.000
120.00
150.00
180.00
210.00
240.00
270.00
300.00

Run 2443
ΔP Between 0 and 8 FT Elevations
(PT51 minus PT55)

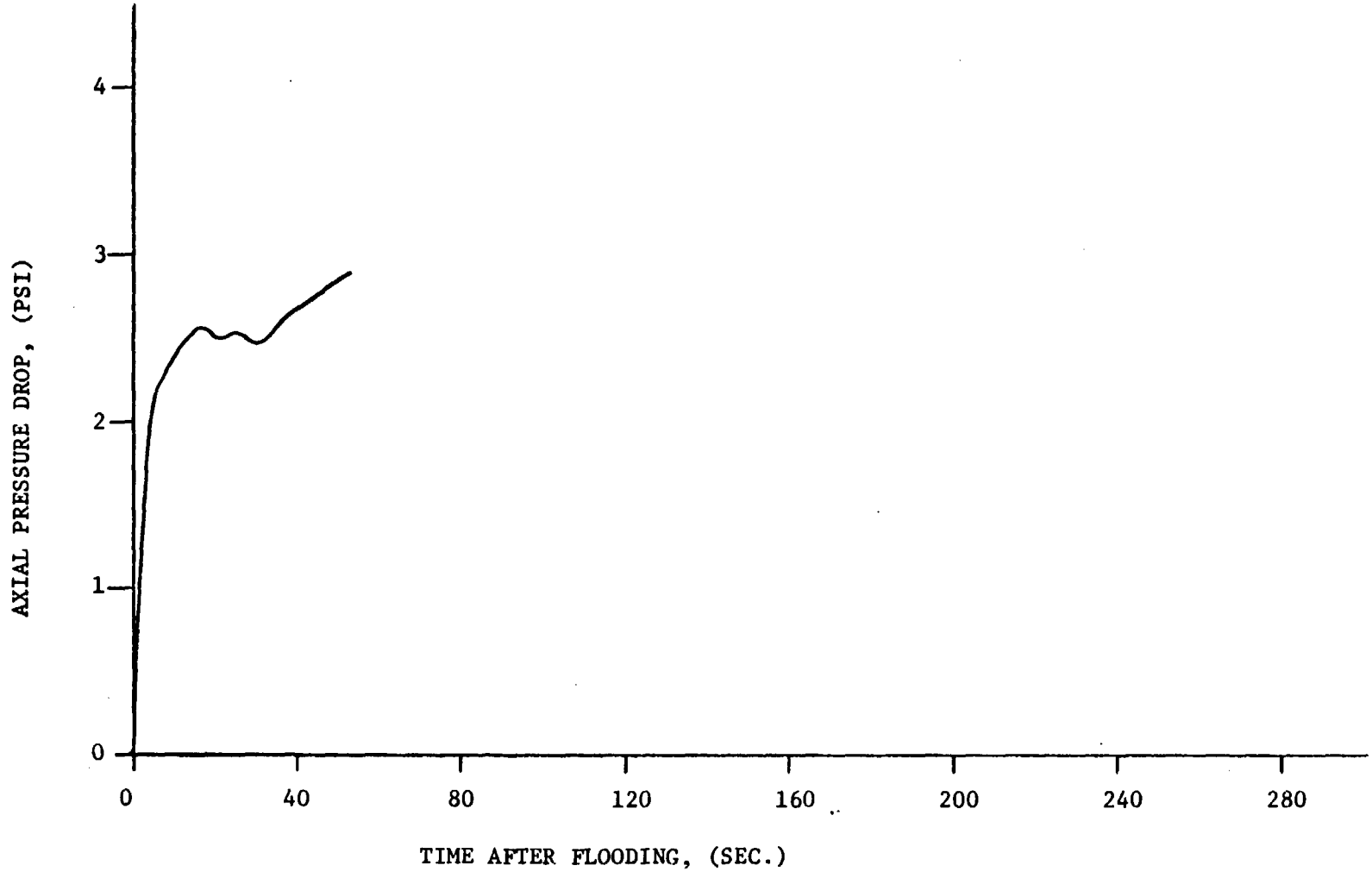

FLECHT RUN SUMMARY SHEET

RUN NO. 2544

DATE 7/10/69

A. RUN CONDITIONS

Bundle Size and Clad	7 x 7 - Zr4
Initial Clad Temperature	2017 °F
Flooding Rate	4.0 in/sec
Peak Power	1.24 kw/ft
Decay Power	Curve A Figure 3-21
Inlet Coolant Temperature	150 °F
Pressure	58 psia
Flow Blockage	0 %

B. HOUSING TEMPERATURES

Elevation (ft)	Initial Temperature (°F)	Temperature at Quench Time of Hot Rod Midplane (66 Sec)
2	375	294
4	488	283
6	599	446
8	647	331
10	346	297

Initial T_{avg} Actual = 450 °F

FLECHT RUN SUMMARY SHEET

RUN NO. 2544 (Cont'd)

DATE 7/10/69

C. HEATER THERMOCOUPLE DATA

T/C Number	Initial Temp. (°F)	Max. Temp. (°F)	Temp. Rise (°F)	Turnaround Time (Sec.)	Quench Temp. (°F)	Quench Time (Sec.)
3D1	937	990	52	9	695	88
3D2	1626	1668	42	6	847	104
3D3	1918	1991	73	8	1202	67
3D4	1591	1616	24	4	1047	43
3D5	857	865	8	2	791	11
2D2	1778	1845	67	7	1428	51
1D2	1772	1818	46	5	1356	44
3E3	1869	1963	95	9	1384	67
4E1	938	988	49	9	596	115
4E2	1610	1642	33	5	810	103
4E3	2012	2102	90	7	Degraded Quench*	
4E4	1630	1653	24	4	1035	39
4E5	908	919	11	2	818	12
5E3	1813	1850	47	5	905	75
5B2	2017	2144	127	12	Degraded Quench*	
3C3	1905	1987	82	7	1060	75

* Hotter rods did not quench normally due to clad swelling

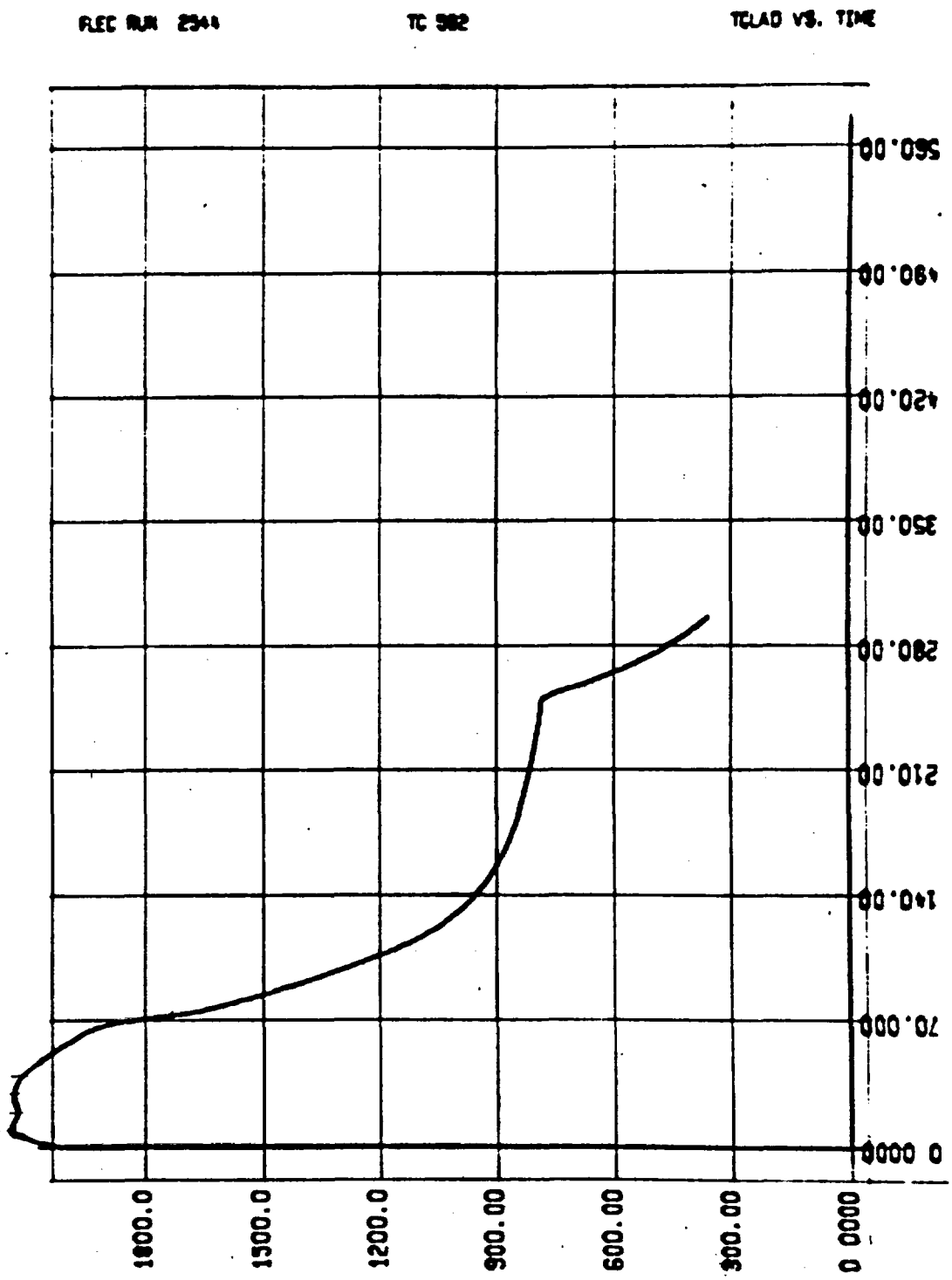
FLEC RUN 2344
TC 582
TCLAD VS. TIME
1800.0
1500.0
1200.0
900.00
600.00
300.00
0.0000
0.0000
70.000
140.00
210.00
280.00
350.00
420.00
490.00
560.00

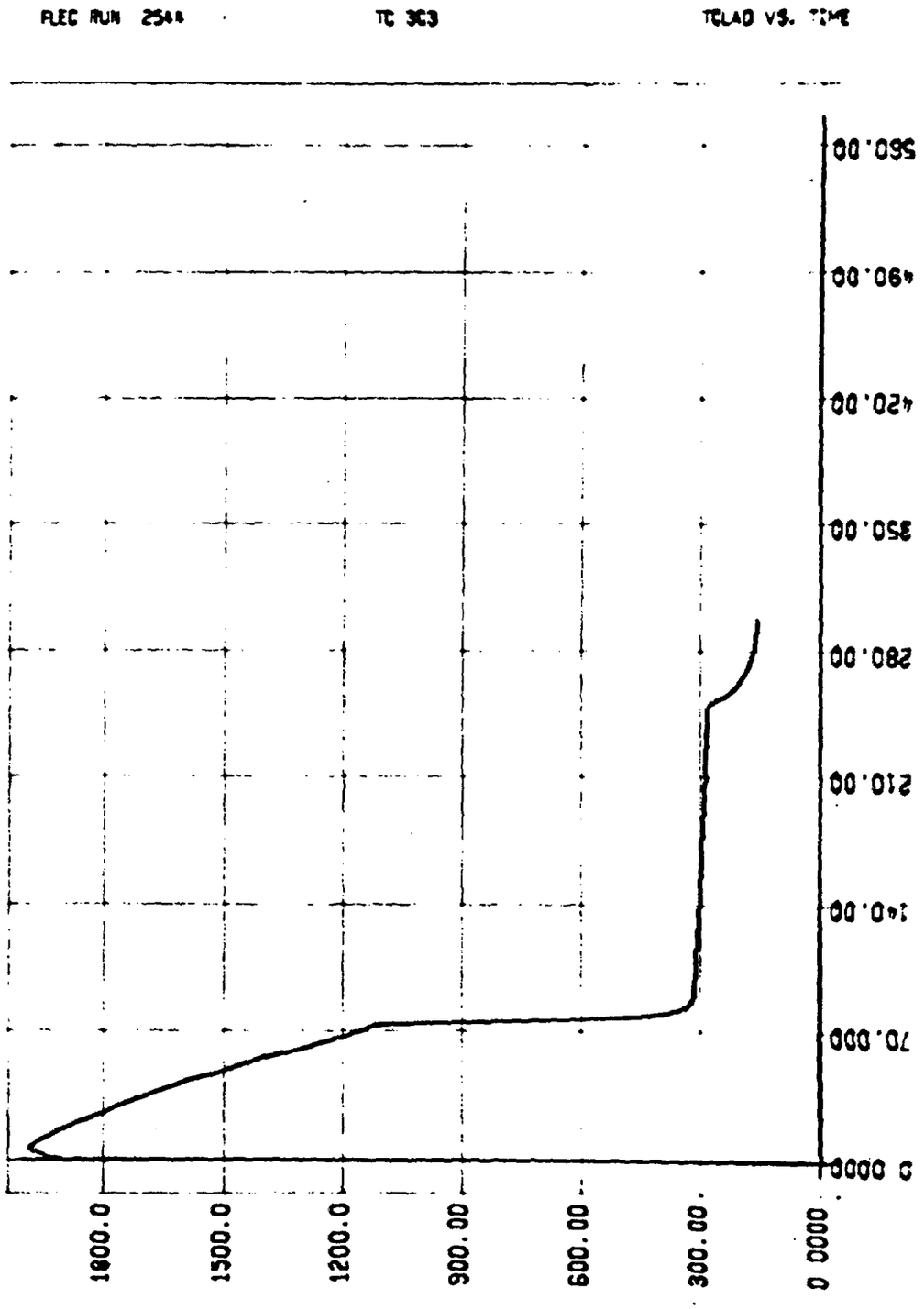
ELEC RUN 254A
TC 3C3
TCLAD VS. TIME
1800.0
1500.0
1200.0
900.00
600.00
300.00
0.0000
0.0000
70.000
140.00
210.00
280.00
350.00
420.00
490.00
560.00

FLEC RUN 2544 TC 3C3 HEAT TRANSFER COEF. VS. TIME

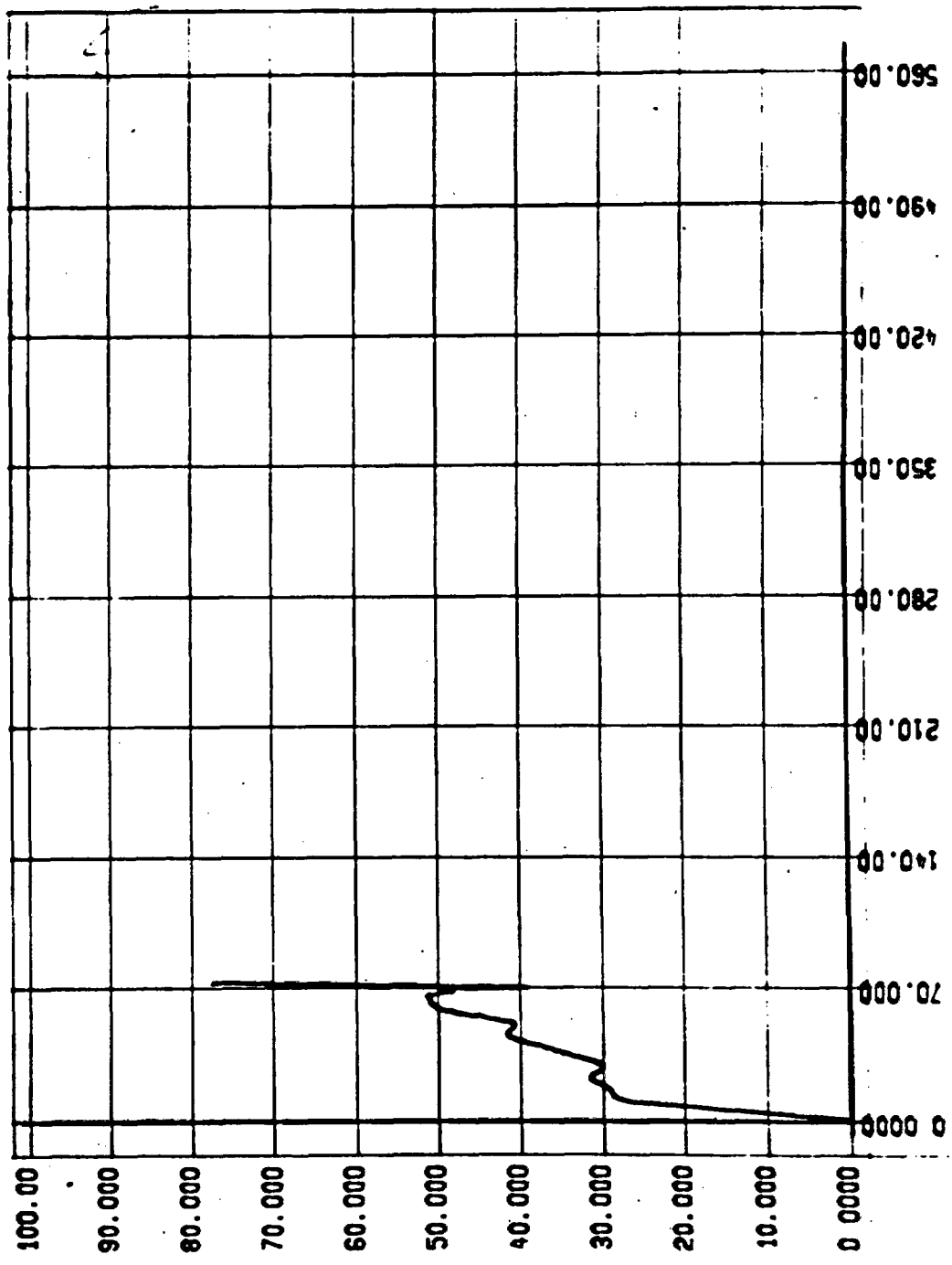

Run 2544
ΔP Between 0 and 8 FT Elevations
(PT 51 minus PT55)

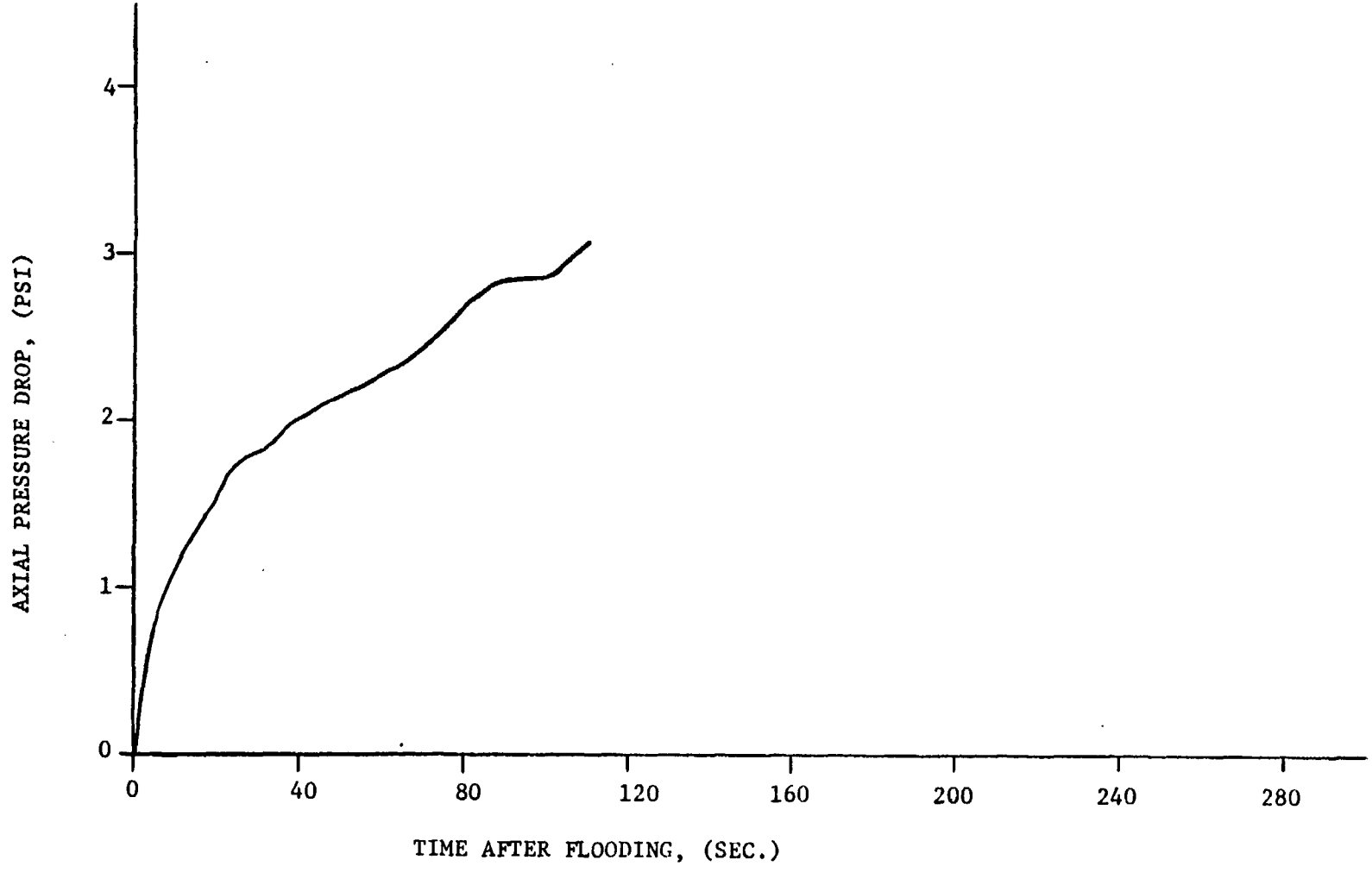

FLECHT RUN SUMMARY SHEET

RUN NO. 8874

DATE 7/21/70

A. RUN CONDITIONS

Bundle Size and Clad	7 x 7*- Zr4
Initial Clad Temperature	2297 °F
Flooding Rate	6.0(8 sec)-1.0 in/sec with "fallback"
Peak Power	1.24 kw/ft
Decay Power	Curve B Figure 3-21
Inlet Coolant Temperature	141 °F
Pressure	64 psia
Flow Blockage	0 %

B. HOUSING TEMPERATURES

Elevation (ft)	Initial Temperature (°F)	Temperature at Quench Time of Hot Rod Midplane (200 Sec)
2	554	228
4	680	294
6	798	890
8	694	841
10	557	691

Initial T_{avg} Actual = 637 °F

* HEATER ROD FAILURES

Rod	Power Zone	Time of Failure (sec)
4B	1.0	9.6
5B	1.1	18.5
4C	1.1	19.3
5C	1.1	29.3
5D	1.1	55.5

FLECHT RUN SUMMARY SHEET

RUN NO. 8874 (Cont'd)

DATE 7/21/70

C. HEATER THERMOCOUPLE DATA

T/C No.	$T_{initial}$ (°F)	T_{Max_1} (°F)	ΔT_{rise_1} (°F)	t_{turn_1} (sec)	T_{Min} (°F)	t_{Min} (sec)	T_{Max_2} (°F)	ΔT_{rise_2} (°F)	t_{turn_2} (sec)	T_{quench} (°F)	t_{quench} (sec)
3D1	1267	1296	29	4	1234	11	1575	341	103	587	371
3D2	2048	2089	41	3	1780	14	1896	116	49	834	292
3D3	2315	2357	42	3	2047	10	2080	33	23	T/C bad at 79 sec after flood	
3D4	2058	2086	28	3	1860	13	1863	3	14	1288	88
3D5	1238	1241	3	1	--	--	--	--	--	972	15
2D2	2234	2264	30	3	1988	11	2045	57	23	1126	207
1D2	1941	1945	4	2	1798	13	1824	26	24	1112	215
3E3	2305	2326	21	2	2093	11	2115	22	14	1125	197
4E1	1282	1324	42	4	1233	12	1527	294	83	682	332
4E2	1918	1969	51	3	1780	12	1846	66	49	941	266
4E3	2238	2284	46	3	1960	11	1978	18	15	1040	200
4E4	1980	2006	26	3	1781	20	1782	1	23	1149	95
4E5	1229	1232	3	1	--	--	--	--	--	974.	15
5E3	2233	2259	26	3	2019	20	2020	1	23	935	208
2F2	2297	2361	63	4	2060	12	2147	87	40	971	204

FLEC RUN 8874 TC 2F2 TCLAD VS. TIME

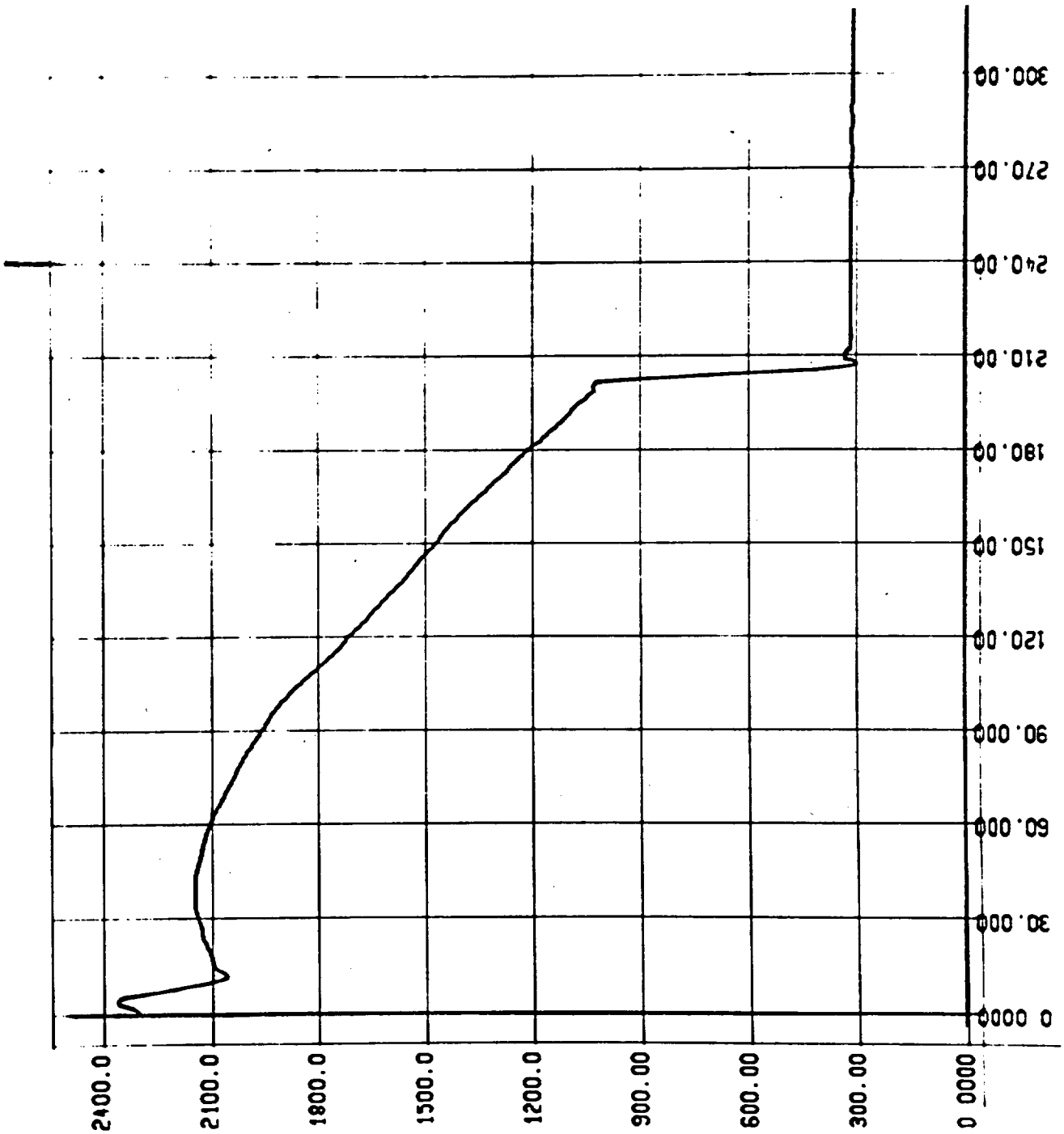

FLEC RUN 8874 TC 2F2 HEAT TRANSFER COEF. VS. TIME

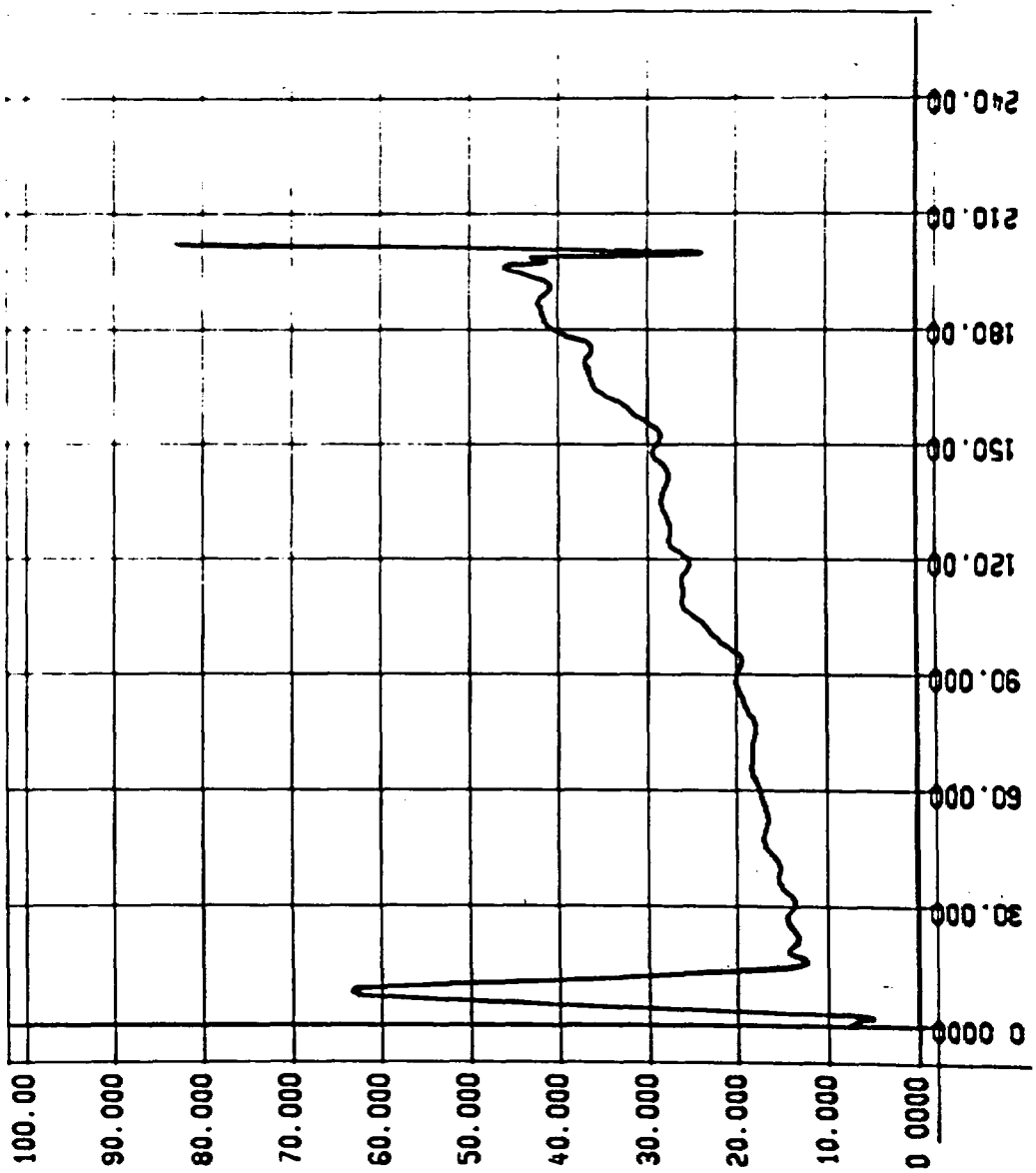

Run 8874
ΔP Between 0 and 8 FT Elevations
(PT51 minus PT55)

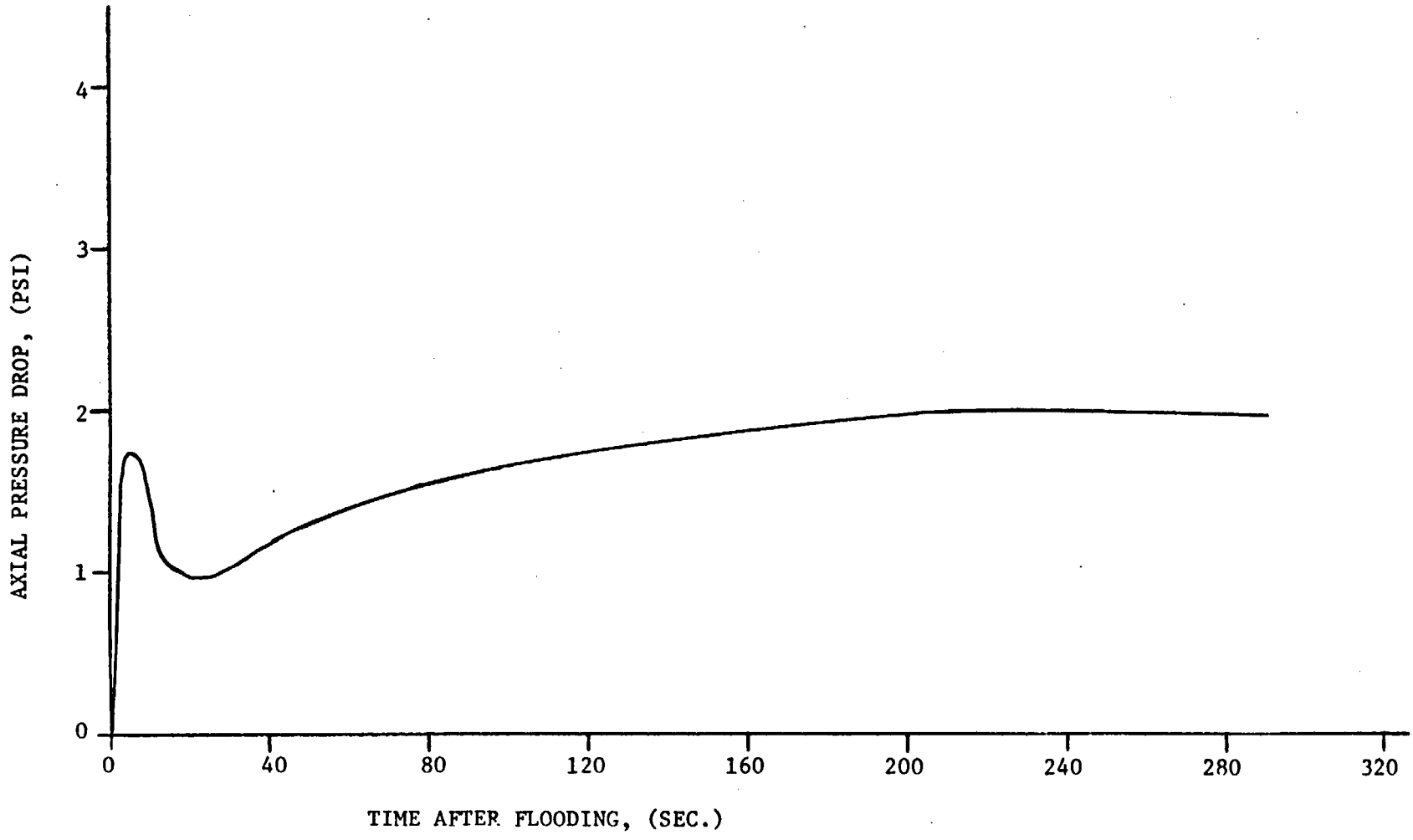

FLECHT RUN SUMMARY SHEET

RUN NO. 8975

DATE 10/15/71

A. RUN CONDITIONS

Bundle Size and Clad	7 x 7* - SS
Initial Clad Temperature	2301 °F
Flooding Rate	5.8(8 sec)-1.0 in/sec with "fallback"
Peak Power	1.24 kw/ft
Decay Power	Curve B Figure 3-21
Inlet Coolant Temperature	144 °F
Pressure	60 psia
Flow Blockage	0 %

B. HOUSING TEMPERATURES

Elevation (ft)	Initial Temperature (°F)	Temperature at Quench Time of Hot Rod Midplane (249 Sec)
2	529	215
4	653	286
6	732	658
8	654	843
10	588	640

Initial T_{avg} Actual = 604 °F

* Rod 3D failed at approximately 110 seconds after flooding

FLECHT RUN SUMMARY SHEET

RUN NO. 8975 (Cont'd)

DATE 10/15/70

C. HEATER THERMOCOUPLE DATA

T/C No.	$T_{initial}$ (°F)	T_{Max_1} (°F)	ΔT_{rise_1} (°F)	t_{turn_1} (sec)	T_{Min} (°F)	t_{Min} (sec)	T_{Max_2} (°F)	ΔT_{rise_2} (°F)	t_{turn_2} (sec)	T_{quench} (°F)	t_{quench} (sec)
3C1	1334	1362	28	6	1336	11	1761	425	135	651	434
3C2	1966	1993	27	3	1887	12	2107	220	93	782	373
3C3	2292	2318	26	4	2169	14	2237	68	38	888	234
3C4	1957	1977	20	3	1823	16	1824	1	18	780	125
3C5	1219	1225	6	2	--	--	--	--	--	880	36
2D2	2301	2346	45	4	2181	13	2250	69	36	930	249
1D2	1985	2007	22	4	1838	15	1839	1	18	912	221
3E3	Instrumentation Malfunction										
4E1	1435	1457	22	5	1412	12	1803	391	137	656	430
4E2	2028	2043	15	3	1921	12	2068	147	65	827	373
4E3	Instrumentation Malfunction										
4E4	2030	2056	26	4	--	--	--	--	--	780	124
4E5	1245	1259	14	3	--	--	--	--	--	878	34
5E3	2255	2288	33	4	2149	14	2205	56	38	802	238

FLEC RUN 8975 TC 2D2 TCLAD VS. TIME

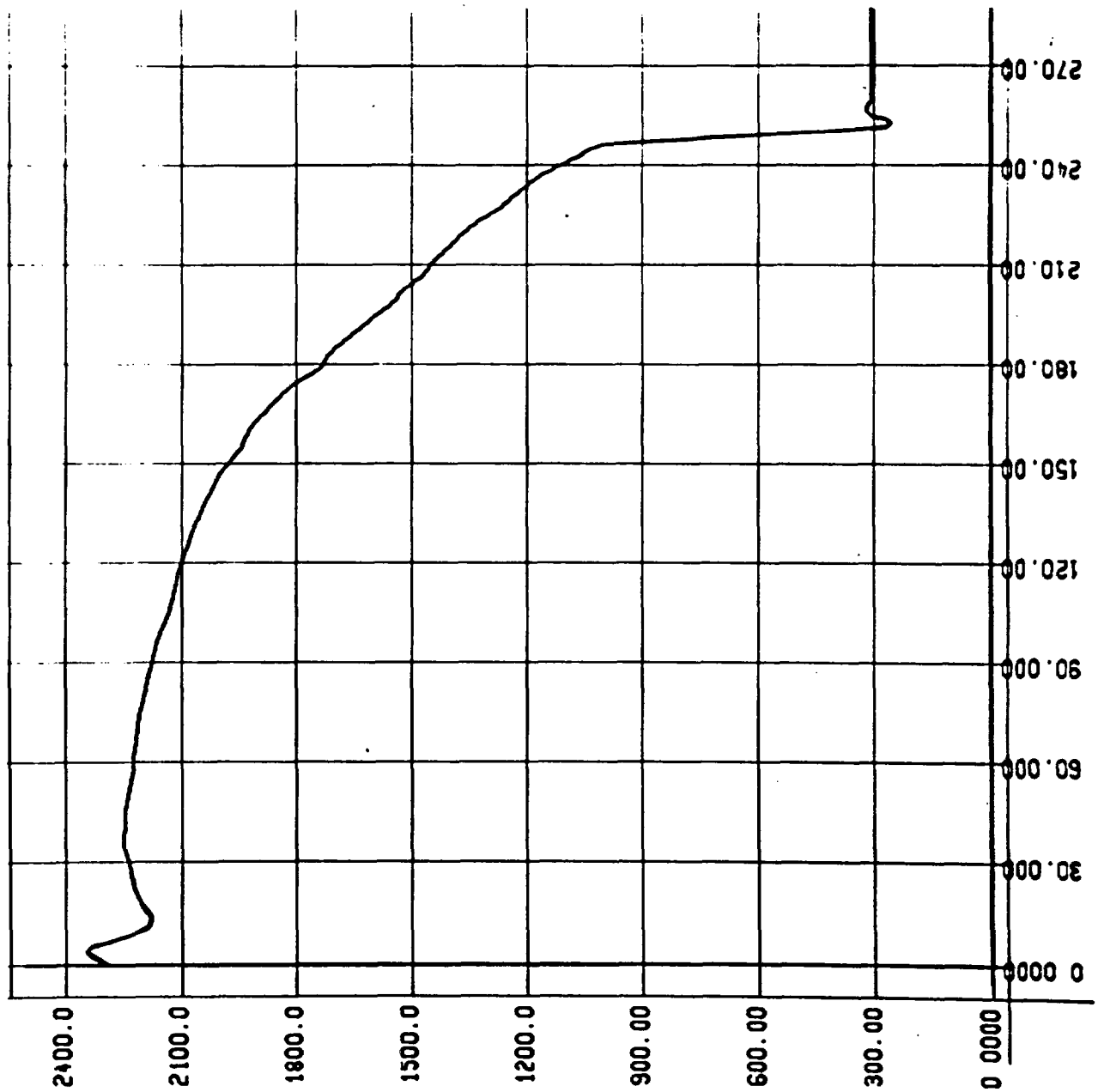

FLEC RUN 0975 TC 202 HEAT TRANSFER COEF. VS. TIME

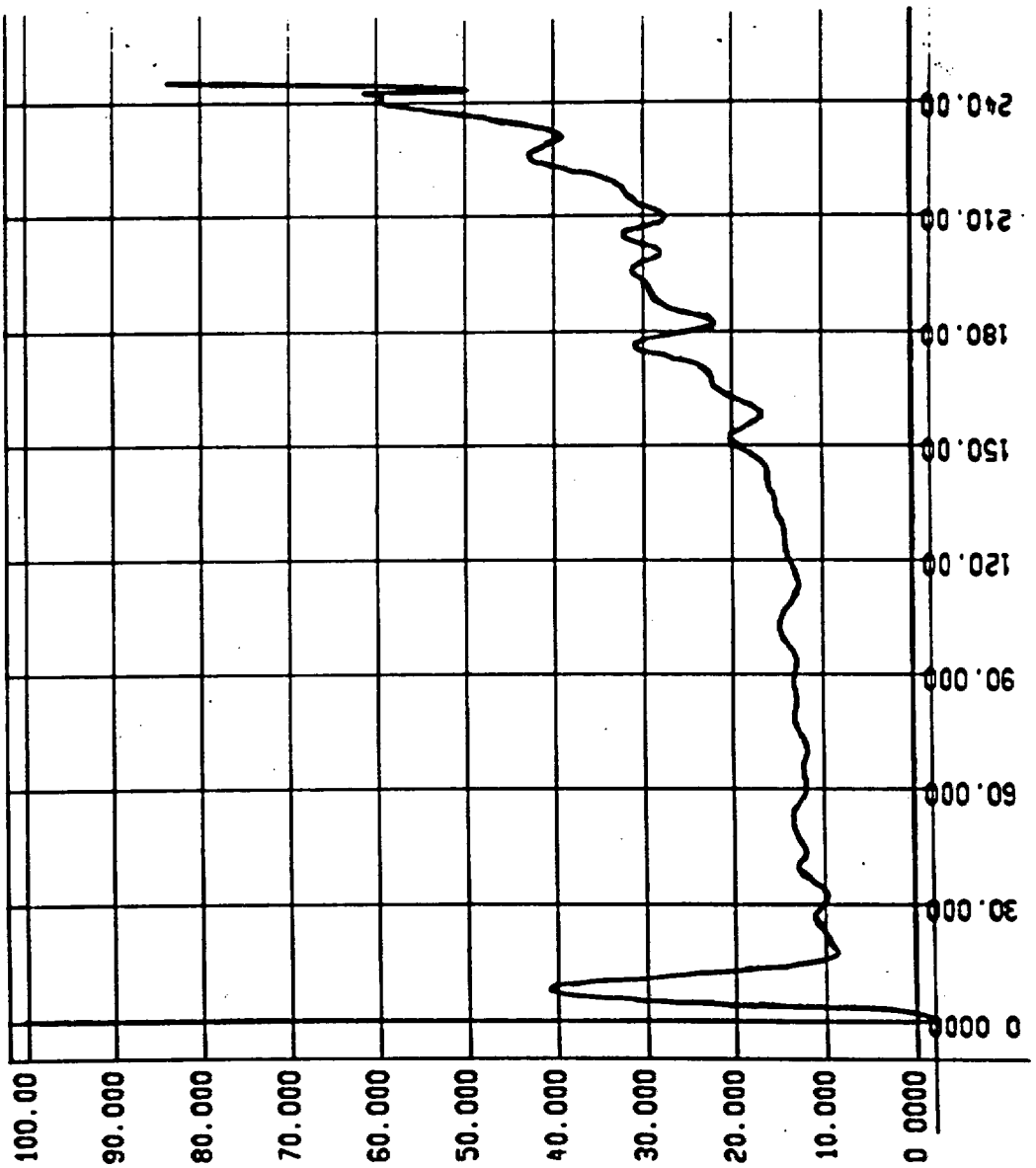

Run 8975
ΔP Between 0 and 8 FT Elevations
(PT51 minus PT55)

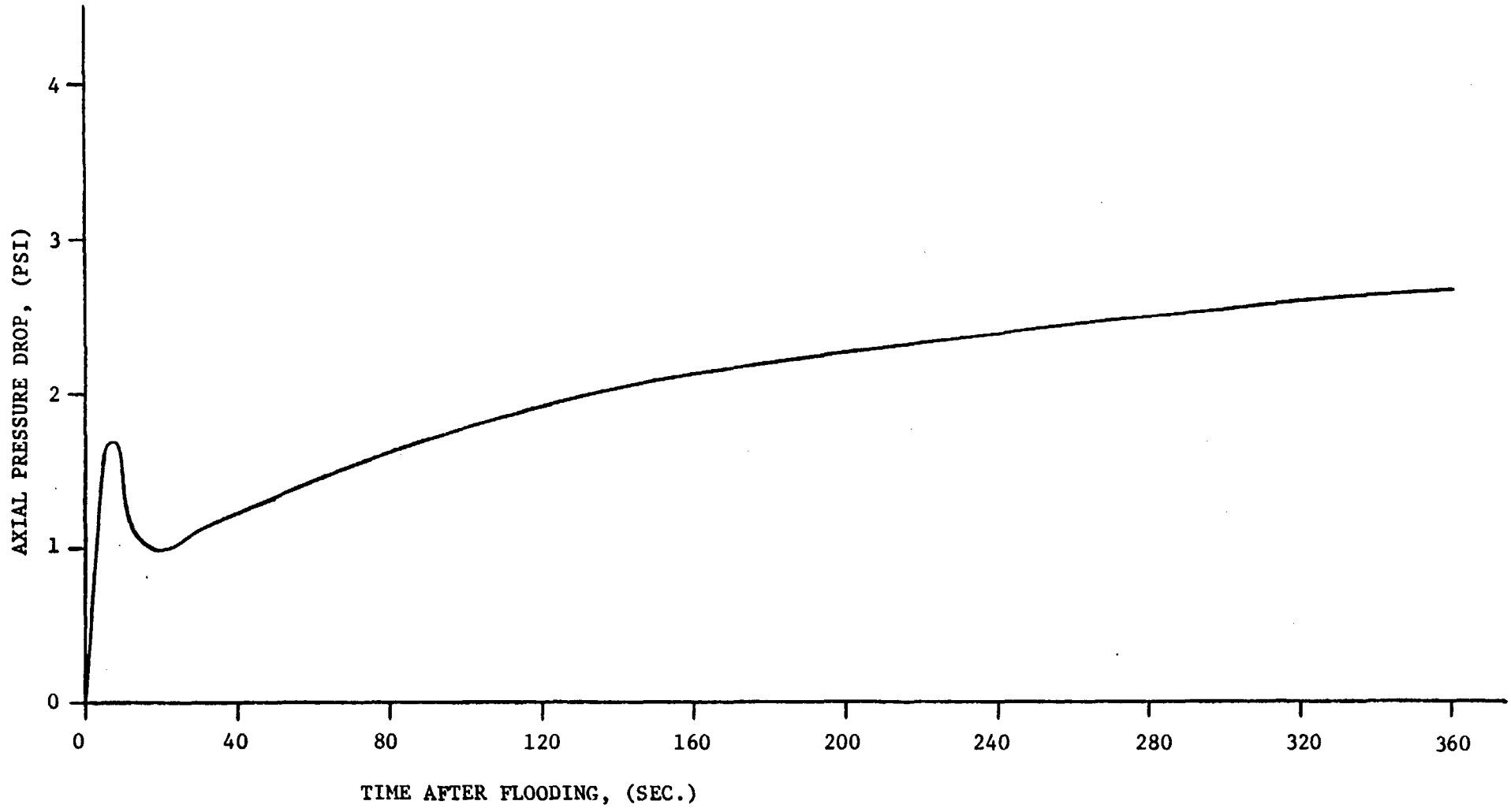

FLECHT RUN SUMMARY SHEET

RUN NO. 9077

DATE 10/19/70

A. RUN CONDITIONS

Bundle Size and Clad	7 x 7* - SS
Initial Clad Temperature	2138 °F
Flooding Rate	6.2(4 sec.)-1.0 in/sec with "fallback"
Peak Power	1.24 kw/ft
Decay Power	Curve B Figure 3-21
Inlet Coolant Temperature	145 °F
Pressure	55 psia
Flow Blockage	0 %

B. HOUSING TEMPERATURES

Elevation (ft)	Initial Temperature (°F)	Temperature at Quench Time of Hot Rod Midplane (276 Sec)
2	554	214
4	679	286
6	783	861
8	689	884
10	564	387

Initial T_{avg} Actual = 634 °F

* Rod 3D inoperative

FLECHT RUN SUMMARY SHEET

RUN NO. 9077 (Cont'd)

DATE 10/19/70

C. HEATER THERMOCOUPLE DATA

T/C No.	$T_{initial}$ (°F)	T_{Max_1} (°F)	ΔT_{rise_1} (°F)	t_{turn_1} (sec)	T_{Min} (°F)	t_{Min} (sec)	T_{Max_2} (°F)	ΔT_{rise_2} (°F)	t_{turn_2} (sec)	T_{quench} (°F)	t_{quench} (sec)
3C1	1251	1281	30	6	1280	8	1686	406	140	445	487
3C2	1822	1861	39	5	1848	9	2096	248	76	843	405
3C3	2070	2115	45	4	2081	9	2171	90	37	951	256
3C4	1834	1869	35	4	1826	10	1840	14	16	815	141
3C5	1191	1208	17	3	--	--	--	--	--	700	46
5B2	2176	2221	45	4	2178	10	2218	40	36	922	260
5B8*	1852	1887	35	6	1883	10	2047	164	67	750	410
4F2	2085	2120	35	4	2099	10	2187	88	48	934	267
2E2	2083	2117	34	4	2111	9	2181	70	41	904	283
2B2	2062	2098	36	4	2067	10	2119	52	30	926	263
5E3	2138	2180	42	4	2151	10	2251	100	54	815	276

* 8 Ft T/c on rod 5B

FLEC RUN 9077 TC 5E3 TCLAD VS. TIME

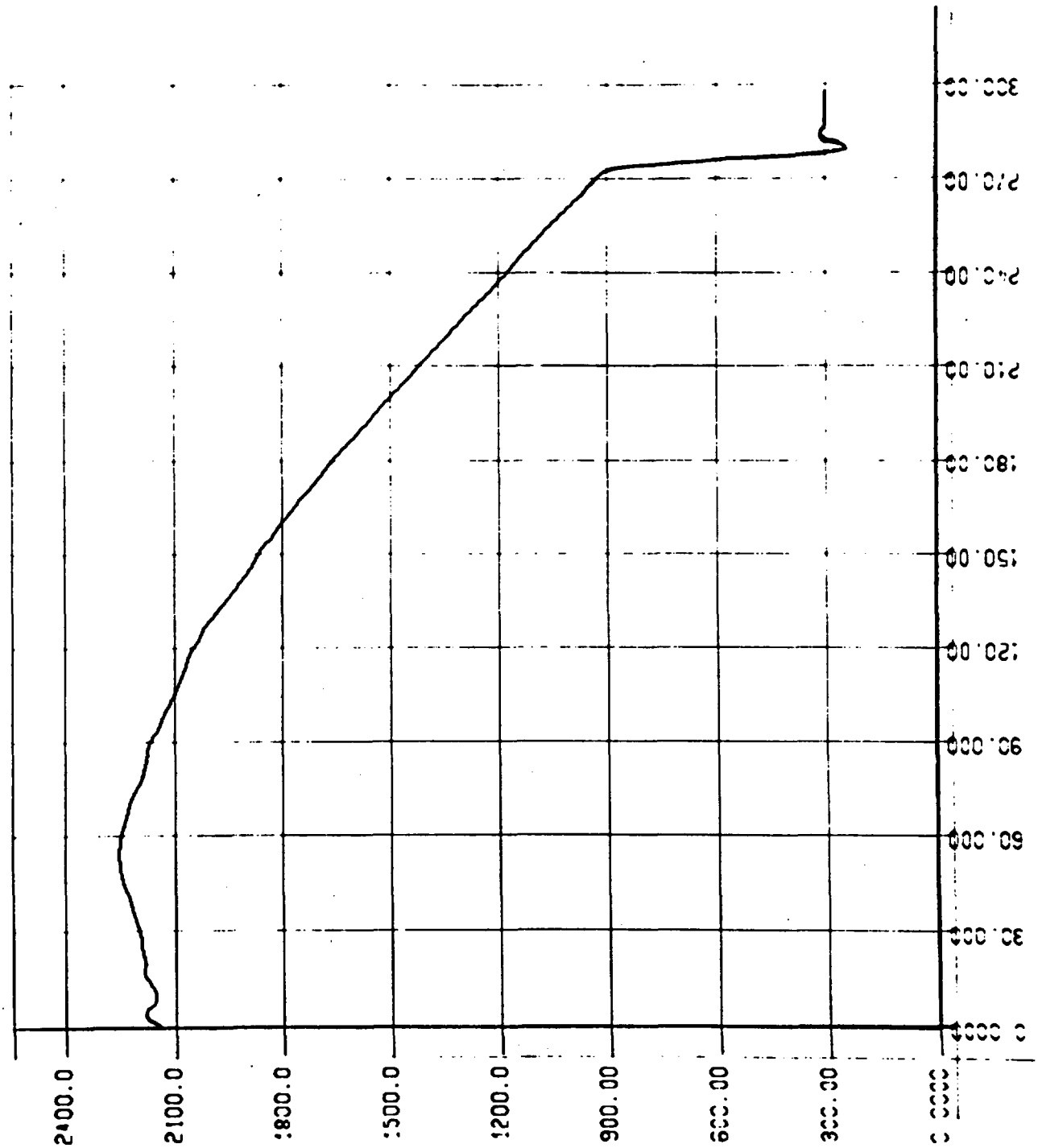

FLEC RUN 9077 TC SE3 HEAT TRANSFER COEF. VS. TIME

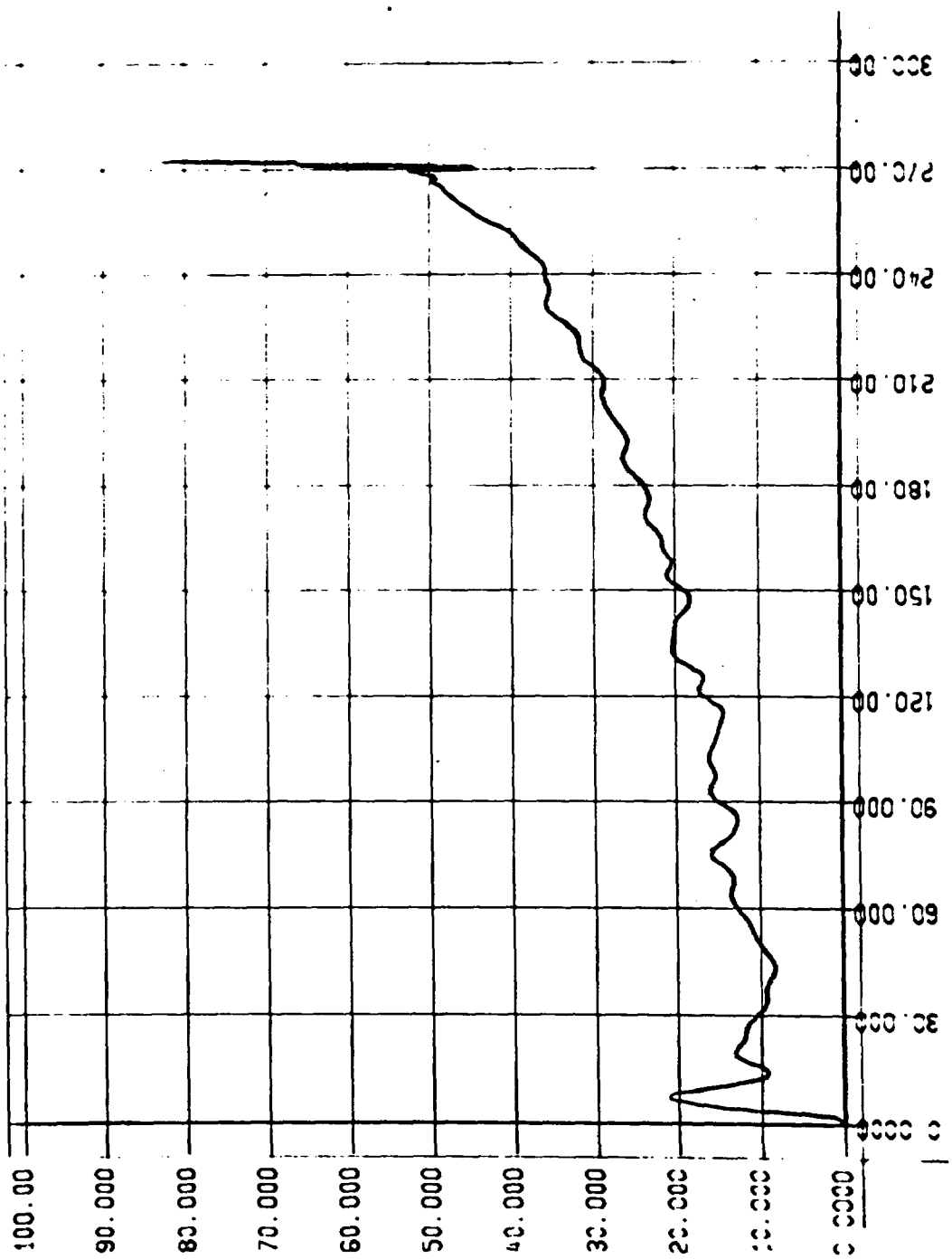

Run 9077
ΔP Between 0 and 8 FT Elevations
(PT51 minus PT55)

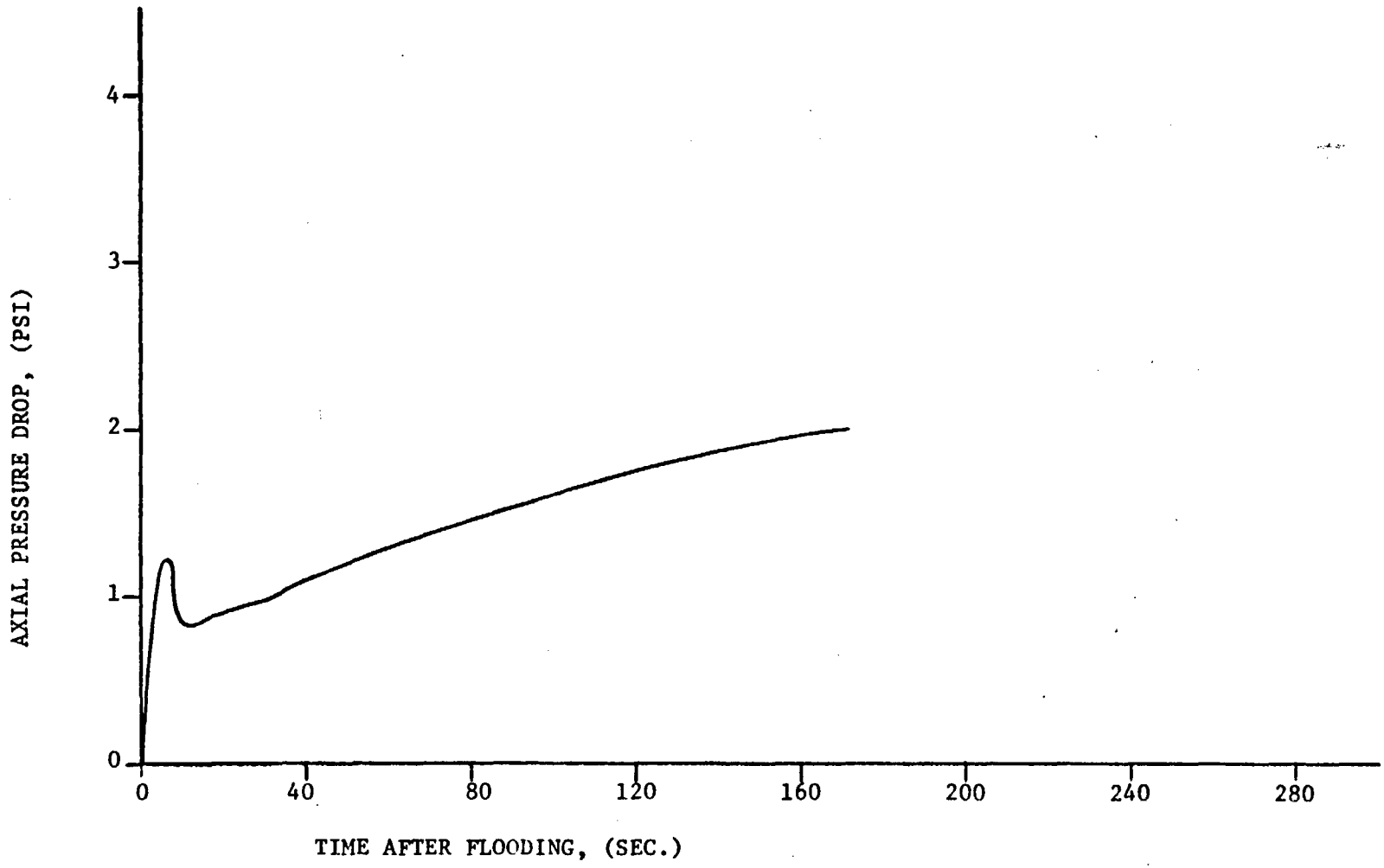

FLECHT RUN SUMMARY SHEET

RUN NO. 9176

DATE 10/22/70

A. RUN CONDITIONS

Bundle Size and Clad	7 x 7* - SS
Initial Clad Temperature	2197 °F
Flooding Rate	5.9(4 sec)-1.0 in/sec with "fallback"
Peak Power	1.24 kw/ft
Decay Power	Curve B Figure 3-21
Inlet Coolant Temperature	150 °F
Pressure	58 psia
Flow Blockage	0 %

B. HOUSING TEMPERATURES

Elevation (ft)	Initial Temperature (°F)	Temperature at Quench Time of Hot Rod Midplane (239 Sec)
2	340	206
4	562	280
6	794	841
8	712	507
10	297	292

Initial T_{avg} Actual = N/A °F

* Rod 3D inoperative

FLECHT RUN SUMMARY SHEET

RUN NO. 9176 (Cont'd)

DATE 10/22/70

C. HEATER THERMOCOUPLE DATA

T/C No.	$T_{initial}$ (°F)	T_{Max_1} (°F)	ΔT_{rise_1} (°F)	t_{turn_1} (sec)	T_{Min} (°F)	t_{Min} (sec)	T_{Max_2} (°F)	ΔT_{rise_2} (°F)	t_{turn_2} (sec)	T_{quench} (°F)	t_{quench} (sec)
3C3	2086	2114	28	4	2102	9	2175	73	52	831	226
5B2	2243	2270	27	4	2247	11	2255	8	17	966	226
4E3	2197	2231	34	4	2202	9	2281	79	41	827	239

FLEC RUN 9176 TC 4E3 TCLAD VS. TIME

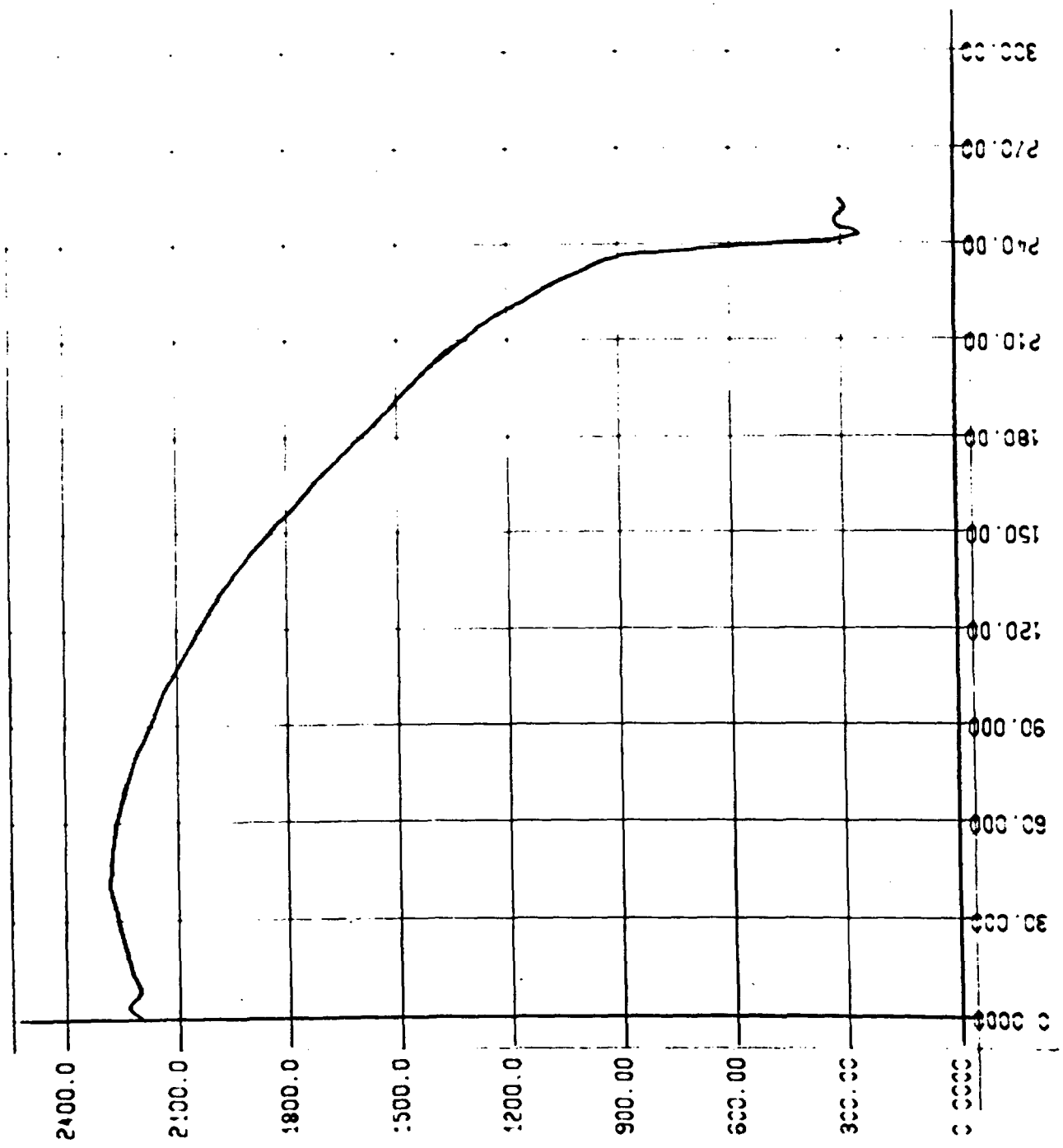

FLEC RUN 9176 TC 4E3 HEAT TRANSFER COEF. VS. TIME

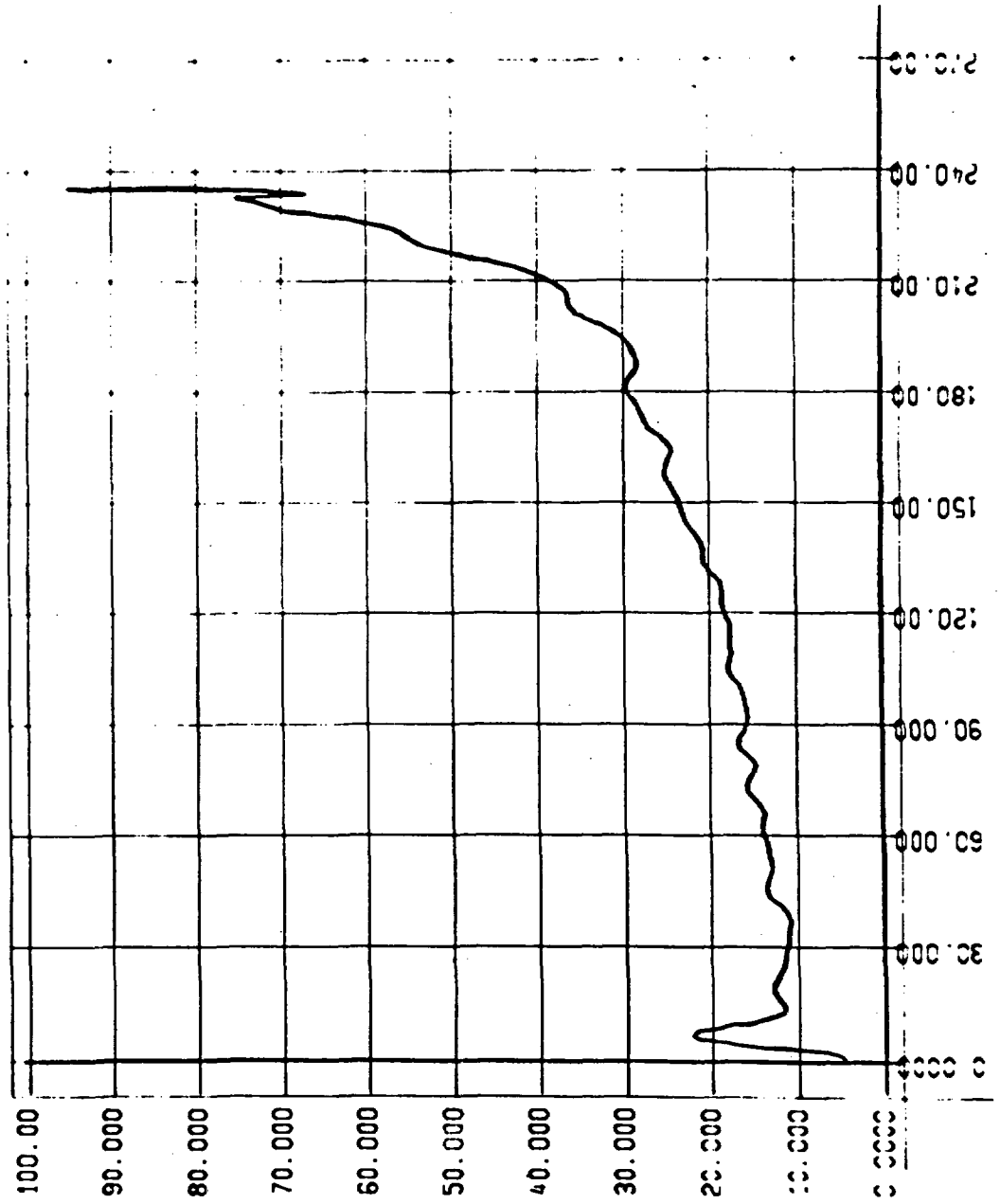

FLECHT RUN SUMMARY SHEET

RUN NO. 9278

DATE 10/23/70

A. RUN CONDITIONS

Bundle Size and Clad	7 x 7* - SS
Initial Clad Temperature	2028 °F
Flooding Rate	1.0 in/sec with "fallback"
Peak Power	1.24 kw/ft
Decay Power	Curve B Figure 3-21
Inlet Coolant Temperature	148 °F
Pressure	58 psia
Flow Blockage	0%

B. HOUSING TEMPERATURES

Elevation (ft)	Initial Temperature (°F)	Temperature at Quench Time of Hot Rod Midplane (260 Sec)
2	522	213
4	662	284
6	774	815
8	707	911
10	393	292

Initial T_{avg} Actual = 611 °F

* Rod 3d inoperative

FLECHT RUN SUMMARY SHEET

RUN NO. 9278 (Cont'd)

DATE 10/23/70

C. HEATER THERMOCOUPLE DATA

T/C Number	Initial Temp. (°F)	Max. Temp. (°F)	Temp. Rise (°F)	Turnaround Time (Sec.)	Quench Temp. (°F)	Quench Time (Sec.)
3C1	973	1671	698	160	694	461
3C2	1705	2132	427	98	876	395
3C3	1955	2172	217	56	891	250
3C4	1712	1839	127	18	826	139
3C5	1028	1083	55	11	785	49
5B2	2122	2262	140	20	913	255
5B8*	1722	2066	344	77	811	400
4F2	1977	2199	222	53	931	257
2E2	1983	2169	186	54	930	266
2B2	1968	2126	158	28	945	254
5E3	2028	2286	258	57	908	260

* 8 Ft TC on rod 5B

FLEC RUN 9278 TC SE3 TCLAD VS. TIME

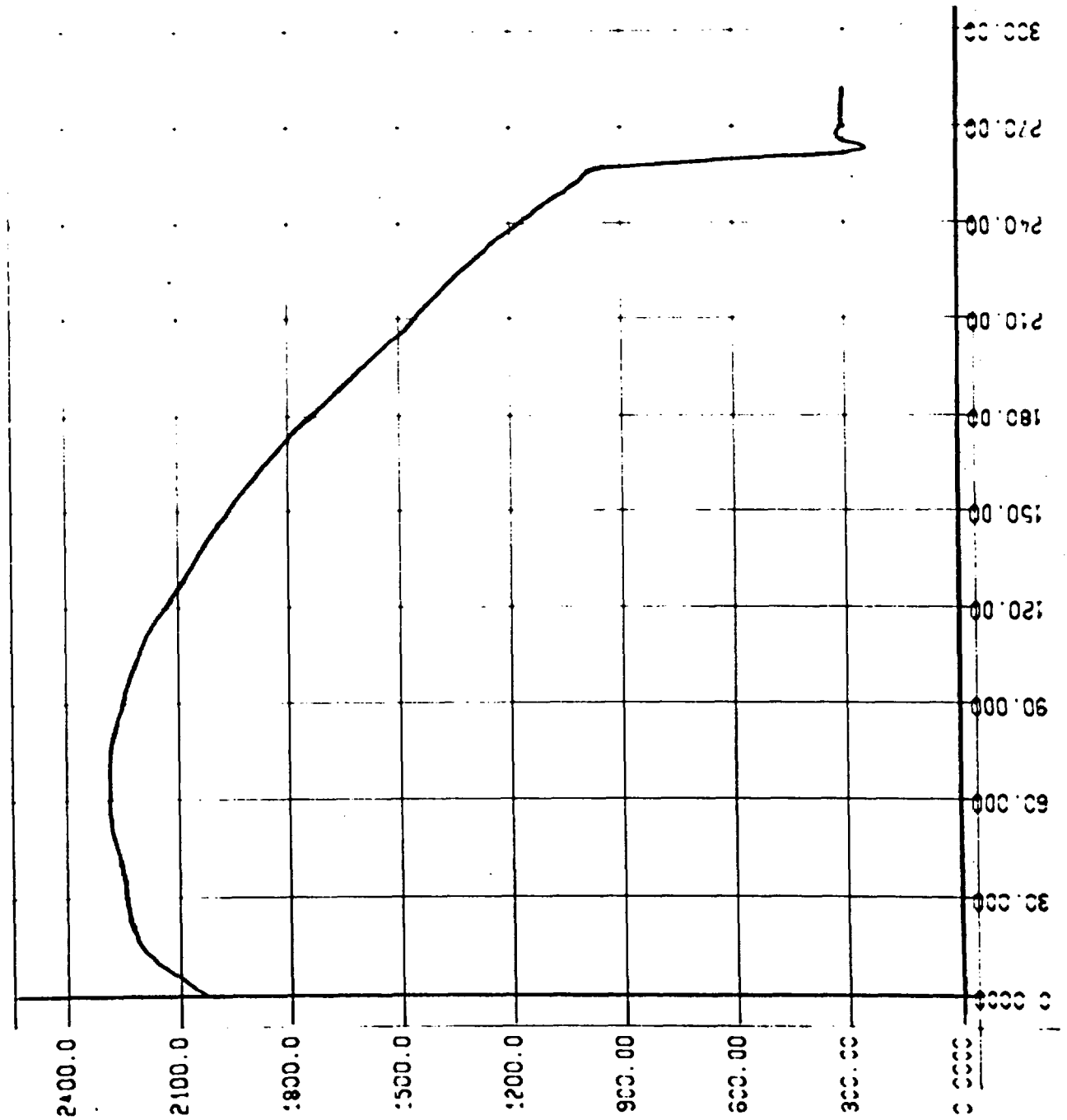

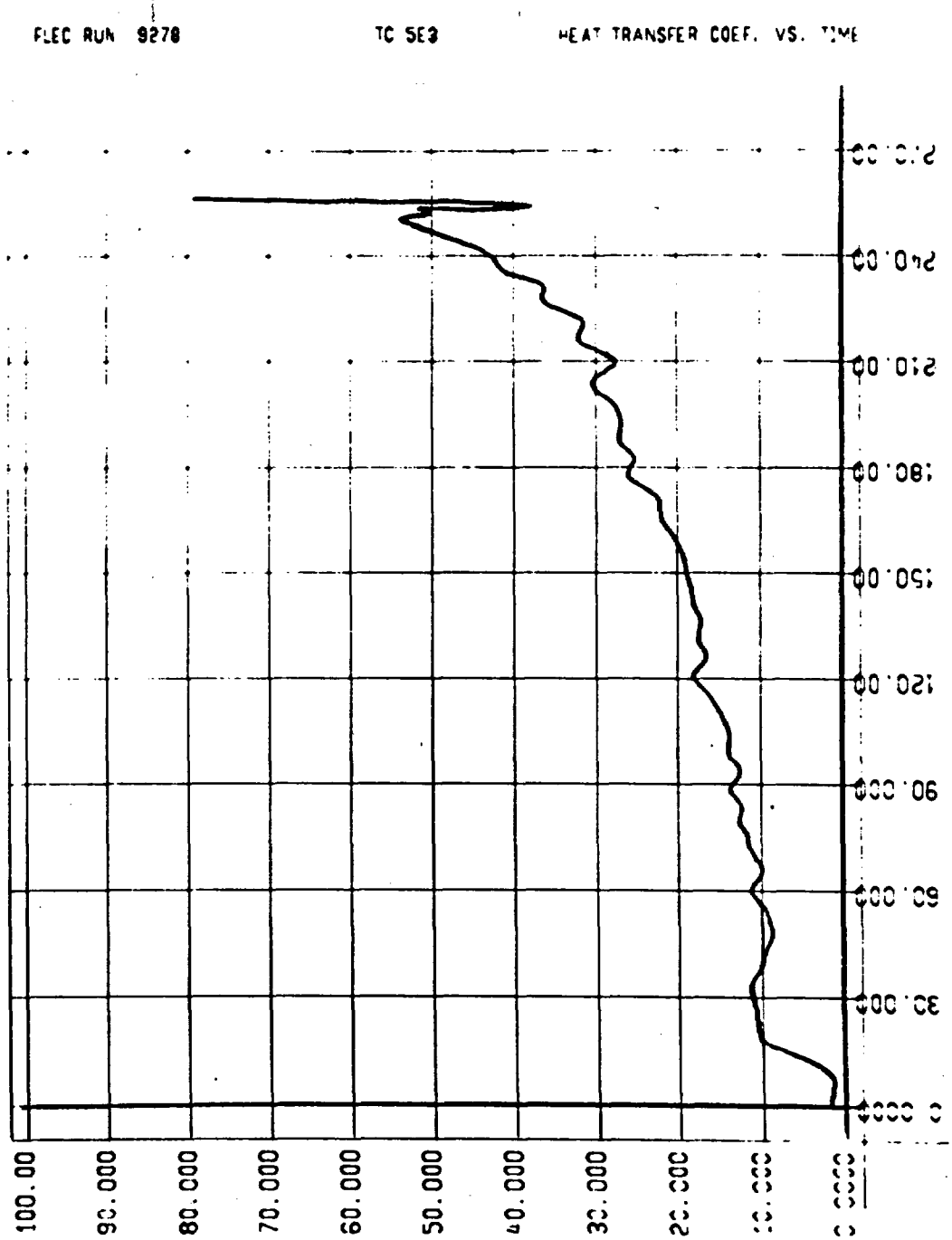
FLEC RUN 9278
TC 5E3
HEAT TRANSFER COEF. VS. TIME
100.00
90.000
80.000
70.000
60.000
50.000
40.000
30.000
20.000
10.000
0.0000
0.0000
30.000
60.000
90.000
120.00
150.00
180.00
210.00
240.00
270.00

FLECHT RUN SUMMARY SHEET

RUN NO. 9379

DATE 10/28/70

A. RUN CONDITIONS

Bundle Size and Clad	7 x 7* - SS
Initial Clad Temperature	2146 °F
Flooding Rate	6.0(4 sec)-1.0 in/sec
Peak Power	1.24 kw/ft
Decay Power	Curve B Figure 3-21
Inlet Coolant Temperature	145 °F
Pressure	61 psia
Flow Blockage	0 %

B. HOUSING TEMPERATURES

Elevation (ft)	Initial Temperature (°F)	Temperature at Quench Time of Hot Rod Midplane (252 Sec)
2	550	216
4	680	286
6	780	830
8	690	887
10	554	672

Initial T_{avg} Actual = 632 °F

* Rod 3D inoperative, Rod 5D failed at approximately 90 seconds after flooding.

FLECHT RUN SUMMARY SHEET

RUN NO. 9379 (Cont'd)

DATE 10/28/70

C. HEATER THERMOCOUPLE DATA

T/C No.	$T_{initial}$ (°F)	T_{Max_1} (°F)	ΔT_{rise_1} (°F)	t_{turn_1} (sec)	T_{Min} (°F)	t_{Min} (sec)	T_{Max_2} (°F)	ΔT_{rise_2} (°F)	t_{turn_2} (sec)	T_{quench} (°F)	t_{quench} (sec)
3C1	1202	1736	534	153	--	--	--	--	--	751	453
3C2	1799	1838	39	4	1823	8	2109	286	88	850	400
3C3	2066	2098	32	3	2067	8	2165	98	46	962	242
3C4	1822	1849	27	3	1817	9	1824	7	15	754	136
3C5	1164	1178	14	2	--	--	--	--	--	804	45
5B2	2229	2262	33	3	2216	9	2236	20	28	964	251
5B8	1845	1871	26	5	1867	8	2034	167	73	789	409
4F2	2086	2104	18	3	2077	9	2169	92	44	927	253
2E2	2072	2092	20	3	2079	9	2130	51	44	934	262
2B2	2078	2101	23	2	2073	8	2099	26	25	970	246
5E3	2146	2191	45	4	2145	8	2280	135	47	964	252

FLEC RUN 9379 TC 5E3 TCLAD VS. TIME

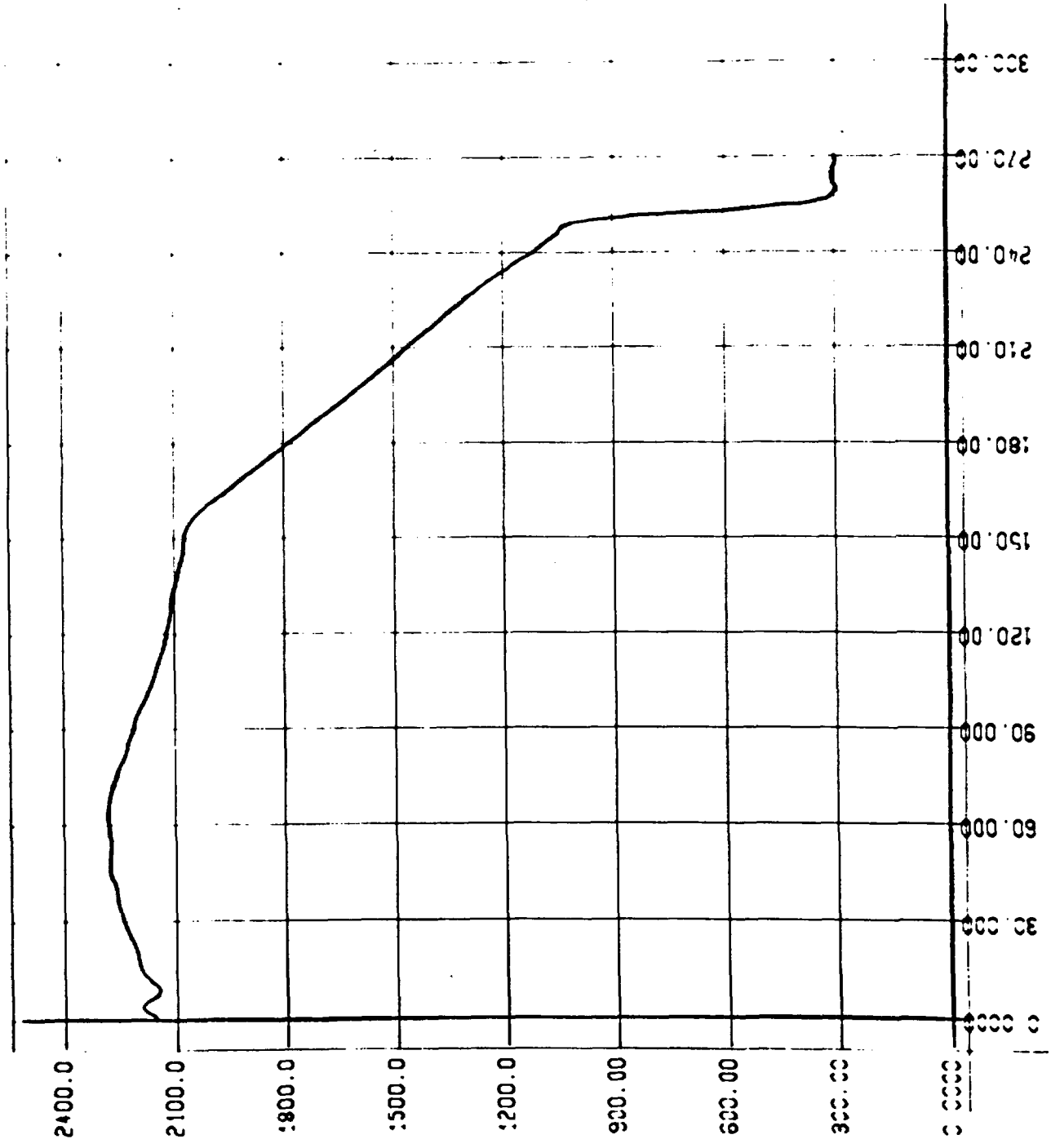

FLEC RUN 9379 TC 5E3 HEAT TRANSFER COEF. VS. TIME

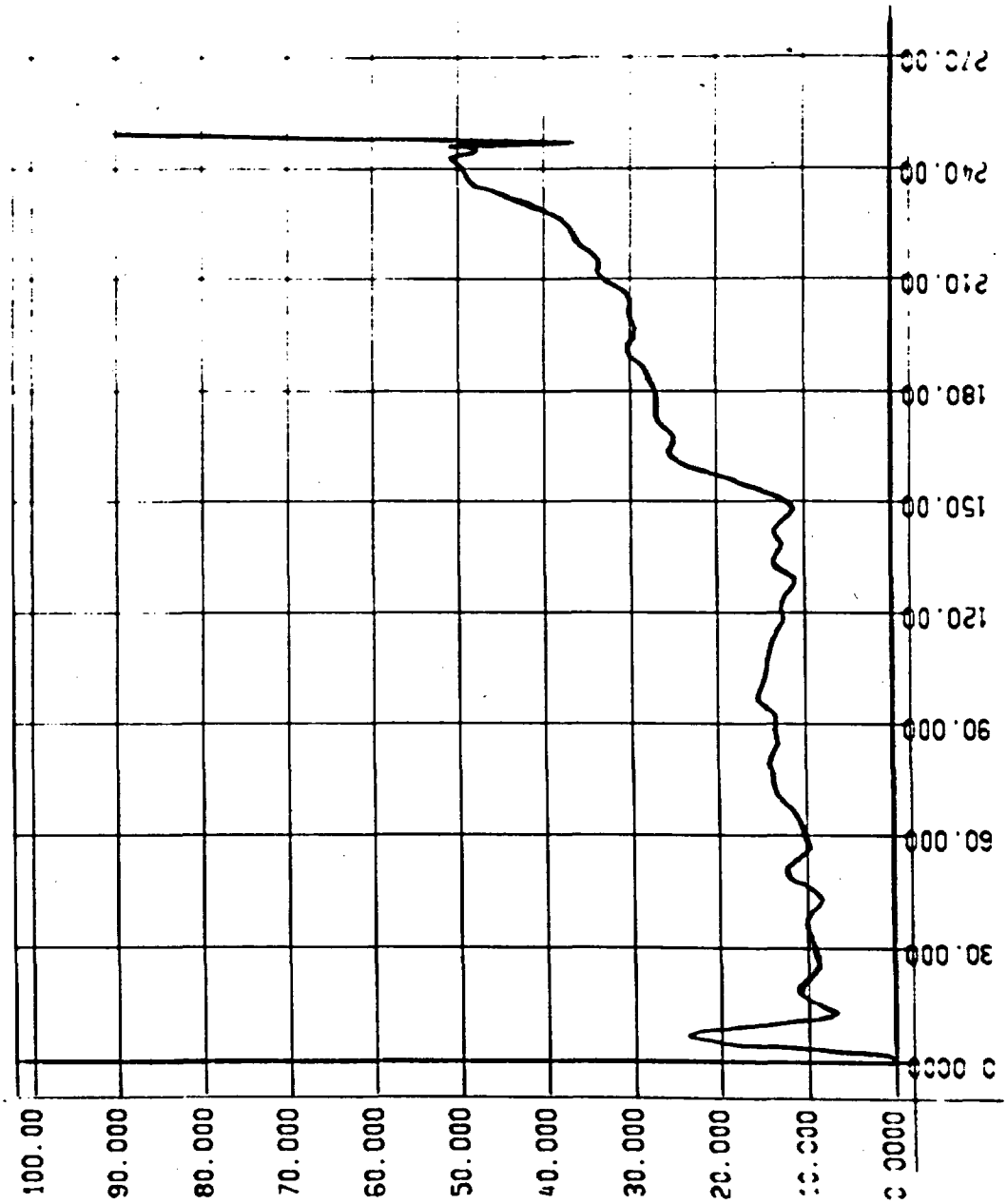

FLECHT RUN SUMMARY SHEET

RUN NO. 9573

DATE 12/11/70

A. RUN CONDITIONS

Bundle Size and Clad	7 x 7* - Zr-4
Initial Clad Temperature	1970 °F
Flooding Rate	1.1 in/sec
Peak Power	1.24 kw/ft
Decay Power	Curve B Figure 3-21
Inlet Coolant Temperature	140 °F
Pressure	61 psia
Flow Blockage	0%

B. HOUSING TEMPERATURES

Elevation (ft)	Initial Temperature (°F)	Temperature at Quench Time of Hot Rod Midplane (-- Sec)
2	522	--
4	660	--
6	738	--
8	670	--
10	533	--

Initial T_{avg} Actual = 604 °F

* Multiple heater rod failures starting at 18.2 seconds

FLECHT RUN SUMMARY SHEET

RUN NO. 9573 (Cont'd)

DATE 12/11/70

C. HEATER THERMOCOUPLE DATA

T/C Number	Initial Temp. (°F)	Temp 18 Sec (°F)
3D1	1191	1345
3D2	1715	1981
3D3*	1970	2320
3D4	1705	1948
3D5	1135	1204
2D2	1895	2208
1D2	1793	2024
3E3	--	--
4E1*	1230	1390
4E2	1744	2053
4E3	1901	2297
4E4	1571	1765
4E5	1030	1054
5E3	1813	2177

* Data from pen recorders

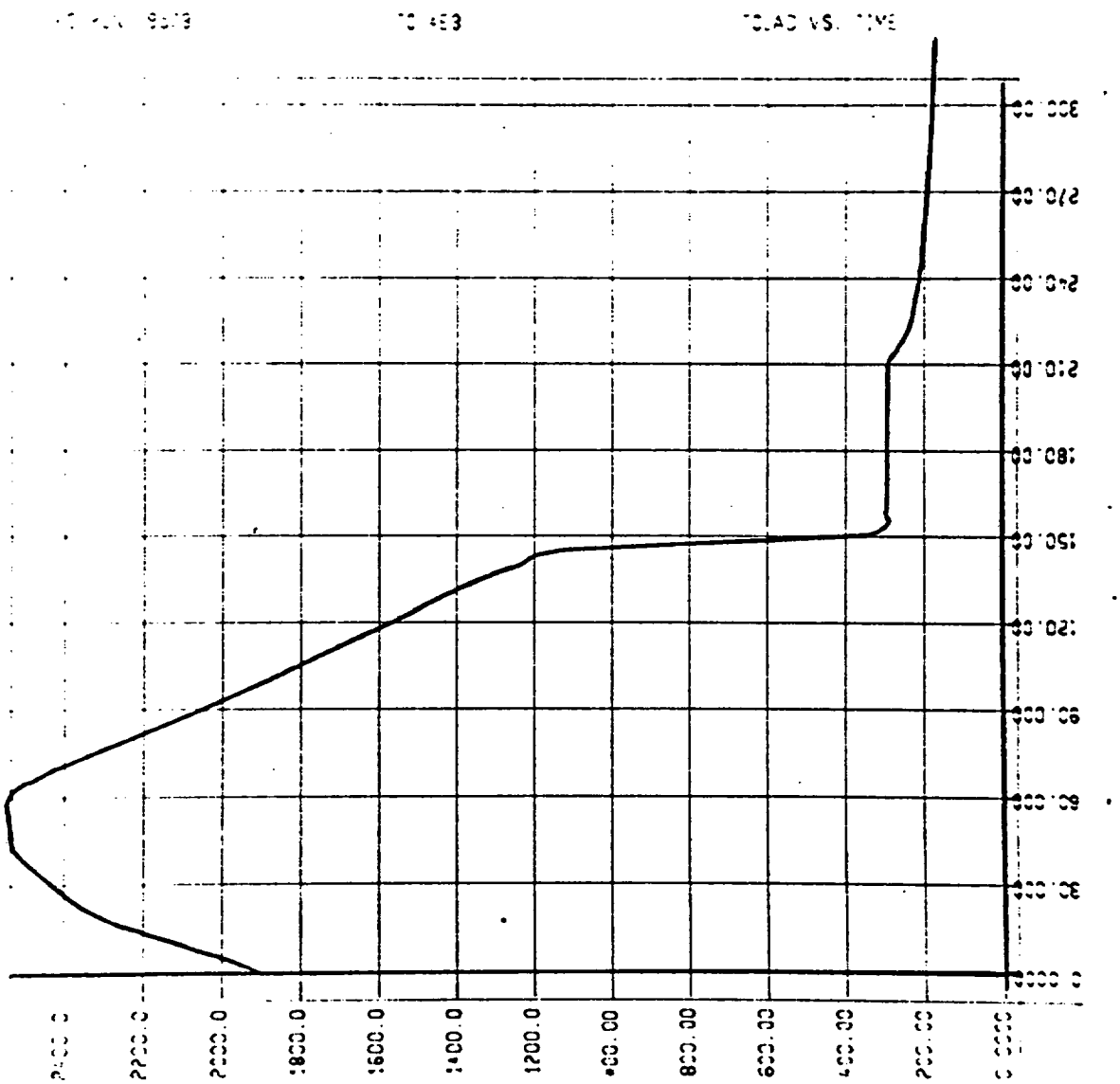
2400.0
2200.0
2000.0
1800.0
1600.0
1400.0
1200.0
1000.00
800.00
600.00
400.00
200.00
0.0000
0.0000
30.0000
60.0000
90.0000
120.0000
150.0000
180.0000
210.0000
240.0000
270.0000
300.0000

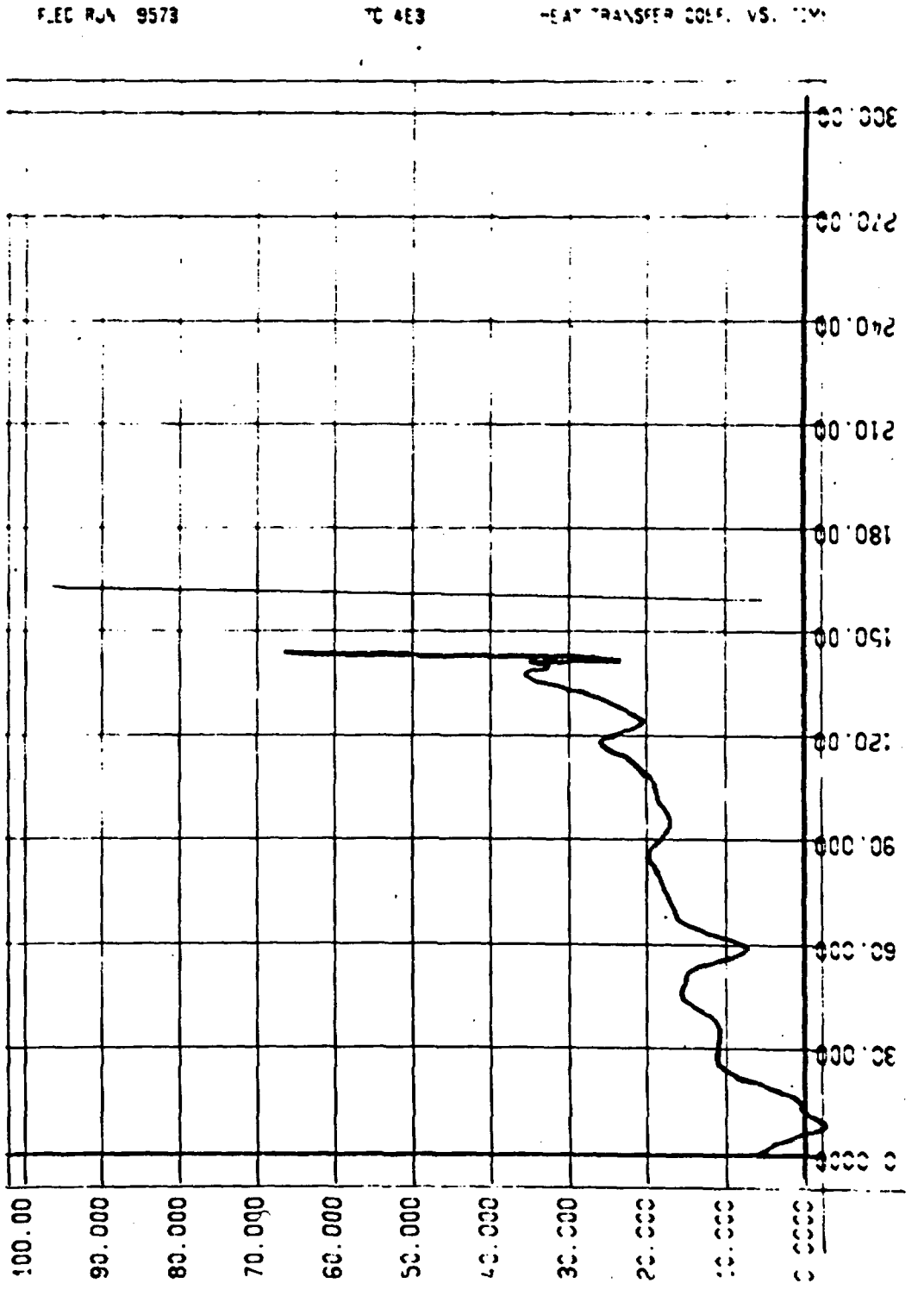
FLEC RUN 9573
TC 4E3
HEAT TRANSFER COEF. VS. TIME
100.00
90.000
80.000
70.000
60.000
50.000
40.000
30.000
20.000
10.000
0.0000
0.0000
30.000
60.000
90.000
120.00
150.00
180.00
210.00
240.00
270.00
300.00

Run 9573
ΔP Between 0 and 8 FT Elevations
(PT51 minus PT55)

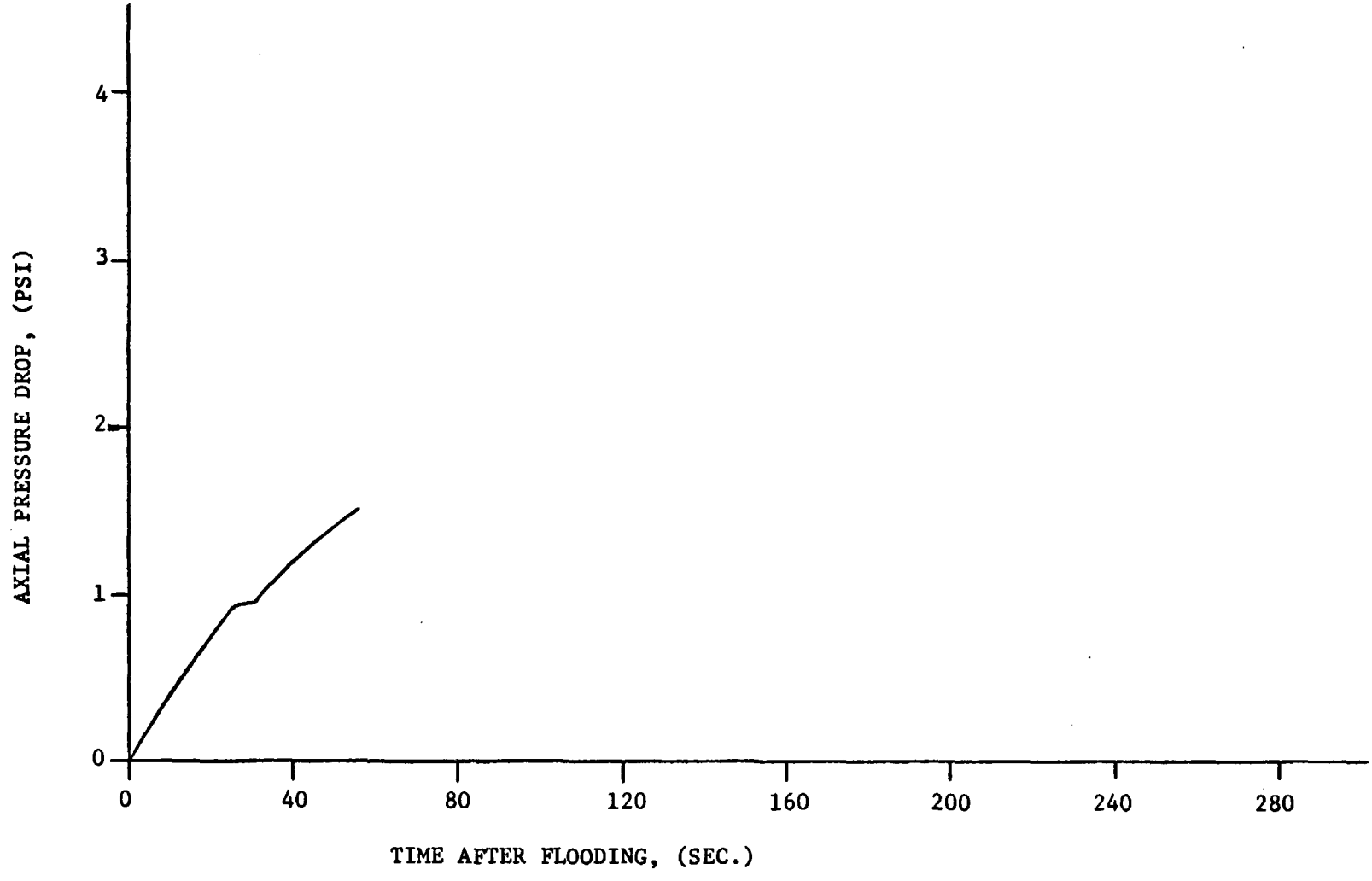

APPENDIX D

DERIVATION OF VARIABLE FLOODING RATE TIME SHIFT CORRELATIONS

(H. C. Yeh)

Equation (2) of Section 3.3.3 was derived based on the following reasoning.

If in Figure 3-56, the high flooding rate period t_v is extended further, it will eventually come to a point where the quench occurs in the high flooding rate period. However, this is exactly the same as the constant flow run with flooding rate V_{inH}. That is, one extreme case of a variable flooding rate run is a constant flow run with flooding rate V_{inH}. Now, the time shift, Δt_{vc}, for matching the heat transfer coefficient of a variable flooding rate run with that of a constant flooding rate run should approach and eventually become equal to the difference in quench time, Δt_q, between two constant flow runs with flooding rates V_{inH} and V_{inL}, respectively.

Figure D-1 shows a plot of Δt_q between two constant flow runs with flooding rates V_{in} ($\equiv V_{inL}$) = 1 in./sec and V_{in} ($\equiv V_{inH}$) = 2, 4, 6, and 10 in./sec, respectively (solid line). Schematic curves of the time shift, Δt_{vc}, for variable flow runs (dotted lines) which approach Δt_q as t_v (or ξ) increases are also included. Notice that instead of t_v, the integral

$$\xi \equiv \int_0^{t_v} \frac{(V_{inH} - V_{inL})}{V_{inL}} dt$$

is used as the abscissa. This term expresses the excess of water supplied to the channel during the high flooding rate period over that in the comparable low flooding rate run divided by V_{inL}. The Δt_q vs ξ curve levels off at 224 seconds for large ξ, which is less than the 267 second quench time of the constant flow

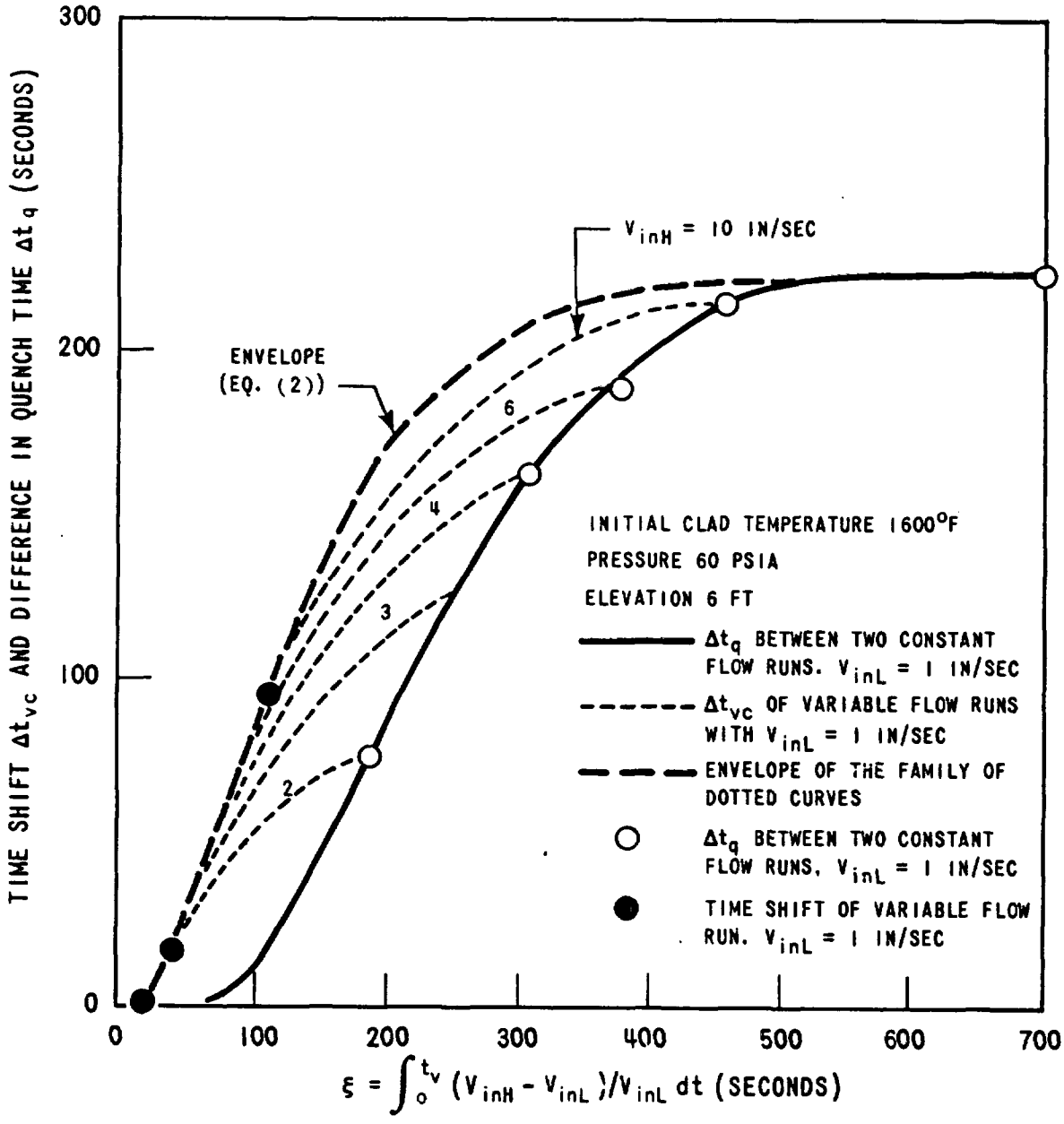

Figure D-1. Time Shift Relationship for V_{INL} = 1 In Sec, Midplane Elevation

run with V_{in} = 1 in./sec. This is because even at high flooding rates it takes a finite time for the quench front to move up to the 6 ft elevation. The time shift, Δt_{vc}, must therefore also level off at 224 sec for large V_{inH} since Δt_q is its limiting value. The envelope of the family of Δt_{vc} vs ξ curves (dashed line in Figure D-1) is the empircally determined time shift of the variable flow runs for all V_{inH} with t_v small in comparison with the quench time of the constant flow run with $V_{in} = V_{inH}$. Equation (2) was derived from the shape of this curve.

Figures D-2 through D-4 show the Δt_q vs ξ curves for V_{inL} = 1, 2, 4, and 6 in/sec at the 4, 6, and 8 ft elevations, respectively. The time shift, Δt_{vc}, predicted by Equation (2) is also shown in these figures. From these plots, it is seen that as V_{inL} increases, the Δt_q vs ξ curve extends toward the left. Thus the envelope of the family of Δt_{vc} vs ξ curves for large V_{inL} will also extend toward the left and the time shift, Δt_{vc}, for V_{inL} larger than 1 in./sec will be larger than that predicted by Equation (2) for small ξ. Equation (3) was therefore derived to fit the shape of the envelope of Δt_{vc} curves for V_{inL} larger than 1 in./sec.

Figure D-5 shows a comparison of the midplane time shifts computed by Equations (2), (3) and $\Delta t_{vc} = \xi$ and the required time shifts for matching seven variable flow runs with their comparable constant flooding rate runs. The agreement obtained can be seen to be quite good.

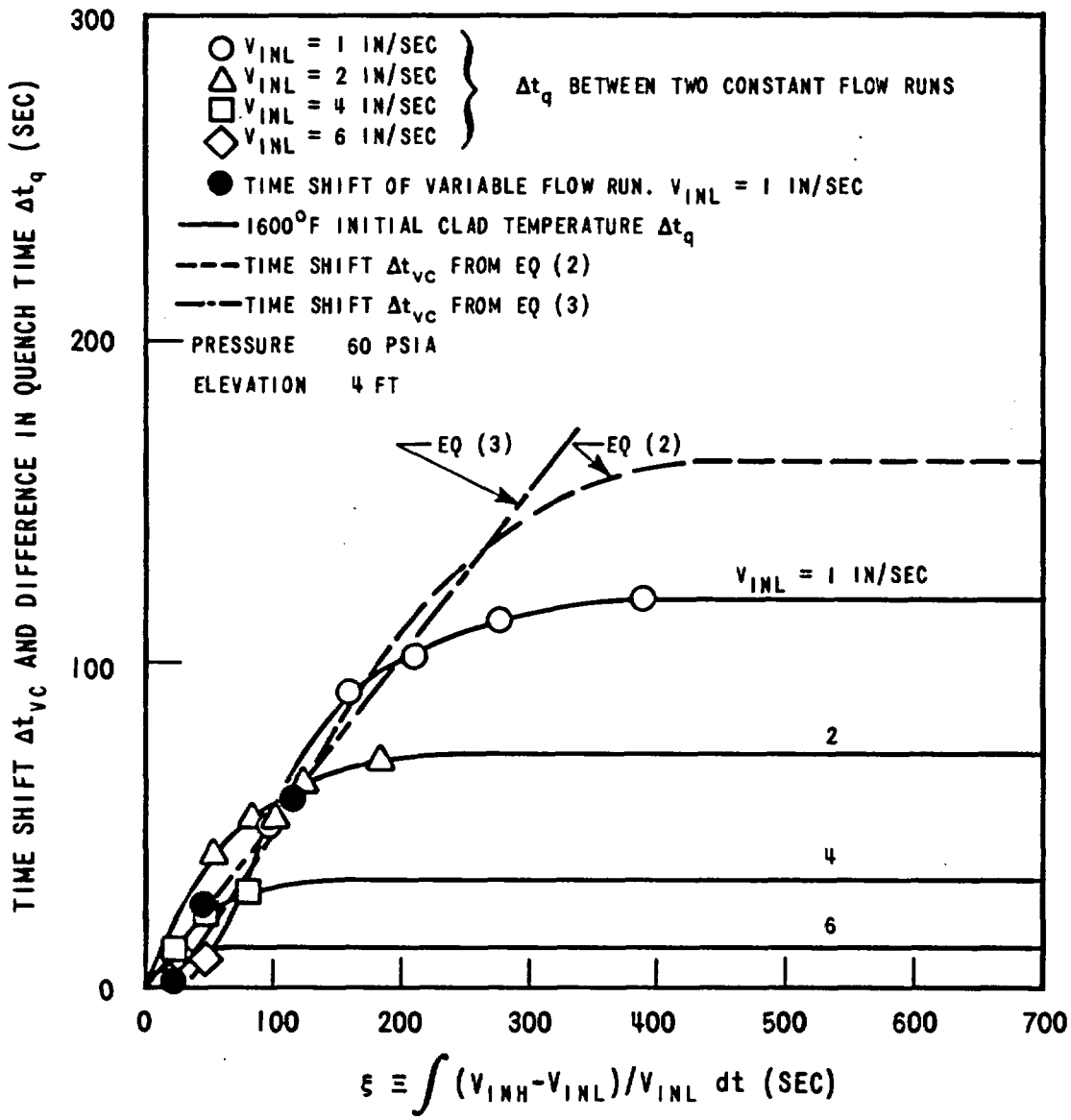

Figure D-2. Time Shift Relationships for Several V_{INL}, 4 FT Elevation

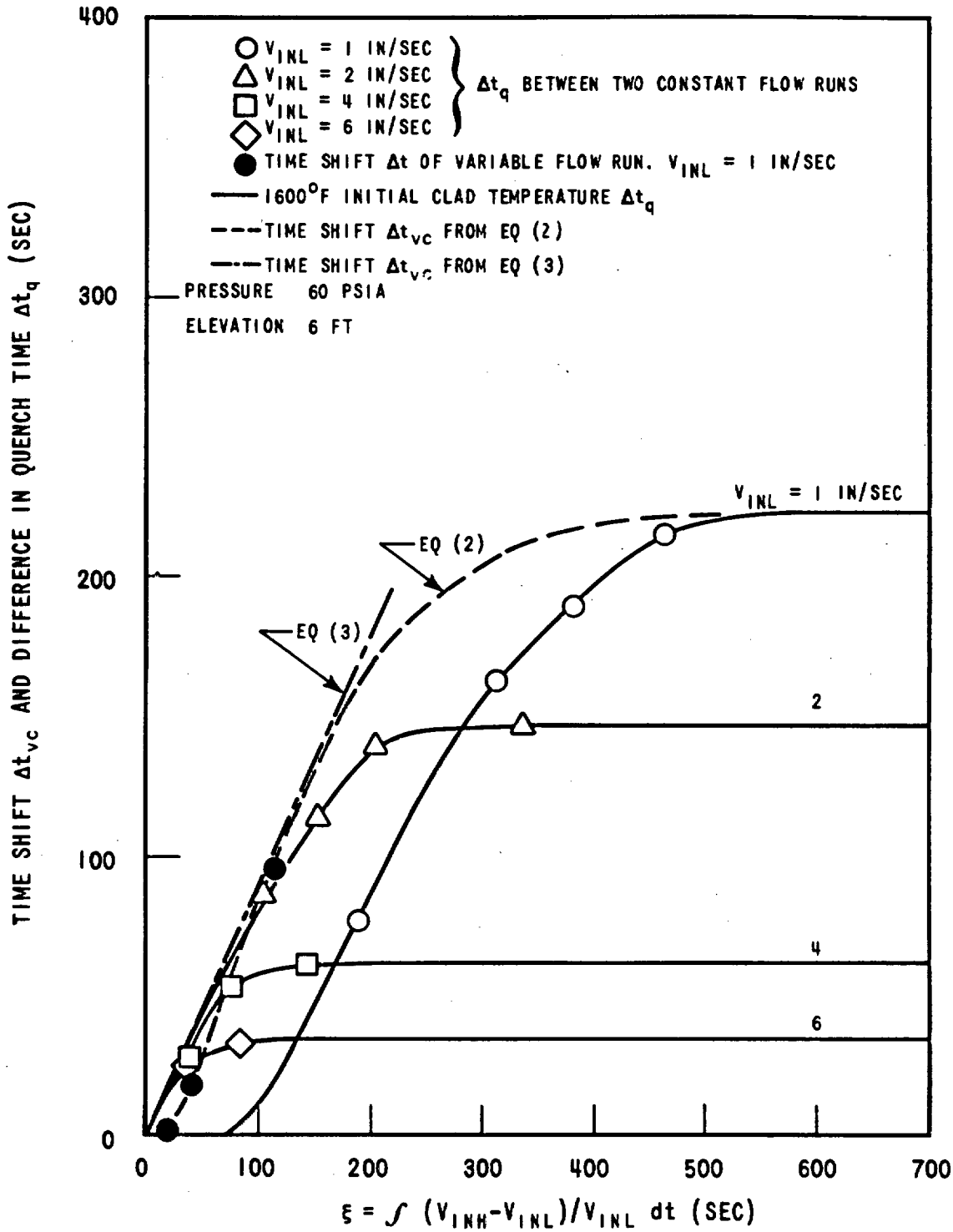

Figure D-3. Time Shift Relationships for Several V_{INL}. Midplane Elevation

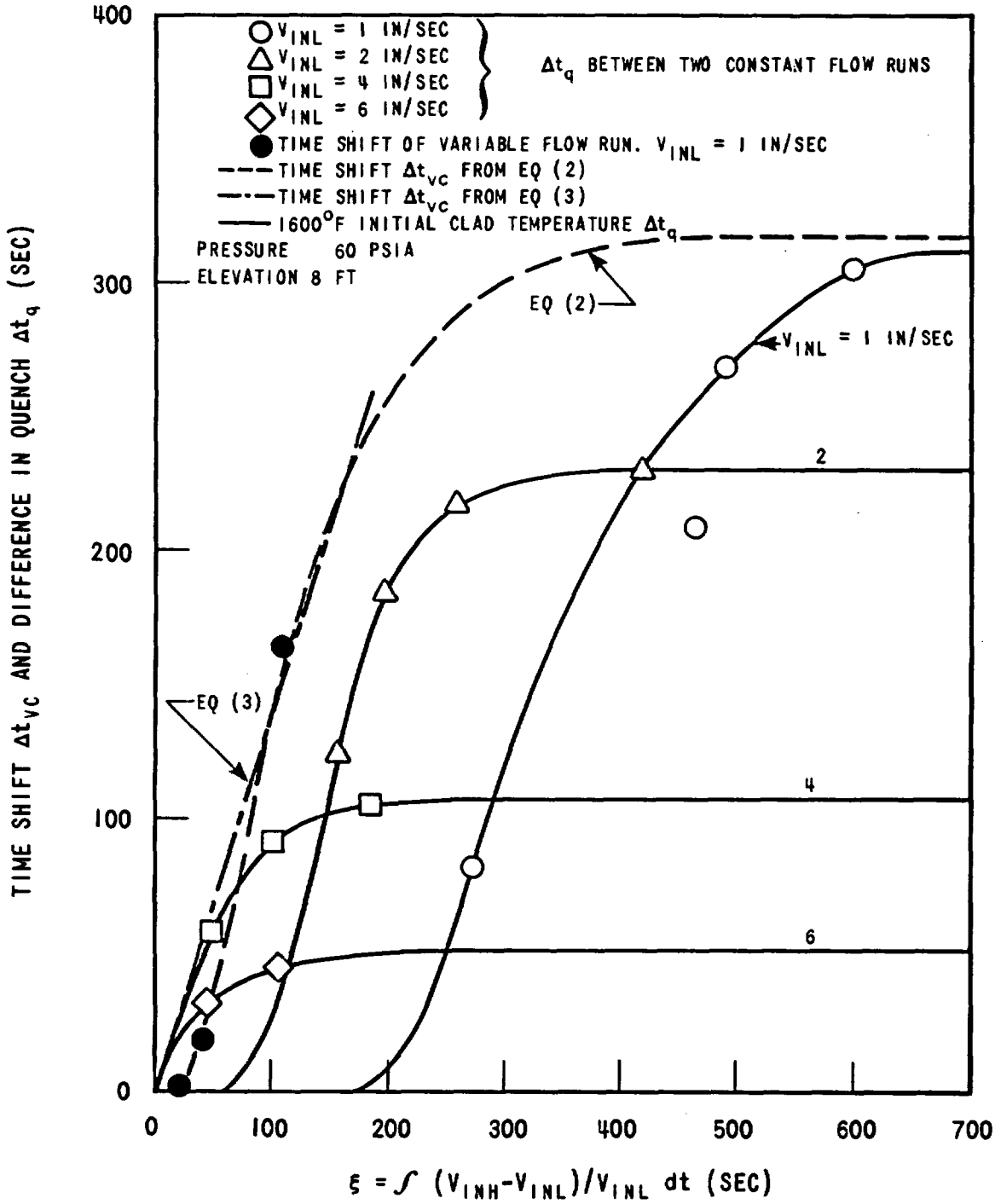

Figure D-4. Time Shift Relationships for Several V_{INL}, 8 FT Elevation

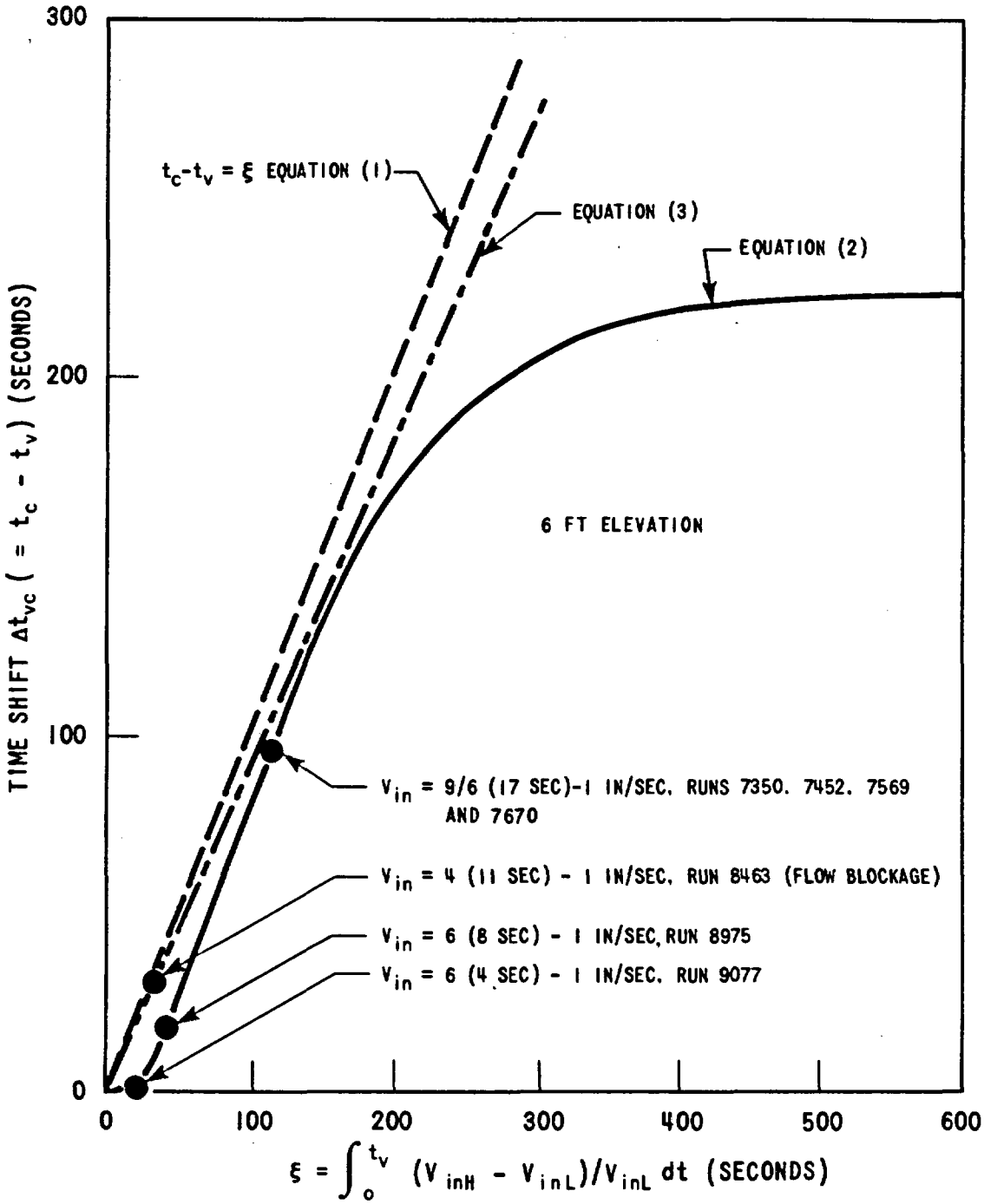

Figure D-5. Comparison of Equations (1), (2) and (3)

APPENDIX E

QUENCH TEMPERATURE DETERMINATION AND ANALYSIS

Most FLECHT transient temperature data was obtained by reading each heater rod thermocouple once during each VIDAR scan, or approximately once every four seconds. Due to the rapid rate of temperature change during quenching, this made a precise determination of quench temperature difficult. To overcome this problem, four thermocouples were read ten times each per VIDAR scan during Runs 6948, 7057 and 7158, or approximately once every half second. This enabled the temperature-time curve to be drawn more precisely and the quench temperature to be determined more accurately than was otherwise possible. (See Figure 3-44).

The shape of the curves thus obtained were then used to obtain more accurate quench temperature data for other selected thermocouples as shown in Figure E-1. The Group I and II data thus obtained is tabulated in Table E-1. Although there still is considerable scatter in the test data, the quench temperature was generally about 780°F at the 2, 4 and 6 ft elevations, 600°F at the 10 ft elevation and between 780°F and 600°F at the 8 ft elevation.

The effects of various system parameters on quench temperatures are shown in Figures E-2 through E-6. The possibility that any trends observed may have been due to local subcooling (computed by assuming the enthalpy rise is equal to the heater rod power) was investigated as shown in Figure E-7. In contrast to reported pool boiling data*, local coolant subcooling did not appear to have had a pronounced effect on quench temperature. Since the system parameter trends observed were generally quite small, the possibility still exists that they may be due, at least in part, to data scatter.

---

*W. S. Bradfield, "On the Effect of Subcooling on Wall Superheat in Pool Boiling," Journal of Heat Transfer, Trans. ASME, Series C, vol. 89, 269 (1967).

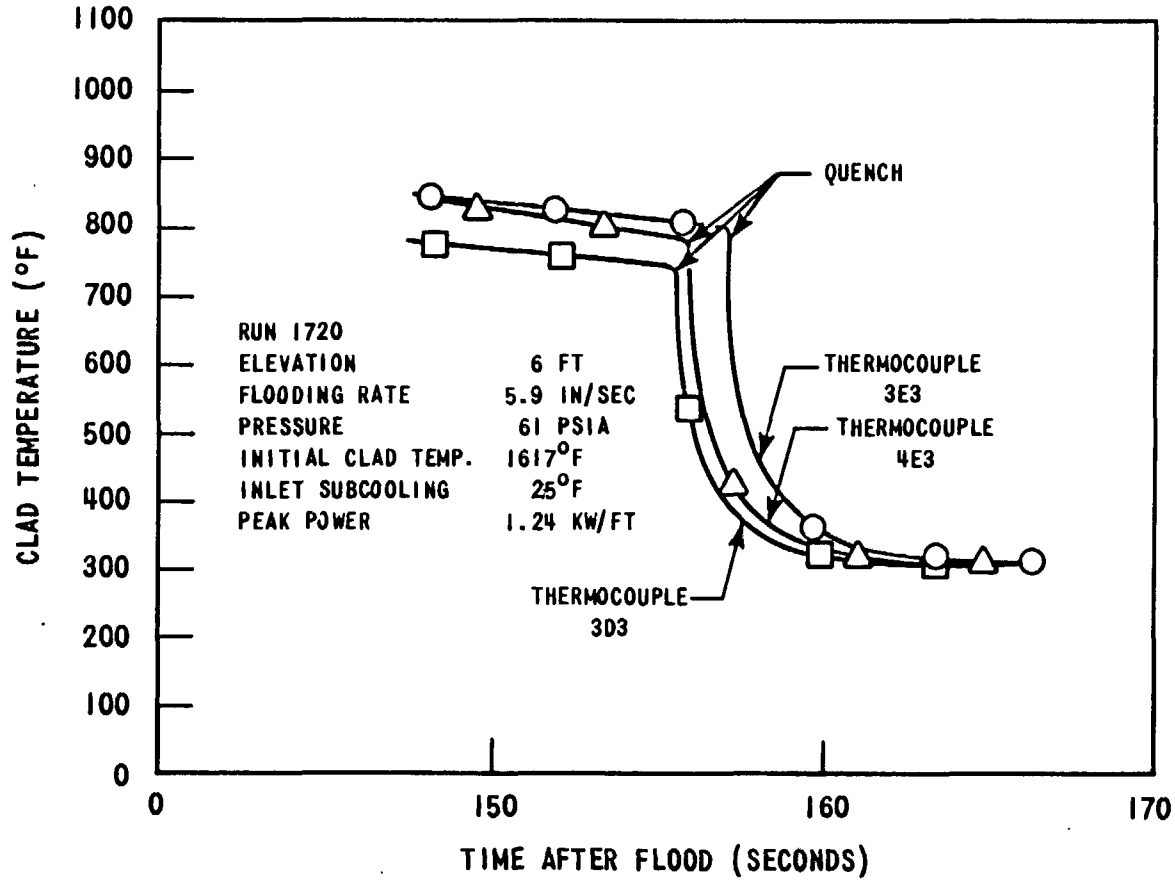

Figure E-1. Use of Multi-Scan Quench Curves to Determine Quench Temperatures

TABLE E-1

QUENCH TEMPERATURE DATA

7 x 7 Bundle

Run Number \ T/C No.	6 ft Elevation						2 ft Elevation			
	1D2	2D2	3D3	3E3	4G3	5E3	3D5	3E5	4E5	5E5
0105		700	740	665	760	630				
0408	800	785	795	815	915		690		690	685
0509	750	790	780	840	860	820	887	843	865	865
0711	810	845	865	850	930	940	810	770	800	770
1002		760	780	790	780	820	810	765	785	790
1116	725	740	745	765	830	790	825	790	790	785
1314	780					850	840	790	820	795
1417	740	745	765	800	775	770	825	810	790	800
1615	760	780	760	770	875		790	790	770	760
1720	730		740	795	785		720	810	695	710
1806	835					865	745	705	740	700
1902							770	845	755	750
6047	760	840	840	820	795	820	910	935	900	890
6155	780	835	870	830		820	895	900	885	865
6256	750	870	830	830	860	850	865	875	870	875
6948		1000	895		885	850	745	750	725	705
8975	925	935				950		850	870	860

10 x 10 Bundle

Run Number \ T/C No.	6 ft Elevation								2 ft Elevation			
	1F2	2F2	3F2	4F2	5F3	5G3	6G3	7G3	5F5	5G5	6G5	7G4
3440	770			760	795	765	760	735	655	680	665	680
3920					755			750	720	720	710	675
4027				695	715	715	740	705				
4129					840	855	865	840				
4225	775						810		770		740	705
4321				730	760				780		785	785
4442	815		765	770	800	790	805	775	845	875	850	825
4526			775		790	815	800	790				
4628	825		750	775	825	800	785					
4718				670	725				780	760	780	640

TABLE E-1

QUENCH TEMPERATURE DATA (Cont.)

7 x 7 Bundle

Run Number \ T/C No.	4 ft Elevation						8 ft Elevation			
	1D3	2D3	3D4	3E4	4E4	5E4	3D2	3E2	4E2	5E2
0408			840	845	870	845	685	710	695	690
0509	845	840	875	840	870	880	720	710	720	710
1002		790	790	780	820	780	670	670	630	625
1806							695	695	695	680
1902							660	650	630	655
6256	850	835	880	870	800	870	730	745	695	695
6948	770	790	915	865	850		720	730	795	810
8975	945	1030		780	790	800		790	815	765

10 x 10 Bundle

Run Number \ T/C No.	4 ft Elevation								8 ft Elevation			
	1F3	2F3	3F3	4F3	5F4	5G4	6G4	7G4	5F2	5G2	6G2	7G2
4225									745	725	745	745
4321				765	795		770		660	660	665	655

7 x 7 Bundle

Run Number \ T/C No.	10 ft Elevation					
	1D1	2D1	3D1	3E1	4E1	5E1
0408			645	560		
1002		495	630	600		
6948			715	725	820	

10 x 10 Bundle

Run Number \ T/C No.	10 ft Elevation							
	1F1	2F1	3F1	4F1	5F1	5G1	6G1	7G1
4225								
4321				605	685	705		

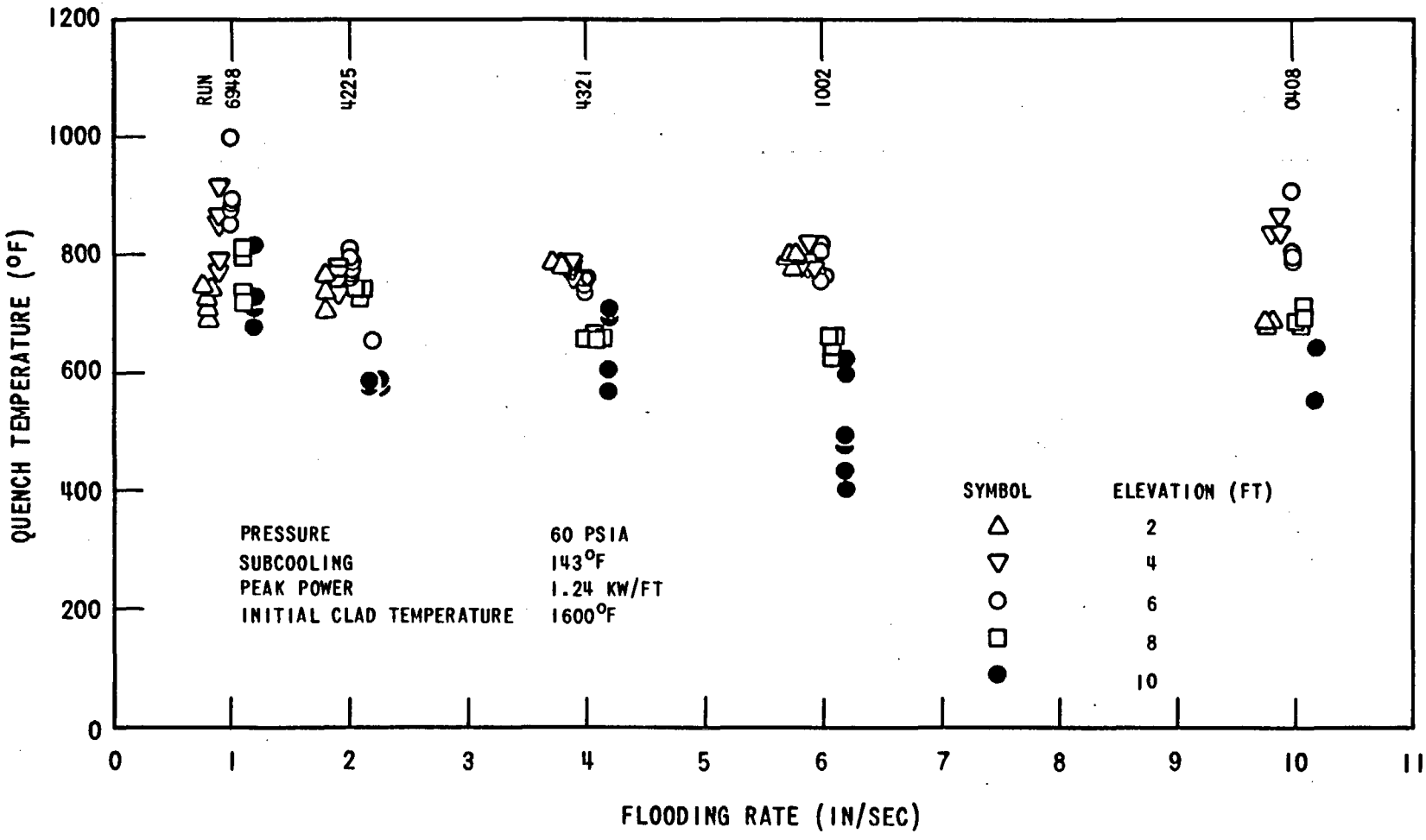

Figure E-2. Effect of Flooding Rate V_{in} on Quench Temperature

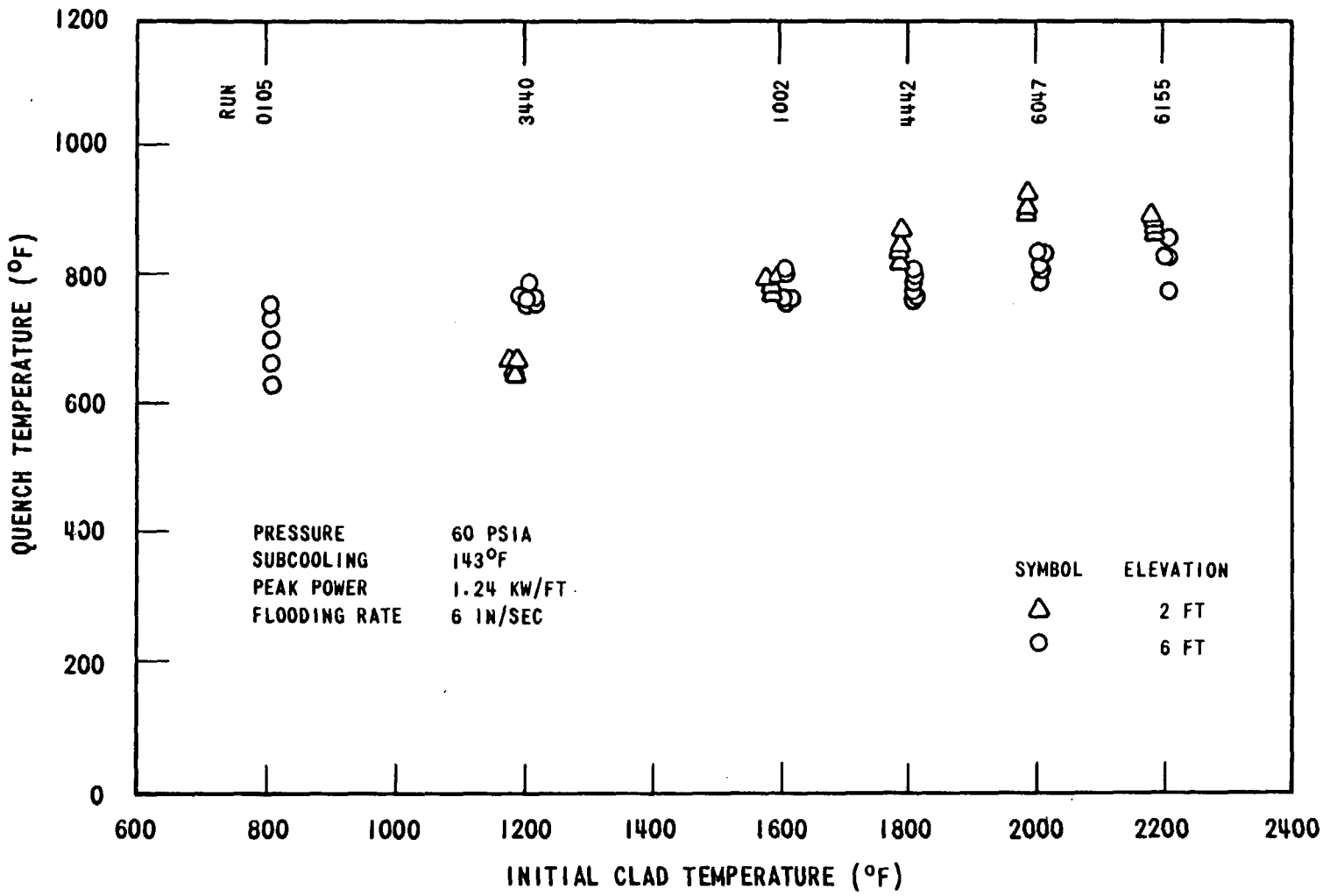

Figure E-3. Effect of Initial Clad Temperature on Quench Temperature

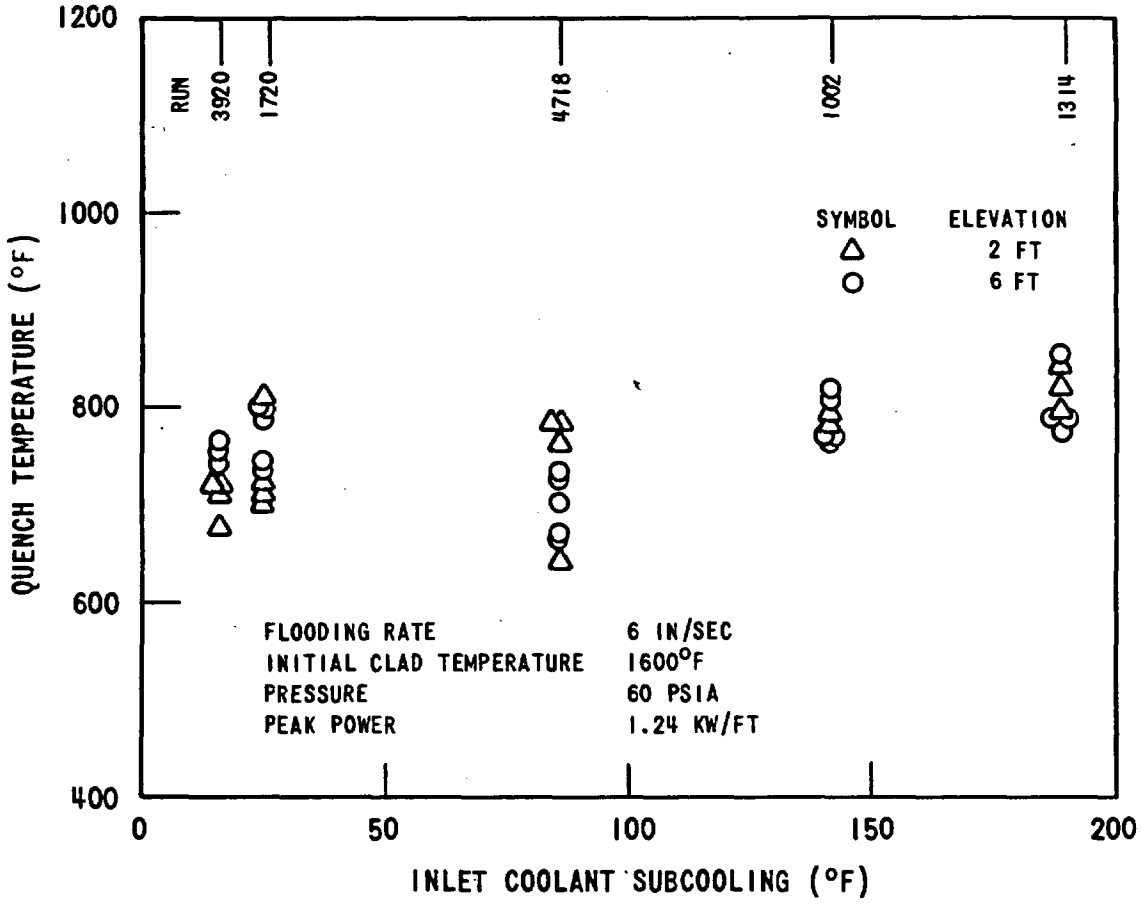

Figure E-4. Effect of Inlet Coolant Subcooling on Quench Temperature

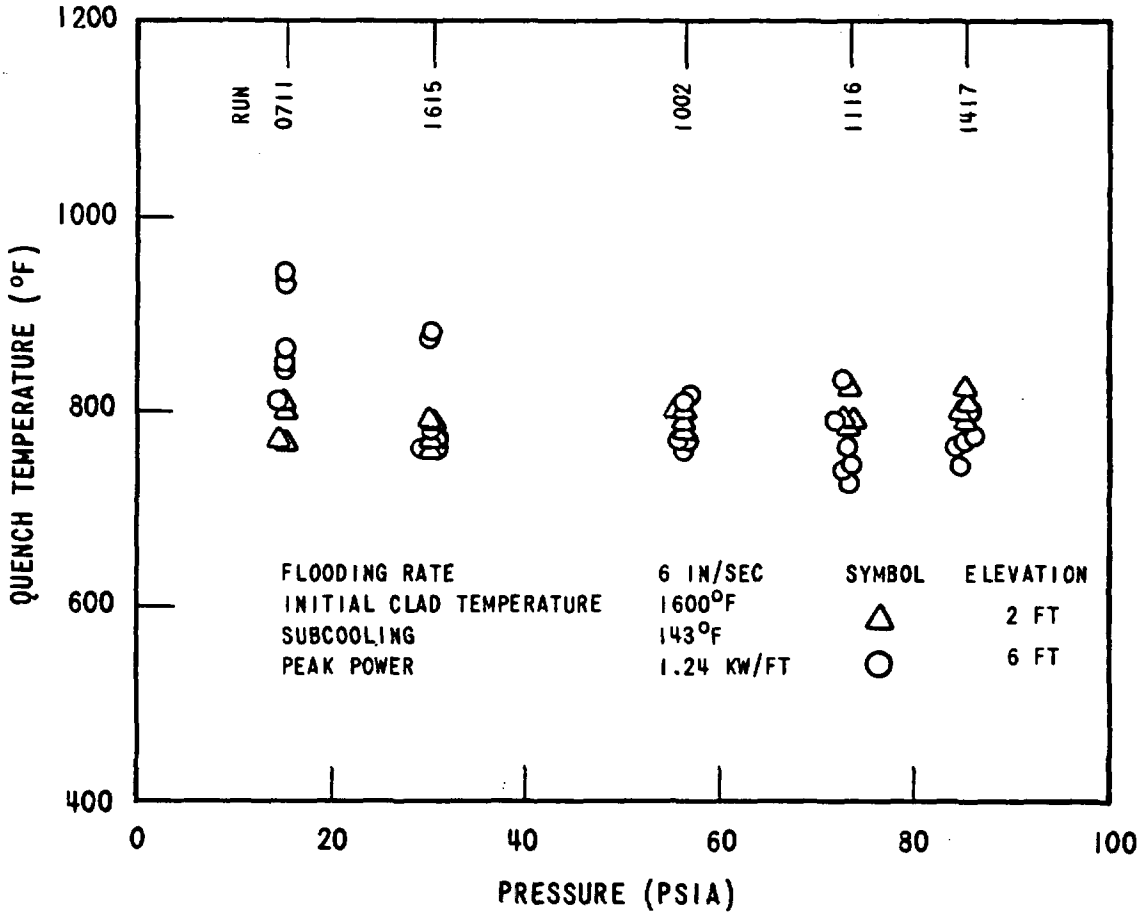

Figure E-5. Effect of Pressure on Quench Temperature

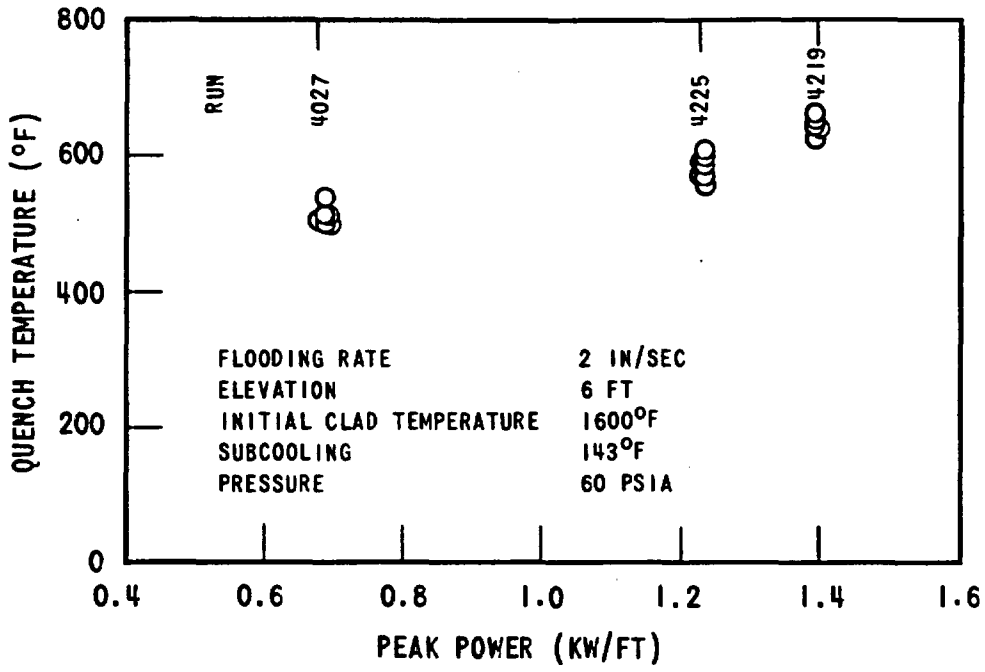

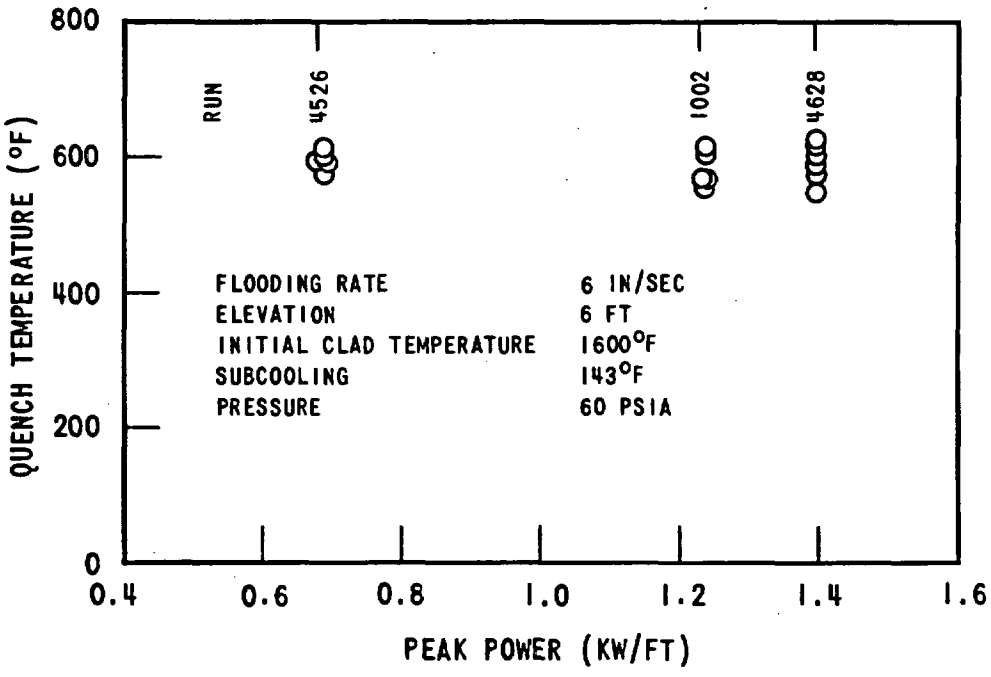

Figure E-6. Effect of Peak Power on Quench Temperature

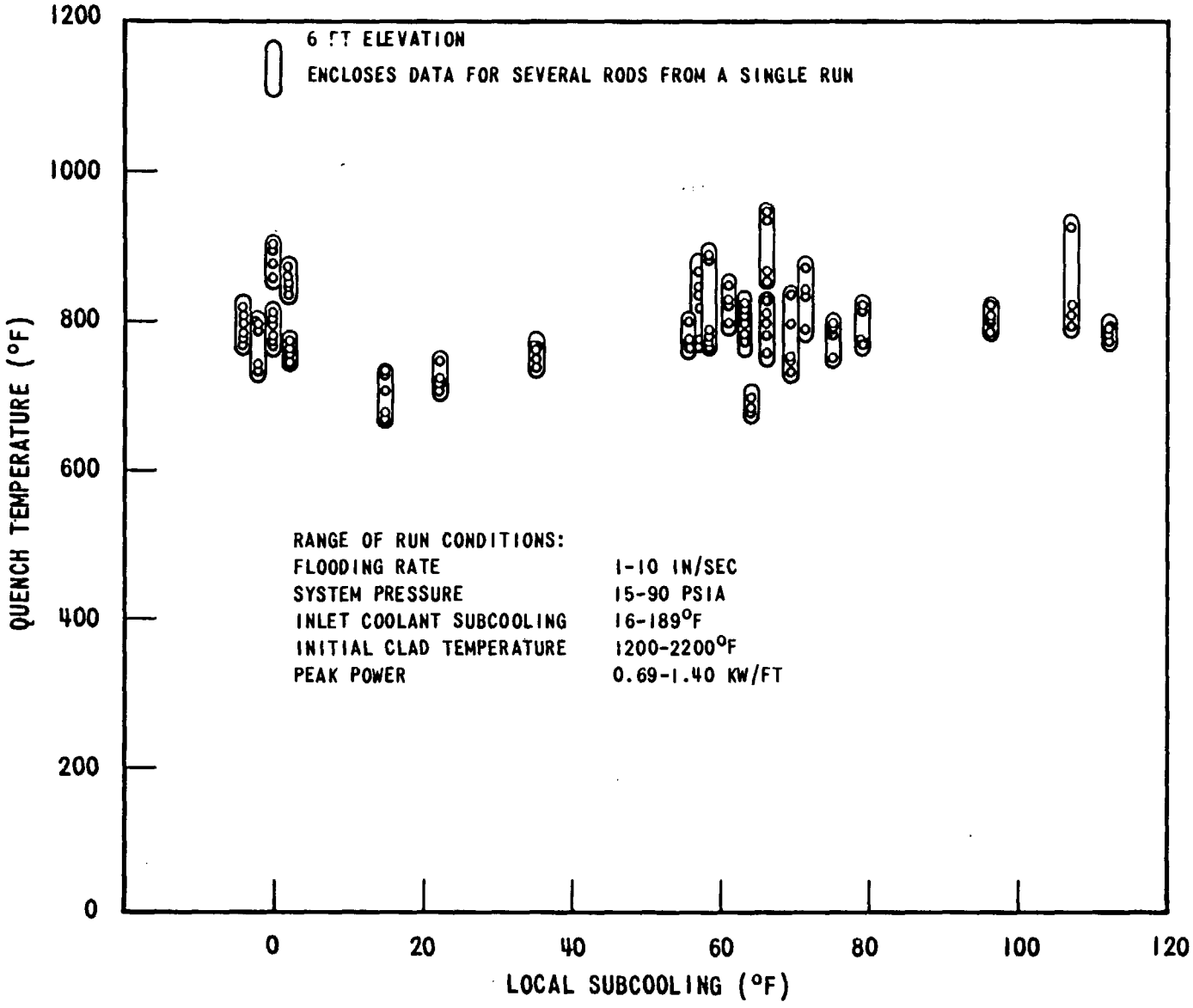

Figure E-7. Effect of Local Subcooling on Quench Temperature